Dissertation

submitted to the

Combined Faculty of Mathematics, Engineering and Natural Sciences

of Heidelberg University, Germany

and to the

Department of Physics

of the University of Trento, Italy

for the degree of

Doctor of Natural Sciences

Put forward by

Kevin Thomas Geier

born in: Mosbach, Germany

Oral examination: July 21, 2022

Probing Dynamics and Correlations in Cold-Atom Quantum Simulators

Supervisors:	Philipp Hauke
	Jürgen Berges
Referees:	Lauriane Chomaz
	José Ramon Crespo López-Urrutia

Abstract

Cold-atom quantum simulators offer unique possibilities to prepare, manipulate, and probe quantum many-body systems. However, despite the high level of control in modern experiments, not all observables of interest are easily accessible. This thesis aims at establishing protocols to measure currently elusive static and dynamic properties of quantum systems. The experimental feasibility of these schemes is illustrated by means of numerical simulations for relevant applications in many-body physics and quantum simulation. In particular, we introduce a general method for measuring dynamical correlations based on non-Hermitian linear response. This enables unbiased tests of the famous fluctuation–dissipation relation as a probe of thermalization in isolated quantum systems. Furthermore, we develop ancilla-based techniques for the measurement of currents and current correlations, permitting the characterization of strongly correlated quantum matter. Another application is geared towards revealing signatures of supersolidity in spin–orbit-coupled Bose gases by exciting the relevant Goldstone modes. Finally, we explore a scenario for quantum-simulating post-inflationary reheating dynamics by parametrically driving a Bose gas into the regime of universal far-from-equilibrium dynamics. The presented protocols also apply to other analog quantum simulation platforms and thus open up promising applications in the field of quantum science and technology.

Zusammenfassung

Quantensimulatoren auf Basis ultrakalter Atome eröffnen einzigartige Möglichkeiten zur Präparation, Manipulation und Untersuchung von Quanten-Vielteilchen-Systemen. Trotz des hohen Maßes an Kontrolle in modernen Experimenten sind jedoch nicht alle interessanten Observablen auf einfache Weise zugänglich. Ziel dieser Arbeit ist es, Protokolle zur Messung aktuell nur schwer erfassbarer statischer und dynamischer Eigenschaften von Quantensystemen zu etablieren. Die experimentelle Realisierbarkeit dieser Verfahren wird durch numerische Simulationen anhand relevanter Anwendungen in der Vielteilchenphysik und Quantensimulation veranschaulicht. Insbesondere wird eine allgemeine Methode zur Messung dynamischer Korrelationen basierend auf der linearen Antwort auf nicht-hermitesche Störungen vorgestellt. Diese ermöglicht unabhängige Tests des berühmten Fluktuations-Dissipations-Theorems als Indikator der Thermalisierung isolierter Quantensysteme. Darüber hinaus werden Verfahren zur Messung von Strömen und Strom-Korrelationen mittels Kopplung an einen Hilfszustand entwickelt, welche die Charakterisierung stark korrelierter Quantenmaterie erlauben. Eine weitere Anwendung zielt auf die Enthüllung spezifischer Merkmale von Supersolidität in Spin-Bahn-gekoppelten Bose-Einstein-Kondensaten ab, indem die relevanten Goldstone-Moden angeregt werden. Schließlich wird ein Szenario zur Quantensimulation post-inflationärer Thermalisierungsdynamik durch die parametrische Anregung eines Bose-Gases in das Regime universeller Dynamik fern des Gleichgewichts erschlossen. Die dargestellten Protokolle lassen sich auch auf andere Plattformen für analoge Quantensimulation übertragen und eröffnen damit vielversprechende Anwendungen auf dem Gebiet der Quantentechnologie.

Sommario

I simulatori quantistici ad atomi freddi offrono possibilità uniche per preparare, manipolare e sondare sistemi quantistici a molti corpi. Tuttavia, nonostante l'alto livello di controllo raggiunto negli esperimenti moderni, non tutte le osservabili di interesse sono facilmente accessibili. Lo scopo di questa tesi è quello di stabilire protocolli per misurare delle proprietà statiche e dinamiche dei sistemi quantistici attualmente inaccessibili. La fattibilità sperimentale di questi schemi è illustrata mediante simulazioni numeriche per applicazioni rilevanti nella fisica a molti corpi e nella simulazione quantistica. In particolare, introduciamo un metodo generale per misurare le correlazioni dinamiche basato su una risposta lineare non hermitiana. Ciò consente test imparziali della famosa relazione fluttuazione-dissipazione come sonda di termalizzazione in sistemi quantistici isolati. Inoltre, sviluppiamo tecniche basate su ancilla per la misura di correnti e correlazioni di corrente, consentendo la caratterizzazione della materia quantistica fortemente correlata. Un'altra applicazione è orientata a rivelare l'impronta della supersolidità nei gas Bose con accoppiamento spin-orbita eccitando il corrispondente modo di Goldstone. Infine, esploriamo uno scenario per la simulazione quantistica della dinamica di riscaldamento post-inflazione modulando parametricamente un gas Bose e portandolo nel regime della dinamica universale lontana dall'equilibrio. I protocolli presentati si applicano anche ad altre piattaforme di simulazione quantistica analogica e aprono quindi applicazioni promettenti nel campo della scienza e della tecnologia quantistica.

Contents

List of Publications

Parts of the results presented in this thesis have been published in peer-reviewed journals and on preprint repositories, or represent work in preparation for publication, as listed below. Some figures and parts of the text have been taken verbatim from these sources. The following list specifies my personal contributions to studies involving collaborations with other researchers. Any results contributed by co-authors of these works are indicated as such by appropriate citations in the text.

- A. Chatrchyan, K. T. Geier, M. K. Oberthaler, J. Berges, and P. Hauke, "Analog cosmological reheating in an ultracold Bose gas," Phys. Rev. A **104**, 023302 (2021).

  A.C. and I share co-first authorship of this publication. My personal contributions were focused on the realization of the cosmological reheating scenario in the ultracold Bose gas. I implemented and conducted all classical–statistical simulations to investigate the accessible (p)reheating-like phenomena in the cold-atom system. My contributions further include the analytical description of parameteric resonances within Gross–Pitaevskii theory, the extraction and analysis of growth rates of primary and secondary instabilities from the numerical data, the extraction of scaling exponents in prescaling and universal regimes using the method of moments, as well as the discussion of experimental perspectives. Parts of the results are also published in A.C.'s PhD thesis [1].

- K. T. Geier, G. I. Martone, P. Hauke, and S. Stringari, "Exciting the Goldstone modes of a supersolid spin–orbit-coupled Bose gas," Phys. Rev. Lett. **127**, 115301 (2021).

  I implemented, conducted, and analyzed all Gross–Pitaevskii simulations to probe equilibrium and dynamical properties of trapped spin–orbit-coupled Bose–Einstein condensates as well as to reveal the emergence of new Goldstone modes in the supersolid phase.

- K. T. Geier and P. Hauke, "From non-Hermitian linear response to dynamical correlations and fluctuation–dissipation relations in quantum many-body systems," arXiv:`2104.03983 [cond-mat.quant-gas]` (2021).

  I worked out the analytical derivation of the non-Hermitian linear response scheme, its proposed realization via the quantum Zeno effect, as well as cross-connections to weak measurements and other schemes. Furthermore, I implemented, conducted, and analyzed all numerical simulations to benchmark the protocols and to illustrate their application to the measurement of fluctuation–dissipation relations.

- K. T. Geier, J. Reichstetter, and P. Hauke, "Non-invasive measurement of currents in analog quantum simulators," arXiv:2106.12599 [quant-ph] (2021).

  This paper is based on preliminary work of the Bachelor's thesis by J.R. [2], who I co-supervised together with P.H. J.R. and I share co-first authorship of this publication. My personal contributions include the design and theoretical derivation of the measurement scheme, the implementation, conduction, and analysis of numerical benchmark simulations, as well as the development of practicable extensions to other platforms and more general observables like current correlations.

- A. Salzinger, K. T. Geier, T. Franz, S. Geier, N. Thaicharoen, A. Tebben, C. Hainaut, R. Ott, M. Gärttner, G. Zürn, P. Hauke, and M. Weidemüller, "There and back again: controlled dephasing and unequal-time correlations in Rydberg qubits," in preparation (2022).

  My contributions to the upcoming publication include the conceptual design and theoretical derivation of the non-Hermitian linear response scheme. Furthermore, I conducted numerical simulations to explore the prospects for probing many-body physics within the experimental capabilities.

List of Figures

List of Abbreviations

BEC Bose–Einstein condensate

ETH eigenstate thermalization hypothesis

FDR fluctuation–dissipation relation

FLRW Friedmann–Lemaître–Robertson–Walker

GPE Gross–Pitaevskii equation

KMS Kubo–Martin–Schwinger

MI Mott insulator

NTFP non-thermal fixed point

ODE ordinary differential equation

RF radio frequency

SDE stochastic differential equation

SF superfluid

SOC BEC spin–orbit-coupled Bose–Einstein condensate

TOF time-of-flight

UV ultraviolet

Introduction

The success of quantum theory has not only revolutionized our view of the world, but it has also enabled major technological breakthroughs. Nowadays, considerable research efforts are geared towards what can arguably be regarded as the holy grail of quantum science and technology: the quantum computer. The vision is to harness and control the peculiar properties of quantum systems like superpositions and entanglement in order to solve real-world problems that are intractable on even the fastest classical computers [3]. Despite major technological and conceptual breakthroughs as well as huge investments of financial and intellectual resources, the development of a scalable and error-corrected digital quantum computing architecture remains a long-term endeavor. However, present-day quantum devices, e.g., based on cold atoms, trapped ions, or superconducting qubits, enable another application that promises a quantum advantage: quantum simulation. Simulating quantum many-body systems is an inherently difficult task due to the exponential growth of the quantum mechanical state space. Already systems of moderate sizes easily exceed both the memory resources and compute capabilities of modern supercomputers[1], such that the simulation of large-scale systems is completely out of reach on any classical machine. A seminal proposal by R. Feynman in 1982 points towards a possible way out [5]: the idea is to simulate a quantum system using a device which itself is governed by the rules of quantum mechanics, a so-called quantum simulator. Such quantum simulators are special-purpose devices that are designed to simulate a special class of target models, often in an analog (as opposed to digital) way. They should allow for easy and reproducible state preparation, precise control to adjust model parameters and manipulate the quantum state, as well as comprehensive readout of the observables of interest [6]. Remarkably, quantum devices currently available in many laboratories across the world have matured to a level where non-trivial applications for quantum simulation purposes are in reach. While system sizes of most setups to date are still moderate such that benchmarks with traditional numerical methods are possible (and actually needed to make quantum simulators reliable [6]), already the next generation of experiments promises to outperform classical simulation techniques.

The platform of ultracold quantum gases has undergone an explosive development within the last few decades. This boom was mainly triggered by the first experimental realization of Bose–Einstein condensation in 1995 [7, 8] — seven decades after the phenomenon had been theoretically predicted by Einstein based on the work of Bose in

[1] One of the world's fastest supercomputers as of 2022 is Fujitsu Fugaku in Kobe, Japan [4]. It permits petascale supercomputing and is equipped with 4.85 PiB of memory. To represent a pure quantum state of N qubits, storage of 2^N complex amplitudes is required. Assuming that each amplitude is stored in double precision, the memory of Fugaku is exhausted by storing the state of just 48 qubits.

1925 [9, 10]. This milestone culminated in the award of the Nobel Prize in Physics 2001 jointly to E. A. Cornell, W. Ketterle, and C. E. Wieman. While much of the early work on ultracold quantum gases concerned the regime of weak interactions, groundbreaking theoretical proposals [11] and experimental advances in the control of cold atoms in optical lattices [12] have paved the road to cold-atom-based quantum simulation of even strongly correlated systems [13–16]. Such optical-lattice setups represent close-to-ideal realizations of many tight-binding models relevant in condensed matter physics like the Hubbard model, which is believed to describe high-temperature superconductivity of cuprates [17]. In contrast to solid state systems, interactions between atoms in optical lattices can be controlled almost at will, offering unprecedented possibilities for studying the physics of strongly correlated materials. A more recent technological breakthrough has been achieved with the invention of the quantum gas microscope, which allows for the preparation, manipulation, and read-out of atoms in optical lattices at both single-site and single-particle resolution [18, 19]. Cold-atom quantum simulators therefore literally provide insights into target systems that are hard or impossible to access by any other means. One should keep in mind, though, that quantum simulators do not replicate the actual target system (e.g., a solid) in miniature, but they simulate an idealized model describing the target system. In the words of Galitski and Spielman: "[t]o study material systems, theorists create 'spherical-cow' models of real materials, while in cold atom physics experimentalists actually make spherical cows" [20].

Despite the impressive capabilities of present-day analog quantum simulators to engineer and control a given target model, readout of the desired observables can often be challenging — be it for technical reasons like limited resolution of an imaging system, the lack of appropriate measurement schemes, or fundamental restrictions posed by the laws of quantum mechanics. The ability to accurately probe a quantum state is viable, for instance, to verify successful state preparation or to disclose novel physics. At the heart of this thesis lies the development of protocols capable of revealing currently inaccessible properties of quantum many-body systems. To demonstrate that the proposed protocols may indeed be executed in state-of-the-art experiments under realistic conditions, we present thorough numerical benchmark simulations and discuss possible experimental error sources. In addition, we illustrate relevant applications that showcase the enormous versatility of the cold-atom quantum simulation platform. In what follows, we introduce the specific problems and applications to be addressed in the course of this thesis.

Following the introduction of the basic theoretical tools and model systems in Chapter 1, we turn our attention in Chapter 2 to the problem of measuring dynamical correlations involving observables at unequal times. In classical systems, such correlations can simply be obtained by measuring the observables of interest at different times and correlating the outcomes. By contrast, the analogous procedure in quantum systems does not yield the desired result due to the collapse of the wave function: a measurement at one instance of time collapses the quantum state, hindering a second measurement at a later time with respect to the original unperturbed state. Nonetheless, Kubo's celebrated linear response theory provides a general way to access the anti-symmetrized two-time correlation function of two observables (unequal-time commutator) by probing the sys-

tem's response to a weak perturbation [21]. While this quantity is a standard observable in many experiments, a measurement of the *symmetrized* two-time correlation function (unequal-time *anti*-commutator) is unfortunately much harder and has to date never been achieved experimentally. In Chapter 2, we develop concrete experimental schemes for measuring this quantity based on a recently proposed extension of linear response theory to non-Hermitian perturbations [22, 23]. The idea is to weakly couple the system to an ancillary state, followed by a post-selected measurement on the condition that no particles occupy the ancilla. The leakage of probability to a complementary state space involved in this procedure effectively corresponds to a non-Hermitian perturbation. We illustrate the scheme through numerical benchmark simulations and discuss perspectives for an experimental realization in Rydberg quantum simulators.

Among the numerous applications of dynamical correlations, the famous fluctuation–dissipation relation (FDR) plays a groundbreaking role [21]. In thermal equilibrium, it connects intrinsic fluctuations of an observable at a certain frequency to the energy dissipated when the system is perturbed at that same frequency. Testing the validity of the FDR therefore provides an excellent probe for thermalization in isolated quantum systems [24]. While the dissipation side of the FDR is determined by the unequal-time commutator and can be measured using standard linear response, the non-Hermitian linear scheme described above enables an independent measurement of the elusive fluctuation side, corresponding to the unequal-time anti-commutator. Motivated by a groundbreaking cold-atom experiment [25], we demonstrate through numerical simulations how such an unbiased measurement of both sides of the FDR allows one to track the evolution of a Bose–Hubbard system from a non-equilibrium initial state to one that locally appears thermal. This analysis represents a blueprint for experimentally studying whether and how isolated quantum systems thermalize — or fail to do so [26–31].

In Chapter 3, we devise a handle on another quantity that is hard to access directly in analog quantum simulators: the current operator. In the simulated solid state system, currents are comparatively easy to measure by connecting wires to the sample, while in the simulating cold-atom system, the same procedure is impossible since high vacuum conditions must be maintained. The standard way of measuring currents in cold-atom systems is to monitor the time evolution of the density and infer the current indirectly by invoking the equation of continuity. By contrast, possibilities to directly access the current operator are sparse. The basic approach pursued in Chapter 3 to enable a direct measurement of the current between two sites in an optical lattice involves coupling both sites to an ancilla, e.g., an auxiliary lattice site. The key is to choose the phases of the coupling appropriately such that the change of the ancilla population becomes sensitive to the desired current. The measurement can be conducted in a non-invasive way, which leaves the quantum state of the target system largely intact, or in a projective way, which achieves a higher signal-to-noise ratio. We discuss several extensions of the scheme to more general observables like current correlations, which can be used, for example, to characterize strongly correlated phases of matter. We illustrate the technique through numerical benchmark simulations for chiral currents of interacting bosons on a Harper–Hofstadter optical-lattice ladder as well as for loop current correlations revealing chiral phases of frustrated hard-core bosons on a spatially anisotropic triangular lattice.

The scheme poses experimental requirements that are readily fulfilled in state-of-the-art setups and can flexibly be extended to other platforms, as we discuss for trapped ions.

Chapter 4 is devoted to the study of the intriguing phenomenon of supersolidity [32–34]. A supersolid combines the properties of a superfluid with that of a solid body. The former is characterized by a spontaneous breaking of gauge symmetry, resulting in typical superfluid properties like frictionless flows of particles and global phase coherence. The latter exhibits spontaneously broken translational invariance, leading to the crystalline structure of solids. Whether this exotic state of matter can actually exist has been long debated, but experiments to demonstrate superfluid properties of solid helium have remained inconclusive [35, 36]. The quest for supersolidity has regained new momentum with the realization of configurations exhibiting typical supersolid features on the platform of ultracold quantum gases. Candidates for supersolids have been realized in Bose–Einstein condensates inside optical resonators [37], spin–orbit-coupled systems [38, 39], as well as dipolar quantum gases [40–42]. In Chapter 4, we explore how supersolid features can be revealed in spin–orbit-coupled Bose–Einstein condensates, where supersolitiy becomes manifest in the form of stripes in the density profile. In this setup, the challenge is to certify the solid character of the system, i.e., the periodic modulation of the density, rather than the superfluid properties, which arise from Bose–Einstein condensation. The most straightforward approach of verifying the existence of the stripes through direct imaging turns out to be impracticable using standard optical techniques since the distance between the stripes is on the order of the wavelength of the optical imaging light. The approach pursued in Chapter 4 is therefore to devise dynamical probes of supersolidity. According to Goldstone's theorem [43–45], the spontaneously broken translational invariance in the supersolid phase implies the existence of a gapless excitation, which in uniform matter corresponds to a translational motion of the stripes. Since this motion costs zero energy in absence of external potentials, we will refer to this crystal Goldstone mode also as the "zero-frequency" Goldstone mode. Exciting this motion and probing its dynamical signatures provides a clear indicator for the supersolid phase, but has so far not been achieved in spin–orbit-coupled systems. We show that in experimentally relevant configurations, including quantum mixtures with symmetric and asymmetric intraspecies interactions, the zero-frequency Goldstone mode can be excited by applying a uniform spin perturbation, and point out accessible static and dynamic probes for its existence. Furthermore, we show that the breathing oscillation in harmonically trapped systems dramatically changes its character once the transition to the supersolid phase is crossed: above the transition, a single mode of hybridized density and spin nature is excited, while in the supersolid phase, a beating of two frequencies indicates the appearance of an additional Goldstone spin-dipole mode. Thus, a measurement of this beating effect provides another hallmark of supersolidity, while the spin nature of the emergent mode illustrates the crucial interplay of density and spin degrees of freedom in spin–orbit-coupled configurations, which enriches the phenomenon of supersolidity.

In addition to the quantum simulation of strongly correlated materials in optical lattices, quantum gases in continuum can act, for example, as simulators of quantum field theories [46, 47] or analog models of gravity [48], promising valuable insights even in

the weakly interacting regime. The prospering field of analog gravity aims at modeling aspects of general relativity in non-relativistic systems. Implementations of such models in quantum simulators not only make otherwise inaccessible physics of curved spacetime available for studies in table-top experiments, but additionally have the potential to elucidate the role of quantum effects for the phenomenon of interest. In Chapter 5, we tap into this development and design a scenario for quantum-simulating post-inflationary reheating dynamics in the early universe. The theory of cosmological inflation states that the early universe went through a phase of exponential expansion, which in typical models is driven by a scalar field known as the inflaton [49]. At the end of inflation, the universe was in a super-cooled state with practically all energy stored in the homogeneous mode of the inflaton field. The following process of cosmological reheating involves the decay of the inflaton into more familiar forms of matter, e.g., standard model particles, which undergo thermalization [50]. We mimic this reheating process in a parametrically excited Bose gas, where the condensate plays the role of the inflaton field and excitations on top of it are identified with particles produced by the decaying inflaton. As we demonstrate through classical–statistical simulations, the system undergoes the characteristic stages of far-from-equilibrium reheating, including a so-called preheating phase of explosive particle production as well as the subsequent stage of turbulent thermalization, characterized by a direct cascade transporting energy in a self-similar way towards higher momenta [51]. The dynamics in the turbulent regime is governed by a non-thermal fixed point, which determines the far-from-equilibrium behavior of an entire universality class [52]. Owing to universality, physical systems at vastly different energy scales, such as ultracold quantum gases in the laboratory, the inflaton in the early universe, or the quark-gluon plasma explored in heavy-ion collisions, can behave quantitatively the same [51, 53–55]. Exploring the dynamics of the Bose gas in the outlined setting can therefore provide relevant insights far beyond the cosmological application. In particular, the outlined "analog reheating" scenario exhibits a prescaling regime of partial universality [55, 56] and may thus pave the road to an experimental observation of this phenomenon.

All methods introduced in this thesis have been designed with the capabilities and limitations of presently available quantum hardware in mind. Major efforts have been invested into numerical simulations to demonstrate that the protocols may indeed be executed under realistic conditions. The proposed techniques, scenarios, and applications are therefore intended to stimulate experimental research to disclose so far unobserved physics in synthetic quantum systems.

1. Theoretical Background

In this chapter, we summarize the theoretical background that this thesis build upon. We first outline the basic physics underlying cold-atom quantum simulators, with a focus on bosonic systems. We start by reviewing the theoretical description of ultracold Bose gases in continuum, which we will use in Chapter 5 to simulate cosmological reheating dynamics. The concepts introduced below also form the basis of our investigations into the phenomenon of supersolidity in Chapter 5, while the relevant model systems, spin–orbit coupled mixtures of Bose gases, will be introduced at the beginning of that chapter. Following the overview on the physics ultracold Bose gases in continuum, we turn to cold atoms in optical lattices and introduce the Bose–Hubbard model, which will be in the center of our applications in Chapters 2 and 3. Then, we review elements of linear response theory, which will accompany us through large parts of the thesis.

1.1. Theory of Ultracold Bose Gases

The theory of ultracold Bose gases is discussed comprehensively in Ref. [57], based on which we summarize below the essential aspects that will turn out to be useful in the course of this thesis.

An ultracold Bose gas is described by a complex field operator $\hat{\Psi}(\boldsymbol{x})$ that satisfies the canonical commutation relations

$$\left[\hat{\Psi}(\boldsymbol{x}), \hat{\Psi}(\boldsymbol{y})\right] = \left[\hat{\Psi}^\dagger(\boldsymbol{x}), \hat{\Psi}^\dagger(\boldsymbol{y})\right] = 0\,, \tag{1.1a}$$

$$\left[\hat{\Psi}(\boldsymbol{x}), \hat{\Psi}^\dagger(\boldsymbol{y})\right] = \delta(\boldsymbol{x}-\boldsymbol{y})\,, \tag{1.1b}$$

where $\delta(\boldsymbol{x}-\boldsymbol{y})$ is the Dirac delta function. Within the formalism of second quantization, the field operator $\hat{\Psi}(\boldsymbol{x})$ and its Hermitian adjoint $\hat{\Psi}^\dagger(\boldsymbol{x})$ can be interpreted as annihilating and creating a boson at position $\boldsymbol{x}$, respectively. The dynamics is governed by the Hamiltonian

$$\hat{H} = \int \mathrm{d}\boldsymbol{x}\, \hat{\Psi}^\dagger(\boldsymbol{x}) \left[-\frac{\hbar^2\nabla^2}{2m} + V_{\mathrm{ext}}(\boldsymbol{x})\right] \hat{\Psi}(\boldsymbol{x}) + \frac{1}{2}\int \mathrm{d}\boldsymbol{x}\, \mathrm{d}\boldsymbol{y}\, \hat{\Psi}^\dagger(\boldsymbol{x})\hat{\Psi}^\dagger(\boldsymbol{y})\mathcal{V}(\boldsymbol{x},\boldsymbol{y})\hat{\Psi}(\boldsymbol{x})\hat{\Psi}(\boldsymbol{y})\,, \tag{1.2}$$

where $\hbar$ is the reduced Planck constant and m the atomic mass. The first term represents the kinetic and potential energy of free particles in an external trapping potential $V_{\mathrm{ext}}(\boldsymbol{x})$, while the second term describes interactions between particles, mediated by the two-body interaction potential $\mathcal{V}(\boldsymbol{x},\boldsymbol{y})$. Throughout, we focus on the regime of weakly interacting

Bose gases where the latter can be replaced by an effective contact potential[1],

$$\mathcal{V}_{\text{eff}}(\boldsymbol{x},\boldsymbol{y}) = g\delta(\boldsymbol{x}-\boldsymbol{y})\,, \tag{1.3}$$

whose interaction strength

$$g = \frac{4\pi\hbar^2 a_s}{m} \tag{1.4}$$

is characterized by a single parameter: the s-wave scattering length a_s. This quantity can not only be measured in experiments, but it is even possible to tune the scattering length, e.g., by means of Feshbach resonances [58], available in many atomic species. The sign of the scattering length determines the character of the interactions: $a_s > 0$ ($a_s < 0$) describes repulsive (attractive) interactions. Numerous experiments have confirmed that the Hamiltonian (1.2) with the effective contact interaction in Eq. (1.3) provides an excellent microscopic description as long as the system is sufficiently dilute. The diluteness condition can be quantified by requiring the smallness of the diluteness parameter $\eta = \sqrt{na_s^3}$, where n represents a typical particle density.

The Hamiltonian (1.2) is invariant under a global $U(1)$ phase transformation of the field operator as $\hat{\Psi}(\boldsymbol{x}) \to \mathrm{e}^{i\theta}\hat{\Psi}(\boldsymbol{x})$. This symmetry transformation is generated by the operator $\hat{U}(\theta) = \exp(i\hat{N}\theta)$, where

$$\hat{N} = \int \mathrm{d}\boldsymbol{x}\, \hat{\Psi}^\dagger(\boldsymbol{x})\hat{\Psi}(\boldsymbol{x}) \tag{1.5}$$

is the total particle number operator. The total particle number N is a conserved quantity since the operator $\hat{N}$ commutes with the Hamiltonian, $[\hat{N},\hat{H}] = 0$. As described below, Bose–Einstein condensation spontaneously breaks $U(1)$ symmetry.

In the Heisenberg picture, the time evolution of the field operator $\hat{\Psi}(\boldsymbol{x},t)$ is governed by the Heisenberg equations of motion

$$i\hbar\frac{\partial}{\partial t}\hat{\Psi}(\boldsymbol{x},t) = \left[\hat{\Psi}(\boldsymbol{x},t),\hat{H}\right] = \left[-\frac{\hbar^2}{2m}\nabla^2 + V_{\text{ext}}(\boldsymbol{x}) + g\hat{\Psi}^\dagger(\boldsymbol{x},t)\hat{\Psi}(\boldsymbol{x},t)\right]\hat{\Psi}(\boldsymbol{x},t)\,. \tag{1.6}$$

Bose–Einstein Condensation

Bose–Einstein condensation, as predicted by Einstein in 1925 [10] based on the statistics of photons conceived by Bose [9], describes the phenomenon where a macroscopic fraction of the particles in a system occupies the state of lowest energy. While Einstein's argumentation is based on purely statistical properties of the ideal Bose gas, the modern definition of Bose–Einstein condensation, which also applies to interacting particles, is based on the existence of off-diagonal long-range order, known as the Penrose–Onsager criterion [59].

To formulate this concept, we introduce the so-called single-particle (or one-body) density matrix

$$n^{(1)}(\boldsymbol{x},\boldsymbol{y}) = \left\langle \hat{\Psi}^\dagger(\boldsymbol{x})\hat{\Psi}(\boldsymbol{y})\right\rangle, \tag{1.7}$$

[1]The expression (1.4) for the interaction constant holds in three spatial dimensions. Effective interactions in low-dimensional systems are discussed below.

where $\langle\cdots\rangle$ denotes the quantum expectation value. This quantity is normalized to the total number of particles $N = \int \mathrm{d}\boldsymbol{x}\, n^{(1)}(\boldsymbol{x},\boldsymbol{x})$.

Furthermore, we define the single-particle momentum distribution

$$f(\boldsymbol{p}) = \frac{1}{V}\left\langle \hat{\Psi}^\dagger(\boldsymbol{p})\hat{\Psi}(\boldsymbol{p})\right\rangle , \tag{1.8}$$

where V is the volume and $\hat{\Psi}(\boldsymbol{p}) = \int \mathrm{d}\boldsymbol{x}\, \hat{\Psi}(\boldsymbol{x})\mathrm{e}^{-i\boldsymbol{p}\boldsymbol{x}/\hbar}$ is the Fourier transform of the field operator $\hat{\Psi}(\boldsymbol{x})$. The normalization is given by $N = V(2\pi\hbar)^{-d}\int \mathrm{d}\boldsymbol{p}\, f(\boldsymbol{p})$, where d is the number of spatial dimensions. The momentum distribution is closely related to the single-particle density matrix via

$$f(\boldsymbol{p}) = \frac{1}{V}\int \mathrm{d}\boldsymbol{R}\,\mathrm{d}\boldsymbol{r}\, n^{(1)}\Big(\boldsymbol{R}+\frac{\boldsymbol{r}}{2},\boldsymbol{R}-\frac{\boldsymbol{r}}{2}\Big)\mathrm{e}^{-i\boldsymbol{p}\boldsymbol{r}/\hbar}\,, \tag{1.9}$$

where $\boldsymbol{R} = (\boldsymbol{x}+\boldsymbol{y})/2$ and $\boldsymbol{r} = \boldsymbol{x}-\boldsymbol{y}$ are the central and relative spatial coordinates, respectively. This relations shows that $f(\boldsymbol{p})$, which can be accessed experimentally in time-of-flight measurements [60], probes spatial correlations in the system.

The single-particle density matrix can be written in diagonal form as

$$n^{(1)}(\boldsymbol{x},\boldsymbol{y}) = \sum_i N_i\varphi_i^*(\boldsymbol{x})\varphi_i(\boldsymbol{y})\,, \tag{1.10}$$

where $\{\varphi_i(\boldsymbol{x})\}$ is an orthonormal and complete set of single-particle eigenfunctions with corresponding eigenvalues $\{N_i\}$, $\sum_i N_i = N$, obtained as solutions to the eigenvalue equation $\int \mathrm{d}\boldsymbol{y}\, n^{(1)}(\boldsymbol{x},\boldsymbol{y})\varphi_i(\boldsymbol{y}) = N_i\varphi_i(\boldsymbol{x})$. A system is said to exhibit off-diagonal long-range order if the single-particle density matrix takes a finite value for $|\boldsymbol{x}-\boldsymbol{y}|\to\infty$ in the thermodynamic limit ($N, V\to\infty$). According to the Penrose–Onsager criterion [59], Bose–Einstein condensation occurs if and only if there is a macroscopically occupied mode, taken here as $i = 0$, such that the eigenvalue N_0 of the single-particle density matrix scales with the total number of particles N. A Bose–Einstein-condensed system thus exhibits off-diagonal long-range order as $n^{(1)}(\boldsymbol{x},\boldsymbol{y})\to n_0$ for $|\boldsymbol{x}-\boldsymbol{y}|\to\infty$, where $n_0 = N_0/V$ is the condensate density.

It should be noted that, according to the famous Mermin–Wagner–Hohenberg theorem [61, 62], long-range order (and thus a true condensate) cannot exist in less than three spatial dimensions at finite temperatures. Nonetheless, so-called quasi-condensates (condensates with fluctuating phase) can be realized in low-dimensional settings through tight trapping potentials [63–65] (see discussion below).

1.1.1. Gross–Pitaevskii Theory of Bose–Einstein Condensates

It is instructive to expand the bosonic field operator $\hat{\Psi}(\boldsymbol{x})$ in the diagonal basis $\{\varphi_i(\boldsymbol{x})\}$ of the single-particle density matrix in Eq. (1.10) as $\hat{\Psi}(\boldsymbol{x}) = \sum_i \varphi_i(\boldsymbol{x})\hat{a}_i$, where the operators $\hat{a}_i$ ($\hat{a}_i^\dagger$) annihilate (create) a particle in the mode i. In the Bose–Einstein-condensed phase, the condensate mode $i = 0$ is macroscopically occupied, $N_0 = \langle a_0^\dagger a_0\rangle \gg 1$, such that one can use the Bogoliubov approximation and make the replacement $\hat{a}_0\to$

$\sqrt{N_0}$. This is equivalent to treating the condensate mode as a classical field $\Psi_0(\boldsymbol{x}) = \sqrt{N_0}\varphi_0(\boldsymbol{x})$, often referred to as the condensate wave function, corresponding to a decomposition of the field operator as

$$\hat{\Psi}(\boldsymbol{x}) = \Psi_0(\boldsymbol{x}) + \delta\hat{\Psi}(\boldsymbol{x}) \tag{1.11}$$

with $\delta\hat{\Psi}(\boldsymbol{x}) = \sum_{i\neq 0}\varphi_i(\boldsymbol{x})\hat{a}_i$. The classical field $\Psi_0(\boldsymbol{x}) = \sqrt{N_0}\varphi_0(\boldsymbol{x})$ plays the role of the order parameter for the Bose–Einstein-condensed phase, which takes a non-zero value below the critical temperature T_c for Bose–Einstein condensation. Being a complex quantity, the order parameter can be written in density–phase representation as $\Psi_0 = \sqrt{n_0}\mathrm{e}^{i\theta_0}$. This shows that the $U(1)$ phase symmetry of the Hamiltonian (1.2) is spontaneously broken, which leads to a gapless excitation spectrum [see Eq. (1.38)], as required by Goldstone's theorem [43–45].

If the depletion of the condensate, i.e., the number of non-condensate atoms $N - N_0$, is sufficiently small, it is permissible to neglect quantum fluctuations described by the term $\delta\hat{\Psi}(\boldsymbol{x})$ in Eq. (1.11). While the thermal depletion vanishes at zero temperature, interactions lead to a quantum depletion of the condensate that persists even at $T = 0$. However, the quantum depletion is often small under realistic experimental conditions, such that the system is well described by a classical field $\Psi(\boldsymbol{x}) \equiv \Psi_0(\boldsymbol{x})$ within Gross–Pitaevskii theory [57].

Inserting Eq. (1.11) into the Hamiltonian (1.2) and neglecting all quantum fluctuations, we obtain the Gross–Pitaevskii energy functional

$$E = \int \mathrm{d}\boldsymbol{x}\left\{\Psi^*(\boldsymbol{x})\left[-\frac{\hbar^2\nabla^2}{2m} + V_\mathrm{ext}(\boldsymbol{x})\right]\Psi(\boldsymbol{x}) + \frac{g}{2}|\Psi(\boldsymbol{x})|^4\right\}. \tag{1.12}$$

The equations of motion for the time-dependent field $\Psi(\boldsymbol{x}, t)$ can be derived by imposing the stationarity condition $\delta S = 0$ on action

$$S = \int \mathrm{d}t\, E - i\hbar\int \mathrm{d}t\,\mathrm{d}\boldsymbol{x}\,\Psi^*\partial_t\Psi\,. \tag{1.13}$$

This yields the famous Gross–Pitaevskii equation (GPE)

$$i\hbar\frac{\partial}{\partial t}\Psi(\boldsymbol{x}, t) = \left[-\frac{\hbar^2\nabla^2}{2m} + V_\mathrm{ext}(\boldsymbol{x}) + g|\Psi(\boldsymbol{x}, t)|^2\right]\Psi(\boldsymbol{x}, t)\,, \tag{1.14}$$

which can also formally be obtained as the classical equation of motion after replacing the Bose field operator in Eq. (1.6) by its expectation value, $\hat{\Psi}(\boldsymbol{x}, t) \to \Psi(\boldsymbol{x}, t) \equiv \langle\hat{\Psi}(\boldsymbol{x}, t)\rangle$.

Hydrodynamic Formulation and Superfluidity

By adopting the Madelung representation, $\Psi(\boldsymbol{x}, t) = \sqrt{n(\boldsymbol{x}, t)}\mathrm{e}^{i\theta(\boldsymbol{x},t)}$, the GPE can be expressed in form of hydrodynamic equations for the density $n(\boldsymbol{x}, t) = |\Psi(\boldsymbol{x}, t)|^2$ and the phase $\theta(\boldsymbol{x}, t) = \arg\Psi(\boldsymbol{x}, t)$ of the condensate [57],

$$\frac{\partial}{\partial t}n = -\frac{\hbar}{m}\nabla(n\nabla\theta)\,, \tag{1.15a}$$

$$\hbar\frac{\partial}{\partial t}\theta = -gn + \frac{\hbar^2}{2m}\left[\frac{\nabla^2\sqrt{n}}{\sqrt{n}} - (\nabla\theta)^2\right]. \tag{1.15b}$$

The equation for the density (1.15a) can be rewritten as a continuity equation,

$$\frac{\partial}{\partial t} n + \nabla \boldsymbol{j} = 0 \,, \tag{1.16}$$

with the current density

$$\boldsymbol{j}(\boldsymbol{x}, t) = -\frac{i\hbar}{2m}(\Psi^* \nabla \Psi - \Psi \nabla \Psi^*) = n(\boldsymbol{x}, t)\frac{\hbar}{m}\nabla\theta(\boldsymbol{x}, t) \,. \tag{1.17}$$

This suggests identifying the gradient of the phase with the superfluid velocity

$$\boldsymbol{v}(\boldsymbol{x}, t) = \frac{\hbar}{m}\nabla\theta(\boldsymbol{x}, t) \,. \tag{1.18}$$

With this definition, Eq. (1.15b) takes a form reminiscent of the Euler equation in hydrodynamics,

$$m\frac{\partial}{\partial t}\boldsymbol{v} + \nabla\left(\frac{1}{2}m\boldsymbol{v}^2 + V_{\text{ext}} + gn - \frac{\hbar^2}{2m\sqrt{n}}\nabla^2\sqrt{n}\right) = 0 \,, \tag{1.19}$$

where the last term is known as the "quantum pressure" term. Being a pure gradient field, $\boldsymbol{v}(\boldsymbol{x}, t)$ is irrotational, i.e., $\nabla \times \boldsymbol{v} = 0$. This condition can only be violated where the density vanishes, giving rise to quantized vortices, a hallmark of superfluids.

Superfluidity. Superfluidity is the property of a fluid to flow entirely without inner friction, i.e., with zero viscosity. According to the Landau criterion for superfluidity, such a dissipationless flow can exists if the fluid velocity v is below the Landau critical velocity v_{s}, given by [57]

$$v_{\text{s}} = \min_{\boldsymbol{p}} \frac{\epsilon(\boldsymbol{p})}{|\boldsymbol{p}|} \,, \tag{1.20}$$

where $\epsilon(\boldsymbol{p})$ denotes the energy of elementary excitations. In a weakly interacting Bose gas, where $\epsilon(\boldsymbol{p})$ is given by the Bogoliubov dispersion relation (1.38), the critical velocity corresponds to the speed of sound, $v_{\text{s}} = c_{\text{s}} = \sqrt{n_0 g/m}$. It should be noted that, though closely related, Bose–Einstein condensation and superfluidity are not the same phenomenon (for example, the ideal Bose gas can condense, but is not superfluid). According to two-fluid hydrodynamics [57], one can think of the density ρ of a fluid as consisting of a normal component ρ_{n} and a superfluid component ρ_{s}, the latter giving rise to superfluid properties like frictionless flows. However, the superfluid density ρ_{s} can in general not be identified with the condensate density n_0 (for example, in a weakly interacting Bose gas at $T = 0$, $\rho_{\text{s}}/\rho = 1$, while $n_0/n < 1$ due to quantum depletion).

Ground State of the Condensate

The ground state wave function of a Bose–Einstein condensate can be written as $\Psi(\boldsymbol{x}, t) = \Psi_0(\boldsymbol{x})\mathrm{e}^{-i\mu t/\hbar}$, where the time evolution corresponds to a pure phase rotation determined

by the chemical potential $\mu = \partial E/\partial N$. With this ansatz, the GPE (1.14) reduces to its time-independent form

$$\left[-\frac{\hbar^2\nabla^2}{2m} + V_{\text{ext}}(\boldsymbol{x}) + g|\Psi_0(\boldsymbol{x},t)|^2\right]\Psi_0(\boldsymbol{x}) = \mu\Psi_0(\boldsymbol{x})\,. \tag{1.21}$$

In uniform matter [$V_{\text{ext}}(\boldsymbol{x}) = 0$], the chemical potential is simply given by $\mu = n_0 g$, where $n_0 = |\Psi_0|^2 = N/V$ is the uniform particle density. In general, the ground state minimizing the energy functional (1.12) must be calculated numerically, e.g., by means of imaginary time evolution [66] or non-linear conjugate gradient methods [67]. The chemical potential is then obtained from Eq. (1.21) as $\mu = E + \int \mathrm{d}\boldsymbol{x}\, g n_0^2(\boldsymbol{x})/2$.

In presence of a harmonic trap,

$$V_{\text{ext}}(\boldsymbol{x}) = \frac{1}{2}m\big(\omega_x^2 x^2 + \omega_y^2 y^2 + \omega_z^2 z^2\big)\,, \tag{1.22}$$

where ω_i are the trapping frequencies, an accurate estimate of the ground state density profile $n_0(\boldsymbol{x})$ can be obtained using the Thomas–Fermi approximation, which consists in neglecting the kinetic term in Eq. (1.21). This approximation is justified for repulsive interactions ($g > 0$) if the number of particles is sufficiently large, such that the ground state density profile varies only slowly in space. By solving Eq. (1.21) for the density, one obtains the Thomas–Fermi density profile

$$n_{\text{TF}}(\boldsymbol{x}) = \frac{1}{g}[\mu_{\text{TF}} - V(\boldsymbol{x})]\,, \tag{1.23}$$

where the value of the chemical potential μ_{TF} is fixed by the normalization $N = \int \mathrm{d}\boldsymbol{x}\, n_{\text{TF}}(\boldsymbol{x})$. Evaluating this integral in d spatial dimensions, one obtains

$$\mu_{\text{TF}} = \frac{\hbar\bar{\omega}}{2}\left[\frac{d+2}{\Omega_d}N\frac{g}{\hbar\bar{\omega}\bar{a}^d}\right]^{2/(d+2)}, \tag{1.24}$$

where $\bar{\omega} = (\prod_i \omega_i)^{1/d}$ is the geometric mean of the trapping frequencies, $\bar{a} = \sqrt{\hbar/m\bar{\omega}}$ is the corresponding harmonic oscillator length, and $\Omega_d = \pi^{d/2}/\Gamma(d/2+1)$ is the volume of the d-dimensional unit sphere [$\Gamma(x)$ is the gamma function]. The boundary of the Thomas–Fermi ellipsoid is given by the condition $n_{\text{TF}}(\boldsymbol{x}) = 0$, i.e., $V(\boldsymbol{x}) = \mu_{\text{TF}}$, which yields $R_i^2 = 2\mu_{\text{TF}}/m\omega_i^2$ for the length of the semi-axis in direction $i = x, y, z$. It is convenient to define the Thomas–Fermi radius as the geometric mean of the semi-axes, $R_{\text{TF}} = (\prod_i R_i)^{1/d}$. For $d = 3$, using Eq. (1.4), we recover the well-known expressions

$$\mu_{\text{TF}} = \frac{\hbar\omega}{2}\Big(15N\frac{a_s}{\bar{a}}\Big)^{2/5}, \tag{1.25}$$

$$R_{\text{TF}} = \bar{a}\Big(15N\frac{a_s}{\bar{a}}\Big)^{1/5}. \tag{1.26}$$

Low-Dimensional Systems

Most of the discussion so far applies to systems in an arbitrary number of spatial dimensions d. However, since the Mermin–Wagner–Hohenberg theorem rules out the existence of a true condensate for $d < 3$ in spatially homogeneous systems at finite temperatures [61, 62], low-dimensional settings require further discussions. Experimentally, an effective reduction of dimensionality can be achieved by a tight harmonic confinement of a three-dimensional (3D) condensate, which can "freeze" the motion of the gas along one axis (pancake or disk geometry) or two axes (cigar geometry) up to zero-point motion. Below the critical temperature, such quasi-two-dimensional (2D) or quasi-one-dimensional (1D) systems enter a so-called quasi-condensate regime, where density fluctuations are suppressed, but phase fluctuations are still present. At sufficiently low temperatures, the quasi-condensate gradually turns to a true condensate through the build-up of phase coherence [63–65].

As will become relevant later in this thesis, we briefly outline the setup for realizing quasi-2D systems [60]. To this end, we consider an axial harmonic trapping potential $V(z) = m\omega_z^2 z^2/2$. In order to effectively freeze the motion along the z axis, the energy scale $\hbar\omega_z$ set by the axial confinement should be large compared to all other relevant energy scales in the system, in particular, compared to the thermal energy $k_\mathrm{B}T$ as well as the typical interaction energy $\mu = ng$. The quasi-2D criterion can equivalently be phrased in terms of characteristic length scales, involving the harmonic oscillator length in z direction $a_z = \sqrt{\hbar/m\omega_z}$, the thermal de Broglie wavelength $\lambda_T = \hbar/\sqrt{2\pi m k_\mathrm{B} T}$, and the so-called healing length of the condensate

$$\xi = \frac{\hbar}{\sqrt{2mng}}\,. \tag{1.27}$$

The healing length is defined by matching the kinetic energy $\hbar^2\xi^{-2}/2m$ with the typical interaction energy ng and sets the characteristic length scale over which the condensate "heals" from local defects like vortices. The quasi-2D condition $k_\mathrm{B}T, ng \ll \hbar\omega_z$ is thus equivalent to demanding $a_z \ll \lambda_T, \xi$.

An effective two-dimensional description of the system can be obtained by making the ansatz

$$\Psi(\boldsymbol{x}, t) = \Psi(x, y, t)\phi(z)\mathrm{e}^{-i\mu_z t/\hbar}\,. \tag{1.28}$$

Deep in the quasi-2D regime, the axial wave function is close to the harmonic oscillator ground state, $\phi(z) = \pi^{-1/4}a_z^{-1/2}\mathrm{e}^{-z^2/2a_z^2}$, and the axial chemical potential is given by the ground state energy $\mu_z = \hbar\omega_z/2$. Inserting the ansatz (1.28) in the GPE (1.14) and integrating out the z direction results in an effective two-dimensional GPE, which has the same form as the 3D equation, but with an effective 2D interaction constant

$$g_\mathrm{2D} = \frac{g_\mathrm{3D}}{\sqrt{2\pi}a_z} = \frac{\hbar^2}{m}\tilde{g} \quad \text{with} \quad \tilde{g} = \sqrt{8\pi}\frac{a_s}{a_z}\,, \tag{1.29}$$

where we have used Eq. (1.4) for the 3D interaction constant g_3D.

It should be noted that the result in Eq. (1.29) for the effective 2D interaction holds if the number of particles is sufficiently large, while otherwise logarithmic corrections need to be taken into account [57, 60]. Furthermore, in some experimental setups, it can be difficult to a achieve a confinement that is strong enough to freeze the motion along the axial direction exactly. A more accurate description of such settings can be obtained by allowing for Gaussian excitations along the confined directions, leading to effective non-polynomial Schrödinger equations [68]. Nonetheless, for the two-dimensional scenarios considered in this thesis, the description in terms of the GPE (1.14) in two spatial dimensions with effective interaction given by Eq. (1.29) is sufficient.

1.1.2. Beyond Mean Field Theory

Gross–Pitaevskii theory belongs to the class of mean-field theories, where, in general, a fluctuating variable is replaced by its mean value (e.g., $\hat{\Psi} \to \Psi = \langle \hat{\Psi} \rangle$). This turns out to be an accurate description of the weakly interacting Bose gas if quantum depletion of the condensate is sufficiently small and the role of quantum fluctuations is unimportant for the particular application. However, in many scenarios, quantum fluctuations give rise to interesting effects not captured by mean-field theory. For example, quantum fluctuations are essential to describe parametric instabilities, where they seed the growth of resonant modes (see Section 5.3.2).

Bogoliubov theory. Bogoliubov theory goes beyond the mean-field description by taking into account quantum fluctuations to leading order. The framework is based on the decomposition of the field operator $\hat{\Psi}(\boldsymbol{x})$ according to Eq. (1.11) into a classical field $\Psi(\boldsymbol{x})$, which describes a macroscopically occupied mode, plus quantum fluctuations $\delta\hat{\Psi}(\boldsymbol{x})$ on top of it. Provided that occupancies of excited modes are small, higher-order terms in $\delta\hat{\Psi}(\boldsymbol{x})$ can be neglected, resulting in a quadratic Hamiltonian. While in general, the Bogoliubov Hamiltonian must be diagonalized numerically, well-known analytical results are available in homogeneous systems [$V_{\mathrm{ext}}(\boldsymbol{x}) = 0$], as outlined in what follows.

It is convenient to work in momentum space, although Bogoliubov theory can also be applied in position space as well as to quasi-condensates in lower dimensions [69]. In a homogeneous system, the field operator can be expanded in the plane wave basis as

$$\hat{\Psi}(\boldsymbol{x}) = \frac{1}{\sqrt{V}} \sum_{\boldsymbol{p}} \hat{a}_{\boldsymbol{p}} \mathrm{e}^{i\boldsymbol{p}\boldsymbol{x}/\hbar} \,. \tag{1.30}$$

The creation and annihilation operators $\hat{a}_{\boldsymbol{p}}$ and $\hat{a}^\dagger_{\boldsymbol{p}}$ of particles with momentum $\boldsymbol{p}$ satisfy the bosonic commutation relations

$$\left[\hat{a}_{\boldsymbol{p}}, \hat{a}_{\boldsymbol{q}}\right] = \left[\hat{a}^\dagger_{\boldsymbol{p}}, \hat{a}^\dagger_{\boldsymbol{q}}\right] = 0 \,, \tag{1.31a}$$

$$\left[\hat{a}_{\boldsymbol{p}}, \hat{a}^\dagger_{\boldsymbol{q}}\right] = \delta_{\boldsymbol{p},\boldsymbol{q}} \,, \tag{1.31b}$$

where $\delta_{\boldsymbol{p},\boldsymbol{q}}$ is the Kronecker delta. Inserting the expansion(1.30) in the Hamiltonian (1.2) [$V_{\rm ext}(\boldsymbol{x}) = 0$], we obtain the momentum space representation

$$\hat{H} = \sum_{\boldsymbol{p}} \epsilon_{\boldsymbol{p},0} \hat{a}^\dagger_{\boldsymbol{p}} \hat{a}_{\boldsymbol{p}} + \frac{g}{2V} \sum_{\boldsymbol{p}_1,\boldsymbol{p}_2,\boldsymbol{p}_3,\boldsymbol{p}_4} \hat{a}^\dagger_{\boldsymbol{p}_1} \hat{a}^\dagger_{\boldsymbol{p}_2} \hat{a}_{\boldsymbol{p}_3} \hat{a}_{\boldsymbol{p}_4} \delta_{\boldsymbol{p}_1+\boldsymbol{p}_2,\boldsymbol{p}_3+\boldsymbol{p}_4} \,, \tag{1.32}$$

where $\epsilon_{\boldsymbol{p},0} = \boldsymbol{p}^2/2m$ denotes the dispersion relation of free particles.

The Bogoliubov approximation involves replacing the macroscopically occupied condensate mode operators by c-numbers, $\hat{a}_0, \hat{a}^\dagger_0 \to \sqrt{N_0}$, and dropping all terms that are of cubic or higher order in excited (non-condensate) modes. This procedure results in the Bogoliubov Hamiltonian[2]

$$\hat{H}_{\rm B} = g\frac{N^2}{2V} + \sum_{\boldsymbol{p}} \epsilon_{\boldsymbol{p},0} \hat{a}^\dagger_{\boldsymbol{p}} \hat{a}_{\boldsymbol{p}} + \frac{1}{2} gn \sum_{\boldsymbol{p}\neq 0} \left(2\hat{a}^\dagger_{\boldsymbol{p}} \hat{a}_{\boldsymbol{p}} + \hat{a}^\dagger_{\boldsymbol{p}} \hat{a}^\dagger_{-\boldsymbol{p}} + \hat{a}_{\boldsymbol{p}} \hat{a}_{-\boldsymbol{p}} + \frac{mgn}{\boldsymbol{p}^2} \right), \tag{1.33}$$

where $n = N/V$ is the uniform density. This Hamiltonian is quadratic in the mode operators an can therefore be diagonalized with the help of the Bogoliubov transformations

$$\hat{a}_{\boldsymbol{p}} = u_{\boldsymbol{p}} \hat{b}_{\boldsymbol{p}} + v^*_{-\boldsymbol{p}} \hat{b}^\dagger_{-\boldsymbol{p}} \,, \qquad \hat{a}^\dagger_{\boldsymbol{p}} = u^*_{\boldsymbol{p}} \hat{b}^\dagger_{\boldsymbol{p}} + v_{-\boldsymbol{p}} \hat{b}_{-\boldsymbol{p}} \,. \tag{1.34}$$

The new operators $\hat{b}_{\boldsymbol{p}}$ and $\hat{b}^\dagger_{\boldsymbol{p}}$ obey bosonic commutation relations as in Eq. (1.31), provided the coefficient functions satisfy $|u_{\boldsymbol{p}}|^2 - |v_{-\boldsymbol{p}}|^2 = 1$. By choosing the coefficients as

$$u_{\boldsymbol{p}}, v_{-\boldsymbol{p}} = \pm \left[\frac{\epsilon_{\boldsymbol{p},0} + ng}{2\epsilon_{\boldsymbol{p}}} \pm \frac{1}{2} \right]^{1/2} , \tag{1.35}$$

the Bogoliubov Hamiltonian (1.33) takes the diagonal form

$$\hat{H}_{\rm B} = E_0 + \sum_{\boldsymbol{p}} \epsilon_{\boldsymbol{p}} \hat{b}^\dagger_{\boldsymbol{p}} \hat{b}_{\boldsymbol{p}} \,, \tag{1.36}$$

where

$$E_0 = g\frac{N^2}{2V} + \frac{1}{2} \sum_{\boldsymbol{p}\neq 0} \left[\epsilon_{\boldsymbol{p}} - gn - \epsilon_{\boldsymbol{p},0} + \frac{m(gn)^2}{\boldsymbol{p}^2} \right] \tag{1.37}$$

is the ground state energy and

$$\epsilon_{\boldsymbol{p}} = \left[\epsilon_{\boldsymbol{p},0} (\epsilon_{\boldsymbol{p},0} + 2ng) \right]^{1/2} = \left[\frac{\boldsymbol{p}^2}{2m} \left(\frac{\boldsymbol{p}^2}{2m} + 2ng \right) \right]^{1/2} \tag{1.38}$$

is the famous Bogoliubov dispersion relation for elementary excitations [70].

At small momenta, the Bogoliubov dispersion (1.38) is linear, $\epsilon_{\boldsymbol{p}} = c_{\rm s}|\boldsymbol{p}|$, where $c_{\rm s} = \sqrt{ng/m}$ is the speed of sound. The quasi-particles excited in this regime have

[2] In deriving the Bogoliubov Hamiltonian (1.33), care must be taken such that all approximations made are on the same level of accuracy. In particular, a consistent approximation requires a more accurate computation of the scattering length beyond the lowest-order Born approximation yielding Eq. (1.4). For details, see Ref. [57].

the character of sound waves or phonons. At momenta on the order of the inverse healing length $\hbar/\xi$, the dispersion changes from linear to quadratic and for large momenta approaches that of free particles, $\epsilon_{\boldsymbol{p}} = ng + \boldsymbol{p}^2/2m$.

The fact that the excitation spectrum is gapless can be regarded as a consequence of Goldstone's theorem, which predicts the existence of a gapless excitation called Goldstone (or Nambu–Goldstone) mode whenever a continuous symmetry is spontaneously broken [43–45]. The transition to the Bose–Einstein-condensed phase, where the complex order parameter Ψ takes a non-zero value, spontaneously breaks the $U(1)$ symmetry of the Hamiltonian (1.2) and the associated Goldstone mode corresponds to the gapless Bogoliubov phonon branch. In Chapter 4, we will explore the phenomenon of supersolidity in spin–orbit-coupled Bose–Einstein condensates, where, in addition to the broken $U(1)$ symmetry responsible for superfluidity, also translational symmetry is spontaneously broken, leading to a periodic density modulation typical of solids.

Beyond Bogoliubov theory. In Chapter 5, we study the far-from-equilibrium dynamics of a parametrically excited ultracold Bose gas by means of classical–statistical (or truncated Wigner) simulations. This technique takes quantum fluctuations into account via a stochastic sampling of the Bogoliubov initial state, but it goes beyond Bogoliubov theory as it captures non-linear interactions between excited quasi-particles, which cannot be described with the Bogoliubov framework. For details on the classical–statistical method, see Appendix B.

1.2. Cold Atoms in Optical Lattices

Having discussed the physics of weakly interacting Bose gases in continuum, we now focus our attention on cold atoms in optical lattices. These setups allow one to realize a variety of tight-binding models relevant in condensed matter physics. This way, the platform of cold atoms enables the quantum simulation of strongly correlated materials despite the fact that the underlying quantum gas is typically weakly interacting. Since model parameters can be tuned almost at will, cold atoms in optical lattices have the potential to provide unique insights into strongly correlated quantum matter, impossible to obtain on any other platform [13–17, 71–74].

1.2.1. Tight-Binding Models

Here, we outline the derivation of the Bose–Hubbard model, following Ref. [11]. Our starting point is the Hamiltonian (1.2) of a weakly interacting Bose gas subject to an optical lattice potential. An optical lattice is formed by intersecting laser beams, creating periodic standing wave patterns. The light field induces an AC Stark shift of atomic energy levels, providing an optical dipole force that can trap atoms [75]. Depending on the addressed atomic state, atoms can be trapped either in intensity maxima (red-detuned optical lattice) or in intensity minima (blue-detuned optical lattice), where the latter has the advantage of reducing photon scattering rates.

In what follows, we assume that the external potential in the Hamiltonian (1.2) consists of an arbitrary trapping potential $V_{\mathrm{T}}(\boldsymbol{x})$ plus an optical lattice potential $V_0(\boldsymbol{x})$. For concreteness, we consider the simplest case of a cubic optical lattice potential

$$V_0(\boldsymbol{x}) = V_{x,0}\sin^2(kx) + V_{y,0}\sin^2(ky) + V_{z,0}\sin^2(kz)\,, \tag{1.39}$$

where $V_{i,0}$ is the depth of the optical lattice in direction $i \in \{x, y, z\}$ and $k = 2\pi/\lambda$ is the wave number of the laser light with wavelength λ, giving rise to a lattice of period $a = \lambda/2$.

The eigenstates of non-interacting particles in the periodic potential (1.39) are given by Bloch wave functions $\phi_{n,\boldsymbol{k}}(\boldsymbol{x})$, characterized by the band index n and the quasi-momentum $\boldsymbol{k}$ [76]. Within a single Bloch band, one can define the Wannier functions [77]

$$w_{n,\boldsymbol{R}}(\boldsymbol{x}) = \frac{1}{\sqrt{N}}\sum_{\boldsymbol{k}} \phi_{n,\boldsymbol{k}}(\boldsymbol{x})\mathrm{e}^{-i\boldsymbol{k}\boldsymbol{R}}\,. \tag{1.40}$$

The Wannier functions $w_{n,\boldsymbol{R}}(\boldsymbol{x}) = w_n(\boldsymbol{x} - \boldsymbol{R})$ are localized around the minima $\boldsymbol{R}$ of the lattice potential (1.39) and form an orthonormal basis. Assuming that temperatures are sufficiently low and that typical interaction energies are small compared to the gap between the lowest and first excited band, it is sufficient to consider only the lowest Bloch band as higher bands remain largely unpopulated (from now on, we omit the band index).

To arrive at a tight-binding description, we expand the field operator in the Wannier basis,

$$\hat{\Psi}(\boldsymbol{x}) = \sum_{\ell} \hat{a}_\ell w_\ell(\boldsymbol{x})\,, \tag{1.41}$$

where $w_\ell(\boldsymbol{x}) = w(\boldsymbol{x} - \boldsymbol{R}_\ell)$ is the Wannier function located at lattice site ℓ. The operators $\hat{a}_\ell$ and $\hat{a}_\ell^\dagger$ annihilate and create bosons at site ℓ, respectively, and satisfy bosonic commutation relations as in Eq. (1.31). Inserting the expansion (1.41) in the Hamiltonian (1.2), and keeping only tunneling terms between nearest neighbors as well as interactions between particles on the same site, we arrive at the Bose–Hubbard model

$$H_{\mathrm{BH}} = -\sum_{\langle \ell,\ell'\rangle} \hbar J_{\ell\ell'} a_\ell^\dagger a_{\ell'} + \sum_{\ell} \epsilon_\ell n_\ell + \frac{\hbar U}{2}\sum_{\ell} n_\ell(n_\ell - 1)\,, \tag{1.42}$$

where $n_\ell = a_\ell^\dagger a_\ell$ is the bosonic number operator at site ℓ (from now on, we omit operator hats where the distinction between operators and classical variables is clear from the context). The first term in the Bose–Hubbard Hamiltonian (1.42) describes hopping of particles between neighboring sites (the sum runs over all pairs of nearest neighbors $\langle \ell, \ell'\rangle$) at a rate

$$\hbar J_{\ell\ell'} = -\int \mathrm{d}\boldsymbol{x}\, w_\ell^*(\boldsymbol{x})\left[-\frac{\hbar^2\nabla^2}{2m} + V_{\mathrm{ext}}(\boldsymbol{x})\right] w_{\ell'}(\boldsymbol{x})\,. \tag{1.43}$$

The second term in Eq. (1.42) represents a local energy shift due to the external trap by an amount

$$\epsilon_\ell = \int \mathrm{d}\boldsymbol{x}\, V_{\mathrm{T}}(\boldsymbol{x})|w_\ell(\boldsymbol{x})|^2 \approx V_{\mathrm{T}}(\boldsymbol{R}_\ell)\,. \tag{1.44}$$

Finally, the on-site interaction energy $\hbar U$ of particles sitting on the same lattice site, as described by the last term in the Hamiltonian (1.42), is given by

$$\hbar U = g \int \mathrm{d}\boldsymbol{x} \, |w_\ell(\boldsymbol{x})|^4 . \tag{1.45}$$

While the Bose–Hubbard model can arguably be regarded as the "workhorse" of the field of cold atoms, much like the Ising model in statistical physics, the Fermi–Hubbard model is actually in the center of interest from a condensed matter physics perspective, as it is believed to describe high-temperature superconductivity in cuprates. Quantum simulations of the Fermi–Hubbard model in optical lattices, which can be realized with ultracold fermions in a similar vein as describe above, may help to shed light on this question [78]. Beyond the standard bosonic and fermionic Hubbard models, a variety of non-standard Hubbard models exhibiting novel exotic quantum phases can be engineered in optical lattices, including the extended Hubbard model featuring long-range dipolar interactions or generalized lowest-band Hubbard models involving nearest-neighbor interactions, density-induced tunneling, as well as pair tunneling processes [17].

1.2.2. Ground State Phases of the Bose–Hubbard Model

The Fock space of a Bose–Hubbard system consisting of L lattice sites is spanned by the basis states

$$|n_1, \dots, n_L\rangle = \frac{1}{\sqrt{n_1! \cdots n_L!}} \left(a_1^\dagger\right)^{n_1} \cdots \left(a_L^\dagger\right)^{n_L} |0\rangle , \tag{1.46}$$

where $n_1, \dots, n_L$ are the occupation numbers of the modes located at the lattice sites $1, \dots, L$ and $|0\rangle \equiv |0, \dots, 0\rangle$ is the bosonic vacuum state. The action of the annihilation and creation operators on the basis states follows the standard rules of second quantization [79],

$$a_\ell \, |n_1, \dots, n_\ell, \dots, n_L\rangle = \sqrt{n_\ell} \, |n_1, \dots, n_\ell - 1, \dots, n_L\rangle , \tag{1.47a}$$

$$a_\ell^\dagger \, |n_1, \dots, n_\ell, \dots, n_L\rangle = \sqrt{n_\ell + 1} \, |n_1, \dots, n_\ell + 1, \dots, n_L\rangle . \tag{1.47b}$$

For a fixed number of particles $N = \sum_{\ell=1}^{L} n_\ell$, the dimension of the Fock space is given by [80]

$$D = \binom{N + L - 1}{N} = \frac{(N + L - 1)!}{N!(L - 1)!} . \tag{1.48}$$

By varying the depth of the optical lattice, the parameters of the Bose–Hubbard model can be tuned to regimes where either the hopping rate J or the interaction rate U dominates [11] (here, we disregard the external potential V_T and consider a homogeneous and isotropic setting where the hopping rate is the same across the lattice).

In the limit $U/J \to \infty$, the repulsive interaction dominates, which disfavors multiple occupancies on the same lattice site. At integer filling $m = N/L$, the ground state is then given by a Mott insulator (MI) [12],

$$|\Psi_\mathrm{MI}\rangle = \frac{1}{\sqrt{m!}} \prod_{\ell=1}^{L} \left(a_\ell^\dagger\right)^m |0\rangle = |m, \dots, m\rangle . \tag{1.49}$$

The MI state corresponds to the population a single Fock state without fluctuations of the number of particles on each site. The energy gap between the first excited state, corresponding to a single particle–hole excitation, and the ground state is given by $\Delta E = U$. It is this gap that is responsible for the insulating character of the MI state, as it reflects the finite amount of energy needed for transporting a single particle from one lattice site to another [80].

In the opposite limit $U/J \to 0$, where the hopping term in the Hamiltonian (1.42) dominates, particles tend to delocalize across all lattice sites. The system is then in the superfluid (SF) ground state [12]

$$|\Psi_{\mathrm{SF}}\rangle = \frac{1}{\sqrt{N!}} \left[\frac{1}{\sqrt{L}} \sum_{\ell=1}^{L} a_\ell^\dagger \right]^N |0\rangle \,. \tag{1.50}$$

In contrast to the MI state, the SF state is a superposition of all Fock states with weights following a multinomial distribution. Importantly, all particles are in the same single-particle state $|\phi\rangle = L^{-1/2} \sum_{\ell=1}^{L} a_\ell^\dagger |0\rangle$, i.e., the system is Bose-condensed. In addition, the SF state is gapless and characterized by large fluctuations of the number of particles on each site [80].

If the ratio U/J is tuned from the superfluid to the Mott-insulating phase (or vice versa), the system undergoes a quantum phase transition [12]. Unlike classical phase transitions, which are driven by thermal fluctuations, quantum phase transitions occur at zero temperature and are driven by quantum fluctuations [81]. In the seminal experiment in Ref. [25], an isolated Bose–Hubbard system quenched from the Mott-insulating to the superfluid regime has been shown to undergo quantum thermalization. In Chapter 2, we will use this very example to benchmark protocols for the measurement of dynamical correlations and fluctuation–dissipation relations based on non-Hermitian linear response. Before turning to this application, we introduce the basics of linear response theory in the next section.

1.3. Linear Response Theory and the Fluctuation–Dissipation Relation

Linear response theory is a powerful framework that allows one to extract dynamical properties of a system from the way it responds to external perturbations [21, 82]. The theory mainly goes back to R. Kubo, who used it to derive the celebrated fluctuation–dissipation relation (FDR) for systems in thermal equilibrium (sometimes also called the fluctuation–dissipation theorem) [83, 84]. In essence, the FDR connects the intrinsic fluctuations of a system in equilibrium at any given frequency to the energy dissipated when the system is perturbed at that same frequency. The famous Einstein relation for Brownian motion [85] is a basic example of such an interplay: the diffusion coefficient D of a Brownian particle in thermal equilibrium is connected to the mobility μ via the relation

$$D = k_{\mathrm{B}} T \mu \,, \tag{1.51}$$

where k_B is the Boltzmann constant and T is the temperature. This result can be viewed as a fluctuation–dissipation relation because D quantifies the "fluctuations" of the particle's position due to the random kicks by the surrounding fluid molecules, whereas μ, the inverse friction constant, represents the "dissipative" force exerted by the medium. Another well-known example of an FDR is the Johnson–Nyquist spectrum generated by thermal fluctuations in electrical resistors [86, 87]. Besides its fundamental importance, the FDR features a wide range of applications across of multitude of disciplines in physics, including fluid dynamics, climate science, granular materials, and biological systems [88].

In this thesis, we will be primarily interested in FDRs for quantum systems. Given its groundbreaking role in statistical mechanics, it is surprising that to date the FDR has never been measured experimentally in a quantum system. The main difficulty stems from the requirement to measure unequal-time correlation functions: a projective von Neumann measurement of an observable at a certain time collapses the quantum state [89, 90], which hinders a measurement of a second observable at a later time with respect to the original state. In Chapter 2, we develop protocols based on non-Hermitian linear response to overcome this measurement back action, enabling unbiased measurements of dynamical correlations and FDRs in quantum many-body systems. With this motivation in mind, in what follows, we set the stage by reviewing the basics of linear response theory and the FDR for general quantum systems. The following sections are mainly based on Refs. [57, 91].

1.3.1. Kubo's Linear Response Formula

Let H_0 denote the unperturbed Hamiltonian of the system and $H_1(t) = -f(t)A$ a perturbation by a Hermitian operator A with a time-dependent modulation $f(t)$. The density operator $\rho(t)$ evolves under the total Hamiltonian $H(t) = H_0 + H_1(t)$ according to the von Neumann equation

$$i\hbar \frac{\mathrm{d}}{\mathrm{d}t}\rho(t) = [H(t), \rho(t)] \tag{1.52}$$

with initial condition $\rho(t_0) = \rho_0$. In many applications of linear response theory, the system of interest is in thermal equilibrium. Furthermore, to ensure regularity of the linear response, the perturbation is typically ramped up adiabatically as $f(t) = \mathrm{e}^{\epsilon t} g(t)$ with $\epsilon > 0$ small, such that at $t_0 = -\infty$ the system is governed solely by the unperturbed Hamiltonian H_0. For the time being, we will nonetheless keep ρ_0 and t_0 general, as the derivation of Kubo's formula does not depend on these assumptions.

It is convenient to transform to the interaction picture (rotating frame) with respect to the unperturbed Hamiltonian H_0. The von Neumann equation then reads

$$i\hbar \frac{\mathrm{d}}{\mathrm{d}t}\tilde{\rho}(t) = \left[\tilde{H}_1(t), \tilde{\rho}(t)\right], \tag{1.53}$$

where $\tilde{\rho}(t) = \mathrm{e}^{iH_0 t/\hbar}\rho(t)\mathrm{e}^{-iH_0 t/\hbar}$ is the density operator and $\tilde{H}_1(t) = -f(t)\tilde{A}(t)$ with $\tilde{A}(t) = \mathrm{e}^{iH_0 t/\hbar} A \mathrm{e}^{-iH_0 t/\hbar}$ is the Hamiltonian in the interaction picture. We can rewrite

this equation equivalently in integral form as

$$\tilde{\rho}(t) = \tilde{\rho}(t_0) - \frac{i}{\hbar}\int_{t_0}^{t} \mathrm{d}t' \left[\tilde{H}_1(t'), \tilde{\rho}(t')\right] \tag{1.54}$$

with $\tilde{\rho}(t_0) = \rho_0$. In time-dependent perturbation theory, repeatedly inserting the left-into the right-hand side leads to the well-known Neumann (or Dyson) series [92]. In linear response theory, we neglect contributions that are of quadratic or higher order in the perturbation. To linear order in the perturbation, we may therefore replace $\tilde{\rho}(t')$ in the integrand by $\tilde{\rho}(t_0)$, yielding

$$\tilde{\rho}(t) = \rho_0 + \frac{i}{\hbar}\int_{t_0}^{t} \mathrm{d}t'\, f(t')\left[\tilde{A}(t'), \rho_0\right]. \tag{1.55}$$

The linear response of an observable B to the perturbation A, i.e., the time evolution of the expectation value $\langle B(t)\rangle = \mathrm{Tr}[B\rho(t)] = \mathrm{Tr}[\tilde{B}(t)\tilde{\rho}(t)]$ under the total Hamiltonian $H(t)$, linearized with respect to the perturbation, is then given by

$$\langle B(t)\rangle = \langle B(t)\rangle_0 + \int_{t_0}^{t} \mathrm{d}t'\, f(t')\phi_{BA}(t,t'), \tag{1.56}$$

where we have introduced the response function

$$\phi_{BA}(t,t') = \frac{i}{\hbar}\theta(t-t')\langle[B(t), A(t')]\rangle_0. \tag{1.57}$$

This important result, known as the Kubo formula [84], states that the perturbation by the operator A causes a deviation $\Delta B(t) = \langle B(t)\rangle - \langle B(t)\rangle_0$ from the unperturbed expectation value $\langle B(t)\rangle_0$, which in the linear regime is proportional to the perturbation strength and given by the convolution of the modulation function $f(t)$ with the response function $\phi_{BA}(t,t')$. The Heaviside step function $\theta(t)$ in Eq. (1.57), defined as $\theta(t) = 0$ for $t < 0$ and $\theta(t) = 1$ for $t \geq 0$, ensures causality of the response (the response must be independent of any future perturbations), so the upper integration bound in Eq. (1.56) can be extended to $+\infty$. The response function (1.57) is determined by the unequal-time commutator of the Heisenberg operators $B(t) = \mathrm{e}^{iH_0 t/\hbar} B \mathrm{e}^{-iH_0 t/\hbar}$ and $A(t') = \mathrm{e}^{iH_0 t'/\hbar} A \mathrm{e}^{-iH_0 t'/\hbar}$. Its complex conjugate reads $\phi^*_{BA}(t,t') = \phi_{B^\dagger A^\dagger}(t,t')$, so the response function is real if A and B are Hermitian. The subscript in the expectation value $\langle\cdots\rangle_0$ reminds us that the operators evolve under the unperturbed Hamiltonian H_0 and that the average is taken with respect to the (unperturbed) initial state ρ_0. This way, linear response theory allows one to probe properties of the *unperturbed* system from the way it responds to external perturbations.

In deriving Eq. (1.57), we have assumed the perturbation operator A to be Hermitian. However, we may also choose a more general perturbation of the form

$$H_1(t) = -\frac{1}{2}\left[f(t)A + f^*(t)A^\dagger\right], \tag{1.58}$$

where $f(t)$ is complex and A is a general (not necessarily Hermitian) operator. Note that this perturbation Hamiltonian is still Hermitian[3]. The linear response then reads

$$\langle B(t)\rangle = \langle B(t)\rangle_0 + \int_{t_0}^{t} \mathrm{d}t' \, \frac{1}{2}[f(t')\phi_{BA}(t,t') + f^*(t')\phi_{BA^\dagger}(t,t')] \,, \tag{1.59}$$

where the response function ϕ_{BA} is again given by Eq. (1.57), even if A is not Hermitian. Most of following discussion therefore applies to general operators A and B.

1.3.2. Dynamical Susceptibility

Kubo's response function (1.57) determines the linear response in time domain. We now consider the equivalent problem in Fourier domain by introducing the dynamical susceptibility, which characterizes how the system reacts when perturbed at a certain frequency. To simplify the discussion, we assume the system to be in a stationary state, e.g., in thermal equilibrium, such that the response function (1.57) depends only on the time difference $\Delta t = t - t'$. In Section 2.2.1, we will discuss generalizations to non-equilibrium states. The dynamical susceptibility is defined as the Fourier transform of the response function with respect to the relative time Δt,

$$\chi_{BA}(\omega) = \lim_{\epsilon \to 0^+} \int_{-\infty}^{\infty} \mathrm{d}\Delta t \, \phi_{BA}(\Delta t) \mathrm{e}^{i\omega \Delta t} \mathrm{e}^{-\epsilon|\Delta t|} \,. \tag{1.60}$$

The factor $\mathrm{e}^{-\epsilon \Delta t}$ in the integrand acts as an exponential frequency filter and ensures convergence of the Fourier integral (note that negative Δt do not contribute to the integral due to causality). Physically, it can be thought of as mimicking finite spectral resolution in an experiment. Taking the limit $\epsilon \to 0$ (from above) makes the final result independent of ϵ. Since the response function (1.57) satisfies $\phi^*_{BA}(t,t') = \phi_{B^\dagger A^\dagger}(t,t')$, the susceptibility obeys the symmetry relation $\chi^*_{BA}(\omega) = \chi_{B^\dagger A^\dagger}(-\omega)$.

If the perturbation is ramped up sufficiently smooth starting at $t_0 = -\infty$ [see comment below Eq. (1.52)], the linear response in Eq. (1.59) can be expressed in Fourier space as

$$\Delta B(\omega) = \frac{1}{2}[f(\omega)\chi_{BA}(\omega) + f^*(-\omega)\chi_{BA^\dagger}(\omega)] \,, \tag{1.61}$$

where $\Delta B(\omega)$ and $f(\omega)$ are the Fourier transforms of $\Delta B(t) = \langle B(t)\rangle - \langle B\rangle_0$ and $f(t)$, respectively. For $A = A^\dagger$ and $f(t)$ real, this result reduces to the compact form $\Delta B(\omega) = f(\omega)\chi_{BA}(\omega)$. In case of a periodic perturbation $f(t) = \lambda \mathrm{e}^{-i\omega t}$, inverse Fourier transform of Eq. (1.61) yields

$$\Delta B(t) = \frac{1}{2}\big[\lambda \mathrm{e}^{-i\omega t}\chi_{BA}(\omega) + \lambda^* \mathrm{e}^{i\omega t}\chi_{BA^\dagger}(-\omega)\big] \,, \tag{1.62}$$

which shows explicitly that the dynamical susceptibility determines the linear response to a perturbation that is modulated at a frequency ω.

[3] In Section 2.1, we consider perturbations by an anti-Hermitian Hamiltonian, where the response function is given by the anti-commutator instead of the commutator.

It is instructive to split the dynamical susceptibility as $\chi_{BA} = \chi'_{BA} + i\chi''_{BA}$ into the components

$$\chi'_{BA}(\omega) = \frac{1}{2}[\chi_{BA}(\omega) + \chi_{AB}(-\omega)]\,, \tag{1.63a}$$

$$\chi''_{BA}(\omega) = \frac{1}{2i}[\chi_{BA}(\omega) - \chi_{AB}(-\omega)]\,, \tag{1.63b}$$

which are commonly referred to as the reactive and dissipative (or absorptive) parts of the dynamical susceptibility, respectively. To see why these names are justified, we consider the response of a Hermitian observable to a perturbation by itself, i.e., $B = A = A^\dagger$, under a periodic modulation $f(t) = \lambda\cos(\omega t)$. The susceptibility components in Eq. (1.63) then become real and the response in Eq. (1.62) reduces to

$$\Delta A(t) = \lambda[\chi'_{AA}(\omega)\cos(\omega t) + \chi''_{AA}(\omega)\sin(\omega t)]\,. \tag{1.64}$$

This shows that χ' determines the part of the response that is in phase with the external perturbation and is therefore called the "reactive" component. The out-of-phase response, determined by χ'', is connected to energy absorption: by virtue of the Hellmann–Feynman theorem, the change of the instantaneous energy $\langle H(t)\rangle$ can easily be calculated as

$$\frac{\mathrm{d}}{\mathrm{d}t}\langle H(t)\rangle = \left\langle \frac{\partial H(t)}{\partial t} \right\rangle = -\frac{1}{2}\big[\dot{f}(t)\langle A(t)\rangle + \dot{f}^*(t)\langle A^\dagger(t)\rangle\big]\,. \tag{1.65}$$

For a periodic perturbation $f(t) = \lambda \mathrm{e}^{-i\omega t}$, using Eq. (1.62), we obtain the mean energy dissipation rate

$$\frac{\mathrm{d}E}{\mathrm{d}t} = \frac{1}{2}|\lambda|^2\omega\chi''_{A^\dagger A}(\omega)\,, \tag{1.66}$$

where oscillating terms in Eq. (1.65) vanish after time-averaging over one oscillation period $2\pi/\omega$. This result makes it plausible why χ'' is commonly referred to as the "dissipative" (or "absorptive") component of the dynamical susceptibility.

As a consequence of causality, the dynamical susceptibility (1.60), when extended into the complex plane, is an analytic function in the upper half of the complex plane. Therefore, the two susceptibility components are not independent, but they are linked by Kramers–Kronig relations [93, 94],

$$\chi'_{BA}(\omega) = \frac{1}{\pi}\,\mathrm{PV}\int_{-\infty}^{\infty} \frac{\chi''_{BA}(\omega')}{\omega' - \omega}\,\mathrm{d}\omega'\,, \tag{1.67a}$$

$$\chi''_{BA}(\omega) = -\frac{1}{\pi}\,\mathrm{PV}\int_{-\infty}^{\infty} \frac{\chi'_{BA}(\omega')}{\omega' - \omega}\,\mathrm{d}\omega'\,, \tag{1.67b}$$

$$\tag{1.67c}$$

where PV denotes the Cauchy principal value.

It is possible to derive an explicit formula for the dynamical susceptibility in frequency space with respect to the energy eigenbasis of the unperturbed Hamiltonian H_0. To this

end, we consider a thermal state described by the canonical[4] density matrix

$$\rho(T) = \frac{1}{Z(T)} \exp\left(-\frac{H_0}{k_\mathrm{B}T}\right), \tag{1.68}$$

where $Z(T) = \mathrm{Tr}[\exp(-H_0/k_\mathrm{B}T)]$ is the canonical partition sum, k_B is the Boltzmann constant, and T is the temperature. Let $\{E_k\}$ denote the spectrum of eigenvalues of H_0 with corresponding eigenstates $\{|k\rangle\}$, i.e., $H_0|k\rangle = E_k|k\rangle$. By inserting identities in the form $\mathbb{1} = \sum_k |k\rangle\langle k|$ into the definition of the susceptibility (1.60), we obtain

$$\chi_{BA}(\omega) = -\lim_{\epsilon\to 0^+} \sum_{k,m} \frac{B_{km}A_{mk}(n_k - n_m)}{\hbar\omega - E_{mk} + i\hbar\epsilon}, \tag{1.69}$$

where $n_k = \mathrm{e}^{-E_k/k_\mathrm{B}T}/Z$ is the Boltzmann factor describing the thermal occupancy of the state $|k\rangle$, $B_{km} = \langle k|B|m\rangle$ are the matrix elements of the operator B (and analogously for A), and $E_{mk} = E_m - E_k$ are the transition energies. Using the Dirac formula

$$\lim_{\epsilon\to 0^+} \frac{1}{x \pm i\epsilon} = \mp i\pi\delta(x) + \mathrm{PV}\,\frac{1}{x}, \tag{1.70}$$

where $\delta(x)$ is the Dirac delta function, the susceptibility components (1.63) can be expressed as

$$\chi'_{BA}(\omega) = -\sum_{E_k\neq E_m} \frac{B_{km}A_{km}(n_k - n_m)}{\hbar\omega - E_{mk}} + \chi'^{(\mathrm{el})}_{BA}\delta_{\omega 0}, \tag{1.71a}$$

$$\chi''_{BA}(\omega) = \pi \sum_{k,m} B_{km}A_{km}(n_k - n_m)\delta(\hbar\omega - E_{mk}), \tag{1.71b}$$

where $\delta_{\omega 0}$ denotes the Kronecker delta. The non-trivial elastic contribution $\chi'^{(\mathrm{el})}_{BA}$ to the reactive component is possible due to the vanishing denominator for $E_k = E_m$ in the static limit $\omega \to 0$. By means of the FDR, one can show that it is given by [91]

$$\chi'^{(\mathrm{el})}_{BA} = \frac{1}{k_\mathrm{B}T} \sum_{E_k = E_m} (B_{km}A_{km}n_k - \langle B\rangle\langle A\rangle). \tag{1.72}$$

While in general the susceptibility components χ' and χ'' are complex, they in fact take real values in many applications of physical interest. For example, the susceptibility components are real for auto-correlations ($B = A^\dagger$), which follows from the definition in Eq. (1.63) by noting that $\chi_{AA^\dagger}(-\omega) = \chi_{A^\dagger A}(\omega)^*$ [and is also evident from the spectral representation in Eq. (1.71)]. This even holds for local operators $B = A^\dagger(\boldsymbol{y})$ and $A = A(\boldsymbol{x})$, provided the system is homogeneous and isotropic, such that the two-point correlator $\langle A^\dagger(\boldsymbol{y})A(\boldsymbol{x})\rangle$ depends only on the distance $|\boldsymbol{y} - \boldsymbol{x}|$. Another important case

[4] For perturbations that do not conserve the total number of particles, it is more convenient to work in the grand canonical ensemble, $\rho(T,\mu) = \exp[-(H_0 - \mu N)/k_\mathrm{B}T]/Z(T,\mu)$, where N is the particle number operator, μ is the chemical potential, and $Z(T,\mu) = \mathrm{Tr}\{\exp[-(H_0 - \mu N)/k_\mathrm{B}T]\}$ is the grand canonical partition sum.

where the susceptibility components are real concerns systems with time reversal symmetry, such that the Hamiltonian H_0 is real and symmetric. Then, if B and A are Hermitian operators that are both even (or odd) under time reversal, the product of matrix elements in Eq. (1.71) is real. In the outlined scenarios where the susceptibility components χ' and χ'' take real values, they simply correspond to the real and imaginary part of the dynamical susceptibility χ, respectively.

1.3.3. The Fluctuation–Dissipation Relation

Before we are in a position to formulate the FDR, we introduce the dynamical correlation function

$$C_{BA}(t,t') = \langle B(t)A(t')\rangle - \langle B(t)\rangle\langle A(t')\rangle \tag{1.73}$$

as well as its symmetrized and anti-symmetrized variants

$$S_{BA}(t,t') = \frac{1}{2}[C_{BA}(t,t') + C_{AB}(t',t)] = \frac{1}{2}\langle\{B(t),A(t')\}\rangle - \langle B(t)\rangle\langle A(t')\rangle\,, \tag{1.74}$$

$$K_{BA}(t,t') = i[C_{BA}(t,t') - C_{AB}(t',t)] \;= i\langle[B(t),A(t')]\rangle\,. \tag{1.75}$$

Here and in what follows, where there are no ambiguities, we omit the subscript in the expectation values indicating that the Heisenberg operators evolve under the unperturbed Hamiltonian H_0. The unequal-time commutator K_{BA} is related to the causal response function (1.57) by $\phi_{BA}(t,t') = \theta(t-t')K_{BA}(t,t')/\hbar$ or $K_{BA}(t,t') = \hbar\phi_{BA}(t,t') - \hbar\phi_{AB}(t',t)$. Furthermore, the correlation functions in Eqs. (1.74) and (1.75) obey the general symmetry relations

$$S_{BA}(t,t') = S_{AB}(t',t)\,, \qquad S^*_{BA}(t,t') = S_{B^\dagger A^\dagger}(t,t')\,, \tag{1.76a}$$

$$K_{BA}(t,t') = -K_{AB}(t',t)\,, \qquad K^*_{BA}(t,t') = K_{B^\dagger A^\dagger}(t,t')\,. \tag{1.76b}$$

In particular, if A and B are Hermitian, we have $S_{BA}(t,t') = \mathrm{Re}[C_{BA}(t,t')]$ and $K_{BA}(t,t') = -2\,\mathrm{Im}[C_{BA}(t,t')]$. In the context of non-equilibrium quantum field theory, the two-time anti-commutator (1.74) and commutator (1.75) are also known as the statistical function F and the spectral function ρ, respectively [95].

We now consider a system in thermal equilibrium described by the density operator $\rho(T)$ in Eq. (1.68). The two-time correlators in Eqs. (1.74) and (1.75) then only depend on the relative time $\Delta t = t - t'$. Moreover, the Fourier transform of the unequal-time commutator is connected to the dissipative part of the dynamical susceptibility via

$$\begin{aligned} K_{BA}(\omega) &= \lim_{\epsilon\to 0^+}\int_{-\infty}^{\infty}\mathrm{d}\Delta t\, K_{BA}(\Delta t)\mathrm{e}^{i\omega\Delta t}\mathrm{e}^{-\epsilon|\Delta t|} \\ &= \lim_{\epsilon\to 0^+}\hbar\left[\int_0^\infty \mathrm{d}\Delta t\,\phi_{BA}(\Delta t)\mathrm{e}^{i\omega\Delta t}\mathrm{e}^{-\epsilon\Delta t} - \int_0^\infty \mathrm{d}\Delta t\,\phi_{AB}(\Delta t)\mathrm{e}^{-i\omega\Delta t}\mathrm{e}^{-\epsilon\Delta t}\right] \\ &= 2i\hbar\chi''_{BA}(\omega)\,, \end{aligned} \tag{1.77}$$

where in the second step we have split the integral into an integration over the positive and negative real line, followed by substituting $\Delta t \to -\Delta t$ and using $K_{BA}(\Delta t) =$

$-K_{AB}(-\Delta t)$ in the latter. Using the definition of K_{BA} in Eq. (1.75) further yields the relation

$$\chi''_{BA}(\omega) = \frac{1}{2\hbar}[C_{BA}(\omega) - C_{AB}(-\omega)]\,, \tag{1.78}$$

where we have introduced the correlation spectrum $C_{BA}(\omega)$ as the Fourier transform of the correlation function (1.73) with respect to Δt.

The key to deriving the FDR is a boundary condition in imaginary time satisfied by quantum systems in thermal equilibrium, the so-called Kubo–Martin–Schwinger (KMS) boundary condition [84, 96],

$$\begin{aligned}\langle B(t)A\rangle &= \frac{1}{Z}\,\mathrm{Tr}\big[\mathrm{e}^{-\beta H}B(t)A\big] \\ &= \frac{1}{Z}\,\mathrm{Tr}\big[\mathrm{e}^{iH(t+i\beta\hbar)/\hbar}B\mathrm{e}^{-iH(t+i\beta\hbar)/\hbar}\mathrm{e}^{-\beta H}A\big] \\ &= \frac{1}{Z}\,\mathrm{Tr}\big[\mathrm{e}^{-\beta H}AB(t+i\beta\hbar)\big] = \langle AB(t+i\beta\hbar)\rangle\,,\end{aligned} \tag{1.79}$$

where $\beta = 1/k_{\mathrm{B}}T$ (and $H = H_0$). The KMS condition implies

$$C_{BA}(\Delta t) = C_{AB}(-\Delta t - i\beta\hbar)\,. \tag{1.80}$$

Using Cauchy's integral theorem on the boundary on the strip $-\beta\hbar \leq \mathrm{Im}(t) \leq 0$ in the complex t-plane, assuming that $C_{BA}(\mathrm{t})$ is analytic in the relevant region and that the observables $B(t)$ and A become uncorrelated for $t \to \pm\infty$, i.e., $C_{BA}(\pm\infty) = 0$, one can show that the above equation in Fourier space reads

$$C_{BA}(\omega) = \mathrm{e}^{\beta\hbar\omega}C_{AB}(-\omega). \tag{1.81}$$

This relation expresses the principle of detailed balance. For $B = A^\dagger$, it states that the probabilities of absorbing and releasing a quantum of energy $\hbar\omega$ in response to the perturbation (1.58), induced by the operators A and $A^\dagger$, respectively, are related in thermal equilibrium by the Boltzmann factor.

Combining Eqs. (1.78) and (1.81) yields the celebrated fluctuation–dissipation relation

$$C_{BA}(\omega) = \frac{2\hbar}{1-\mathrm{e}^{-\beta\hbar\omega}}\chi''_{BA}(\omega)\,. \tag{1.82}$$

For quantum systems, the FDR is more commonly phrased in terms of the symmetrized correlation spectrum $S_{BA}(\omega)$. Using the definitions (1.63b) and (1.74), the FDR (1.82) can be rewritten as

$$S_{BA}(\omega) = \hbar\coth\left(\frac{\hbar\omega}{2k_{\mathrm{B}}T}\right)\chi''_{BA}(\omega)\,. \tag{1.83}$$

This elegant relation connects the correlation spectrum, i.e., the Fourier transform of the two-time *anti-commutator* of any two operators A and B, with the dissipative component of the dynamical susceptibility, i.e., the Fourier transform of the two-time *commutator* of A and B, across the entire frequency spectrum, requiring only a single input parameter, the global temperature T. In the light of Eq. (1.66), for $B = A^\dagger$, it links the intrinsic

fluctuations of an observable A at any given frequency ω to the energy dissipated when the system is perturbed at that frequency. It is worth emphasizing that the crucial assumption of thermal equilibrium enters via the KMS condition (1.79). While other symmetry relations like the result in Eq. (1.78) hold also out of equilibrium if the relevant quantities are generalized in a suitable manner (see Section 2.2.1), the KMS condition is characteristic to thermal equilibrium and consequently the FDR is an excellent probe of thermalization, which is our main application in Section 2.2.

Classical Limit of the Fluctuation–Dissipation Relation

It is instructive to consider the classical limit of the FDR (1.83), which formally corresponds to $\hbar \to 0$. Thus, if characteristic energies are small as compared to the energy scale set by the temperature, we can expand the hyperbolic cotangent and recover the classical FDR

$$S_{BA}(\omega) = \frac{2k_{\mathrm{B}}T}{\omega}\chi''_{BA}(\omega) \tag{1.84}$$

or

$$\partial_t S_{BA}(t-t') = -k_{\mathrm{B}}T\left[\phi_{BA}(t-t') - \phi_{AB}(t'-t)\right] \tag{1.85}$$

after Fourier-transforming back to time domain. Multiplying both sides by $\theta(t-t')$, i.e., considering only $t \geq t'$, this relation simplifies to

$$\phi_{BA}(t-t') = -\beta\theta(t-t')\partial_t S_{BA}(t-t')\,. \tag{1.86}$$

The Fourier transform of this equation with respect to the relative time $t-t'$, using $\partial_t S_{BA}(t,t') = -\partial_{t'} S_{BA}(t,t')$, reads

$$\chi_{BA}(\omega) = \beta\int_0^\infty \mathrm{d}t\,\left\langle B(t)\dot{A}(0)\right\rangle \mathrm{e}^{i\omega t}\,. \tag{1.87}$$

This result is another well-known manifestation of the FDR [21], phrased here for classical observables A and B. Note that in classical systems, the response function is obtained from the relation (1.56) rather than from the Kubo formula (1.57).

In fact, Eq. (1.87) is a direct generalization of the Einstein relation (1.51). To see this, we consider the Langevin equation

$$\frac{\mathrm{d}v}{\mathrm{d}t} = -\gamma v - \frac{1}{m}\frac{\partial V(x,t)}{\partial x} + \sqrt{\frac{2\gamma k_{\mathrm{B}}T}{m}}\xi(t)\,, \tag{1.88}$$

describing the stochastic dynamics of a Brownian particle [97]. Here, $x(t)$ and $v(t) = \dot{x}(t)$ denote the particle's position and velocity, respectively, γ is the friction coefficient, m is the mass, and $V(x,t)$ is an external potential. The random kicks exerted by the surrounding fluid molecules are described by the Gaussian white noise process $\xi(t)$, which satisfies $\langle\!\langle \xi(t)\rangle\!\rangle = 0$ and $\langle\!\langle \xi(t)\xi(t')\rangle\!\rangle = \delta(t-t')$, where $\langle\!\langle\cdots\rangle\!\rangle$ denotes the ensemble average. Langevin's equation is the historic prototype of a stochastic differential equation (SDE), whose basic properties we review in Appendix A.1, and allows for an elegant derivation of the Einstein relation [97]. Here, we illustrate how the FDR (1.87) specializes when

applied to the problem of Brownian motion. To this end, we consider the perturbation $V(x,t) = -xF(t)$ with a time-dependent force $F(t)$. The relevant perturbation operator thus corresponds to the position, $A = x$. Solving Eq. (1.88), one finds the mean velocity

$$\langle\!\langle v(t) \rangle\!\rangle = \langle\!\langle v(0) \rangle\!\rangle \mathrm{e}^{-\gamma t} + \frac{1}{m} \int_0^t \mathrm{d}t' \, F(t') \mathrm{e}^{-\gamma(t-t')} \,. \tag{1.89}$$

A comparison with the linear response relation in Eq. (1.56) ($B = v$) allows one to identify the response function $\phi_{vx}(t-t') = \mathrm{e}^{-\gamma(t-t')}/m$, which readily yields the susceptibility

$$\chi_{vx}(\omega) = \frac{1}{m} \frac{1}{\gamma - i\omega} \,. \tag{1.90}$$

In the static limit $\omega \to 0$, Eq. (1.87) then reduces to the Einstein relation

$$\mu = \beta \int_0^\infty \mathrm{d}t \, \langle v(t) v(0) \rangle = \beta D \,, \tag{1.91}$$

where we have identified the mobility $\mu = 1/m\gamma$ and the diffusion constant [21]

$$\begin{aligned} D &= \lim_{t\to\infty} \frac{1}{2t} \left\langle [x(t) - x(0)]^2 \right\rangle \\ &= \lim_{t\to\infty} \frac{1}{t} \int_0^t \mathrm{d}t' \int_0^{t-t'} \mathrm{d}\Delta t \, \langle v(t') v(t'+\Delta t) \rangle \\ &= \int_0^\infty \mathrm{d}t \, \langle v(t_0+t) v(t_0) \rangle \,, \end{aligned} \tag{1.92}$$

Here, in the first step we have used the relation $v = \dot{x}$ in integral form and the last line follows from stationarity. All in all, we have recovered the Einstein relation as a special case of the classical FDR in the form of Eqs. (1.84), (1.85) and (1.87), which in turn arises as the classical limit of the general FDR (1.83) for quantum systems.

1.3.4. Sum Rules

Sum rules have played a groundbreaking role in the development of quantum mechanics and other fields of physics. The historically most prominent example is the Thomas–Reiche–Kuhn sum rule (or f sum rule) for the energy-weighted moment of the position operator x [98–100],

$$\sum_j f_{jk} = \frac{2m}{\hbar^2} \sum_j |\langle j|x|k\rangle|^2 (E_j - E_k) = 1 \,. \tag{1.93}$$

Here, the sum ranges over a complete set of eigenstates $\{|j\rangle\}$ of a single-particle Hamiltonian of the form $H = p^2/2m + V(x)$, where $\{E_j\}$ are the corresponding eigenenergies. The quantity $f_{jk} = 2m|\langle j|x|k\rangle|^2 (E_j - E_k)/\hbar^2$ is called the oscillator strength of the transition between the states $|j\rangle$ and $|k\rangle$.

In what follows, based on the discussion in Ref. [57], we review important sum rules for the moments of the dynamic structure factor and point out their connection to quantities accessible from linear response theory like the dynamical susceptibility. This framework provides a powerful and general way of characterizing the excitation spectrum of a system.

For a system in thermal equilibrium, we define the dynamic structure factor relative to the operators A and B as

$$F_{BA}(\omega) = \sum_{k,m} n_k B_{km} A_{mk} \delta(\hbar\omega - E_{mk}) \,, \tag{1.94}$$

where the notation is the same as in Eq. (1.69). This quantity is the Fourier transform of the unequal-time correlation function

$$\tilde{C}_{BA}(t - t') = \frac{1}{2\pi\hbar} \langle B(t) A(t') \rangle \,, \tag{1.95}$$

expressed in the energy eigenbasis the Hamiltonian H (referring to the unperturbed Hamiltonian in a linear response context), which can be shown following similar steps as in the derivation of the spectral representation of the dynamical susceptibility leading to Eq. (1.63). Upon comparison with Eq. (1.73), the dynamic structure factor is related to the correlation spectrum via $C_{BA}(\omega) = 2\pi\hbar[F_{BA}(\omega) - \langle B\rangle\langle A\rangle\delta(\hbar\omega)]$.

The p-th moment of the dynamic structure factor is defined as

$$m_p(B, A) = \hbar^{p+1} \int_{-\infty}^{\infty} \mathrm{d}\omega \, \omega^p F_{BA}(\omega) = \sum_{m,k} n_k B_{km} A_{mk} (E_m - E_k)^p \,. \tag{1.96}$$

Using the completeness relation $\mathbb{1} = \sum_m |m\rangle\langle m|$, one can derive the identities

$$m_0(B, A) \pm m_0(A, B) = \langle [B, A]_{\pm} \rangle \,, \tag{1.97}$$

$$m_1(B, A) \pm m_1(A, B) = \langle [B, [H, A]_{-}]_{\mp} \rangle \,, \tag{1.98}$$

where $[\cdot, \cdot]_+$ and $[\cdot, \cdot]_-$ denote the anti-commutator and commutator, respectively. In fact, Eqs. (1.97) and (1.98) are the lowest-order representatives of a hierarchy of sum rules, which for $p \geq 0$ can be reduced in terms of commutators with the Hamiltonian [101, 102]. These sum rules thus provide an algebraic way of evaluating the moments of the dynamic structure factor.

Importantly, the moments of the dynamic structure factor are also closely related to the properties of the response function. For instance, Eqs. (1.97) and (1.98) determine the high-frequency expansion of the dynamical susceptibility,

$$\begin{aligned} \chi_{BA}(\omega) &= -\lim_{\epsilon \to 0^+} \int_{-\infty}^{\infty} \mathrm{d}\omega' \left[\frac{F_{BA}(\omega')}{\omega - \omega' + i\epsilon} - \frac{F_{AB}(\omega')}{\omega + \omega' + i\epsilon} \right] \\ &= -\frac{1}{\hbar\omega} \langle [B, A] \rangle_0 - \frac{1}{(\hbar\omega)^2} \langle [B, [H_0, A]] \rangle_0 + \mathcal{O}(\omega^{-3}) \,, \end{aligned} \tag{1.99}$$

where the representation of $\chi_{BA}(\omega)$ in the first line follows by combining Eqs. (1.69) and (1.94), and the second line is obtained by expanding the frequency denominators around $|\omega| = \infty$. This shows that in general the dynamical susceptibility vanishes at high frequencies like ω^{-1}, whereas if the operators A and B commute, the leading contribution comes from the second term which decreases like ω^{-2}. In the opposite limit at low frequencies, the dynamical susceptibility tends to its static limit

$$\chi_{BA}(\omega \to 0) = m_{-1}(B, A) + m_{-1}(A, B)\,. \tag{1.100}$$

This important relation allows one to access the inverse energy-weighted moments of the dynamic structure factor, which cannot be reduced in terms of commutators, by measuring the static susceptibility.

We close our discussion of sum rules by quoting a number of general inequalities satisfied by the moments of the dynamic structure factor if the system is in its ground state, i.e., at zero temperature. Since the excitation energies $E_{m0} = E_m - E_0$ are always positive (E_0 is the ground state energy), $F_{BA}(\omega < 0)$ vanishes identically at $T = 0$. For $B = A^\dagger$, the dynamic structure factor then reduces to

$$F_A(\omega) \equiv F_{A^\dagger A}(\omega) = \sum_m |\langle m|A|0\rangle|^2 \delta(\hbar\omega - E_{m0})\,, \tag{1.101}$$

where $|\langle m|A|0\rangle|^2$ is called the strength of the operator A relative to the state $|m\rangle$. In this case, the moments (1.96) take the form

$$m_p(A) \equiv m_p(A^\dagger, A) = \sum_m |\langle m|A|0\rangle|^2 (E_m - E_0)^p\,. \tag{1.102}$$

From the energy-weighted sum rule (1.98), we then recover the f sum rule (1.93) for $A = x$, assuming a Hamiltonian of the form $H = p^2/2m + V(x)$ and using the canonical commutation relation $[x, p] = i\hbar$.

Exploiting the non-negativity of the dynamic structure factor in Eq. (1.101) and the fact that it vanishes for $\omega < 0$, one can derive the general inequality

$$\frac{m_{p+1}(A)}{m_p(A)} \geq \frac{m_p(A)}{m_{p-1}(A)}\,. \tag{1.103}$$

In addition, one readily obtains the rigorous upper bound for the frequency of the lowest mode excited by the operator A,

$$\hbar\omega_{\min} \leq \frac{m_{p+1}(A)}{m_p(A)}\,. \tag{1.104}$$

Combining, Eqs. (1.103) and (1.104) further yields

$$\hbar\omega_{\min} \leq \sqrt{\frac{m_{p+1}(A)}{m_{p-1}(A)}}\,. \tag{1.105}$$

The above inequalities hold for any value of p and become identities if a single excited state exhausts the strength of the operator A, i.e., if the dynamic structure factor is proportional to a single delta function, $F_{BA}(\omega) \propto \delta(\hbar\omega - \hbar\omega_{\mathrm{min}})$.

As a concluding remark, it is worth highlighting that sum rule theory draws its outstanding power from the generality of the underlying approach, which makes the framework completely model-independent. All results presented in this section essentially require only the assumption that the system is in thermal equilibrium. The moments of the dynamic structure factor can be evaluated based on general algebraic properties of the system under investigation, e.g., commutation relations, or can be expressed in terms of fundamental measurable quantities like susceptibilities. Thus, sum rules play a fundamental role in physics as they set rigorous bounds which any physical theory must obey. In Section 4.3.2, we will see how sum rule arguments provide evidence for the emergence of a new Goldstone mode in the supersolid phase of a spin–orbit-coupled Bose–Einstein condensate.

2. Probing Dynamical Correlations and Fluctuation–Dissipation Relations via Non-Hermitian Linear Response

This chapter is mainly based on Ref. [103]. Most figures and major parts of the text have been taken verbatim from that work, occasionally with minor modifications and supplemental analyses for a better embedding in the context of this thesis. The discussion of experimental realizations in Rydberg quantum simulators is part of ongoing work currently in preparation for publication [104]. See List of Publications for a statement of contributions.

Dynamical correlations involving observables at unequal times are ubiquitous across a multitude of disciplines in physics. They encode fundamental properties of quantum many-body systems, ranging from optical coherence [105, 106] and transport properties [82, 91], over far-from-equilibrium universality [53–55, 107, 108], dynamical topological transitions [109], as well as glassy dynamics and aging [110–112], up to thermalization, integrability, and quantum chaos [26–31, 113, 114]. In Section 1.3, we have already encountered specific types of temporal correlations in the context of linear response theory. On the one hand, according to Kubo's formula for the response function (1.57), the two-time commutator of two observables determines how a system reacts to external perturbations. On the other hand, the two-time anti-commutator encodes the intrinsic fluctuations of the corresponding observables. In thermal equilibrium, these quantities are deeply connected via the fluctuation–dissipation relation (FDR). Since the FDR (1.83) holds for any observables and across the entire frequency spectrum, given only the temperature as a single global parameter, it represents an excellent probe of thermalization in closed quantum systems [24, 115–118]. Certifying that a given quantum state is thermal can also be valuable in novel quantum technologies, e.g., for applying dynamical protocols to detect entanglement [119–121] — a key resource for quantum-enhanced metrology [122, 123].

However, despite its key role in statistical mechanics, the FDR has so far only been tested experimentally in classical systems [124–127]. Such a test requires an independent measurement of both sides of the relation, but for quantum systems, only the dissipation side, i.e., the unequal-time commutator, is easily accessible by probing the linear response to an external perturbation (see Section 1.3). What hinders a straightforward measurement of dynamical correlations in quantum systems is the inevitable measurement back action: a projective von Neumann measurement collapses the quantum state [89, 90],

such that a subsequent measurement at a later time probes a perturbed state, which typically causes a sizable bias in the temporal correlation. Various pioneering proposals for measuring unequal-time correlations on various platforms exist [24, 128–136], but attempts to overcome the inherent difficulties of such a measurement are often specific to certain setups or apply only to a limited set of observables. As of today, an experimental observation of the unequal-time anti-commutator in a quantum many-body system remains elusive.

Here, we approach this problem from the perspective of non-Hermitian linear response [22, 23]. In recent years, a tremendous interest in non-Hermitian physics has emerged [137, 138], stimulated by the rapid progress in the experimental generation and control of non-Hermitian systems [139–144]. Indeed, non-Hermiticity gives rise to a wealth of new physics with novel (topological) phases and unconventional critical behavior [145–151], bearing a vast potential for applications, e.g., in strongly enhanced quantum sensing [152, 153] or adiabatic quantum optimization [154, 155]. Leveraging on this development, we exploit the linear response to a non-Hermitian perturbation [22, 23] in order to design protocols that permit a direct experimental observation of the unequal-time anti-commutator. This promotes linear response theory to a unifying framework for measuring both sides of the FDR independently: in the same way as the two-time commutator can be extracted from how the system responds to a Hermitian perturbation, the response to a non-Hermitian perturbation gives access to the two-time anti-commutator.

The plan for this chapter is as follows. To start with, we derive the relevant formulas that characterize the linear response to a non-Hermitian perturbation and connect the results to the desired unequal-time correlation functions. With this general, model-independent, and platform-agnostic formulation of non-Hermitian linear response at hand, we then develop concrete schemes that realize this scenario, focusing on cold atoms in optical lattices. These protocols are most conveniently phrased as an application of the quantum Zeno effect [156, 157], combining outcoupling to an ancillary system with a projection on the Zeno subspace that contains no particles in the ancilla. We illustrate several variants of the scheme, including possible realizations harnessing engineered dissipation [16, 158], by means of numerical simulations at an example motivated by a ground-breaking cold-atom experiment [25] — a Bose–Hubbard system that is quenched from a Mott-insulating initial state to the superfluid phase (see Fig. 2.1), where monitoring the FDR allows one to track the system's evolution towards thermal equilibrium. Moreover, we put the non-Hermitian linear response approach in perspective with other methods for measuring the unequal-time anti-commutator, e.g., projective protocols [24, 129, 131–133]. We also examine formal relations to open quantum systems [97, 159], where non-Hermitian dynamics can be generated by post-selecting individual quantum trajectories on the absence of quantum jumps [143, 151, 160–162], and establish general cross-connections between (non-)Hermitian linear response and ancilla-based weak measurements of dynamical correlations [131, 132]. Finally, we discuss experimental error sources and assess ways to overcome potential challenges for experimental implementations of the non-Hermitian linear response scheme at the example of Rydberg quantum simulators.

2.1. Non-Hermitian Linear Response Theory

In this section, we develop the general non-Hermitian linear response formalism in analogy to the discussion of standard linear response in Section 1.3. After deriving a counterpart of Kubo's linear response formula (1.57) for anti-Hermitian perturbations [22, 23], we show how this result gives access to the correlation spectrum on the left-hand side of the FDR (1.83).

Kubo Formula for Anti-Hermitian Perturbations

In contrast to standard linear response theory (see Section 1.3), we assume that the system is effectively described by a non-Hermitian Hamiltonian $H(t) = H_0 + H_1(t)$, where H_0 is the unperturbed Hermitian Hamiltonian and $H_1(t) = -if(t)A$ is an anti-Hermitian perturbation with a positive semi-definite operator A and a non-negative time-dependent function $f(t)$. For example, such a scenario arises in the quantum trajectories approach to open quantum systems [160–162] if the evolution is conditioned on the absence of quantum jumps [141, 143, 151] [see also paragraph below Eq. (2.45)]. In Section 2.3, we show how to engineer effective non-Hermitian Hamiltonians based on the quantum Zeno effect, allowing one to probe the response to such perturbations, even frequency-resolved, for a wide range of observables. Furthermore, we show in Section 2.4.1 that existing ancilla-based weak measurement protocols for the unequal-time anti-commutator [131, 132] can also be rephrased in the framework of non-Hermitian linear response.

A quantum state described by the density operator $\rho(t)$ evolves in time under the non-Hermitian Hamiltonian $H(t)$ according to the von Neumann equation

$$i\hbar \frac{\mathrm{d}}{\mathrm{d}t}\rho = H(t)\rho - \rho H^\dagger(t) = [H_0, \rho] + \{H_1(t), \rho\} \tag{2.1}$$

with initial condition $\rho(0) = \rho_0$.

In analogy to Section 1.3.1, we first transform to the interaction picture with respect to the unperturbed (Hermitian) Hamiltonian H_0. The von Neumann equation (2.1) then reads

$$\frac{\mathrm{d}}{\mathrm{d}t}\tilde{\rho} = -\frac{i}{\hbar}\big\{\tilde{H}_1(t), \tilde{\rho}\big\}\,, \tag{2.2}$$

where $\tilde{\rho}(t) = \mathrm{e}^{iH_0 t/\hbar}\rho(t)\mathrm{e}^{-iH_0 t/\hbar}$ is the density operator and $\tilde{H}_1(t) = -if(t)\tilde{A}(t)$ with $\tilde{A}(t) = \mathrm{e}^{iH_0 t/\hbar}A\mathrm{e}^{-iH_0 t/\hbar}$ is the anti-Hermitian perturbation in the interaction picture. This equation can equivalently be expressed in integral form as

$$\tilde{\rho}(t) = \tilde{\rho}(0) - \frac{i}{\hbar}\int_0^t \mathrm{d}t' \,\big\{\tilde{H}_1(t'), \tilde{\rho}(t')\big\} \tag{2.3}$$

with $\tilde{\rho}(0) = \rho_0$. To linear order in the perturbation, we can replace $\tilde{\rho}(t')$ in the integrand by ρ_0, yielding

$$\tilde{\rho}(t) = \rho_0 - \frac{1}{\hbar}\int_0^t \mathrm{d}t' \,\big\{\tilde{A}_1(t'), \rho_0\big\} f(t')\,. \tag{2.4}$$

The expectation value of a (Hermitian) observable B can be computed in the interaction picture as $\mathrm{Tr}[B\rho(t)] = \mathrm{Tr}[\tilde{B}(t)\tilde{\rho}(t)]$, where $\tilde{B}(t) = \mathrm{e}^{iH_0 t/\hbar} B \mathrm{e}^{-iH_0 t/\hbar}$, which leads to

$$\mathrm{Tr}[B\rho(t)] = \langle B(t)\rangle_0 - \frac{1}{\hbar}\int_0^t \mathrm{d}t' \, \langle\{B(t), A(t')\}\rangle_0 \,. \tag{2.5}$$

As in Section 1.3, the subscript in the expectation value $\langle\cdots\rangle_0$ signifies that the Heisenberg operators evolve under the unperturbed Hamiltonian H_0. The non-Hermiticity of the perturbed Hamiltonian has the important consequence that the state $\rho(t)$ is no longer normalized: as can be seen by inserting the identity operator for B in Eq. (2.5), its norm decreases with time, to linear order, as

$$\mathrm{Tr}[\rho(t)] = 1 - \frac{2}{\hbar}\int_0^t \mathrm{d}t' \, \langle A(t')\rangle_0 \, f(t') \,. \tag{2.6}$$

Physically, this decrease can be interpreted as the leakage of the wave function into a complementary state space (see also Section 2.3). To account for this loss of probability, we consider the normalized expectation value $\langle B(t)\rangle = \mathrm{Tr}[B\rho(t)]/\,\mathrm{Tr}[\rho(t)]$, describing a post-selected measurement [163]. Combining Eqs. (2.5) and (2.6), the disconnected correlations drop out to linear order, and we can write the response as

$$\langle B(t)\rangle = \langle B(t)\rangle_0 + \int_0^t \mathrm{d}t' \, \phi_{BA}^{(\mathrm{NH})}(t,t') f(t') \tag{2.7}$$

with the "non-Hermitian" response function

$$\phi_{BA}^{(\mathrm{NH})}(t,t') = -\frac{1}{\hbar}\theta(t-t')\big[\langle\{B(t), A(t')\}\rangle_0 - 2\langle B(t)\rangle_0\langle A(t')\rangle_0\big] \,. \tag{2.8}$$

Here, we have inserted the Heaviside step function θ to ensure causality of the response. The non-Hermitian response function (2.8) is the analog of Kubo's response function (1.57) for anti-Hermitian perturbations. This result has first been reported in Ref. [22] and has been generalized in Ref. [23] to situations where both the unperturbed system and the perturbation may be non-Hermitian. Remarkably, $\phi_{BA}^{(\mathrm{NH})}$ is the desired measurable quantity that gives direct access to the unequal-time anti-commutator (1.74) by virtue of the relation $\phi_{BA}^{(\mathrm{NH})}(t,t') = -2\theta(t-t')S_{BA}(t,t')/\hbar$.

Non-Hermitian Linear Response and the Fluctuation–Dissipation Relation

Our goal is to establish a link between the response function (2.8) and the correlation spectrum appearing on the left-hand side of the FDR (1.83). To this end, similarly to Eq. (1.60), we define the "non-Hermitian" dynamical susceptibility for a stationary system, where the response function depends only on the relative time $\Delta t = t - t'$, as the Fourier transform

$$\chi_{BA}^{(\mathrm{NH})}(\omega) = \lim_{\epsilon\to 0^+}\int_{-\infty}^{\infty} \mathrm{d}\Delta t \, \phi_{BA}^{(\mathrm{NH})}(\Delta t)\mathrm{e}^{i\omega\Delta t}\mathrm{e}^{-\epsilon\Delta t} \,. \tag{2.9}$$

We can split this quantity as $\chi^{(\mathrm{NH})}_{BA} = \chi'^{(\mathrm{NH})}_{BA} + i\chi''^{(\mathrm{NH})}_{BA}$ into the components

$$\chi'^{(\mathrm{NH})}_{BA}(\omega) = \frac{1}{2}\left[\chi^{(\mathrm{NH})}_{BA}(\omega) + \chi^{(\mathrm{NH})}_{AB}(-\omega)\right], \tag{2.10a}$$

$$\chi''^{(\mathrm{NH})}_{BA}(\omega) = \frac{1}{2i}\left[\chi^{(\mathrm{NH})}_{BA}(\omega) - \chi^{(\mathrm{NH})}_{AB}(-\omega)\right], \tag{2.10b}$$

which we refer to, in analogy to their Hermitian counterparts in Eq. (1.63), as the reactive and dissipative parts of the non-Hermitian susceptibility, respectively. Importantly, the reactive component (2.10a) gives access to the correlation spectrum $S_{BA}(\omega)$. To see this, we note that for a stationary system, the symmetry relation in Eq. (1.76a) becomes $S_{BA}(\Delta t) = S_{AB}(-\Delta t)$. Thus, similarly to Eq. (1.77), we find

$$\begin{aligned} S_{BA}(\omega) &= \lim_{\epsilon\to 0^+}\int_{-\infty}^{\infty} \mathrm{d}\Delta t\, S_{BA}(\Delta t)\mathrm{e}^{i\omega\Delta t}\mathrm{e}^{-\epsilon|\Delta t|} \\ &= \lim_{\epsilon\to 0^+}\left[\int_0^{\infty} \mathrm{d}\Delta t\, S_{BA}(\Delta t)\mathrm{e}^{i\omega\Delta t}\mathrm{e}^{-\epsilon\Delta t} + \int_0^{\infty} \mathrm{d}\Delta t\, S_{AB}(\Delta t)\mathrm{e}^{-i\omega\Delta t}\mathrm{e}^{-\epsilon\Delta t}\right] \\ &= \lim_{\epsilon\to 0^+}\frac{(-\hbar)}{2}\left[\int_{-\infty}^{\infty} \mathrm{d}\Delta t\, \phi^{(\mathrm{NH})}_{BA}(\Delta t)\mathrm{e}^{i\omega\Delta t}\mathrm{e}^{-\epsilon\Delta t} + \int_{-\infty}^{\infty} \mathrm{d}\Delta t\, \phi^{(\mathrm{NH})}_{AB}(\Delta t)\mathrm{e}^{-i\omega\Delta t}\mathrm{e}^{-\epsilon\Delta t}\right] \\ &= -\hbar\chi'^{(\mathrm{NH})}_{BA}(\omega)\,. \end{aligned} \tag{2.11}$$

This result allows us to rewrite the FDR (1.83) in thermal equilibrium as

$$\chi'^{(\mathrm{NH})}_{BA}(\omega) = -\coth\left(\frac{\hbar\omega}{2k_{\mathrm{B}}T}\right)\chi''_{BA}(\omega)\,, \tag{2.12}$$

which is expressed entirely in terms of the susceptibilities $\chi'^{(\mathrm{NH})}_{BA}$ and χ''_{BA}, accessible using non-Hermitian and standard (Hermitian) linear response, respectively. As such, linear response theory provides an elegant and general framework for independently probing both sides of the FDR (2.12), which works for arbitrary observables in any quantum many-body system.

It is worthwhile emphasizing that the outlined derivation of the response to a non-Hermitian perturbation is by no means restricted to the linear regime only, but, as well-known in standard response theory [84], can be extended to non-linear responses. In fact, by calculating the expansions in Eqs. (2.5) and (2.6) to the desired non-linear order, one can in principle access an infinite hierarchy of nested unequal-time anti-commutators, order by order. By perturbing the system at multiple sites simultaneously, non-linear responses could therefore also enable access to (global) many-body operators which are expected not to thermalize (see Section 2.2.1) and consequently violate the FDR.

Approaching the problem of measuring dynamical correlations from the (non-)Hermitian linear response perspective turns out to be fruitful for a number of reasons. For one, non-Hermitian linear response is completely agnostic to the way the non-Hermitian perturbation is implemented and therefore directly benefits from any advancements in

the field of non-Hermitian physics regarding the generation and control of non-Hermitian Hamiltonians. Furthermore, it provides an ancilla-free interpretation of common ancilla-based weak measurement schemes for the unequal-time anti-commutator [131, 132]. So far, it has not been clear whether ancilla-free formulations of such protocols lend for a meaningful physical interpretation [132], but, as we show in Section 2.4.1, this is indeed possible in the light of non-Hermitian linear response. Conversely, any non-Hermitian perturbation can in principle be realized with the help of an ancilla using only unitary evolution and standard projective measurements, although the required couplings may not always be straightforward to implement. In Section 2.3, we consider specific ancilla-based schemes with experimentally feasible system–ancilla couplings, providing access to dynamical correlations for a wide range of observables. Finally, from a linear response point of view, it is natural to study responses to periodic perturbations that directly give access to frequency-resolved susceptibilities. As we will see in Sections 2.3.2 and 2.3.3, this becomes practical within the present framework also for non-Hermitian perturbations by exploiting the quantum Zeno effect.

2.2. Application: Tracking Quantum Thermalization After a Quench

In this section, we demonstrate how (non-)Hermitian linear response allows one to access both sides of the FDR (2.12) independently. Such measurements can be used to either probe thermalization or the absence thereof [24].

2.2.1. Thermalization in Isolated Quantum Systems

If a system of interest is coupled to a large thermal bath, it will sooner or later always approach thermal equilibrium with the bath temperature [159], and the FDR will eventually hold. In contrast, the question whether and how a *closed* quantum system thermalizes once it is brought out of equilibrium is much more subtle [26–31].

On the one hand, thermal equilibrium is characterized by only a few macroscopic parameters, e.g., the global temperature T in a canonical ensemble. Thus, starting from a non-equilibrium initial state, the approach to thermal equilibrium is accompanied by an effective loss of memory on the microscopic details of the initial condition. On the other hand, an isolated quantum system undergoes unitary time evolution, which is completely reversible and thus retains all information on the initial state. In what follows, we outline how this apparent paradox can be resolved.

Consider a system in a pure[1] initial state $|\psi_0\rangle$ evolving under a Hamiltonian H. The expectation value of an observable O can be written as

$$\langle O(t)\rangle = \sum_k |c_k|^2 O_{kk} + \sum_{k\neq m} c_k^* c_m O_{km} \mathrm{e}^{i(E_k-E_m)t/\hbar}\,, \tag{2.13}$$

[1] A generalization to mixed states is straightforward.

where $\{E_k\}$ are the eigenenergies of H with corresponding eigenstates $\{|k\rangle\}$, $c_k = \langle k|\psi_0\rangle$ is the overlap of the initial state with the k-th eigenstate, and $O_{km} = \langle k|O|m\rangle$ are the matrix elements of O with respect to the energy eigenbasis. Assuming that the spectrum of H is non-degenerate, the long-time average of the oscillating off-diagonal part of Eq. (2.13) vanishes, such that the time average is given only by the diagonal part [28],

$$\overline{\langle O(t)\rangle} = \lim_{t\to\infty} \frac{1}{t} \int_0^t \mathrm{d}t' \, \langle O(t')\rangle = \sum_k |c_k|^2 O_{kk} \,. \tag{2.14}$$

This result can be thought of as the prediction of the expectation value of O in the so-called diagonal ensemble [28],

$$\langle O\rangle_{\mathrm{diag}} = \mathrm{Tr}\big[O\rho_{\mathrm{diag}}\big] \,, \quad \rho_{\mathrm{diag}} = \sum_k |c_k|^2 \, |k\rangle\langle k| \,. \tag{2.15}$$

Obviously, it explicitly depends on the initial state $|\psi_0\rangle$ via the coefficients $|c_k|^2$, which are constant in time.

In a thermalizing system, we expect the predictions of statistical mechanics to hold. In a microcanonical ensemble at energy E, the average of an observable reads

$$\langle O\rangle_{\mathrm{mc}} = \mathrm{Tr}[O\rho_{\mathrm{mc}}(E)] \,, \quad \rho_{\mathrm{mc}}(E) = \frac{1}{\mathcal{N}} \sum_{|E_k - E| < \delta E} |k\rangle\langle k| \,, \tag{2.16}$$

where δE is the width of the microcanonical shell (which is small compared to the spectral width, but sufficiently large to encompass many states) and the normalization factor $\mathcal{N}$ corresponds to the number of terms in the sum. Thermalization in a weak sense can be defined as the requirement that the long-time average of observables should coincide with the statistical average in the microcanonical ensemble at the energy set by the initial state, $E = \langle\psi_0|H|\psi_0\rangle$ [28]. For our purposes, we will adopt a definition of thermalization in the strong sense: instead of referring to the time average, we require the instantaneous values of observables to approach the microcanonical prediction and remain close to it most of the time [28]. By virtue of ensemble equivalence [79], we could as well consider a different thermal ensemble, e.g., the canonical ensemble, described by the density matrix (1.68). In this case, the temperature of the canonical ensemble should be such that the thermal expectation value of the energy matches the energy of the initial state, $\mathrm{Tr}[H\rho(T)] = \langle\psi_0|H|\psi_0\rangle$.

The precise conditions under which thermalization occurs remain yet to be understood and are subject of extensive research [26–31]. Generally, local observables in generic interacting quantum many-body systems are expected to thermalize. This means that unless very special conditions are met, e.g., integrability, localization, or scar states (see discussion below), all local (or few-body) observables, which only involve the degrees of freedom of a sufficiently small subsystem, should exhibit thermal behavior. By contrast, global observables often fail to thermalize, which is the case, e.g., for projectors on individual energy eigenstates.

The requirement that any local observable thermalizes (in the strong sense) can be rephrased as the condition that in the limit of long times and large systems, the reduced density matrix of any sufficiently small subsystem $\mathcal{A}$ approaches that of a thermal state [26, 164],

$$\rho_{\mathcal{A}}(t) = \mathrm{Tr}_{\bar{\mathcal{A}}}\{|\psi(t)\rangle\langle\psi(t)|\} \xrightarrow{t\to\infty} \rho_{\mathcal{A}}(T) = \mathrm{Tr}_{\bar{\mathcal{A}}}[\rho(T)]\,. \tag{2.17}$$

Here $\mathrm{Tr}_{\bar{\mathcal{A}}}$ denotes the partial trace over the complement of subsystem $\mathcal{A}$ (i.e., the remaining part of the system), $|\psi(t)\rangle = \mathrm{e}^{-iHt/\hbar}|\psi_0\rangle$ is the time-evolved state under the Hamiltonian H, and the temperature of the canonical density matrix $\rho(T)$ is fixed by the initial state via $\mathrm{Tr}[H\rho(T)] = \langle\psi_0|H|\psi_0\rangle$. Equation (2.17) suggests that the system, in some sense, acts as its own bath: unitary dynamics entangles the subsystem with the rest of the system, thereby spreading the information on the initial condition across the entire system such that it becomes inaccessible through local measurements alone. The entanglement entropy built up in this process can be thought of as playing the role of the thermodynamic entropy [26]. The subsystem thus thermalizes with respect to the "bath" provided by the remaining (and typically much larger) part of the system. This picture is consistent with groundbreaking experiments on ultra-cold bosons in optical lattices, where expectation values of local observables after a quench have been shown to reach stationary values in agreement with thermal equilibrium, while retaining the purity of the global quantum state [25]. Thus, the observation that a closed quantum system can locally appear thermal is in no contradiction with the fact that globally the system undergoes unitary time evolution and retains all information about the initial state.

Eigenstate Thermalization Hypothesis

One way to ensure that the long-time average in Eq. (2.14) agrees with the prediction of the microcanonical ensemble in Eq. (2.16) for generic initial states is to assume that the matrix elements O_{kk} with respect to the energy eigenbasis match the microcanonical prediction individually. This key idea leads to the famous eigenstate thermalization hypothesis (ETH) [28, 29, 113, 114], according to which thermalization occurs on the level of individual eigenstates. It is generally believed that ETH holds for local observables and eigenstates in the bulk of the spectrum of generic interacting many-body Hamiltonians (see exceptions discussed below) [28]. A remarkable consequence of ETH is that thermal properties of local subsystems can be deduced from just a *single* eigenstate at the relevant energy scale [164].

Formally, the ETH can be phrased as an ansatz for the matrix elements of local observables in the energy eigenbasis [165],

$$O_{km} = O(E_{km})\delta_{km} + \mathrm{e}^{-S(E_{km})/2} f_O(E_{km}, \omega_{km}) R_{km}. \tag{2.18}$$

Here, $E_{km} = (E_k + E_m)/2$ and $\omega_{km} = E_m - E_k$ are the mean energy and the energy difference of the involved eigenstates, respectively, $S(E)$ is the thermodynamic entropy, and R_{km} are Gaussian random variables with zero mean and unit variance, which are

real (complex) in presence (absence) of time reversal symmetry [28]. The diagonal part is characterized by the smooth function $O(E)$, which coincides with the expectation value of the observable O in the microcanonical ensemble at energy E. Inserting the ETH ansatz (2.18) into Eq. (2.14), and expanding $O(E_{kk})$ around the mean energy $E = \langle\psi_0|H|\psi_0\rangle$, one easily finds that the long-time average agrees with the microcanonical prediction (2.16), provided that energy fluctuations are not too large [28]. The second term in Eq. (2.18), the off-diagonal part of the ETH, describes fluctuations around equilibrium, which decrease exponentially as the system size and thus the entropy grows. The smooth function $f(E, \omega)$ is closely connected to unequal-time correlations of the observable O. In fact, the ETH implies the validity of the FDR (1.83) for $B = A = O$ [28]. Thus, independent measurements of both sides of the FDR can be used to probe the off-diagonal part of the ETH, as has been proposed in Ref. [24].

Failure of Thermalization

There are a number of notable scenarios where thermalization (and ETH in particular) fails. For instance, integrable models feature an extensive number of conserved quantities, which constrain the dynamics and prevent the system from thermalizing [28, 117]. Instead, these systems relax to so-called generalized Gibbs ensembles [28]. In addition, disordered systems can escape thermalization due to many-body localization [26, 30]. Besides these paradigmatic examples of deviations from thermal behavior, systems can also exhibit disorder-free localization due to Hilbert space fragmentation (or Hilbert space shattering), where dynamical constraints restrict the evolution to a finite number of disconnected subspaces and thus hinder the approach to equilibrium [166, 167]. This is also related to the existence of particular (typically highly excited) eigenstates of the Hamiltonian which violate ETH, so-called quantum many-body scars [31, 168].

Thermalization and Fluctuation–Dissipation Relations

The most straightforward way to probe thermalization is to test whether local observables reach stationary values that agree with the prediction from thermal equilibrium ensembles, e.g., the microcanonical prediction in Eq. (2.16). Such a behavior has been demonstrated in seminal cold-atom experiments on Bose–Hubbard systems consisting of only six lattice sites [25]. Intriguingly, a large bath (i.e., a large system) is not necessary in order to observe thermal behavior in isolated quantum systems.

In Section 1.3.3, we have seen that a system in thermal equilibrium must satisfy the FDR (1.83) for any two observables A and B across the entire frequency spectrum. The FDR follows from a special symmetry in imaginary time, the KMS boundary condition (1.79), which is characteristic to thermal states. For this reason, the testing the validity of the FDR represents a powerful way to study when and how isolated quantum many-body systems approach thermal equilibrium [24, 115–118]. As the FDR involves two-time correlations, demonstrating its fulfillment is a much finer probe of thermalization compared to matching equal-time expectation values with thermal predictions. On top of that, the FDR yields the effective temperature at which the system thermal-

izes [24, 115–118]. This can be thought of as an independent way of defining temperature in the first place, which remarkably does not require any a priori assumptions other than the FDR itself. In a thermalizing system, the effective temperature obtained from the FDR should agree with the temperature of a thermal state whose mean energy matches that of the initial state.

It is important to stress that independent measurements of both sides of the FDR can be used to reveal both thermalization or the absence thereof [24]. In particular, the FDR is expected to be violated in the above-mentioned scenarios where thermalization fails, e.g., due to integrability, localization, or scar states. Moreover, broken FDRs are characteristic signatures of far-from-equilibrium systems near a non-thermal fixed point [107, 118]. All of these settings represent promising targets for schemes based on (non-)Hermitian linear response to reveal either the validity or the breakdown of the FDR. For illustrative purposes, we focus in what follows on the generic case where the system does thermalize and the FDR is expected to hold. In the next section, we illustrate how (non-)Hermitian linear response could enable experiments like those in Ref. [25] to go one step further and certify thermalization by demonstrating the validity of the FDR.

Non-Equilibrium Generalizations of the Dynamical Susceptibility. Before turning to our application of probing FDRs in Bose–Hubbard systems, we need to generalize the definitions of the dynamical susceptibilities in Eqs. (1.60) and (2.9), characterizing the frequency-dependent linear response to Hermitian and anti-Hermitian perturbations, respectively, to non-equilibrium scenarios. Out of equilibrium, the response functions in Eqs. (1.57) and (2.8) generally depend on the two times t and t' separately. In this situation, it is common to introduce Wigner coordinates [169],

$$\tau = \frac{t+t'}{2}, \quad \Delta t = t - t' \,, \tag{2.19}$$

where τ and Δt are referred to as central and relative time, respectively. The inverse transformations are given by $t = \tau + \Delta t/2$ and $t' = \tau - \Delta t/2$. The dynamical susceptibility can then be defined out of equilibrium as the Fourier transform of the response function with respect to the relative time at a fixed central time,

$$\chi_{BA}(\tau,\omega) = \int_{-2\tau}^{2\tau} \mathrm{d}\Delta t \, \phi_{BA}\Big(\tau + \frac{\Delta t}{2}, \tau - \frac{\Delta t}{2}\Big) \mathrm{e}^{i\omega\Delta t} \,. \tag{2.20}$$

In an analogous way, one can define non-equilibrium generalizations of the non-Hermitian dynamic susceptibility (2.9) as well as of the Fourier transforms of the symmetric unequal-time correlations in Eq. (1.73). One advantage of using Wigner coordinates is that the symmetrized correlations functions in Eqs. (1.74) and (1.75), i.e., the two-time anti-commutator and commutator, obey useful symmetry relations with respect to relative time Δt,

$$S_{BA}(\tau,\Delta t) = S_{AB}(\tau,-\Delta t) \,, \tag{2.21a}$$

$$K_{BA}(\tau,\Delta t) = -K_{AB}(\tau,-\Delta t) \,, \tag{2.21b}$$

which follow directly from Eq. (1.76). Here, we have used the shorthand notation $S_{BA}(\tau, \Delta t) = S_{BA}(t = \tau + \Delta t/2, t' = \tau - \Delta t/2)$ and similarly for $K_{BA}(\tau, \Delta t)$. Consequently, if we define the Fourier transforms these quantities analogously to Eq. (2.19), generalizations of the relations in Eqs. (1.77) and (2.11) hold also out of equilibrium,

$$S_{BA}(\tau, \omega) = -\hbar \chi'^{(\mathrm{NH})}_{BA}(\tau, \omega)\,, \tag{2.22a}$$

$$K_{BA}(\tau, \omega) = 2i\hbar \chi''_{BA}(\tau, \omega)\,. \tag{2.22b}$$

Nonetheless, using Wigner coordinates is not the only way to define the dynamical susceptibility in a non-equilibrium scenario. For later purposes, we introduce two alternative conventions for the Fourier transform of the response function out of equilibrium, which are directly related to certain linear response protocols. After a quench, it is common to probe the response to an external perturbation applied in form of a delta-like pulse, $f(t) \propto \delta(t - t_\mathrm{w})$, after a certain waiting time t_w [118]. According to Eq. (1.56), the time trace of the linear response then gives access to the response function $\phi_{BA}(t_\mathrm{w} + \Delta t, t_\mathrm{w})$ as a function of the relative time Δt. From such measurements, the Fourier transform in Eq. (2.19) at a fixed central time τ can be obtained by varying both the waiting time t_w and the observation time $t = t_\mathrm{w} + \Delta t$. It would be simpler to keep the waiting time fixed and vary only the relative time. This suggests defining the dynamical susceptibility as the Fourier transform with respect to Δt at a fixed waiting time t_w,

$$\chi_{BA}(t_\mathrm{w}, \omega) = \lim_{\epsilon \to 0^+} \int_{-\infty}^{\infty} \mathrm{d}\Delta t\, \phi_{BA}(t_\mathrm{w} + \Delta t, t_\mathrm{w}) \mathrm{e}^{i\omega \Delta t} \mathrm{e}^{-\epsilon |\Delta t|}\,. \tag{2.23}$$

As the response function must typically be sampled at a high resolution in Δt to compute the Fourier transform with respect to this variable, the susceptibility at a fixed waiting time can often be evaluated more efficiently than the one at a fixed central time, which is especially true in numerical simulations, where the integrand in Eq. (2.23) can be obtained from a single time evolution [170]. Furthermore, the definition of the Fourier integral in Eq. (2.23) is preferable to the one in Eq. (2.19) at early times, as in the former the integration domain is unbounded (note that negative Δt do not contribute due to causality), while in the latter the integration domain is limited to only a short range of Δt if the central time is close to the initial time.

As a second alternative, we introduce the dynamical susceptibility evaluated at a fixed final time t_f,

$$\chi_{BA}(t_\mathrm{f}, \omega) = \int_{-t_\mathrm{f}}^{t_\mathrm{f}} \mathrm{d}\Delta t\, \phi_{BA}(t_\mathrm{f}, t_\mathrm{f} - \Delta t) \mathrm{e}^{i\omega \Delta t}\,. \tag{2.24}$$

This variant turns out to be useful when considering periodic perturbations because it can directly be obtained from the linear response in this scenario.

It is worthwhile remarking that out of equilibrium, the susceptibilities defined in Eqs. (2.19), (2.23) and (2.24) generally disagree. In particular, the Fourier transforms of the symmetrized correlation functions (1.74) and (1.75) at fixed waiting time or fixed final time can in general not be related to the susceptibility components as in Eq. (2.22) due to a lack of similar symmetries with respect to the relative time as in Eq. (2.21).

However, these relations are restored once the system reaches a stationary state, where two-time correlators depend only on the relative time Δt and consequently the different conventions for the Fourier transform become equivalent, provided the integration domains are chosen appropriately.

2.2.2. Fluctuation–Dissipation Relations in Bose–Hubbard Systems

We now illustrate how to extract FDRs using (non-)Hermitian linear response. Motivated by the experiment in Ref. [25], we demonstrate this framework for a 1D Bose–Hubbard chain[2] [cf. Eq. (1.42)], described by the Hamiltonian

$$H_{\mathrm{BH}} = -\hbar J \sum_{\ell=1}^{L} (a_\ell^\dagger a_{\ell+1} + a_{\ell+1}^\dagger a_\ell) + \frac{\hbar U}{2} \sum_{\ell=1}^{L} n_\ell (n_\ell - 1)\,. \tag{2.25}$$

Here, the index $\ell = 1 \ldots L$ labels optical lattice sites with associated bosonic annihilation, creation, and number (density) operators a_ℓ, $a_\ell^\dagger$, and n_ℓ, respectively. J is the strength of the nearest-neighbor hopping, for which we assume periodic boundary conditions, and U is the on-site interaction rate. The numerical simulations presented in this chapter have been conducted using an adaptive Krylov subspace method to solve the full quantum dynamics without truncating the local Hilbert space dimension [80, 171–173]. While previous numerical studies of FDRs in Bose–Hubbard models have focused on density autocorrelations at large U/J and low fillings [24], here we consider quenches into the superfluid regime ($U/J \sim 1$) at unit filling and explore off-site correlations as a function of distance.

The linear response protocol is illustrated at the top of Fig. 2.1. We initialize the system of $N = L$ bosons in a Mott-insulating state at $U/J \to \infty$ and then quench it at time $t = 0$ into the superfluid phase at $U/J = 1.5625$, chosen consistent[3] with the experiment in Ref. [25]. This quench throws the system heavily out of equilibrium. After a variable waiting time t_{w}, we either apply a Hermitian or an anti-Hermitian perturbation in order access the desired response functions in Eq. (1.57) or Eq. (2.8), respectively. The perturbation is applied as a rectangular pulse of strength s and duration δt, $f(t) = \hbar s[\theta(t - t_{\mathrm{w}}) - \theta(t - t_{\mathrm{w}} - \delta t)]/\delta t$. The exact shape of the pulse is unimportant as long as the pulse duration is sufficiently short compared to the characteristic time scales of the system (see Section 2.3.1). In this case, the pulse can be approximated by a delta function as $f(t) \approx \hbar s \delta(t - t_{\mathrm{w}})$. Figure 2.1a shows the time trace of the response to a (non-)Hermitian perturbation giving access to density auto-correlations ($B = A = n$)[4], computed in a system of $L = 12$ sites for a perturbation of strength $s = 0.05$ and duration $J\delta t = 0.01$.

The thermalization dynamics of the corresponding dynamic susceptibilities $\chi'^{(\mathrm{NH})}$ and χ'' is depicted in Fig. 2.1b. For the purposes of this section, we have evaluated

[2] We emphasize that our approach does not depend on such a model choice and can be applied to general quantum systems.

[3] The results are insensitive to the precise choice of parameters.

[4] It does not matter at which site the perturbation is applied as the model is translationally invariant for periodic boundary conditions.

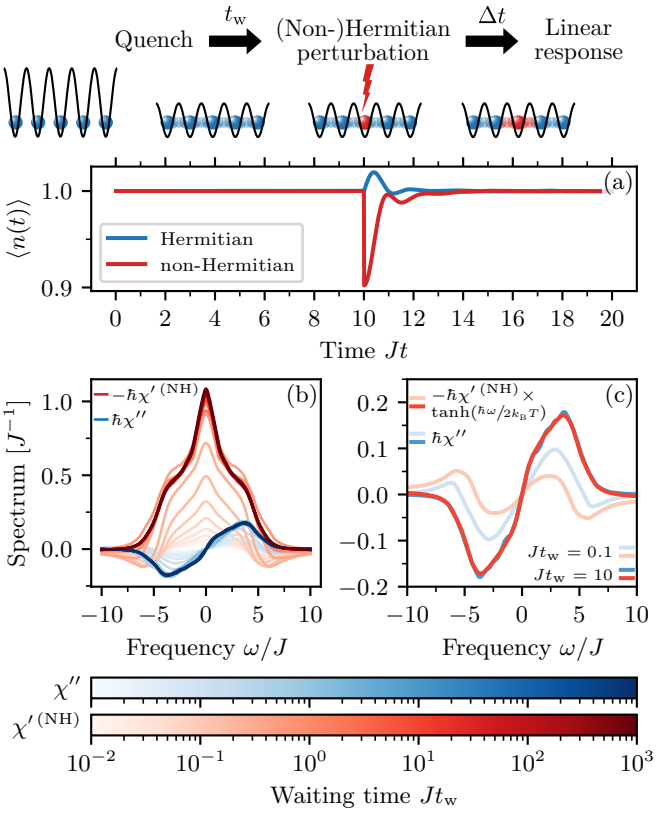

Figure 2.1.: (Non-)Hermitian linear response protocol for measuring fluctuation–dissipation relations (FDRs), exemplified for a Bose–Hubbard chain. (a) Schematic illustration of the protocol and response of the density $\langle n(t) \rangle$ to an (anti-)Hermitian perturbation $H_1(t) = -(i)\hbar s\delta(t - t_w)n$ of strength $s = 0.05$, applied at the waiting time $Jt_w = 10$. (b) Thermalization dynamics of the dissipative part of the "Hermitian" dynamic susceptibility $\chi''_{nn}(t_w, \omega)$ ("commutator") and the reactive part of the "non-Hermitian" dynamic susceptibility $\chi'^{(NH)}_{nn}(t_w, \omega)$ ("anti-commutator"). (c) Dynamic susceptibilities, rescaled according to the FDR (2.12) at early and late waiting times. The effective temperatures $k_BT/\hbar J = \{4.5, 4.2\}$ for $Jt_w = \{0.1, 10\}$, respectively, are determined by Eq. (2.26) using the least squares method. The FDR is clearly violated at early times, but it is restored at late times when the system has thermalized.

the susceptibilities at fixed waiting time t_w according to Eq. (2.23). To regulate the Fourier integrals, we have used an exponential filter of characteristic frequency $\gamma/J = 0.2$ [corresponding to a finite value of ϵ in Eq. (2.23)], which accounts for a finite spectral resolution in experiments. As discussed in Section 1.3.2, the susceptibility components for density correlations are real due to homogeneity and isotropy of the periodic 1D Bose–Hubbard chain. $\chi'^{(NH)}$ is symmetric in ω and grows as a broad central peak with small wings of opposite sign that gradually disappear as t_w increases, while χ'' is antisymmetric and develops characteristic peaks around non-zero frequencies. To assess whether the two functions satisfy the FDR, we use the least squares method to find the effective temperature T that best relates the susceptibilities via the FDR (2.12), i.e., for

a fixed waiting time t_w,

$$T = \arg\min_{\Theta} \int \mathrm{d}\omega \left[-\chi'^{(\mathrm{NH})} \tanh\left(\frac{\hbar\omega}{2k_\mathrm{B}\Theta} \right) - \chi'' \right]^2 . \tag{2.26}$$

In Fig. 2.1c, one can see that the FDR is clearly violated at early times, i.e., there exists no global value of T such that Eq. (2.12) holds, but at later times, the agreement is remarkable and supports the interpretation that the system undergoes thermalization.

Off-Site Density Correlations

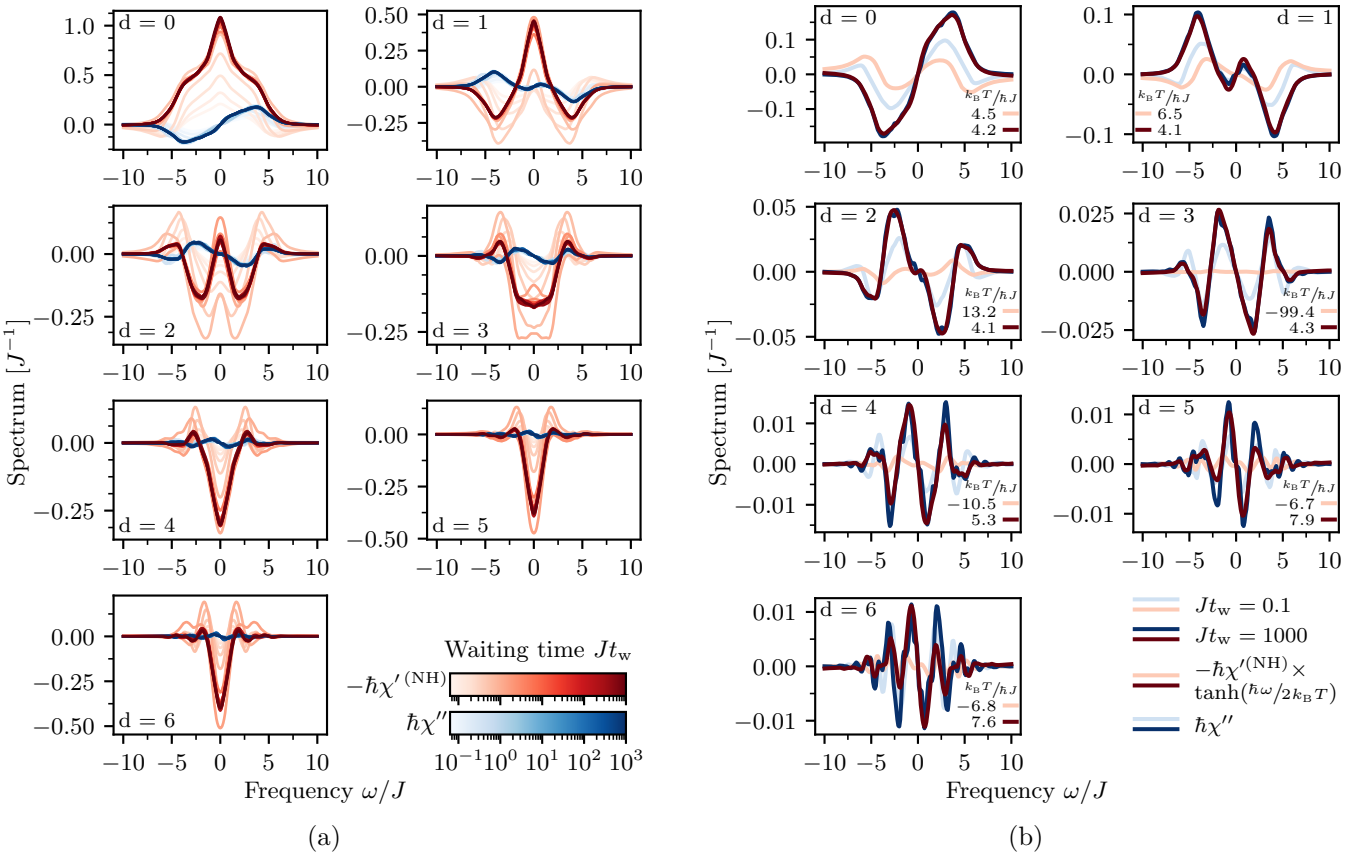

Figure 2.2.: Thermalization dynamics and FDRs for off-site density correlations in a 1D Bose–Hubbard chain. (a) Dynamical susceptibility $\chi'^{(\mathrm{NH})}$ (red) and χ'' (blue) for several waiting times t_w and distances d. (b) Comparison of FDRs at early and late waiting times. The quantity $\chi'^{(\mathrm{NH})}$ has been rescaled according to the FDR (2.12) using the least squares result for the effective temperature indicated in the plots. At small distances and late times, the curves overlap well, while at larger distances discrepancies persist even after long times.

A distinct feature of the FDR in equilibrium is that it holds across the entire frequency spectrum and for any pair of observables A and B. To confirm this prediction

for our model system, we investigate $\chi'^{(\mathrm{NH})}$ and χ'' for off-site density correlations corresponding to $A = n_\ell$ and $B = n_{\ell+d}$ as a function of the distance d. These quantities are shown in Fig. 2.2a at different waiting times for all distinct distances in the periodic chain. As in the case of density auto-correlations ($d = 0$) already discussed above, we observe the development of stationary spectra after times on the order of J^{-1}, where larger distances tend to reach their stationary distribution slightly delayed, in line with intuition. Interestingly, the slope of χ'' at $\omega = 0$ changes sign from positive at $d = 0$ to negative at $d \neq 0$. In fact, such a behavior is enforced by symmetry. As a consequence of particle number conservation, the symmetrized correlation functions (1.74) and (1.75) satisfy the sum rules

$$\sum_\ell S_{n_\ell n_{\ell'}}(t,t') = \frac{1}{2}\langle\{N, n_{\ell'}(t')\}\rangle - N\langle n_{\ell'}(t')\rangle = 0\,, \tag{2.27a}$$

$$\sum_\ell K_{n_\ell n_{\ell'}}(t,t') = \langle[N, n_{\ell'}(t')]\rangle \qquad\qquad = 0\,. \tag{2.27b}$$

In particular, their respective Fourier transforms must sum to zero for any frequency ω, as do the susceptibility components $\chi'^{(\mathrm{NH})}_{n_\ell n_{\ell'}}$ and $\chi''_{n_\ell n_{\ell'}}$. As a consequence, the shape of the density auto-correlation spectrum in Fig. 2.5a ($d = 0$) implies that at least for some distance $d \neq 0$ the slope must be reversed.

Figure 2.2b shows the extracted FDRs at early and late waiting times for the individual distances. The susceptibility $\chi'^{(\mathrm{NH})}$ has been rescaled according to the FDR (2.12) using the indicated effective temperature T obtained from the least squares fit in Eq. (2.26). At early waiting times, there is no global value of T to make $\chi'^{(\mathrm{NH})}$ and χ'' overlap, and the FDR is clearly violated (in some cases, an attempted fit can even yield unphysical negative temperatures). By contrast, at late waiting times, $\chi'^{(\mathrm{NH})}$ and χ'' fulfill the FDR, and at small distances, the extracted effective temperatures are consistent with the temperature $k_\mathrm{B}T/\hbar J = 4.27$ of a thermal state at the same energy density as the initial state (see discussion below). At larger distances, some peaks in Fig. 2.2b exhibit clear deviations which persist even after very long times.

To quantify deviations from the FDR (2.12), we introduce the absolute error

$$\epsilon_\mathrm{abs} = \left\| -\chi'^{(\mathrm{NH})} \tanh\left(\frac{\hbar\omega}{2k_\mathrm{B}T}\right) - \chi'' \right\|_2 , \tag{2.28}$$

where $\|\cdot\|_2$ denotes the L^2 norm, which we define by

$$\|f\|_2^2 = \frac{1}{|\Omega|}\int_\Omega \mathrm{d}\omega\, |f(\omega)|^2\,. \tag{2.29}$$

Unless stated otherwise, the errors have been computed on the fixed integration domain $\Omega = \{\omega \,|\, \omega/J \in [-10, 10]\}$. The relative error is obtained by normalizing the absolute error with respect to the sum of the individual norms,

$$\epsilon_\mathrm{rel} = \frac{\epsilon_\mathrm{abs}}{\|\chi'^{(\mathrm{NH})} \tanh(\hbar\omega/2k_\mathrm{B}T)\|_2 + \|\chi''\|_2}\,. \tag{2.30}$$

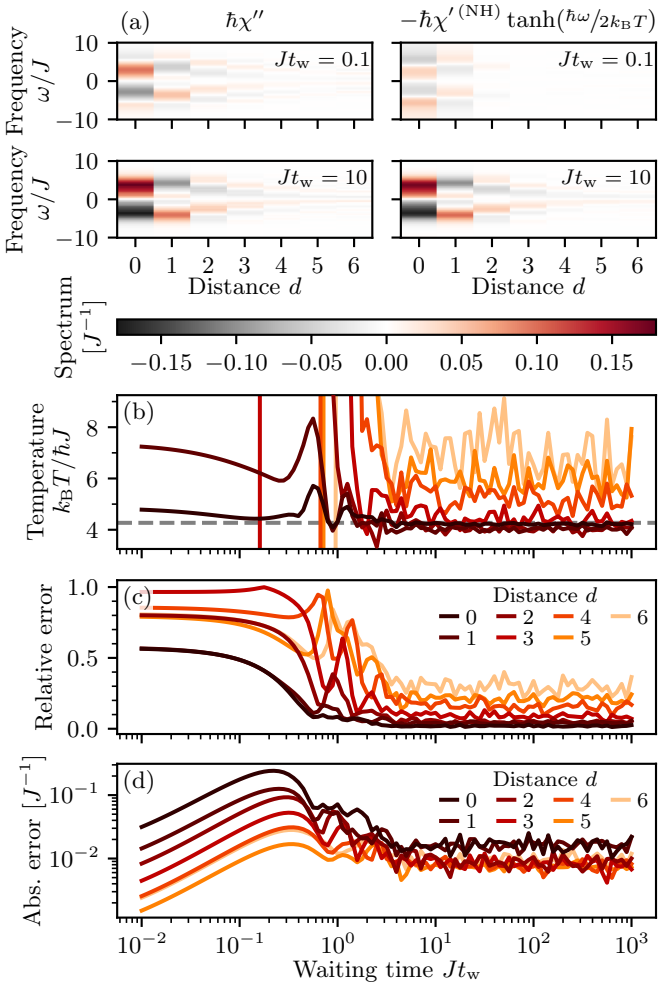

Figure 2.3.: Analysis of deviations from the FDR for density correlations in a 1D Bose–Hubbard chain. (a) Comparison of the dynamic susceptibilities $\chi''_{n_\ell n_{\ell+d}}$ and $\chi'^{(\mathrm{NH})}_{n_\ell n_{\ell+d}}$, rescaled according to the FDR (2.12), for different waiting times t_w as a function of the spatial distance d. At early times, clear deviations are visible, but for late times, the two quantities agree and the FDR (2.12) is fulfilled. (b) Least squares value of the effective temperature T, (c) relative error, and (d) absolute error of the FDR as a function of the waiting time t_w for several distances d. At small distances, after times on the order of J^{-1}, the effective temperature approaches a constant value consistent with the prediction $\langle H_\mathrm{BH}\rangle_T = E$ for a thermal state (grey dashed line), and the relative error becomes small. As the distance increases, the relative error grows, but the absolute deviation remains small.

The errors defined this way act as a figure of merit measuring how well the FDR (2.12) is fulfilled at a particular instance of time.

In Fig. 2.3, we analyze how well the FDR is fulfilled as a function of both the waiting time t_w and the distance d. Figure 2.3a summarizes the detailed data shown in Fig. 2.2b and illustrates the initial violation and eventual fulfillment of the FDR qualitatively.

Here, $\chi'^{(\mathrm{NH})}$ has been rescaled according to Eq. (2.12) with the best-fitting effective temperature T obtained from Eq. (2.26) for each configuration (t_w, d). In Figs. 2.3c and 2.3d, it can be seen that for small distances, the relative error becomes vanishingly small after waiting times on the order of J^{-1}, while for larger distances, the error tends to drop later and fluctuates around a non-zero offset. A similar behavior is exhibited by the effective temperature (see Fig. 2.3b): at small distances and late times, the temperatures are approximately constant and agree with each other, while this is no longer true for larger distances. Only in the former case, where the relative error is small, the effective temperature can be attributed the physical meaning of the temperature at which the subsystem degrees of freedom thermalize. This temperature is consistent with the one obtained for a thermal state at the equivalent energy density using the condition $\langle H_\mathrm{BH}\rangle_T = E$ (grey dashed line at $k_\mathrm{B}T/\hbar J = 4.27$ in Fig. 2.3b, calculated for $L = 8$ using exact diagonalization), where $\langle\cdots\rangle_T$ denotes the expectation value with respect to a canonical ensemble at temperature T, and E is the energy of the initial state after the quench (see Section 2.2.1).

While global many-body observables are expected to violate the FDR due to the purity of the global quantum state, one would expect two-site observables like the off-site density correlations shown in Fig. 2.3 to thermalize and thus satisfy the FDR for sufficiently large systems and late times, regardless of the distance between the two sites in real space. Although the absolute error gradually decreases with increasing distance due to the lower signal strength, relative discrepancies persist even after very long times. The observed deviations in Figs. 2.2 and 2.3 may therefore be an artifact of the finite system size, which we investigate in what follows.

Finite-Size Behavior

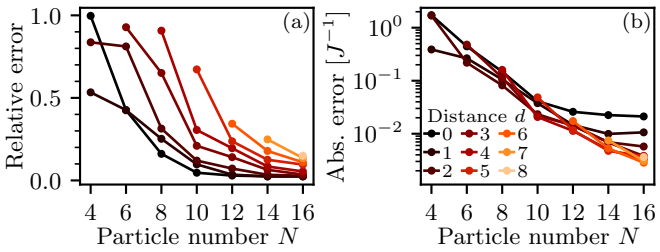

Figure 2.4.: Finite-size behavior of the deviations from the FDR in a 1D Bose–Hubbard chain. (a) Relative error and (b) absolute error as a function of the particle number N (= number of lattice sites L at unit filling) at waiting time $Jt_\mathrm{w} = 10$ for all possible distances in the periodic chain. Both errors clearly decrease with increasing system size.

To study the influence of finite-size effects, we consider the error as a function of the particle number N (corresponding to the number of lattice sites L at unit filling) up to $N = L = 16$. Figure 2.4 shows the relative and absolute errors at the moderate waiting time $Jt_\mathrm{w} = 10$ for all possible distances d in the respective systems. Note that for a periodic chain of length L, the maximum distance is $d = \lfloor L/2 \rfloor$. The Fourier

integrals have been truncated at $J\Delta t = 30$ using an exponential filter of characteristic frequency $\gamma/J = 0.1$. Both the relative and the absolute errors for all distances decrease as the system size increases until the relative error saturates at a value close to zero. Although the exponential growth of the Hilbert space dimension makes an exact numerical treatment of even larger systems inaccessible, the clear trend in Fig. 2.4 suggests that the deviations from the FDR in Figs. 2.2 and 2.3 at large distances for $L = 12$ are likely due to finite-size effects. Apart from finite-size errors, numerical errors induced in the course of the data analysis, e.g., integration and truncation errors in the evaluation of Fourier integrals or distortions caused by the frequency filter, may contribute to the deviation. However, it turns out that improving on these points does not alter the picture qualitatively. Our analysis thus confirms the expectation that the two-site subsystems relevant for off-site density correlations thermalize and thus fulfill the FDR, provided the system is not too small.

Two-Dimensional Bose–Hubbard System

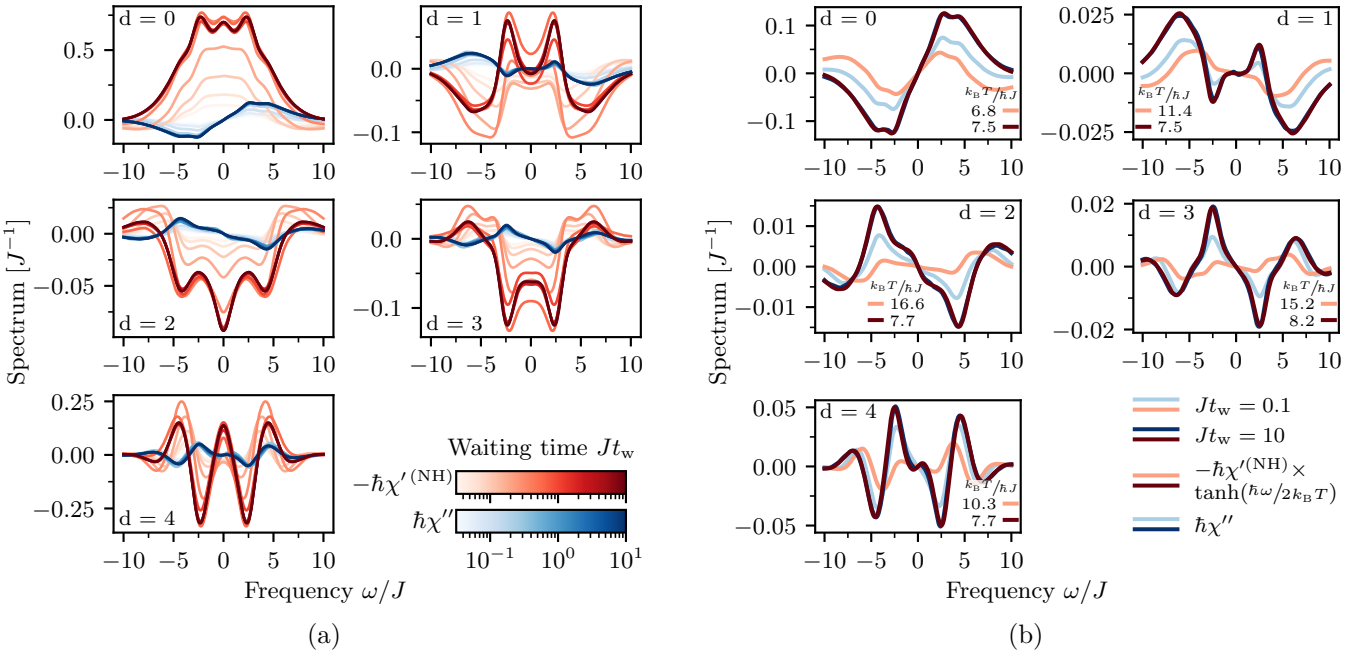

Figure 2.5.: Same as Fig. 2.2, but for a 2D Bose–Hubbard system. At long waiting times, the dynamic susceptibility χ'' (blue) agrees well with $\chi'^{(NH)}$ (red) after the latter is rescaled according to the FDR (2.12).

To show that our conclusions for the 1D Bose–Hubbard chain are generic, we study the analogous quench scenario in a 2D Bose–Hubbard system. We consider a system of 4×4 lattice sites with $N = 16$ particles (unit filling) and periodic boundary conditions in each direction. The larger system size compared to the 1D setting above allows us to support the conjecture that the FDR is better fulfilled as the system size increases. As

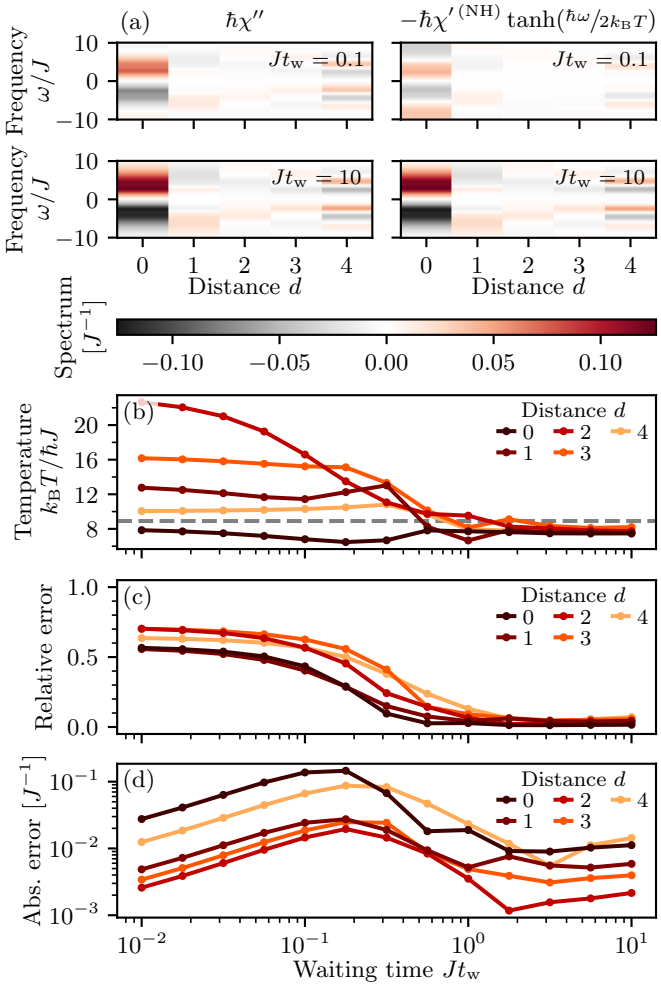

Figure 2.6.: Same as Fig. 2.3, but for a 2D Bose–Hubbard system. After waiting times t_w on the order of J^{-1}, the relative error (c) of the FDR remains small for all distinct lattice distances d.

before, we initialize the system in a Mott-insulating state and quench at time $t = 0$ into the superfluid phase at $U/J = 1.5625$.

Figures 2.5 and 2.6 show the same analysis for the 2D system as carried out in Figs. 2.2 and 2.3, respectively, for the 1D chain. Due to the periodic boundary conditions and the isotropy of the hopping, the curves fall into five classes corresponding to distances $d = 0 \ldots 4$ between the perturbed and probed lattice site. Note that these distances do not correspond to the physical distances in the 4×4 lattice, but to the minimum number of hopping events connecting the two sites. Similarly to the 1D setting, the FDR is violated at short waiting times, indicated by the large relative error in Fig. 2.6c. After times on the order of J^{-1}, the errors decrease dramatically and the FDR is fulfilled for all accessible distances with only a minor trend towards larger relative errors for larger distances. The remarkable agreement between χ'' and the rescaled $\chi'^{(\mathrm{NH})}$ at

late times is also evident from Fig. 2.5b. The effective temperatures in Fig. 2.6b for the individual distances reach approximately constant values that mutually agree up to deviations of about ten percent or less. Furthermore, the effective temperatures are close to the temperature $k_{\mathrm{B}}T/\hbar J = 8.91$ of a thermal state at the same energy density as the initial state (calculated for a 3×3 system using exact diagonalization). This supports our conclusion from before that the deviations observed for smaller systems are likely due to finite-size effects, while sufficiently large systems thermalize as expected.

Having illustrated how the FDR becomes accessible via (non-)Hermitian linear response, we now turn to the question of how to realize the corresponding non-Hermitian perturbations experimentally.

2.3. Realization of Non-Hermitian Linear Response

There exists a growing body of work that describes how non-Hermitian physics can be generated in quantum many-body systems [137, 138]. Non-Hermitian Hamiltonians naturally arise in the context of dissipative quantum systems [97, 159], where they govern the evolution of individual quantum trajectories conditioned on the absence of quantum jumps [160–162]. This way, it is possible to harness natural sources of dissipation in order to explore novel non-Hermitian physics [141, 143, 151]. Over the years, ever better techniques of screening experiments as much as possible from any sources of dissipation have been developed, with the goal of observing clean unitary dynamics in isolated quantum systems. This bears the potential to re-introduce channels of engineered dissipation using specifically designed control schemes.

In this section, we introduce an ancilla-based protocol that relies entirely on synthetic sources of dissipation in order to realize an effective non-Hermitian Hamiltonian. The perturbation can selectively be applied as a short pulse or under continuous modulation of its strength, allowing one to probe frequency-dependent responses in the same way as in standard linear response scenarios. Moreover, the choice of system–ancilla coupling is both flexible and experimentally feasible, giving access to a wide range of observables.

Figure 2.7 gives an overview of the scheme, which is most conveniently phrased as an application of the quantum Zeno effect [156, 157]. In its basic form, the quantum Zeno effect describes the phenomenon that frequent measurements can keep a quantum system in a certain eigenstate for an infinite amount of time. If the measurements act only on a certain subsystem, the evolution is effectively constrained to a part of the Hilbert space corresponding to a certain measurement outcome, but non-trivial dynamics is still possible within this so-called Zeno subspace. In our case, the total Hilbert space comprises the target system plus an ancillary system, and the relevant Zeno subspace is spanned by all states without any particles in the ancilla. The protocol for realizing non-Hermitian linear response works as follows. Depending on the desired perturbation operator A, the relevant subsystem, e.g., a single site or two neighboring sites in an optical lattice, is coherently coupled to the initially empty ancilla, as depicted in Figs. 2.7a and 2.7b. A measurement of the ancilla population projects the system on the subspace with a definite number of particles in the ancilla. As will become clear

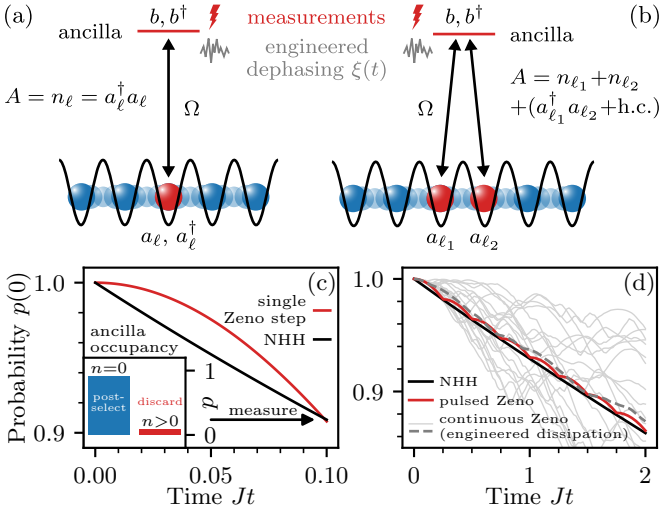

Figure 2.7.: Realization of an effective non-Hermitian Hamiltonian using the quantum Zeno effect, illustrated for an optical lattice. (a) Coupling a single lattice site ℓ to an ancilla gives rise to a perturbation by the density operator $A = n_\ell$ at that site. (b) A perturbation by the hopping operator $a_{\ell_1}^\dagger a_{\ell_2} + a_{\ell_2}^\dagger a_{\ell_1}$ can be achieved by coupling two sites ℓ_1 and ℓ_2 simultaneously to an ancilla. (c) Single step in the quantum Zeno evolution. The probability $p(0)$ of detecting no particles in the ancilla gradually decreases over time (red). A measurement of the ancilla population, post-selected on the condition that the ancilla is empty (inset), projects the system on the empty-ancilla subspace. The coupled evolution plus projection corresponds to an effective non-Hermitian perturbation (NHH, black). (d) When the projective measurement is performed frequently as compared to the strength of the coherent coupling Ω, the system plus ancilla is kept in the quantum Zeno regime for a prolonged period of time. The resulting pulsed Zeno evolution (red) is interpolated by the evolution under an effective non-Hermitian Hamiltonian (NHH, black). Alternatively, the repeated measurements can be substituted by strong engineered dissipation on the ancilla. The light grey lines show 20 trajectories corresponding to different realizations of engineered classical dephasing noise $\xi(t)$ on the ancilla, whose ensemble average (grey dashed line) approximates an effective non-Hermitian evolution.

further below, non-Hermitian dynamics is realized by post-selecting those measurement outcomes where the ancilla remains empty (see Fig. 2.7c). Repeating this measurement frequently gives rise to a quantum Zeno effect: in the quantum Zeno limit, as the measurement frequency tends to infinity, the probability of populating the ancilla vanishes. If, instead, the measurement frequency is finite, there is a finite probability of populating the ancilla. As illustrated in Fig. 2.7d, this leads to a "pulsed" leakage of probability from the subspace where the ancilla is empty to a complementary subspace with non-vanishing ancilla population. Instead of the pulsed Zeno effect, we can also use the continuous Zeno effect [157], which can be realized by substituting the repeated measurements with strong engineered dissipation on the ancilla [158]. This has the advantage of not requiring any non-destructive measurements during the evolution, but only a single post-selected measurement at the final evolution time. Both the pulsed Zeno evolution and the ensemble average over many noise realizations in the continu-

ous case can be described by an effective non-Hermitian Hamiltonian [157, 174, 175] (see Fig. 2.7d), which realizes the desired anti-Hermitian perturbation for measuring the unequal-time anti-commutator.

While the scheme can be implemented on various platforms, for the sake of concreteness, we focus here on bosons in optical lattices, where the ancilla may correspond to an auxiliary lattice site or an additional internal state. A crucial experimental requirement is the ability to distinguish an empty ancilla from one with non-zero population, which enables the projection on the empty-ancilla Zeno subspace. This requirement is met, for instance, by modern quantum gas microscopes, which reach both single-site and single-particle resolution [18, 19].

It is instructive to first consider a single step in the Zeno evolution consisting of a short coupling pulse followed by a projection, as depicted in Fig. 2.7c. It turns out that this scenario corresponds to applying a delta-like perturbation suitable for measuring the time trace of the non-Hermitian response function (2.8) like in Section 2.2.2. Subsequently, we explain how the quantum Zeno effect enables a prolonged evolution under a non-Hermitian Hamiltonian, focusing on the scenario with strong engineered dephasing noise that induces a continuous Zeno effect (cf. Fig. 2.7d).

We benchmark variants of the scheme for measurements in both time and frequency domain at the example of the Bose–Hubbard chain introduced in Section 2.2.2. Bose–Hubbard systems subject to dissipation have been extensively studied with the goal of exploring the rich dynamics of open quantum systems [151, 176, 177], whereas here, we use engineered dissipation as a tool [16] to probe dynamical correlations in closed systems via non-Hermitian linear response. In Section 2.4, we compare our approach with other protocols for measuring unequal-time anti-commutators, including ancilla-based weak measurement schemes [131, 132] and projective protocols [24, 129, 131–133], and discuss potential sources of errors as well as strategies how to mitigate them.

2.3.1. Non-Hermitian Linear Response as a Single Step in the Quantum Zeno Evolution

In this section, we discuss a single step in the Zeno evolution consisting of coupling to the ancilla and a projection on the empyt-ancilla subspace. Using time-dependent perturbation theory, we show that this process corresponds to applying an effective non-Hermitian delta-like perturbation as in Section 2.2.2 and allows one to access the unequal-time anti-commutator (2.8) in time domain.

Derivation of the scheme

For the sake of concreteness, we formulate the protocol for a bosonic lattice system (such as the Bose–Hubbard model discussed in Section 2.2.2) as well as an ancilla with bosonic degrees of freedom. We emphasize, however, that the protocol is general and immediately applies to other scenarios like fermions, spin systems, or continuous systems.

System–ancilla coupling. We consider a system–ancilla coupling Hamiltonian of the form

$$H_{\mathrm{cpl}} = \hbar\Omega(b^\dagger a + a^\dagger b)\,. \tag{2.31}$$

where a ($a^\dagger$) and b ($b^\dagger$) represent the bosonic annihilation (creation) operators of the system mode to be probed and the ancilla, respectively, and Ω is the coupling strength. In the coupling scheme depicted in Fig. 2.7a, the operator a represents a single lattice site ℓ, giving rise to an effective anti-Hermitian perturbation by the density (number) operator $A = n_\ell = a_\ell^\dagger a_\ell$, as will become clear below. The scheme in Fig. 2.7b couples two lattice sites ℓ_1 and ℓ_2, which may or may not be nearest neighbors, simultaneously to the ancilla. This corresponds to the replacement $a \to a_{\ell_1} + a_{\ell_2}$ in Eq. (2.31) and produces a non-Hermitian perturbation by the operator $A = n_{\ell_1} + n_{\ell_2} + a_{\ell_1}^\dagger a_{\ell_2} + a_{\ell_2}^\dagger a_{\ell_1}$. This type of perturbation can therefore be used to access FDRs for the hopping operator $a_{\ell_1}^\dagger a_{\ell_2} + a_{\ell_2}^\dagger a_{\ell_1}$, as demonstrated below for nearest neighbors. It is possible to consider even more general setups. For example, laser-assisted tunneling [178] can be used to add a relative phase between the two couplings in Fig. 2.7b, which gives rise to perturbations by the current operator. In Section 3.1, we will use this idea to develop schemes for measuring currents and current correlations. Furthermore, coupling a multitude of sites to one or more ancillas enables global perturbations by sums of local operators. The general form of the accessible perturbations is given further below in this section.

Single Zeno step. The protocol starts by evolving the initial state ρ_0 under the unperturbed Hamiltonian H_0 up to the waiting time t_{w}, at which the perturbation is applied. Before the coupling, the state is given by $\rho(t_{\mathrm{w}}) = \mathrm{e}^{-iH_0 t_{\mathrm{w}}/\hbar}\rho_0 \mathrm{e}^{iH_0 t_{\mathrm{w}}/\hbar}$. The coupled system evolves under the total Hamiltonian $H = H_0 + H_{\mathrm{cpl}}$ (for simplicity, we assume the ancilla to have no internal dynamics). During one Zeno step, the state changes, up to a normalization, as [157]

$$\rho(t_{\mathrm{w}}) \to \rho'(t_{\mathrm{w}} + \delta t) = PU(\delta t)\rho(t_{\mathrm{w}})U^\dagger(\delta t)P\,. \tag{2.32}$$

First, the coupled system evolves unitarily for a short time δt, described by the time evolution operator $U(\delta t) = \exp(-iH\delta t/\hbar)$. Second, a measurement of the ancilla population, post-selected on the condition that no particles are detected in the ancilla, projects the system on the empty-ancilla Zeno subspace, as expressed by the projection operator P. Let us now analyze these two processes in detail and derive the effective non-Hermitian Hamiltonian generated this way.

Unitary coupled evolution. It is convenient to work in the interaction picture with respect to the unperturbed Hamiltonian H_0. Time evolution is then governed by the von Neumann equation

$$i\hbar\frac{\mathrm{d}}{\mathrm{d}t}\tilde{\rho}(t) = \left[\tilde{H}_{\mathrm{cpl}}(t), \tilde{\rho}(t)\right], \tag{2.33}$$

where $\tilde{\rho}(t) = \mathrm{e}^{iH_0 t/\hbar}\rho(t)\mathrm{e}^{-iH_0 t/\hbar}$ and $\tilde{H}_{\mathrm{cpl}}(t) = \hbar\Omega[\tilde{a}^\dagger(t)b + b^\dagger\tilde{a}(t)]$, along with $\tilde{a}(t) = \mathrm{e}^{iH_0 t/\hbar}a\mathrm{e}^{-iH_0 t/\hbar}$, denote the density operator and the coupling Hamiltonian in the inter-

action picture, respectively. Rewriting Eq. (2.33) as an integral equation and substituting the left-hand side into the right-hand side, we arrive at

$$\tilde{\rho}(t) = \tilde{\rho}(t_\mathrm{w}) - \frac{i}{\hbar}\int_{t_\mathrm{w}}^{t} \mathrm{d}t' \left[\tilde{H}_\mathrm{cpl}(t'), \tilde{\rho}(t_\mathrm{w})\right] - \frac{1}{\hbar^2}\int_{t_\mathrm{w}}^{t} \mathrm{d}t' \int_{t_\mathrm{w}}^{t'} \mathrm{d}t'' \left[\tilde{H}_\mathrm{cpl}(t'), \left[\tilde{H}_\mathrm{cpl}(t''), \tilde{\rho}(t'')\right]\right]. \tag{2.34}$$

For the discussion of a single step in the quantum Zeno evolution, we consider a pulse[5] of duration δt much shorter than the characteristic time scales of H_0. We can then approximate $\tilde{\rho}(t'') \approx \tilde{\rho}(t_\mathrm{w})$ and $\tilde{H}_\mathrm{cpl}(t') \approx \tilde{H}_\mathrm{cpl}(t'') \approx \tilde{H}_\mathrm{cpl}(t_\mathrm{w})$ in the integrands, yielding

$$\begin{aligned}\tilde{\rho}(t_\mathrm{w}+\delta t) = \tilde{\rho}(t_\mathrm{w}) &- \frac{i}{\hbar}\delta t\left[\tilde{H}_\mathrm{cpl}(t_\mathrm{w}), \tilde{\rho}(t_\mathrm{w})\right] \\ &- \frac{\delta t^2}{2\hbar^2}\Big(\left\{\tilde{H}^2_\mathrm{cpl}(t_\mathrm{w}), \tilde{\rho}(t_\mathrm{w})\right\} - 2\tilde{H}_\mathrm{cpl}(t_\mathrm{w})\tilde{\rho}(t_\mathrm{w})\tilde{H}_\mathrm{cpl}(t_\mathrm{w})\Big) + \mathcal{O}(\delta t^3).\end{aligned} \tag{2.35}$$

We require the ancilla to be empty before the coupling. More specifically, we assume that the combined state of system and ancilla at the waiting time t_w is given by the product state $\tilde{\rho}(t_\mathrm{w}) = \tilde{\rho}_\mathrm{S}(t_\mathrm{w}) \otimes \tilde{\rho}_\mathrm{A}$, where the ancilla is in the pure bosonic[6] vacuum state $\tilde{\rho}_\mathrm{A} = |0\rangle\langle 0|$. Inserting this state into Eq. (2.35), we obtain

$$\begin{aligned}\tilde{\rho}(t_\mathrm{w}+\delta t) = \tilde{\rho}_\mathrm{S}(t_\mathrm{w}) \otimes |0\rangle\langle 0| &- i\Omega\delta t[\tilde{a}(t_\mathrm{w})\tilde{\rho}_\mathrm{S}(t_\mathrm{w}) \otimes |1\rangle\langle 0| - \mathrm{h.c.}] \\ &- \frac{(\Omega\delta t)^2}{2}\Big[\{\tilde{n}(t_\mathrm{w}), \tilde{\rho}_\mathrm{S}(t_\mathrm{w})\} \otimes |0\rangle\langle 0| - 2\tilde{a}(t_\mathrm{w})\tilde{\rho}_\mathrm{S}(t_\mathrm{w})\tilde{a}^\dagger(t_\mathrm{w}) \otimes |1\rangle\langle 1| \\ &\qquad + \sqrt{2}(\tilde{a}^2(t_\mathrm{w})\tilde{\rho}_\mathrm{S}(t_\mathrm{w}) \otimes |2\rangle\langle 0| + \mathrm{h.c.})\Big],\end{aligned} \tag{2.36}$$

where $\tilde{n}(t_\mathrm{w}) = \tilde{a}^\dagger(t_\mathrm{w})\tilde{a}(t_\mathrm{w})$ is the number operator and h.c. denotes the Hermitian conjugate.

Measurement of the ancilla population. After coupling the system to the ancilla, a single step in the Zeno evolution is completed by measuring the ancilla population, projecting the state on a subspace with a definite number of particles in the ancilla. Let $P_n = \mathbb{1} \otimes |n\rangle\langle n|$ denote the projection operator on the subspace with n particles in the ancilla. Since $[P_n, H_0] = 0$, the measurement can optionally be deferred up to the final observation time (cf. Ref. [131]). The projected states read

$$P_0\tilde{\rho}(t_\mathrm{w}+\delta t)P_0 = [\tilde{\rho}_\mathrm{S}(t_\mathrm{w}) - s\{\tilde{n}(t_\mathrm{w}), \tilde{\rho}_\mathrm{S}(t_\mathrm{w})\}] \otimes |0\rangle\langle 0|, \tag{2.37a}$$

$$P_1\tilde{\rho}(t_\mathrm{w}+\delta t)P_1 = 2s\tilde{a}(t_\mathrm{w})\tilde{\rho}_\mathrm{S}(t_\mathrm{w})\tilde{a}^\dagger(t_\mathrm{w}) \otimes |1\rangle\langle 1|, \tag{2.37b}$$

[5] For simplicity, we consider a rectangular pulse of duration δt. However, the pulse shape is in fact arbitrary as long as δt is sufficiently short. That is, we may equivalently substitute $H_\mathrm{cpl} \to g(t)H_\mathrm{cpl}$ for any function $g(t)$ with compact support on the interval $[t_\mathrm{w}, t_\mathrm{w}+\delta t]$, normalized such that $\int_{t_\mathrm{w}}^{t_\mathrm{w}+\delta t} \mathrm{d}t\, g(t) = \delta t$.

[6] For concreteness, we focus here on bosonic systems, but the derivation for fermions proceeds analogously and yields the same result for the unequal-time anti-commutator.

where $s = (\Omega\delta t)^2/2$ is the effective coupling strength, and $P_n\tilde{\rho}(t_\mathrm{w}+\delta t)P_n = 0$ for $n \geq 2$, up to second order in δt. The probability of detecting n particles in the ancilla is then given by $p(n) = \mathrm{Tr}[P_n\tilde{\rho}(t_\mathrm{w}+\delta t)P_n]$, which yields

$$p(0) = 1 - 2s\langle n(t_\mathrm{w})\rangle_0\,, \tag{2.38a}$$

$$p(1) = 2s\langle n(t_\mathrm{w})\rangle_0\,, \tag{2.38b}$$

and $p(n \geq 2) = 0$, up to second order in δt. Here, we have used $\mathrm{Tr}[\tilde{\rho}(t_\mathrm{w})\tilde{n}(t_\mathrm{w})] = \mathrm{Tr}[\rho_0 n(t_\mathrm{w})] = \langle n(t_\mathrm{w})\rangle_0$.

Remarkably, the result in Eq. (2.37a) can, to leading order in the coupling, be expressed as the evolution under an effective non-Hermitian Hamiltonian,

$$P_0\tilde{\rho}(t_\mathrm{w}+\delta t)P_0 = \mathrm{e}^{-i\tilde{H}_\mathrm{eff}(t_\mathrm{w})\delta t}\tilde{\rho}(t_\mathrm{w})\mathrm{e}^{i\tilde{H}^\dagger_\mathrm{eff}(t_\mathrm{w})\delta t}, \tag{2.39}$$

with $\tilde{H}_\mathrm{eff}(t) = -i\hbar s\tilde{A}(t)/\delta t$ and the perturbation operator $A = n = a^\dagger a$.

According to Lüders' rule [179], the conditional state, given that n particles have been detected in the ancilla, is obtained by normalizing the projected states (2.37) by the respective probabilities (2.38), i.e., $\tilde{\rho}(t_\mathrm{w}+\delta t \mid n) = P_n\tilde{\rho}(t_\mathrm{w}+\delta t)P_n/p(n)$. Up to leading order in s, we find

$$\tilde{\rho}(t_\mathrm{w}+\delta t \mid 0) = \tilde{\rho}(t_\mathrm{w}) - s\big[\{\tilde{n}(t_\mathrm{w}),\tilde{\rho}(t_\mathrm{w})\} - 2\langle n(t_\mathrm{w})\rangle_0\tilde{\rho}(t_\mathrm{w})\big]\,, \tag{2.40a}$$

$$\tilde{\rho}(t_\mathrm{w}+\delta t \mid 1) = \frac{\tilde{a}(t_\mathrm{w})\tilde{\rho}(t_\mathrm{w})\tilde{a}^\dagger(t_\mathrm{w})}{\langle n(t_\mathrm{w})\rangle_0}\,, \tag{2.40b}$$

where we have discarded (or traced out) the ancilla and omitted the subscripts indicating system density operators. By contrast, if the ancilla population is not measured or if the measurement outcomes are ignored, the state after the coupling is instead described by the unconditional density operator

$$\begin{aligned}\tilde{\rho}(t_\mathrm{w}+\delta t) &= \sum_n p(n)\tilde{\rho}(t_\mathrm{w}+\delta t \mid n)\\ &= \tilde{\rho}(t_\mathrm{w}) - s\big[\{\tilde{n}(t_\mathrm{w}),\tilde{\rho}(t_\mathrm{w})\} - 2\tilde{a}(t_\mathrm{w})\tilde{\rho}(t_\mathrm{w})\tilde{a}^\dagger(t_\mathrm{w})\big]\,,\end{aligned} \tag{2.41}$$

which can be obtained directly from Eq. (2.36) after tracing out the ancilla.

Non-Hermitian linear response. For times $t > t_\mathrm{w} + \delta t$, the coupling is switched off and the system evolves solely under the Hamiltonian H_0. According to Eq. (2.33), this evolution is trivial in the interaction picture, such that $\tilde{\rho}(t) = \tilde{\rho}(t_\mathrm{w}+\delta t)$. The (unnormalized) expectation value of an observable B with respect to the state (2.37a) projected on the empty-ancilla subspace reads

$$\begin{aligned}\mathrm{Tr}[B\,P_0\rho(t)P_0] &= \mathrm{Tr}\big[\tilde{B}(t)P_0\tilde{\rho}(t)P_0\big]\\ &= \mathrm{Tr}\big[\tilde{B}(t)\tilde{\rho}(t_\mathrm{w})\big] - s\,\mathrm{Tr}\big[\tilde{B}(t)\{\tilde{n}(t_\mathrm{w}),\tilde{\rho}(t_\mathrm{w})\}\big]\\ &= \mathrm{Tr}[B(t)\rho_0] - s\,\mathrm{Tr}[B(t)\{n(t_\mathrm{w}),\rho_0\}]\\ &= \langle B(t)\rangle_0 - s\langle\{B(t),n(t_\mathrm{w})\}\rangle_0\,,\end{aligned} \tag{2.42}$$

where we have used the cyclic property of the tract as well as the fact that interaction picture operators with respect to the total Hamiltonian H correspond to Heisenberg picture operators with respect to the unperturbed Hamiltonian H_0. Normalizing Eq. (2.42) by the probability (2.38a) finally yields, to leading order in s, the conditional expectation value with respect to the state (2.40a),

$$\langle B(t)\rangle_P = \mathrm{Tr}[B\rho(t\,|\,0)] = \langle B(t)\rangle_0 - s\big[\langle\{B(t), A(t_\mathrm{w})\}\rangle_0 - 2\langle B(t)\rangle_0\langle A(t_\mathrm{w})\rangle_0\big]\,, \quad (2.43)$$

representing a post-selected measurement conditioned on the empty ancilla ($P = P_0$). As anticipated, a comparison with Eqs. (1.56) and (2.8) shows that this result effectively corresponds to a linear response after applying the anti-Hermitian perturbation $H_1(t) = -i\hbar s\delta(t - t_\mathrm{w})A$, giving direct access to the unequal-time anti-commutator (1.74) via $S_{BA}(t, t_\mathrm{w}) = -[\langle B(t)\rangle_P - \langle B(t)\rangle_0]/2s$. As required in Section 2.1, the perturbation operator $A = a^\dagger a$ is indeed positive semi-definite, in line with the physical intuition that the norm of the state can only decrease through outcoupling followed by a projection.

Unconditional response. It is instructive to compare the result in Eq. (2.43) with the one obtained if no projection on the empty-ancilla subspace is performed, e.g., if the measurement apparatus is unable to distinguish an empty ancilla from one with non-vanishing population or the result of the ancilla measurement is ignored. In this case, a simple average over all ancilla populations is obtained, where, to leading order in the effective coupling strength s, only single occupancies of the ancilla contribute.

The conditional expectation value with respect to the state Eq. (2.40b), given that a single particle is detected in the ancilla, reads

$$\langle B(t)\rangle_Q = \mathrm{Tr}[B\rho(t\,|\,1)] = \frac{\langle a^\dagger(t_\mathrm{w})B(t)a(t_\mathrm{w})\rangle_0}{\langle n(t_\mathrm{w})\rangle_0}\,. \quad (2.44)$$

Here, $Q = \mathbb{1} - P$ denotes the projector on the subspace complementary to that projected on by P. According to Eq. (2.41), we thus obtain the unconditional response

$$\langle B(t)\rangle = \langle B(t)\rangle_0 - s\langle\{B(t), a^\dagger(t_\mathrm{w})a(t_\mathrm{w})\} - 2a^\dagger(t_\mathrm{w})B(t)a(t_\mathrm{w})\rangle_0. \quad (2.45)$$

The last term stems from a process where a single particle ends up in the ancilla after the coupling, as expressed by Eq. (2.44). This quantity contributes a systematic error in the case of faulty detection with false negatives (see the discussion in Section 2.5). Post-selecting on the empty ancilla eliminates this undesired contribution, yielding a pure non-Hermitian evolution that gives access to the unequal-time anti-commutator.

Connection to open quantum systems. The structure of the second term on the right-hand side of Eq. (2.45), characterizing the unconditional response after coupling to the ancilla without measuring the ancilla population, resembles to the "recycling term" in Lindblad master equations [159, 162]. In fact, the short coupling pulse to the ancilla can be viewed as an effective dissipative perturbation, $\rho(t_\mathrm{w}) \to \rho(t_\mathrm{w} + \delta t) =$

$\rho(t_w)+\delta t\mathcal{D}[\rho(t_w)]$, where $\mathcal{D}[\rho] = \gamma(2a\rho a^\dagger - \{a^\dagger a, \rho\})$ is the Lindblad dissipator with dissipation rate $\gamma = s/\delta t$. This yields Eq. (2.45) for the expectation value of an observable B after a unitary evolution up to time t. In the quantum trajectories picture [160–162], the Lindblad dissipator $\mathcal{D}[\rho]$ generates an evolution under the non-Hermitian Hamiltonian $H_1 = -i\hbar\gamma a^\dagger a$, subject to quantum jumps described by the "recycling term" $2\gamma a\rho a^\dagger$. By post-selecting on the absence of quantum jumps, it is possible to isolate the pure non-Hermitian evolution [141, 143, 151]. From this point of view, the projection on the empty-ancilla subspace in Eq. (2.32) can be interpreted as a post-selection on the absence of quantum jumps, i.e., particles hopping to the ancilla. This allows us to eliminate the undesired contribution in Eq. (2.45) due to the "recycling term" and obtain instead the result in Eq. (2.43), reflecting a purely non-Hermitian perturbation that gives access to the unequal-time anti-commutator.

Numerical Benchmark: Non-Hermitian Linear Response in Time Domain

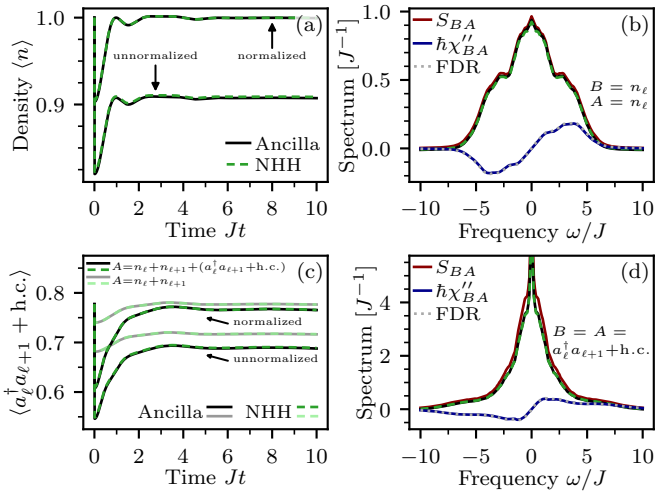

Figure 2.8.: Simulation of the linear response to a non-Hermitian perturbation generated by a single step in the Zeno evolution of coupling to an ancilla followed by a projection on the empty-ancilla subspace (see Fig. 2.7c). (a) Time trace of the density after applying the perturbation to a single site as in Fig. 2.7a. The unnormalized and normalized responses correspond to Eqs. (2.42) and (2.43), respectively. The result agrees well with the response to a non-Hermitian perturbation by the density operator $A = n_\ell$ (NHH, green dashed line). (b) The correlation spectrum extracted from the response in (a) agrees well with the exact result S_{BA}. The FDR (1.83) between χ''_{BA} and S_{BA}, calculated using the known temperature $k_BT/\hbar J = 4.27$ of the thermal state, is shown for comparison. (c) Time trace of the nearest-neighbor correlator after coupling two neighboring sites simultaneously (black, see Fig. 2.7b) or individually (grey, Fig. 2.7a) to the ancilla. Subtracting the latter quantity from the former yields the response to a perturbation by the hopping operator $A = a^\dagger_\ell a_{\ell+1} + a^\dagger_{\ell+1}a_\ell$. The respective responses agree well with their effective descriptions in terms of non-Hermitian Hamiltonians (NHH, green dashed lines). (d) The extracted correlation spectrum reproduces the exact one to good accuracy.

To benchmark the above scheme, we numerically solve the full quantum evolution de-

scribing a measurement of $S_{BA}(t, t_\mathrm{w})$ for a thermal state $\rho_T = \exp(-H_0/k_\mathrm{B}T)/Z(T)$ in a Bose–Hubbard chain of $L = 8$ sites at unit filling and with periodic boundary conditions. Here, $Z(T) = \mathrm{Tr}[\exp(-H_0/k_\mathrm{B}T)]$ is the canonical partition sum, and the temperature T is chosen such that the mean energy $\langle H_0\rangle_T = \mathrm{Tr}(H_0\rho_T)$ corresponds to that of a Mott-insulating state. A thermal state is an ideal benchmark for our purposes since the temperature T is known and the FDR is satisfied exactly, so any deviations from the FDR indicate deficiencies of the method.

In Figs. 2.8a and 2.8c, we show the time traces of the responses to perturbations corresponding to the coupling configurations in Figs. 2.7a and 2.7b, respectively, i.e., for on-site densities ($A = B = n_\ell$) and nearest-neighbor correlators ($A = n_\ell + n_{\ell+1} + a_\ell^\dagger a_{\ell+1} + a_{\ell+1}^\dagger a_\ell$, $B = a_\ell^\dagger a_{\ell+1} + a_{\ell+1}^\dagger a_\ell$). From the latter measurement, the response for the combination $A = B = a_\ell^\dagger a_{\ell+1} + a_{\ell+1}^\dagger a_\ell$ can be obtained by subtracting the response of the same observable B to perturbations A involving only the densities at the relevant sites. Experimentally, the nearest-neighbor correlator $\langle B\rangle = \langle a_\ell^\dagger a_{\ell+1} + \mathrm{h.c.}\rangle$ can be measured, for example, using the projective current measurement protocol that will be discussed in Section 3.3 with properly adjusted phases or by projecting the system on non-interacting double wells and monitoring the double well occupancy as a function of time [180, 181]. The coupling to the ancilla is applied as a rectangular pulse of duration $J\delta t = 0.01$ and its strength is chosen such that the effective coupling becomes $s = 0.05$ for the density and $s = 0.02$ for the correlator, corresponding to a decay of the norm by about 10 % in both cases. As can be seen in Figs. 2.8a and 2.8c, the simulated ancilla measurement agrees well with the description in terms of the effective non-Hermitian Hamiltonian in Eq. (2.39). Since the thermal state is stationary, the waiting time t_w, at which the perturbation is applied, does not matter, and has been chosen as $t_\mathrm{w} = 0$. Moreover, the conventions for the dynamical susceptibilities in Eqs. (2.19) and (2.23) are equivalent for a thermal state, such that the correlation spectrum is given by $S_{BA}(\omega) = -\hbar\chi''^{(\mathrm{NH})}_{BA}(\omega)$ according to Eq. (2.11). In Figs. 2.8b and 2.8d, we compare the correlation spectra extracted from the responses in Figs. 2.8a and 2.8c, respectively, with the exact result. The Fourier integrals have been calculated using exponential filters of characteristic frequencies $\gamma/J = 0.1$ for the density and $\gamma/J = 0.05$ for the correlator. Due to the sizable static contribution to the response in the latter case, the height of the central peak in Fig. 2.8d strongly depends on the choice of γ, but this is irrelevant for probing FDRs because the value of the correlation spectrum at $\omega = 0$ is not constrained by the FDR (1.83). Up to small deviations resulting from non-linear effects, which can be reduced at the cost of a lower signal-to-noise ratio (see discussion in Section 2.5), the scheme presented in this section provides an accurate measurement of the correlation spectrum, capable of certifying the validity of the FDR (1.83) for both densities and correlators.

General System–Ancilla Couplings

The coupling schemes in Figs. 2.7a and 2.7b are designed to realize non-Hermitian perturbations by the density operator and the hopping operator, respectively. We now consider the general situation where an arbitrary number of system modes is coupled to

up to M ancillary modes. This scenario is described by the general coupling Hamiltonian

$$H_{\mathrm{cpl}} = \sum_{m=1}^{M} \hbar\Omega_m \left(b_m^\dagger \alpha_m + \alpha_m^\dagger b_m \right), \tag{2.46}$$

where the operator

$$\alpha_m = \sum_\ell \lambda_{m\ell} a_\ell \tag{2.47}$$

is a linear combination of system modes a_ℓ with coefficients $\lambda_{m\ell} \in \mathbb{C}$, coupled to the m-th ancilla with coupling strength $\Omega_m \geq 0$. The configuration in Fig. 2.7a, a single lattice site ℓ^* coupled to a single ancilla, is recovered for $M = 1$ and $\lambda_{1\ell} = \delta_{\ell\ell^*}$, while Fig. 2.7b, two sites ℓ_1 and ℓ_2 simultaneously coupled to a single ancilla, corresponds to $M = 1$ and $\lambda_{1\ell} = \delta_{\ell\ell_1} + \delta_{\ell\ell_2}$.

As before, we consider a short coupling pulse of duration δt such that the state after the coupling is given by Eq. (2.35). Subsequently, a measurement of the individual ancilla occupancies is performed and the state is conditioned on the outcome of that measurement (as mentioned above, the measurement may also be deferred up to the final observation time). Given the outcome $(n_1, \ldots, n_M)$, the post-measurement state, up to a normalization, reads $P_{n_1 \ldots n_M} \tilde{\rho}(t_\mathrm{w} + \delta t) P_{n_1 \ldots n_M}$, where $P_{n_1 \ldots n_M} = \mathbb{1} \otimes |n_1 \cdots n_M\rangle\langle n_1 \cdots n_M|$ is the projection operator on the subspace with a definite ancilla population corresponding to the measurement outcome.

Up to leading order in the coupling, only processes where at most a single particle ends up in one of the ancillas contribute. Let $P_0 = P_{0\ldots0}$ denote the projector on the subspace with all ancillas empty. The projector on the subspace with a single particle in the m-th ancilla and all others empty can then be expressed as $P_1^{(m)} = b_m^\dagger P_0 b_m$. Using the bosonic commutation relations

$$[\alpha_m, b_{m'}] = [\alpha_m, b_{m'}^\dagger] = 0\,, \tag{2.48a}$$

$$[b_m, b_{m'}^\dagger] = \delta_{mm'}, \tag{2.48b}$$

we find the (unnormalized) post-measurement states

$$P_0 \tilde{\rho}(t_\mathrm{w} + \delta t) P_0 = \tilde{\rho}(t_\mathrm{w}) - \sum_{m=1}^{M} s_m \left\{ \tilde{\alpha}_m^\dagger(t_\mathrm{w}) \tilde{\alpha}_m(t_\mathrm{w}), \tilde{\rho}(t_\mathrm{w}) \right\}, \tag{2.49a}$$

$$P_1^{(m)} \tilde{\rho}(t_\mathrm{w} + \delta t) P_1^{(m)} = 2 s_m \tilde{a}_m(t_\mathrm{w}) \tilde{\rho}(t_\mathrm{w}) \tilde{a}_m^\dagger(t_\mathrm{w})\,, \tag{2.49b}$$

where we have traced out the ancillas and introduced the effective coupling strengths $s_m = (\Omega_m \delta t)^2/2$. We note that this result holds for fermions as well, where instead of Eq. (2.48) the corresponding fermionic anti-commutation relations apply. The respective probabilities of finding no particles in any ancilla or a single particle in the m-th ancilla read

$$P_0 = 1 - 2 \sum_{m=1}^{M} s_m \left\langle \alpha_m^\dagger(t_\mathrm{w}) \alpha_m(t_\mathrm{w}) \right\rangle_0, \tag{2.50a}$$

$$P_1^{(m)} = 2 s_m \left\langle \alpha_m^\dagger(t_\mathrm{w}) \alpha_m(t_\mathrm{w}) \right\rangle_0. \tag{2.50b}$$

A comparison of Eqs. (2.49) and (2.50) with Eqs. (2.37) and (2.38) shows that the coupling to the m-th ancilla in the general coupling Hamiltonian (2.46) generates an effective non-Hermitian perturbation by the operator

$$A_m = \alpha_m^\dagger \alpha_m = \sum_{\ell\ell'} \lambda_{m\ell}^* \lambda_{m\ell'} a_l^\dagger a_{\ell'} \,. \tag{2.51}$$

Coupling to multiple ancillas simultaneously can be used to realize perturbation by (arbitrarily weighted) sums of the operators A_m. This demonstrates that the presented scheme enables flexible access to unequal-time correlations and FDRs for a wide range of observables, two specific examples of which, namely densities and nearest-neighbor correlators, are illustrated in Fig. 2.8.

2.3.2. Non-Hermitian Linear Response via the Pulsed Quantum Zeno Effect

We now explain how to realize a prolonged evolution under a (possibly time-dependent) effective non-Hermitian Hamiltonian, suitable for probing frequency-resolved responses as is common in standard linear response experiments. To this end, we generalize the coupling Hamiltonian in (2.31) by allowing for an arbitrary modulation $g(t)$ of the coupling strength, i.e.,

$$H_{\mathrm{cpl}}(t) = g(t)\hbar\Omega(b^\dagger a + a^\dagger b). \tag{2.52}$$

The key to obtaining a response as in Eq. (2.5) is to iterate the Zeno step presented in the previous subsection as depicted in Fig. 2.7d. Such a repeated series of measurements is the common scenario for the pulsed quantum Zeno effect [156, 157, 175]. To this end, we split the interval $[t_{\mathrm{w}}, t]$ into n steps such that $t_{\mathrm{w}} = t_0 < t_1 < \cdots < t_n = t$ with $t_{i+1} - t_i = \delta t = (t - t_{\mathrm{w}})/n$. The evolution from t_i to t_{i+1} is described by Eq. (2.32), corresponding to an individual Zeno step of unitary evolution under the Hamiltonian $H(t) = H_0 + H_{\mathrm{cpl}}(t)$, followed by a measurement of the ancilla population that projects the system on the subspace with empty ancilla (realizations where one or more particles are detected in the ancilla are discarded). Thus, the state evolves, up to a normalization, as

$$\rho(t_{\mathrm{w}}) \to \rho'(t) = PU_nP \cdots PU_1\rho(t_{\mathrm{w}})U_1^\dagger P \cdots PU_n^\dagger P \tag{2.53}$$

where $U_i = U(t_i, t_{i-1})$ denotes the time evolution operator from time t_{i-1} to t_i. This equation describes the evolution under a continuously applied system–ancilla coupling with intermittent measurements of the ancilla population. The role of the measurements is to destroy the coherences between the relevant Zeno subspaces. To gain a deeper insight into this mechanism, we will now consider in detail two consecutive Zeno steps, using a similar formalism as in Ref. [157].

The Role of the Measurement Between Two Zeno Steps

Let P denote the projection operator on the empty-ancilla subspace $\mathscr{H}_P$ and $Q = \mathbb{1} - P$ the projector on the complementary subspace $\mathscr{H}_Q = \mathscr{H}_P^\perp$ with at least one particle

in the ancilla. It is convenient to write the density operator ρ on the total Hilbert space $\mathscr{H} = \mathscr{H}_P \oplus \mathscr{H}_Q$ in the form

$$\rho = \begin{pmatrix} \rho_{PP} & \rho_{PQ} \\ \rho_{QP} & \rho_{QQ} \end{pmatrix}, \tag{2.54}$$

where $\rho_{PP} = P\rho P$ and $\rho_{QQ} = Q\rho Q$ are the populations of $\mathscr{H}_P$ and $\mathscr{H}_Q$, respectively, and $\rho_{PQ} = P\rho Q = \rho_{QP}^\dagger$ are the coherences between these two subspaces. Similarly, the time evolution operator from time t_0 to t, representing the evolution under the von Neumann equation (2.33), can be expressed as

$$U(t,t_0) = \begin{pmatrix} U_{PP}(t,t_0) & U_{PQ}(t,t_0) \\ U_{QP}(t,t_0) & U_{QQ}(t,t_0) \end{pmatrix} \tag{2.55}$$

with $U_{PQ}(t,t_0) = PU(t,t_0)Q$.

First Zeno step. Let us denote the initial state $\tilde{\rho}(t_\mathrm{w})$ of the Zeno evolution by ρ^0 and set $t_0 = t_\mathrm{w}$. Since the ancilla is initially empty, we have $\rho^0_{PQ} = \rho^0_{QQ} = 0$. The unitary evolution from time t_0 to t_1 in presence of the system–ancilla coupling changes the state as

$$\rho^0 = \begin{pmatrix} \rho^0_{PP} & 0 \\ 0 & 0 \end{pmatrix} \xrightarrow{U(t_1,t_0)} \rho^1 = \begin{pmatrix} U^1_{PP}\rho^0_{PP}(U^1_{PP})^\dagger & U^1_{PP}\rho^0_{PP}(U^1_{QP})^\dagger \\ U^1_{QP}\rho^0_{PP}(U^1_{PP})^\dagger & U^1_{QP}\rho^0_{PP}(U^1_{QP})^\dagger \end{pmatrix}, \tag{2.56}$$

where $U^i_{PQ} = PU(t_i,t_{i-1})Q$. From Eq. (2.34), using $P^2 = P$, $Q^2 = Q$, $PQ = QP = 0$, and $PH_\mathrm{cpl}(t)P = 0$, we obtain the populations and coherences of ρ^1, up to quadratic order in the coupling, as

$$\rho^1_{PP} = \rho^0_{PP} - \frac{1}{\hbar^2}\int_{t_0}^{t_1} \mathrm{d}t' \int_{t_0}^{t'} \mathrm{d}t'' \big[\mathcal{H}_{PQ}(t')\mathcal{H}_{QP}(t'')\rho^0_{PP} + \mathrm{h.c.}\big], \tag{2.57}$$

$$\rho^1_{PQ} = \frac{i}{\hbar}\int_{t_0}^{t_1} \rho^0_{PP}H_{PQ}(t') - \frac{1}{\hbar^2}\int_{t_0}^{t_1} \mathrm{d}t' \int_{t_0}^{t'} \mathrm{d}t''\, \rho^0_{PP}\mathcal{H}_{PQ}(t'')\mathcal{H}_{QQ}(t'), \tag{2.58}$$

$$\rho^1_{QQ} = \frac{1}{\hbar^2}\int_{t_0}^{t_1} \mathrm{d}t' \int_{t_0}^{t_1} \mathrm{d}t''\, \mathcal{H}_{QP}(t')\rho^0_{PP}\mathcal{H}_{PQ}(t''), \tag{2.59}$$

where $\mathcal{H}_{PQ}(t) = \mathcal{H}^\dagger_{QP}(t) = P\tilde{H}_\mathrm{cpl}(t)Q = g(t)\hbar\Omega P\tilde{a}^\dagger(t)bQ$. Measuring the ancilla population projects the state on the subspace with a definite number of particles in the ancilla. Without registering the measurement outcome, this yields the unconditional state $P\rho^1P + Q\rho^1Q$. Crucially, the measurement process destroys any coherences ρ_{PQ} and ρ_{QP} between the Zeno subspaces $\mathscr{H}_P$ and $\mathscr{H}_Q$. We are interested in measurement outcomes where no particles are detected in the ancilla. Conditioning the state on this outcome corresponds to a projection on the empty-ancilla subspace $\mathscr{H}_P$,

$$\rho^1 = \begin{pmatrix} \rho^1_{PP} & \rho^1_{PQ} \\ \rho^1_{QP} & \rho^1_{QQ} \end{pmatrix} \xrightarrow{P} P\rho^1P = \begin{pmatrix} \rho^1_{PP} & 0 \\ 0 & 0 \end{pmatrix}. \tag{2.60}$$

Second Zeno step. The second Zeno step proceeds in complete analogy to Eqs. (2.56) and (2.60): the state first evolves unitarily from time t_1 to t_2 in presence of the system–ancilla coupling and is then projected on the empty-ancilla subspace $\mathscr{H}_P$,

$$P\rho^1 P \xrightarrow{U(t_2,t_1)} \rho^2 = \begin{pmatrix} \rho^2_{PP} & \rho^2_{PQ} \\ \rho^2_{QP} & \rho^2_{QQ} \end{pmatrix} \xrightarrow{P} P\rho^2 P = \begin{pmatrix} \rho^2_{PP} & 0 \\ 0 & 0 \end{pmatrix}, \tag{2.61}$$

with

$$\begin{aligned} \rho^2_{PP} &= U_{PP}(t_2,t_1)\rho^1_{PP}U^\dagger_{PP}(t_2,t_1) \\ &= U^2_{PP}U^1_{PP}\rho^0_{PP}(U^1_{PP})^\dagger(U^2_{PP})^\dagger \\ &= \rho^0_{PP} - \frac{1}{\hbar^2}\bigg(\int_{t_0}^{t_1}\mathrm{d}t'\int_{t_0}^{t'}\mathrm{d}t'' + \int_{t_1}^{t_2}\mathrm{d}t'\int_{t_1}^{t'}\mathrm{d}t''\bigg)\left[\mathcal{H}_{PQ}(t')\mathcal{H}_{QP}(t'')\rho^0_{PP} + \text{h.c.}\right], \end{aligned} \tag{2.62}$$

up to leading order in the coupling. It is instructive to compare this result to the one obtained if no measurement is performed after the first step. The state then receives additional contributions from the coherences, yielding, to leading order in the coupling,

$$\begin{aligned} P\rho(t_2)P &= PU(t_2,t_1)\rho^1 U^\dagger(t_2,t_1)P \\ &= U^2_{PP}\rho^1_{PP}(U^2_{PP})^\dagger + U^2_{PP}\rho^1_{PQ}(U^2_{PQ})^\dagger + U^2_{PQ}\rho^1_{QP}(U^2_{PP})^\dagger + U^2_{PQ}\rho^1_{QQ}(U^2_{PQ})^\dagger \\ &= \rho^2_{PP} - \int_{t_0}^{t_1}\mathrm{d}t'\int_{t_1}^{t_2}\mathrm{d}t''\left[\rho^0_{PP}\mathcal{H}_{PQ}(t')\mathcal{H}_{QP}(t'') + \text{h.c.}\right] \\ &= \rho^0_{PP} - \int_{t_0}^{t_2}\mathrm{d}t'\int_{t_0}^{t'}\mathrm{d}t''\left[\mathcal{H}_{PQ}(t')\mathcal{H}_{QP}(t'')\rho^0_{PP} + \text{h.c.}\right]. \end{aligned} \tag{2.63}$$

The result in the last line could have been directly obtained from Eq. (2.34) for $t = t_2$ by applying the projector P on both sides. This is evident because without the projection after the first step, the system plus ancilla evolves unitarily from time t_0 to t_2. However, Eq. (2.63) explicitly exposes the crucial effect of the measurement after the first step: the last term in the second-to-last line is precisely the contribution from the coherences ρ^1_{PQ} and ρ^1_{QP} which is missing in Eq. (2.62) since the coherences have been destroyed by the measurement.

Pulsed Zeno Evolution and Effective Non-Hermitian Hamiltonian

Iterating the Zeno evolution for n steps up to time t_n (including projections after each step), the resulting state is given, to leading order in the coupling, by

$$\rho^n_{PP} = \rho^0_{PP} - \frac{1}{\hbar^2}\sum_{i=0}^{n-1}\int_{t_i}^{t_{i+1}}\mathrm{d}t'\int_{t_i}^{t'}\mathrm{d}t''\left[\mathcal{H}_{PQ}(t')H_{QP}(t'')\rho^0_{PP} + \text{h.c.}\right]. \tag{2.64}$$

If the duration $\delta t = t_{i+1} - t_i$ of each Zeno step is sufficiently short compared to the time scales of the unperturbed Hamiltonian H_0 as well as the modulation $g(t)$, the integrand

in each integral is approximately constant, such that the (unnormalized) expectation value of an observable B after the Zeno evolution is given by

$$\mathrm{Tr}[B\rho'(t)] = \langle B(t)\rangle_0 - s\sum_{i=0}^{n-1} g^2(t_i)\langle\{B(t), A(t_i)\}\rangle_0 \tag{2.65}$$

with $A = a^\dagger a$ and $s = (\Omega\delta t)^2/2$. Approximating the sum by an integral, the pulsed evolution in Eq. (2.65) can be interpolated by a continuous evolution under an effective non-Hermitian Hamiltonian (see Fig. 2.7c). In fact, this result then coincides with a linear response to the anti-Hermitian perturbation $H_1(t) = -if(t)A$ according to Eq. (2.5), where $f(t) = g^2(t)\Omega^2\delta t/2$. Since the operator $f(t)A$ is positive semi-definite (cf. Section 2.1), this effective non-Hermitian Hamiltonian describes a gradual leakage of probability out of the empty-ancilla Zeno subspace (see Fig. 2.7d).

By contrast, if the state is only projected at the final observation time, but no projections are performed during the evolution as in Eq. (2.63), we obtain, to leading order in the coupling,

$$P\rho(t_n)P = \rho^0_{PP} - \frac{1}{\hbar^2}\int_{t_0}^{t_n} \mathrm{d}t' \int_{t_0}^{t'} \mathrm{d}t'' \left[\mathcal{H}_{PQ}(t')H_{QP}(t'')\rho^0_{PP} + \mathrm{h.c.}\right], \tag{2.66}$$

which yields the (unnormalized) expectation value

$$\mathrm{Tr}[B\,P\rho(t)P] = \langle B(t)\rangle_0 - \Omega^2\int_{t_\mathrm{w}}^{t} \mathrm{d}t' g(t') \int_{t_\mathrm{w}}^{t'} \mathrm{d}t'' g(t'')\big\langle B(t)a^\dagger(t')a(t'') + \mathrm{h.c.}\big\rangle_0 . \tag{2.67}$$

If $g(t)$ is properly normalized and has compact support on the interval $[t_\mathrm{w}, t_\mathrm{w}+\delta t]$ with δt sufficiently short as compared to the characteristic time scales of H_0, Eq. (2.67) reduces to Eq. (2.42). However, for longer evolution times $t - t_\mathrm{w}$ that are on the same order or longer than the characteristic time scales of the unperturbed Hamiltonian, it is not possible to approximate the integrand as constant here. Consequently, this procedure does *not* yield the desired two-time anti-commutator in general due to the three-time correlations in the integrand of Eq. (2.67), which appear because the leading perturbative contribution to the response is of quadratic order in the coupling Hamiltonian.

As these discussions show, exploiting the Zeno effect allows us to apply effective non-Hermitian perturbations for an extended period of time according to Eq. (2.65). The essential mechanism is the destruction of the coherences between the Zeno subspaces due to the intermittent measurements. As we will see in the next section, this effect can be mimicked if the ancilla is exposed to strong (engineered) dissipation, which represents an alternative way of realizing non-Hermitian linear response via the quantum Zeno effect.

2.3.3. Non-Hermitian Linear Response via the Continuous Quantum Zeno Effect

Unfortunately, implementing the pulsed Zeno effect without destroying the sample during the intermittent measurements poses a prohibitive layer of complexity for many

experiments. For this reason, we instead exploit the *continuous* Zeno effect in what follows (see Fig. 2.7d). This formulation of the Zeno effect arises in the presence of a strong coupling to an external system, which plays the role of a measurement apparatus and leads to wildly fluctuating phases between the relevant Zeno subspaces [157]. One way of generating such a continuous Zeno effect is by adding engineered classical noise to the system, which has been proposed, e.g., in Ref. [158] to constrain the dynamics of quantum simulators for lattice gauge theories. Here, we apply this idea to realize a time-dependent effective non-Hermitian perturbation.

From engineered dissipation to non-Hermitian dynamics

We consider the ancilla to be subject to classical dephasing noise, as indicated in Fig. 2.7. Such a source of noise can be engineered via a rapidly fluctuating effective detuning, e.g., in form of a Zeeman or AC Stark shift, acting on the ancilla only. We assume that the fluctuations are sufficiently fast compared to all relevant physical time scales, such that their effect can be approximated by a Gaussian white noise process $\xi(t)$ satisfying $\langle\!\langle \xi(t) \rangle\!\rangle = 0$ and $\langle\!\langle \xi(t)\xi(t') \rangle\!\rangle = \delta(t-t')$, where $\langle\!\langle \cdots \rangle\!\rangle$ denotes the ensemble average over all noise realizations. For example, using lasers to generate an AC Stark shift, this technical requirement can be fulfilled using acousto-optical devices [182]. The evolution of the density operator $\rho(t)$ can then be described by the stochastic von Neumann equation [158]

$$\mathrm{d}\rho(t) = -\frac{i}{\hbar}[H(t), \rho(t)]\,\mathrm{d}t - i\sqrt{2\kappa}[b^\dagger b, \rho(t)] \circ \mathrm{d}W(t)\,. \tag{2.68}$$

Here, $\kappa > 0$ is the dephasing rate and $\circ\,\mathrm{d}W(t) = \xi(t)\,\mathrm{d}t$ are Wiener increments, where the circle indicates the use of the Stratonovich interpretation of stochastic calculus [183, 184] (see Appendix A.1). The deterministic part of Eq. (2.68) is governed by the Hamiltonian $H(t) = H_0 + H_{\mathrm{cpl}}(t)$, where the coupling Hamiltonian $H_{\mathrm{cpl}}(t)$ is given by Eq. (2.52).

The Gaussian white noise process $\xi(t)$ can be viewed as the idealization of a smooth physical noise process with finite correlation time, arising, for example, from a rapidly fluctuating electric or magnetic field. As such, it is appropriate to interpret the stochastic von Neumann equation Eq. (2.68) as an SDE in Stratonovich form, which obeys the rules of ordinary calculus [183, 184]. In addition, in the form of Eq. (2.68), unitary evolution of each realization ($\mathrm{d}\,\mathrm{Tr}[\rho(t)]/\,\mathrm{d}t = 0$) is only guaranteed if the Stratonovich interpretation is used [185].

Master equation for the noise-averaged density operator. In order to compute noise-averaged observables, we average the von Neumann equation Eq. (2.68) over all noise realizations. However, in the Stratonovich interpretation, the Wiener increments $\circ\,\mathrm{d}W(t)$ and the stochastic variable $\rho(t)$ are not statistically independent at equal times, i.e., $\langle\!\langle \rho(t) \circ \mathrm{d}W(t) \rangle\!\rangle \neq 0$ in general. It is therefore advantageous to convert Eq. (2.68) to an Itô SDE, where $\langle\!\langle \rho(t)\,\mathrm{d}W(t) \rangle\!\rangle = \langle\!\langle \rho(t) \rangle\!\rangle \langle\!\langle \mathrm{d}W(t) \rangle\!\rangle = 0$ holds since the solution of an Itô SDE is non-anticipating [183, 184]. According to the Itô–Stratonovich

conversion rules (see Appendices A.1 and A.3.3), the linear Stratonovich SDE

$$\mathrm{d}\rho = L_0(t)\rho\,\mathrm{d}t + L_1(t)\rho \circ \mathrm{d}W \tag{2.69}$$

is equivalent to the linear Itô SDE

$$\mathrm{d}\rho = \big[L_0(t) + L_1^2(t)/2\big]\rho\,\mathrm{d}t + L_1(t)\rho\,\mathrm{d}W\,. \tag{2.70}$$

In the case of Eq. (2.68), L_0 and L_1 are given by the Liouvillian superoperators $L_0(t)\rho = -i[H(t),\rho]/\hbar$ and $L_1\rho = -i\sqrt{2\kappa}[b^\dagger b,\rho]$, respectively. Thus Eq. (2.68) is equivalent to the Itô SDE

$$\begin{aligned}\mathrm{d}\rho =& -\frac{i}{\hbar}[H(t),\rho]\,\mathrm{d}t - \kappa\big(\big\{L^\dagger L,\rho\big\} - 2L\rho L^\dagger\big)\,\mathrm{d}t \\ & - i\sqrt{2\kappa}\big[b^\dagger b,\rho\big]\,\mathrm{d}W\end{aligned} \tag{2.71}$$

with $L = b^\dagger b$. Taking the ensemble average of Eq. (2.71), the stochastic term vanishes, and the noise-averaged density operator $\sigma(t) = \langle\!\langle \rho(t) \rangle\!\rangle$ obeys the Lindblad master equation

$$\frac{\mathrm{d}}{\mathrm{d}t}\sigma = -\frac{i}{\hbar}[H(t),\sigma] - \kappa\big(\big\{L^\dagger L,\sigma\big\} - 2L\sigma L^\dagger\big) \tag{2.72}$$

with the Hermitian Lindblad operator $L = b^\dagger b$.

The stochastic von Neumann equation (2.68) represents a diffusive unraveling [186] of the master equation (2.72). Such diffusive unravelings typically arise in the theory of continuous measurements, where a quantum system is continuously monitored and the resulting measurement back action gives rise to diffusive quantum trajectories [187, 188]. By contrast, in our case, there are no actual measurements involved and Eq. (2.68) describes a random unitary evolution with pure dephasing [185, 189]. In fact, there exists an infinite number of stochastic unravelings, both diffusive and jump-like, whose ensemble average is described by the master equation (2.72) [159, 160, 190]. As an alternative to the approach in Eq. (2.68) using engineered dephasing, we could also start from Eq. (2.72) with the Lindblad operator $L = b$, describing a spontaneous decay of particles in the ancilla at a decay rate κ. As shown below, such a setting gives rise to the same effective non-Hermitian Hamiltonian as in the engineered dephasing scenario.

Strong-noise limit and effective non-Hermitian Hamiltonian. The quantum Zeno effect is realized in the strong-noise limit $\kappa \to \infty$ [158]. The strong dissipation leads to an exponential decay of coherences between Zeno subspaces, in analogy to the effect of repeated measurements, and thereby suppresses the build-up of population in the ancilla.

To derive the effective non-Hermitian Hamiltonian governing the time evolution in this regime, following Ref. [158], we consider the strong noise limit of the master equation (2.72) projected on the empty-ancilla subspace. It is convenient to work in the interaction picture, i.e, in a rotating frame with respect to the unperturbed Hamiltonian H_0. Equation (2.72) then reads

$$\frac{\mathrm{d}}{\mathrm{d}t}\tilde{\sigma} = -\frac{i}{\hbar}\big[\tilde{H}_{\mathrm{cpl}}(t),\tilde{\sigma}\big] - \kappa\big(\big\{L^\dagger L,\tilde{\sigma}\big\} - 2L\tilde{\sigma}L^\dagger\big), \tag{2.73}$$

where $\tilde{\sigma}(t) = \mathrm{e}^{iH_0 t/\hbar}\sigma(t)\mathrm{e}^{-iH_0 t/\hbar}$ and $\tilde{H}_{\mathrm{cpl}}(t) = g(t)\hbar\Omega\big[\tilde{a}^\dagger(t)b + b^\dagger\tilde{a}(t)\big]$ with $\tilde{a}(t) = \mathrm{e}^{iH_0 t/\hbar}a\mathrm{e}^{-iH_0 t/\hbar}$. The operators b and $b^\dagger$ as well as the Lindblad operators remain unchanged as they act on the ancilla only and therefore commute with H_0.

We now use the projection operator on the empty-ancilla subspace $P = P_0$ as well as its complement $Q = \mathbb{1} - P$ to derive coupled equations for the populations $\tilde{\sigma}_{PP} = P\tilde{\sigma}P$ and $\tilde{\sigma}_{QQ} = Q\tilde{\sigma}Q$ of the two subspaces, as well as for their coherences $\tilde{\sigma}_{PQ} = P\tilde{\sigma}Q$ and $\tilde{\sigma}_{QP} = Q\tilde{\sigma}P$. The projection operators are Hermitian and satisfy the properties $P^2 = P$, $Q^2 = Q$, $PQ = QP = 0$, as well as $[P, H_0] = [Q, H_0] = 0$, the latter following from the fact that H_0 does not change the number of particles in the ancilla. Furthermore, since P projects on the empty-ancilla subspace, we have $bP = Pb^\dagger = 0$. Applying the projectors P and Q to Eq. (2.73) from the left and from the right yields the coupled system of equations

$$\frac{\mathrm{d}}{\mathrm{d}t}\tilde{\sigma}_{PP} = -\frac{i}{\hbar}\big(\tilde{H}_{PQ}\tilde{\sigma}_{QP} - \tilde{\sigma}_{PQ}\tilde{H}_{QP}\big)\,, \tag{2.74a}$$

$$\frac{\mathrm{d}}{\mathrm{d}t}\tilde{\sigma}_{PQ} = -\frac{i}{\hbar}\big(\tilde{H}_{PQ}\tilde{\sigma}_{QQ} - \tilde{\sigma}_{PP}\tilde{H}_{PQ}\big) + \frac{i}{\hbar}\tilde{\sigma}_{PQ}Q\tilde{H}_{\mathrm{cpl}}Q - \kappa\tilde{\sigma}_{PQ}QL^\dagger LQ\,, \tag{2.74b}$$

$$\frac{\mathrm{d}}{\mathrm{d}t}\tilde{\sigma}_{QP} = -\frac{i}{\hbar}\big(\tilde{H}_{QP}\tilde{\sigma}_{PP} - \tilde{\sigma}_{QQ}\tilde{H}_{QP}\big) - \frac{i}{\hbar}Q\tilde{H}_{\mathrm{cpl}}Q\tilde{\sigma}_{QP} - \kappa QL^\dagger LQ\tilde{\sigma}_{QP}\,, \tag{2.74c}$$

$$\begin{aligned}\frac{\mathrm{d}}{\mathrm{d}t}\tilde{\sigma}_{QQ} = &-\frac{i}{\hbar}\big(\tilde{H}_{QP}\tilde{\sigma}_{PQ} - \tilde{\sigma}_{QP}\tilde{H}_{PQ}\big) - \frac{i}{\hbar}\big[Q\tilde{H}_{\mathrm{cpl}}Q, \tilde{\sigma}_{QQ}\big] \\ &- \kappa Q\big(\big\{L^\dagger L, \tilde{\sigma}_{QQ}\big\} - 2L\tilde{\sigma}_{QQ}L^\dagger\big)Q\,,\end{aligned} \tag{2.74d}$$

where the operators $\tilde{H}_{PQ}(t) = g(t)\hbar\Omega P\tilde{a}^\dagger(t)bQ$ and $\tilde{H}_{QP}(t) = g(t)\hbar\Omega Qb^\dagger\tilde{a}(t)P$ mix the two subspaces. In deriving Eq. (2.73), we have considered the engineered dephasing scenario described by the stochastic von Neumann equation (2.68), in which case the Lindblad operator $L = b^\dagger b$ is Hermitian and the projectors commute with L. In the alternative setting, where the ancilla is subject to spontaneous decay, the Lindblad operator is given by $L = b$ and does not commute with the projectors. In this case, Eqs. (2.74a) to (2.74c) receive an additional contribution from the "recycling terms" $2\kappa b\tilde{\sigma}_{QQ}b^\dagger$, whose effect is to incoherently remove particles from the ancilla. Since these terms are proportional to $\tilde{\sigma}_{QQ}$, which is initially zero and whose growth is suppressed by the Zeno effect, their presence does not change the following line of arguments. Nonetheless, it is possible to get rid of these terms completely by keeping track of all the modes the ancilla decays to and post-selecting on the condition that the ancilla plus these additional modes are empty. To see this, we can assume that the ancilla decays only to a single mode with associated annihilation and creation operators c and $c^\dagger$. The corresponding Lindblad operator $L = c^\dagger b$ now conserves the number of particles in the ancilla plus the extra mode. Consequently, the contribution from the "recycling terms" to Eqs. (2.74a) to (2.74c) vanishes due to the action of the projector P.

We now consider the strong noise limit of Eq. (2.74). The terms on the right-hand side of the equations for the coherences (2.74b) and (2.74c) rotate at characteristic frequencies of the unperturbed Hamiltonian H_0 via $\tilde{a}(t) = \mathrm{e}^{iH_0 t/\hbar}a\mathrm{e}^{-iH_0 t/\hbar}$ as well as via the modulation function $g(t)$, whose role is to probe dynamic correlations in the system

at a given frequency. In contrast, the terms proportional to the dissipation rate κ cause a damping of the coherences. If κ is sufficiently large, in particular, if it is much larger than the characteristic frequencies of H_0, we can make the approximation that the coherences are instantaneously damped to a momentary equilibrium state given by $\mathrm{d}\tilde{\sigma}_{PQ}/\,\mathrm{d}t \approx 0$ (and analogously for $\tilde{\sigma}_{QP}$). This allows us to adiabatically eliminate the fast incoherent dynamics and to solve Eqs. (2.74b) and (2.74c) for the coherences. To leading order in Ω/κ, we find

$$\tilde{\sigma}_{PQ} = -\frac{i}{\hbar\kappa}\big(\tilde{H}_{PQ}\tilde{\sigma}_{QQ} - \tilde{\sigma}_{PP}\tilde{H}_{PQ}\big)(QL^\dagger LQ)^{-1}\,, \tag{2.75a}$$

$$\tilde{\sigma}_{QP} = -\frac{i}{\hbar\kappa}(QL^\dagger LQ)^{-1}\big(\tilde{H}_{QP}\tilde{\sigma}_{PP} - \tilde{\sigma}_{QQ}\tilde{H}_{QP}\big)\,, \tag{2.75b}$$

where $(\cdots)^{-1}$ denotes the Moore–Penrose pseudoinverse. To leading order in Ω/κ, we can furthermore neglect the terms proportional to $\tilde{\sigma}_{QQ}$, which is initially zero and grows, according to Eqs. (2.74d) and (2.75), only slowly at a rate Ω^2/κ. This suppression of the growth of population in the ancilla is precisely a manifestation of the Zeno effect. Thus, plugging Eq. (2.75) into Eq. (2.74a), we obtain

$$\frac{\mathrm{d}}{\mathrm{d}t}\tilde{\sigma}_{PP} = -\frac{i}{\hbar}\big\{\tilde{H}_{\mathrm{eff}}(t), \tilde{\sigma}_{PP}\big\} \tag{2.76}$$

with the effective non-Hermitian Hamiltonian

$$\tilde{H}_{\mathrm{eff}}(t) = -ig^2(t)\frac{\hbar\Omega^2}{\kappa}P\tilde{a}^\dagger(t)b(QL^\dagger LQ)^{-1}b^\dagger\tilde{a}(t)P\,. \tag{2.77}$$

Due to the action of the projector P in this expression, the pseudoinverse acts only on states with exactly one particle in the ancilla, where it reduces to a multiplication by unity. Thus, the effective non-Hermitian Hamiltonian takes the simple form $\tilde{H}_{\mathrm{eff}}(t) = -ig^2(t)\hbar\Omega^2 P\tilde{a}^\dagger(t)\tilde{a}(t)P/\kappa$. Finally, after transforming back to the non-rotating frame, we arrive at the evolution equation

$$i\hbar\frac{\mathrm{d}}{\mathrm{d}t}\sigma_{PP} = H_{\mathrm{eff}}(t)\sigma_{PP} - \sigma_{PP}H_{\mathrm{eff}}^\dagger(t)\,, \tag{2.78}$$

generated by the effective non-Hermitian Hamiltonian $H_{\mathrm{eff}}(t) = H_0 - if(t)A$ with $A = a^\dagger a$ and $f(t) = g^2(t)\hbar\Omega^2/\kappa$. As required in Section 2.1, the perturbation operator A is positive semi-definite and $f(t)$ is non-negative, describing a leakage of probability out of the empty-ancilla subspace. Figure 2.7d illustrates that this effective non-Hermitian dynamics arises as the ensemble average over stochastic trajectories governed by the stochastic von Neumann equation (2.68). The crucial advantage of the continuous Zeno effect over the pulsed formulation, where repeated non-destructive measurements are required, is that a single projection at the final measurement time is sufficient, which can conveniently be realized as a post-selection on measurement outcomes where no particles are detected in the ancilla.

Numerical Benchmark: Non-Hermitian Linear Response in Frequency Domain

We now demonstrate how the above scheme enables access to the FDR directly in frequency domain. From the structure of the general linear response formula (1.56) it becomes clear that by applying a non-Hermitian perturbation under a suitable periodic modulation $f(t)$ continuously until the final observation time t_f, it is possible to directly measure non-Hermitian dynamic susceptibilities at fixed final time t_f defined in Eq. (2.24).

It is our goal to extract the reactive suceptibility component $\chi'^{(\mathrm{NH})}(t_\mathrm{f},\omega)$ from the linear response to the effective non-Hermitian Hamiltonian in Eq. (2.78). For simplicity, we focus on the common case where $\chi'^{(\mathrm{NH})}$ corresponds to the real part of the susceptibility (2.24), and we consider Hermitian operators A and B such that the response function (2.8) is real. Due to the non-negativity constraint on $f(t)$, it is not possible to modulate the effective coupling around zero. Instead, we choose the modulation in Eq. (2.68) as $g(t) = \sqrt{2}\cos[\omega(t_\mathrm{f}-t)/2]$, for a fixed final observation time t_f, such that $f(t) = [1+\cos\omega(t_\mathrm{f}-t)]\hbar\Omega^2/\kappa$. According to Eq. (2.7), the response is then given by

$$\langle B(t_\mathrm{f})\rangle_P = \langle B(t_\mathrm{f})\rangle_0 + \frac{\hbar\Omega^2}{\kappa}\int_0^{t_\mathrm{f}} \mathrm{d}t\, \phi_{BA}^{(\mathrm{NH})}(t_\mathrm{f},t) + \frac{\hbar\Omega^2}{\kappa}\int_0^{t_\mathrm{f}} \mathrm{d}t\, \phi_{BA}^{(\mathrm{NH})}(t_\mathrm{f},t)\cos[\omega(t_\mathrm{f}-t)]\,, \tag{2.79}$$

where $\langle B(t_\mathrm{f})\rangle_P = \mathrm{Tr}[B\sigma_{PP}(t_\mathrm{f})]/\,\mathrm{Tr}[\sigma_{PP}(t_\mathrm{f})]$ is the conditional expectation value obtained from post-selection. The first two terms on the right-hand side of Eq. (2.79) represent the response to a static non-Hermitian perturbation with $g(t)\equiv 1$ and the last term is proportional to the desired real part of the susceptibility (2.24), which can be seen after changing the integration variable to $\Delta t = t_\mathrm{f} - t$. Thus, it is possible to extract the quantity $\chi_{BA}'^{(\mathrm{NH})}(t_\mathrm{f},\omega)$ for a given probe frequency ω from two linear response measurements, one with a periodic modulation and one with a constant perturbation, the latter being subtracted from the former.

To benchmark to above protocol, we resort to the previous example of the density autocorrelation spectrum $S_{BA}(\omega) = -\hbar\chi_{BA}'^{(\mathrm{NH})}(\omega)$ ($B=A=n$) of a thermal state in a periodic 1D Bose–Hubbard chain. For this purpose, we numerically solve the stochastic von Neumann equation (2.68) — the most fundamental equation in our approach — using the stochastic Magnus scheme presented in Appendix A.3.3. By comparing the results of the stochastic simulation to those obtained based on Eqs. (2.72) and (2.78), we demonstrate the validity of the approximations underlying the effective description in terms of a non-Hermitian Hamiltonian. To account for the different sensitivities of the responses at different probe frequencies, we parametrize the perturbation strength in terms of the norm decay q due to the effective non-Hermitian Hamiltonian. That is, for each frequency ω, given a fixed final observation time t_f and dephasing rate κ, we adjust the coupling strength Ω such that according to Eq. (2.6) the norm of the state has decreased by the amount q at the end of the evolution. For a translationally invariant system at unit filling, we have $\langle A(t)\rangle_0 = \langle n(t)\rangle_0 = 1$, and therefore $\Omega = [\kappa q/2t_\mathrm{f}(1+\mathrm{sinc}(\omega t_\mathrm{f}/\pi))]^{1/2}$, where $\mathrm{sinc}(x) = \sin(\pi x)/\pi x$.

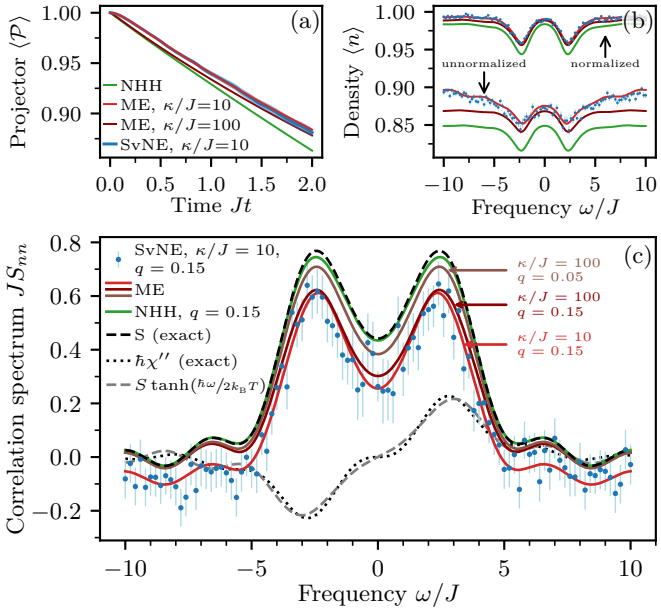

Figure 2.9.: Simulation of the non-Hermitian linear response scheme for measuring the density autocorrelation spectrum in frequency domain. The effective non-Hermitian perturbation is generated through coupling to an ancilla subject to strong engineered dephasing, exploiting the continuous quantum Zeno effect. The simulations are based on the stochastic von Neumann equation (2.68) (SvNE), the master equation (2.72) (ME), and the effective non-Hermitian Hamiltonian (2.78) (NHH). The stochastic simulation has been averaged over 200 realizations, and the error bars show the ensemble standard deviation of the mean. (a) Decrease of the norm resulting from the projection on the empty-ancilla subspace as a function of time for the probe frequency $\omega = 0$ and norm decay $q = 0.15$. A stronger dephasing rate κ improves the agreement between the ME (SvNE) and NHH descriptions at early times, while the deviations at later times are due to non-linear effects. (b) Unnormalized and normalized (conditional) responses, corresponding to Eqs. (2.5) and (2.79), respectively, as a function of frequency for a fixed final time $Jt_\mathrm{f} = 2$ and norm decay $q = 0.15$. (c) Correlation spectra S_{nn} extracted from the responses in (b) according to Eq. (2.79), in comparison with the exact result and the FDR (1.83) between S and χ''. The different combinations of the parameters κ and q for the ME simulation show that the agreement with the exact result can be improved by going deeper into the limit of strong dissipation and weak perturbations.

In Fig. 2.9, we compare various simulations of the scheme based on Eqs. (2.68), (2.72) and (2.78) for a system of $L = 4$ lattice sites. Figure 2.9a illustrates a typical decay of the norm over time due to the effective non-Hermitian perturbation. The simulated unnormalized and normalized (conditional) responses as a function of frequency are shown in Fig. 2.9b, from which we have extracted the correlation spectra presented in Fig. 2.9c along with a comparison to the exact results. The evolution has been computed up to the final time $Jt_\mathrm{f} = 2$, truncating[7] the Fourier integral in Eq. (2.79), which for

[7]Continuing the evolution to longer times, the spectrum attains more structure, but the validity of the FDR is only marginally affected by the chosen truncation.

our small system does not converge due to revivals. For the stochastic simulation, we have chosen accessible parameters corresponding to a relatively moderate dephasing of strength $\kappa/J = 10$ and a norm decay $q = 0.15$ that results in a good signal-to-noise ratio, but lies slightly beyond the onset of the non-linear regime. As can be seen in Fig. 2.9, the stochastic simulation based on Eq. (2.68) agrees with the simulation based on the master equation (2.72) within the statistical error bars, showing the ensemble standard deviation of the mean for an accessible number of 200 realizations. Moreover, Fig. 2.9c shows that these parameters already yield the correlation spectrum at a reasonable accuracy suitable for certifying the validity of the FDR (1.83). The description in terms of the effective non-Hermitian Hamiltonian in Eq. (2.78) is closer to the exact result than the description in terms of the master equation (2.72) for the same parameters, revealing that the linear regime is wider for the former than for the latter, which could be remedied through extrapolation. In the effective non-Hermitian description (2.78), the coupling strength Ω and the dephasing rate κ enter only via the ratio Ω^2/κ, which is proportional to the norm decay q, while these two parameters enter Eqs. (2.68) and (2.72) individually. Going deeper into the Zeno limit of large κ improves the validity of Eq. (2.78) at early times and at larger frequencies, shown in Fig. 2.9 for $\kappa/J = 100$. Decreasing at the same time the effective coupling strength, as illustrated in Fig. 2.9 for $q = 0.05$, the agreement between the extracted correlation spectrum and the exact result improves further, which shows that, at the cost of decreasing the signal-to-noise ratio, the exact correlation spectrum can in principle be approximated to arbitrary accuracy.

2.4. Comparison to Other Schemes

In this section, we put the above non-Hermitian linear response approach for measuring dynamical correlations and FDRs in perspective with other schemes. We first demonstrate that common ancilla-based weak measurement protocols [131, 132] fit into this general framework since their ancilla-free formulations can be interpreted as a non-Hermitian linear response. In addition, we compare the ancilla-based technique for realizing non-Hermitian linear response presented in Section 2.3 with other schemes for accessing non-Hermitian dynamics or measuring dynamical correlations, including non-invasive and projective protocols [24, 129, 131–133].

2.4.1. Ancilla-Based Weak Measurements

Ancilla-based weak measurement schemes for dynamical correlations can be adapted to probe either the unequal-time commutator or anti-commutator through a suitable choice of the ancilla state, the system–ancilla coupling, and the projective measurement performed on the ancilla [131, 132]. It has been shown that those variants that probe the unequal-time commutator can be cast into an ancilla-free formulation [132], giving rise, e.g., to rotation-based protocols [24, 129, 131–133]. For weak perturbations, e.g., small rotation angles, these ancilla-free schemes correspond in fact to (standard) linear response. By contrast, the interpretation of ancilla-based weak measurement protocols that target the unequal-time anti-commutator is far less obvious. For instance, Ref. [132]

poses the question whether an ancilla-free measurement of this quantity is possible in general. Here, we show that, indeed, any ancilla-based weak measurement protocol for the unequal-time anti-commutator can be described in an ancilla-free way as a non-Hermitian linear response, exposing the close connection between these frameworks.

General relation between non-Hermitian linear response and ancilla-based weak measurements

We consider a general ancilla-based weak measurement that uses only projective measurements of standard (Hermitian) operators on the ancilla. The following derivation proceeds in analogy to the one for spin systems presented in Refs. [131, 132], but here we consider a more general scenario: we do not specify the type of system, work with general mixed states, and consider arbitrary durations of the system–ancilla coupling. Let us denote the initial state of system and ancilla by ρ_{S} and ρ_{A}, respectively, and assume the combined system to be in a product state initially, $\rho_0 = \rho_{\mathrm{S}} \otimes \rho_{\mathrm{A}}$. The target system evolves under the Hamiltonian H_0, while we assume the ancilla to have no internal dynamics. System and ancilla are coupled via the general coupling Hamiltonian

$$H_{\mathrm{cpl}}(t) = f(t) A \otimes X \tag{2.80}$$

with a time-dependent function $f(t)$ and Hermitian operators A and X acting on system and ancilla, respectively. The total Hamiltonian of the combined system then reads $H(t) = H_0 \otimes \mathbb{1} + H_{\mathrm{cpl}}(t)$. It is convenient to work in the interaction picture, $\tilde{\rho}(t) = \mathrm{e}^{iH_0 t/\hbar} \rho(t) \mathrm{e}^{-iH_0 t/\hbar}$. The von Neumann equation

$$i\hbar \frac{\mathrm{d}}{\mathrm{d}t} \tilde{\rho}(t) = \left[\tilde{H}_{\mathrm{cpl}}(t), \tilde{\rho}(t) \right] \tag{2.81}$$

can equivalently be expressed in integral form as

$$\tilde{\rho}(t) = \tilde{\rho}(0) - \frac{i}{\hbar} \int_0^t \mathrm{d}t' \left[\tilde{H}_{\mathrm{cpl}}(t'), \tilde{\rho}(t') \right] \simeq \tilde{\rho}(0) - \frac{i}{\hbar} \int_0^t \mathrm{d}t' \left[\tilde{H}_{\mathrm{cpl}}(t'), \tilde{\rho}(0) \right], \tag{2.82}$$

where $\tilde{H}_{\mathrm{cpl}}(t) = f(t) \tilde{A}(t) \otimes X$ is the interaction-picture coupling Hamiltonian with $\tilde{A}(t) = \mathrm{e}^{iH_0 t/\hbar} A \mathrm{e}^{-iH_0 t/\hbar}$. In the last line, we have assumed the coupling to be sufficiently weak such that we can replace $\tilde{\rho}(t')$ in the integral, to linear order in H_{cpl}, by $\tilde{\rho}(0)$. Note that the validity of this linear approximation is not necessarily restricted to short times t, but can also be ensured for longer times by a sufficiently weak coupling strength $f(t)$.

After a coupled evolution up to time t, during which system and ancilla become entangled, we measure projectively the observable $B \otimes Y$, where B and Y are Hermitian operators acting on system and ancilla, respectively, and post-select on the outcome of the ancilla measurement. Although in practice system and ancilla are often measured simultaneously, it is instructive to treat this process as a consecutive measurement of the ancilla first and the system second. Without loss of generality, we assume the observable Y to have a discrete spectrum of (real) eigenvalues $\{y\}$. Let P_y denote the

projector on the eigenspace of the eigenvalue y. After obtaining this outcome, according to Lüders' rule [179], the state collapses to

$$\tilde{\rho}_y(t) = \frac{1}{p(y)} P_y \tilde{\rho}(t) P_y \,, \tag{2.83}$$

where $p(y) = \mathrm{Tr}\big[P_y \tilde{\rho}(t) P_y\big]$ is the probability of measuring the outcome y. For the coupling Hamiltonian (2.80), the unnormalized post-measurement state reads

$$P_y \tilde{\rho}(t) P_y = \rho_\mathrm{S} \otimes P_y \rho_\mathrm{A} P_y - \frac{i}{\hbar} \int_0^t \mathrm{d}t' \, f(t') \big[\tilde{A}(t') \rho_\mathrm{S} \otimes P_y X \rho_\mathrm{A} P_y - \mathrm{h.c.} \big] \,, \tag{2.84}$$

where h.c. denotes the Hermitian conjugate, while the probability of measuring y becomes

$$p(y) = \big\langle P_y \big\rangle_0 - i \int_0^t \mathrm{d}t' f(t') \langle A(t') \rangle_0 \big[\big\langle P_y X \big\rangle_0 - \big\langle X P_y \big\rangle_0 \big]. \tag{2.85}$$

Here, $\langle O(t) \rangle_0$ denotes the expectation value of the Heisenberg operator $O(t)$, evolving under the unperturbed Hamiltonian H_0, with respect to the initial state $\rho_0 = \rho_\mathrm{S} \otimes \rho_\mathrm{A}$. Note that expectation values involving only ancilla operators are time-independent since we assumed the ancilla to have no internal dynamics. Using $(1+x)^{-1} = 1 - x + \mathcal{O}(x^2)$, we obtain the normalized, conditional post-measurement state, to linear order in the coupling, as

$$\tilde{\rho}_y(t) = \rho_\mathrm{S} \otimes \frac{P_y \rho_\mathrm{A} P_y}{\big\langle P_y \big\rangle_0} - \frac{i}{\hbar} \int_0^t \mathrm{d}t' \, f(t') \left\{ \left[\tilde{A}(t') \rho_\mathrm{S} \otimes \frac{P_y X \rho_\mathrm{A} P_y}{\big\langle P_y \big\rangle_0} - \langle A(t') \rangle_0 \frac{\big\langle P_y X \big\rangle_0}{\big\langle P_y \big\rangle_0} \right] - \mathrm{h.c.} \right\}. \tag{2.86}$$

Next, we are interested in the conditional expectation value of the system observable B, given that the measurement of Y on the ancilla yields the outcome y. In a first step, we trace out the ancilla,

$$\mathrm{Tr}_\mathrm{A}\big[\tilde{\rho}_y(t)\big] = \rho_\mathrm{S} - \frac{i}{\hbar} \int_0^t \mathrm{d}t' \, f(t') \left\{ \frac{\big\langle P_y X \big\rangle_0}{\big\langle P_y \big\rangle_0} \big[\tilde{A}(t') - \langle A(t') \rangle_0 \big] \rho_\mathrm{S} - \mathrm{h.c.} \right\}. \tag{2.87}$$

This yields the conditional expectation value

$$\begin{aligned} \big\langle B(t) \big\rangle_y &= \mathrm{Tr}\big[\tilde{B}(t) \tilde{\rho}_y(t) \big] \\ &= \langle B(t) \rangle_0 - \frac{i}{\hbar} \int_0^t \mathrm{d}t' f(t') \left\{ \frac{\big\langle P_y X \big\rangle_0}{\big\langle P_y \big\rangle_0} \big[\langle B(t) A(t') \rangle_0 - \langle B(t) \rangle_0 \langle A(t') \rangle_0 \big] - \mathrm{c.c.} \right\}, \end{aligned} \tag{2.88}$$

where c.c. denotes the complex conjugate. With this result at hand, we can choose the ancilla state ρ_A as well as the ancilla operators X and Y such that the integrand contains either the unequal-time commutator or the anti-commutator of the system observables A and B.

Relation to standard linear response: two-time commutator. If $\langle P_y X\rangle_0 = \mathrm{Tr}[P_y X \rho_\mathrm{A}]$ is real, i.e., $\langle P_y X\rangle_0/\langle P_y\rangle_0 = -s$ with $s \in \mathbb{R}$, Eq. (2.88) gives access to the unequal-time commutator,

$$\langle B(t)\rangle_y = \langle B(t)\rangle_0 + \frac{i}{\hbar} s \int_0^t \mathrm{d}t' f(t') \langle [B(t), A(t')]\rangle_0 \,. \tag{2.89}$$

This expression coincides with Kubo's linear response formula [cf. Eqs. (1.56) and (1.57)] up to a constant factor in the response function. There are two special cases worth discussing. First, if $X = \mathbb{1}$, $\langle P_y X\rangle_0 = \langle P_y\rangle$ is always real and the scheme always yields the unequal-time commutator. This is not surprising: for $X = \mathbb{1}$, system and ancilla always remain in a product state and the coupling Hamiltonian (2.80) corresponds to a Hermitian perturbation on the target system only, which is exactly the linear response scenario. Second, it is instructive to consider the unconditional expectation value $\langle B(t)\rangle = \sum_y \langle B(t)\rangle_y p(y)$, which corresponds to not measuring the ancilla at all or disregarding the outcome of the ancilla measurement. By combining Eqs. (2.85) and (2.88), and using the completeness relation $\sum_y P_y = \mathbb{1}$, we find, to linear order,

$$\langle B(t)\rangle = \langle B(t)\rangle_0 - \frac{i}{\hbar} \langle X\rangle_0 \int_0^t \mathrm{d}t' f(t') \langle [B(t), A(t')]\rangle_0 \,, \tag{2.90}$$

which again always yields the unequal-time commutator. These two examples illustrate two essential ingredients for extracting the unequal-time anti-commutator from ancilla-based weak measurements: one in hand, the coupling must entangle system and ancilla, and second in hand, it is necessary to correlate the measurement on the target system in some way with the outcome of the ancilla measurement, e.g., through post-selection.

Relation to non-Hermitian linear response: two-time anti-commutator. In order to extract the unequal-time anti-commutator from Eq. (2.88), $\langle P_y X\rangle_0$ must be purely imaginary, i.e., $\langle P_y X\rangle_0/\langle P_y\rangle_0 = -is$ with $s \in \mathbb{R}$, yielding

$$\langle B(t)\rangle_y = \langle B(t)\rangle_0 - \frac{1}{\hbar} s \int_0^t \mathrm{d}t' f(t') \big[\langle \{B(t), A(t')\}\rangle_0 - 2\langle B(t)\rangle_0 \langle A(t')\rangle_0\big] \,. \tag{2.91}$$

This expression corresponds, up to a constant factor in the response function, directly to the non-Hermitian linear response scenario in Eqs. (2.7) and (2.8).

Equations (2.89) and (2.91) demonstrate the fact that any ancilla-based weak measurement designed to probe the (anti-)commutator can effectively be described as a (non-)Hermitian linear response. To make this connection even more explicit, we trace out the ancilla in the unnormalized post-measurement state (2.84),

$$\mathrm{Tr}_\mathrm{A}\big[P_y \tilde{\rho}(t) P_y\big] = \big\langle P_y \big\rangle_0 \rho_\mathrm{S} - \frac{i}{\hbar} \int_0^t \mathrm{d}t' f(t') \big[\big\langle P_y X\big\rangle_0 \tilde{A}(t') \rho_\mathrm{S} - \mathrm{h.c.}\big] \,. \tag{2.92}$$

In analogy to Ref. [132], to linear order, this result can be re-written in terms of generalized measurement (or Kraus) operators [3, 188] as

$$\mathrm{Tr}_\mathrm{A}\big[P_y \tilde{\rho}(t) P_y\big] = M_y \rho_\mathrm{S} M_y^\dagger \tag{2.93}$$

with

$$M_y = \sqrt{\langle P_y \rangle_0} \exp\left\{ -\frac{i}{\hbar} \frac{\langle P_y X \rangle_0}{\langle P_y \rangle_0} \int_0^t \mathrm{d}t' \, f(t') \tilde{A}(t') \right\}. \tag{2.94}$$

It is easy to verify that, to linear order, these operators fulfill the completeness relation $\sum_y M_y^\dagger M_y = \mathbb{1}$. The measurement operator M_y describes the effect of the system–ancilla coupling, conditioned on the outcome y of the ancilla measurement, without explicitly referencing the ancilla. This ancilla-free description corresponds to the evolution under the effective Hamiltonian $H_{\mathrm{eff}}(t) = H_0 + H_1(t)$ with

$$H_1(t) = \frac{\langle P_y X \rangle_0}{\langle P_y \rangle_0} f(t) A. \tag{2.95}$$

For real $\langle P_y X \rangle$, this evolution is unitary [132] and corresponds to standard (Hermitian) linear response, giving access to the unequal-time commutator. Remarkably, the case of purely imaginary $\langle P_y X \rangle$, which according to Eq. (2.91) probes the unequal-time anti-commutator, corresponds to an anti-Hermitian perturbation and maps directly to the non-Hermitian linear response scenario described in Section 2.1. This shows that for any ancilla-based weak measurement of dynamical correlations there is a corresponding ancilla-free linear response description.

Conversely, any linear response protocol can, at least in principle, be realized via an ancilla-based weak measurement. While obvious for standard (Hermitian) linear response, in the non-Hermitian case, the challenge is to choose the ancilla state as well as the ancilla operators X and Y appropriately such that $\langle P_y X \rangle \in i\mathbb{R}$. To see that this is always possible in general, let Y be any Hermitian operator on a (complex) Hilbert space of dimension two or higher with at least two distinct eigenvalues y_1 and y_2. Then, take the ancilla state to be the equal superposition of the corresponding eigenstates, $|\phi\rangle = (|y_1\rangle + |y_2\rangle)/\sqrt{2}$, with $\rho_{\mathrm{A}} = |\phi\rangle\langle\phi|$. Now, let $P_y = P_{y_1}$ be the projector on the eigenspace with eigenvalue y_1 and set $X = -i(|y_1\rangle\langle y_2| - |y_2\rangle\langle y_1|)$. Then, we have $\langle P_y X \rangle_0 / \langle P_y \rangle_0 = -i$, as desired.

Clearly, for a given anti-Hermitian perturbation, the choice of ρ_{A}, X, and Y is not unique, and the challenge consists in finding the configuration that is most convenient for the desired application. Appropriate choices for spin systems have been discussed, for instance, in Refs. [131, 132], but their experimental realization on other platforms, e.g., bosons in optical lattices, is unfortunately not straightforward. To illustrate this, assume we are interested in perturbations by the density operator $A = n$ and consider the above scenario of achieving purely imaginary $\langle P_y X \rangle_0$ for a bosonic ancilla, which translates to $Y = b^\dagger b$ (measurement of the occupancy), $X = -i(b - b^\dagger)$, and $|\phi\rangle = (|0\rangle + |1\rangle)/\sqrt{2}$. However, neither the superposition of Fock states $|\phi\rangle$ nor the coupling Hamiltonian $H_{\mathrm{cpl}} \propto n \otimes X$, which would be cubic in boson operators, can be realized with massive, non-relativistic particles. More generally, in order to probe unequal-time anti-commutators involving the density $A = n$ through a particle number measurement $Y = b^\dagger b$ on a bosonic ancilla, the operator X cannot be diagonal in the Fock basis, as this would imply $\langle P_y X \rangle \in \mathbb{R}$, regardless of the ancilla state. In other words, a particle number

non-conserving coupling Hamiltonian would be required in such a setting. In the scheme presented in Section 2.3, this difficulty does not arise because the leading contribution to the response is quadratic in the coupling Hamiltonian, which enables non-Hermitian perturbations for a wide range of observables including densities and correlators with experimentally feasible system–ancilla couplings.

The general connection between non-Hermitian linear response and ancilla-based weak measurements is beneficial for both disciplines: particular observables previously only accessible via ancilla-based schemes may be obtainable more efficiently in an ancilla-free way using the tools of non-Hermitian physics, while certain non-Hermitian Hamiltonians difficult to engineer directly may be realized with the help of an ancilla.

Differences Between Ancilla-Based Weak Measurements and Non-Hermitian Linear Response via the Quantum Zeno Effect

One of the main challenges of the ancilla-based weak measurement scheme for the unequal-time anti-commutator discussed above is to engineer the ancilla state as well as the observables X and Y in such a way that $\langle P_y X \rangle_0$ becomes purely imaginary. While Refs. [131, 132] discuss suitable configurations for spin systems, it is far less obvious how to choose the setup in an experimentally feasible way on other platforms such as bosons in optical lattices, as discussed above.

By contrast, the scheme based on the Zeno effect in Section 2.3 relies on the system–ancilla coupling in Eq. (2.31), which is quadratic in the creation and annihilation operators. Despite its simple form, the coupling can flexibly be adapted to measure the unequal-time anti-commutator of a wide range of previously inaccessible observables such as nearest-neighbor correlators, as discussed in Section 2.3.1. In addition, for the protocol in Section 2.3, the choice of the initial ancilla state in form of the vacuum is particularly easy to prepare experimentally. On the formal level, an important difference to the common weak measurement approach is that the coupling Hamiltonian (2.31) for the Zeno-based scheme, the linear order in perturbation theory vanishes and the leading contribution to the response stems from the quadratic order (see Section 2.3.1), where the anti-commutator naturally arises and can be isolated by post-selection on realizations without any particles in the ancilla.

2.4.2. Projective Protocols

Projective protocols allow one to probe dynamical correlations of dichotomic observables (observables with two eigenvalues) by performing consecutive projective measurements directly on the system and correlating the outcomes in a suitable way [24, 129, 131–133]. As such, compared to schemes based on weak perturbations such as linear response, projective protocols are backaction-free and feature a higher signal-to-noise ratio. Despite these advantages, the fact that projective protocols work only for dichotomic observables restricts their general applicability.

In Ref. [24], it has been analyzed how projective protocols can be applied to approximately dichotomic observables, in particular densities in Bose–Hubbard systems close

to the hard-core limit. In what follows, we assess to what extent projective protocols represent a good alternative for measuring unequal-time anti-commutators of observables that are not strictly dichotomic. To this end, we first formulate the protocol for general observables A and B, where A has precisely two eigenvalues. We then investigate with the help of numerical benchmarks at the example of the Bose–Hubbard model how well the scheme reproduces the exact density autocorrelation spectrum in comparison to non-Hermitian linear response as a function of both the filling and the on-site interaction.

General Projective Protocol

We begin by briefly reviewing the projective protocol for measuring unequal-time anti-commutators [24, 129, 131–133]. Here, we formulate the scheme for a general Hermitian operator A with two distinct eigenvalues $a_1, a_2 \in \mathbb{R}$. Let P_1 and P_2 be the projection operators on the corresponding eigenspaces such that $A = a_1 P_1 + a_2 P_2$ with $P_1 + P_2 = \mathbb{1}$. This allows us to express both projectors entirely through the operator A and the known eigenvalues,

$$P_1 = \frac{1}{a_1 - a_2}(A - a_2 \mathbb{1})\,, \tag{2.96a}$$

$$P_2 = \frac{1}{a_2 - a_1}(A - a_1 \mathbb{1})\,, \tag{2.96b}$$

which would not be possible if A had more than two eigenvalues. The protocol starts by evolving the initial state ρ_0 (under the target Hamiltonian H_0) to the waiting time t_w. Then, the observable A is measured projectively and the state is conditioned on the outcome a_1 or a_2 of this measurement, yielding the conditional post-measurement states

$$\rho(t_\mathrm{w} \mid a_i) = \frac{1}{p(a_i)} P_i \rho(t_\mathrm{w}) P_i \tag{2.97}$$

with $i \in \{1, 2\}$, where $p(a_i) = \mathrm{Tr}[P_i \rho(t_\mathrm{w}) P_i]$ is the probability of obtaining the measurement outcome a_i at time t_w. Subsequently, the conditional state is evolved to the final observation time $t \geq t_\mathrm{w}$. The conditional expectation values of an observable B then reads

$$\langle B(t) \rangle_{a_i} = \mathrm{Tr}[B \rho(t \mid a_i, t_\mathrm{w})] = \frac{\big\langle A(t_\mathrm{w}) B(t) A(t_\mathrm{w}) - a_j \{B(t), A(t_\mathrm{w})\} + a_j^2 B(t) \big\rangle}{p(a_i)(a_i - a_j)^2}\,, \tag{2.98}$$

with $(i, j) \in \{(1, 2), (2, 1)\}$, where we have switched to the Heisenberg picture. Solving for the unequal-time anti-commutator, we obtain

$$\langle \{B(t), A(t_\mathrm{w})\} \rangle = \langle B(t) \rangle (a_1 + a_2) + \Big[\langle B(t) \rangle_{a_1} p(a_1) - \langle B(t) \rangle_{a_2} p(a_2) \Big] (a_1 - a_2)\,. \tag{2.99}$$

The probabilities $p(a_i)$ can be expressed through the expectation value $\langle A(t_\mathrm{w}) \rangle$ with the help of Eq. (2.96), yielding

$$\langle \{B(t), A(t_\mathrm{w})\} \rangle = \langle B(t) \rangle_{a_1} [\langle A(t_\mathrm{w}) \rangle - a_2] + \langle B(t) \rangle_{a_2} [\langle A(t_\mathrm{w}) \rangle - a_1] + \langle B(t) \rangle (a_1 + a_2)\,. \tag{2.100}$$

This result states that the desired unequal-time anti-commutator of A and B can be extracted from a measurement of the unconditional expectation value $\langle B(t)\rangle$ (without previous projective measurement) as well as the conditional expectation values $\langle B(t)\rangle_{a_1}$ and $\langle B(t)\rangle_{a_2}$, given that the outcomes a_1 and a_2 have been obtained from the projective measurement of A at the waiting time t_w, respectively.

A few remarks are in order. The projective measurement of A at time t_w can be deferred up to the final observation time t with the help of an ancilla using shelving techniques [24]. This way, the need for non-destructive measurements can be avoided. Furthermore, it is worth emphasizing that there is no restriction on the number of eigenvalues of the operator B, i.e., the dichotomic constraint applies only to A.

Numerical Benchmark: Projective Protocols Versus Non-Hermitian Linear Response

We now specialize the projective protocol in Eq. (2.100) to density correlations in a Bose–Hubbard system. In the hard-core limit $U/J \to \infty$, multiple occupancies of the same lattice site are prohibited. The density n_ℓ at site ℓ then becomes a dichotomic observable with only two eigenvalues 0 and 1. We thus recover the protocol reported in Ref. [24],

$$\Big\langle \Big\{ n_{\ell_2}(t), n_{\ell_1}(t_\mathrm{w}) \Big\} \Big\rangle = \Big\langle n_{\ell_2}(t) \Big\rangle + \Big\langle n_{\ell_2}(t) \Big\rangle_1 \Big\langle n_{\ell_1}(t_\mathrm{w}) \Big\rangle - \Big\langle n_{\ell_2}(t) \Big\rangle_0 \Big(1 - \Big\langle n_{\ell_1}(t_\mathrm{w}) \Big\rangle \Big) \,. \tag{2.101}$$

For soft-core bosons, Eq. (2.101) does not hold in general since the density operator $A = n_{\ell_1}$ can take more than two eigenvalues. However, the projective protocols in Eqs. (2.99) and (2.100) can still be used to measure the *exact* unequal-time anti-commutator for an arbitrary observable B and any dichotomic observable A. For instance, a possible choice of A is the parity Π_ℓ of the particle number at site ℓ, which in conventional quantum gas microscopes is even more easily accessible than the density itself due to pairwise atom loss caused by the near-resonant imaging light [16]. If we associate the eigenvalues 0 and 1 to even and odd parity, respectively, the operator $\Pi_\ell = 0 \cdot P_{\ell,\mathrm{even}} + 1 \cdot P_{\ell,\mathrm{odd}}$ coincides with the density in the hard-core limit. Thus, in the regime where multiple occupancies can be neglected, we can approximate the density–density anti-commutator in Eq. (2.101) by the (exactly obtainable) quantity $\langle \{ n_{\ell_2}(t), \Pi_{\ell_1}(t_\mathrm{w}) \} \rangle$.

An alternative strategy to approximate $\langle \{ n_{\ell_2}(t), n_{\ell_1}(t_\mathrm{w}) \} \rangle$ for soft-core bosons is to take Eq. (2.101) literally and compute the conditional expectation values $\langle n_{\ell_2}(t) \rangle_0$ and $\langle n_{\ell_2}(t) \rangle_1$ from only those realizations where the projective measurement of $n_{\ell_1}(t_\mathrm{w})$ yields the outcomes 0 and 1, respectively, discarding realizations with higher occupancies. By contrast, $\langle n_{\ell_2}(t) \rangle$ still represents the (full) unperturbed expectation value. This way, the asymptotic behavior of the unequal-time anti-commutator for $t \gg t_\mathrm{w}$ is correctly reproduced: two local observables A and B typically become uncorrelated in an ergodic system after sufficiently long times and the anti-commutator reduces to the disconnected product $2\langle B(t) \rangle \langle A(t_\mathrm{w}) \rangle$. For the Bose–Hubbard model, the conditional expectation values of the local densities in Eq. (2.101) are expected to eventually re-equilibrate to their unper-

turbed value $\langle n_{\ell_2}(t)\rangle$, such that the right-hand side indeed becomes $2\langle n_{\ell_2}(t)\rangle\langle n_{\ell_1}(t_\mathrm{w})\rangle$. As long as the system is sufficiently close to the hardcore limit, we can expect Eq. (2.101) to reproduce the unequal-time anti-commutator for any $t \geq t_\mathrm{w}$ to good accuracy. In what follows, we analyze how well this approximation works for on-site densities ($B = A = n_\ell$) as a function of the filling and the on-site interaction.

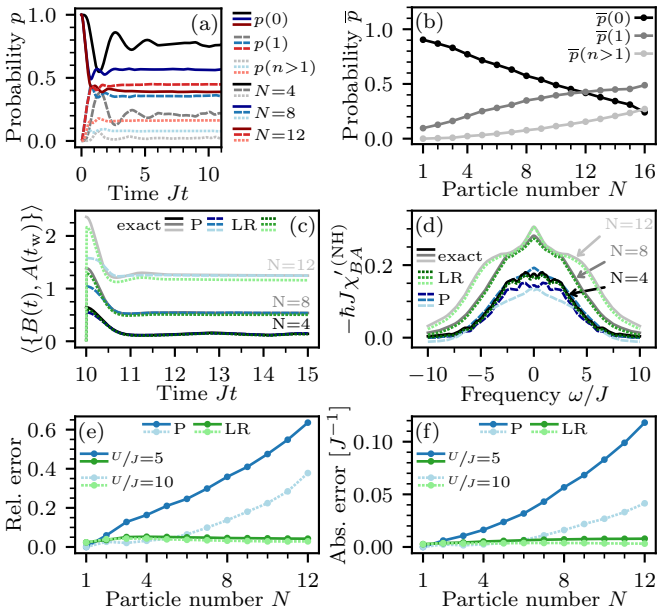

Figure 2.10.: Comparison of the projective protocol (P) and non-Hermitian linear response (LR) for extracting the unequal-time anti-commutator of the on-site density ($B = A = n_{2,2}$) in a 4×4 Bose–Hubbard system with on-site interaction $U/J = 5$ as a function of the filling. (a) Time trace of the probability $p(n)$ of finding n particles at site $(2, 2)$. (b) Time-averaged probability $\overline{p}(n)$ as a function of the particle number N. For small N, higher occupancies are negligible and the on-site density $n_{2,2}$ is approximately dichotomic. (c) Time trace of the unequal-time anti-commutator and (d) correlation spectrum extracted from simulations of the different measurement schemes at $Jt_\mathrm{w} = 10$. (e) Relative error and (f) absolute error of the correlation spectra in (d) with respect to the exact results. The projective protocol (P) yields good accuracy at low fillings where multiple occupancies are suppressed, but fails as the filling approaches unity. Increasing the on-site interaction U extends the regime of validity. The non-Hermitian linear response scheme (LR) performs well irrespective of the filling and the value of U/J.

Performance of the projective protocol as a function of the filling. In Fig. 2.10, we compare the performance of the projective protocol in Eq. (2.101) to that of the non-Hermitian linear response scheme discussed in Section 2.2 for a 2D Bose–Hubbard system as a function of the filling. To this end, we vary the number of particles N on a square lattice with open boundary conditions consisting of 4×4 sites, labeled by a pair of indices (ℓ_x, ℓ_y) with $\ell_x, \ell_y \in \{1, \ldots, 4\}$. We initialize the system in a single Fock state where the particles are distributed to maximize their mutual distances without initially occupying the interior site $(2, 2)$, at which we probe the density correlations.

Figure 2.10a shows the probability $p(n)$ of finding zero, one, or more than one particle at the probe site for $U/J = 5$ as a function of time. The initial oscillations quickly damp and the probabilities become approximately stationary. In Fig. 2.10b, we can see the probability $\overline{p}(n) = t^{-1} \int_0^t \mathrm{d}t'\, p(n, t')$, time-averaged up to time $Jt = 10$, as a function of the particle number N. For small N, higher occupancies $n > 1$ can be neglected and the density operator at the probe site is approximately dichotomic.

Figures 2.10c and 2.10d show, respectively, the time trace of the unequal-time anti-commutator ($B = A = n_{2,2}$) and the reactive part of the non-Hermitian dynamic susceptibility $\chi'^{(\mathrm{NH})}$ (correlation spectrum) at the waiting time $Jt_\mathrm{w} = 10$ for several values of N. The exact results are compared to those extracted using the projective protocol (P) and the non-Hermitian linear response scheme (LR). For the latter, we have used a rectangular pulse of duration $J\delta t = 0.01$ and a perturbation strength $s = 0.05$ as in Section 2.2. The Fourier integral in Eq. (2.23) has been computed using an exponential filter of characteristic frequency $\gamma/J = 0.2$. While for small N the projective protocol correctly reproduces both the exact time trace and the exact spectrum, there are sizable deviations as the number of particles N (and thus the contribution of higher occupancies) grows. By contrast, the non-Hermitian linear response scheme reproduces the exact results to good accuracy regardless of the filling.

In Figs. 2.10e and 2.10f, we can see, respectively, the L^2 norm of the relative error $\|\chi'^{(\mathrm{NH})}_\mathrm{sim} - \chi'^{(\mathrm{NH})}_\mathrm{exact}\|_2 / \|\chi'^{(\mathrm{NH})}_\mathrm{exact}\|_2$ and the absolute error $\|\hbar\chi'^{(\mathrm{NH})}_\mathrm{sim} - \hbar\chi'^{(\mathrm{NH})}_\mathrm{exact}\|_2$ of the spectra extracted from the simulated measurement protocols in Fig. 2.10d. For the projective protocol, both errors increase with increasing particle number, while the errors remain small for the non-Hermitian linear response scheme. For larger on-site interactions U, higher occupancies are suppressed more strongly, which delays the rise of the error curve for the projective protocol as the filling increases: given a certain acceptable tolerance for the relative error of, say, less than 20 %, the projective protocol for $U/J = 5$ ($U/J = 10$) yields acceptable results for up to $N = 4$ ($N = 9$) particles.

Performance of the projective protocol as a function of the interaction. We now investigate the performance of projective protocols for the scenario in Section 2.2, i.e., a quench in a 1D Bose–Hubbard chain of length $L = 12$ with periodic boundary conditions at unit filling, initially prepared in a Mott-insulating state. Since $\langle n_\ell(t)\rangle \equiv 1$ in this case, the projective protocol in Eq. (2.101) reduces to $\langle\{n_{\ell_2}(t), n_{\ell_1}(t_\mathrm{w})\}\rangle \approx 1 + \langle n_{\ell_2}(t)\rangle_1$. If we evaluate this expression at $t = t_\mathrm{w}$, the right-hand side takes the value 2 and therefore the connected anti-commutator extracted from the projective protocol vanishes. This behavior is qualitatively different from that of the true anti-commutator, which is maximal at $t = t_\mathrm{w}$. Consequently, Eq. (2.101) represents a rather poor approximation of the unequal-time anti-commutator in this scenario, especially at small U/J. To obtain a slightly better approximation, we resort to the projective protocol in Eq. (2.99), which is no longer equivalent to Eq. (2.100) if A has more than two eigenvalues. However, unlike Eq. (2.100), the protocol in Eq. (2.99) does not reproduce the correct asymptotic behavior of the anti-commutator for $t \gg t_\mathrm{w}$ if A is not dichotomic. This can be fixed by replacing $\langle B(t)\rangle(a_1 + a_2)$ on the right-hand side by

$\alpha\langle B(t)\rangle$ with $\alpha = 2\langle A(t_\mathrm{w})\rangle - (a_1 - a_2)[p(a_1) - p(a_2)]$. Since $\langle B(t)\rangle$ is usually stationary in the regime of interest, this replacement merely contributes a constant offset to the time trace of the anti-commutator, which ensures $\langle\{B(t), A(t_\mathrm{w})\}\rangle \to 2\langle B(t)\rangle\langle A(t_\mathrm{w})\rangle$ for $t \gg t_\mathrm{w}$ and avoids spurious static peaks in the correlation spectrum.

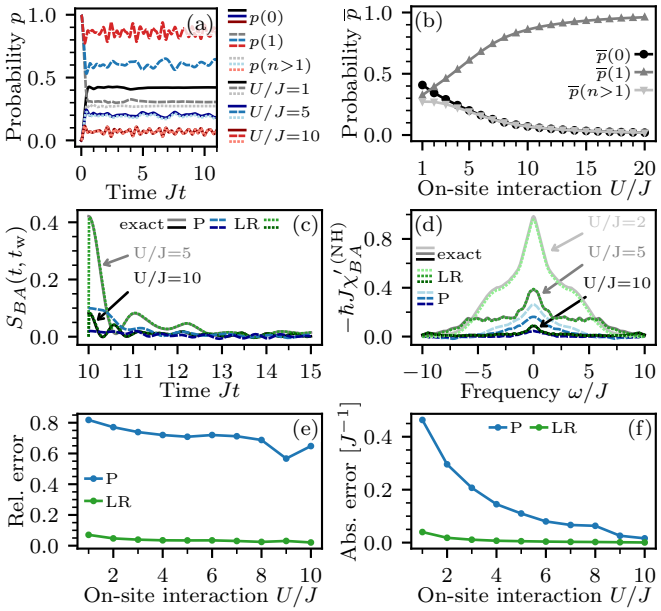

Figure 2.11.: Same as Fig. 2.10, but for a 1D Bose–Hubbard system at unit filling as a function of the on-site interaction U. Despite the suppression of higher occupancies at large U (b), the relative error (e) of the projective protocol (P) remains sizable. By contrast, the non-Hermitian linear response scheme (LR) yields good results for any value of U.

Figure 2.11 shows a similar analysis as in Fig. 2.10 for the 1D system at unit filling as a function of the on-site interaction U. In Fig. 2.11b, it can be seen be seen that there is a significant contribution from states with higher occupancies at small on-site interactions U/J. As expected, the projective protocol does not perform well in this regime, while the non-Hermitian linear response scheme yields good results. As we move to larger U/J, we enter the Mott-insulating regime where single occupancies dominate and the dynamics is governed by particle–hole excitations [191]. Although the probability of higher occupancies $p(n > 1)$ diminishes with increasing U/J, its contribution remains on the same order as that of the probability for vacancies $p(0)$. Thus, the density is nowhere well approximated by a dichotomic observable since the neglected higher occupancies (particle excitations on top of the Mott insulator) are of equal importance as vacancies (hole excitations). This explains why the absolute error of the projective protocol in Fig. 2.11f decreases substantially with increasing U/J, while the relative error in Fig. 2.11e decreases only slowly and remains comparatively large even at large U/J. In fact, the error behaves similarly if one approximates the density–density unequal-time anti-commutator by replacing $A = n_{\ell_1}$ with the parity Π_{ℓ_1} as discussed above (not shown). Thus, as opposed to non-Hermitian linear response, projective protocols are

not well suited for probing unequal-time anti-commutators and the associated FDRs for densities at unit filling.

2.5. Experimental Perspectives for an Implementation in Rydberg Quantum Simulators

As an outlook, we explore the prospects for an experimental realization of the above ancilla-based non-Hermitian linear response schemes in Rydberg quantum simulators. We first discuss generic error sources that apply to any potential experimental realization. Then, we describe how the non-Hermitian linear response protocol can be implemented in Rydberg quantum simulators for spin systems and investigate potential challenges and error sources specific to this implementation.

2.5.1. Generic Experimental Error Sources

Many experimental setups such as quantum gas microscopes permit the simultaneous readout of all site populations in a single shot [18, 19]. This is convenient for simultaneously measuring the responses of different observables B, e.g., $B = n_\ell$ for $\ell = 1 \dots L$, to a fixed perturbation A determined by the coupling scheme. In addition, for the single Zeno step and the continuous Zeno evolution in Sections 2.3.1 and 2.3.3, respectively, the measurement of the ancilla population can be deferred up to the final observation time t and measured along with the other site populations (cf. Ref. [131]). The projection on the empty-ancilla subspace is then achieved by post-selecting those realizations where no particles are detected in the ancilla. Since the effective coupling s needs to be chosen sufficiently weak to stay within the regime of linear response, the fidelity of the post-selection is typically high (see Fig. 2.7c). However, there is the usual linear response tradeoff between maximizing the measurement signal (large s) and staying within the perturbative regime where the linear approximation is valid (small s).

One can distinguish two types of detection errors: false positives, i.e., at least one particle is detected in the ancilla, but there is actually none, and false negatives, i.e., no particles are detected, but there is at least one. Let α be the false positive rate and let β be the false negative rate. If the measurement is post-selected on the condition that no particles are detected in the ancilla, which may in some cases be erroneous, the conditional state in Eq. (2.32) is replaced by

$$\rho' = (1-\alpha) P\rho P + \beta Q\rho Q\,, \tag{2.102}$$

where ρ is the state right after the coupling and before the projection, and $Q = \mathbb{1} - P$ is the projector on the subspace with a non-vanishing ancilla population (for simplicity, we do not distinguish different false-negative probabilities within the Q-subspace since the error due to single occupancies dominates in the linear regime). This shows that false positives lower the measurement fidelity, while false negatives contribute a systematic error to the result, arising from the inadvertent projection on a complementary subspace [see the discussion in the context of Eq. (2.45)].

2.5.2. Non-Hermitian Linear Response in Rydberg Quantum Simulators for Spin Systems

In Rydberg atoms, electrons are excited to high principal quantum numbers n, causing atomic radii to increase by several orders of magnitude with respect to the non-Rydberg state. This unique property allows for a high degree of experimental control over interactions between Rydberg atoms, and Rydberg systems have emerged as a competitive platform for quantum simulation and computation [192]. A spin-1/2 degree of freedom can be encoded in two Rydberg states, e.g., $|\uparrow\rangle = |nP\rangle$ and $|\downarrow\rangle = |nS\rangle$ in ^{87}Rb [104]. A third Rydberg state, e.g., $|\mathrm{A}\rangle = |(n-1)P\rangle$, can then play the role of the ancilla for probing dynamical correlations in the spin-1/2 system via non-Hermitian linear response [104]. Since the ancilla state is available to each Rydberg atom individually, this setup corresponds to the general system–ancilla coupling scheme described in Section 2.3.1, where each mode (here each spin) is coupled to a separate ancilla. This setting allows one to probe global quantities like the total magnetization in a single configuration. The populations of the individual states can be resolved using electric field ionization [104], which enables post-selecting realizations where no ancilla state is populated, as required to generate effective non-Hermitian perturbations.

A first step towards the implementation of the non-Hermitian linear response protocol with engineered dephasing in Section 2.3.3 consists in the generation of the appropriate dephasing noise on the ancilla. In Appendix A.2, we show at the example of a single qubit that the stochastic von Neumann equation (2.68) (or stochastic Schrödinger equation in case of a pure state) can be obtained by engineering a random walk of the phase of the driving field. This basic building block has been achieved according to preliminary experimental results demonstrating unitary stochastic evolutions of individual realizations, whose ensemble average obeys a Lindblad master equation [104]. Furthermore, the same experiment demonstrates the extraction of the unequal-time (anti-)commutator using (non-)Hermitian linear response in a system of non-interacting Rydberg qubits [104]. In the (non-interacting) single-particle case, the non-Hermitian linear response protocols in Section 2.3 simplify because no post-selection is required.

The final step for an experimental realization of the proposed non-Hermitian linear response measurement in the many-body case consists in post-selecting on realizations where no particles occupy the ancilla state. While in principle this can be achieved in the outlined Rydberg experiment [104], in practice post-selection can severely increase the number of experimental runs to accumulate sufficient statistics. This is because post-selection on the condition that no particles are detected in the ancilla involves discarding runs where this condition cannot be guaranteed. In practice, a statement whether or not a particle was present in a single realization can often be made only with a certain probability, which depends on the efficiency of the detection system. Thus, it would constitute an enormous experimental simplification to relax the requirement of strict post-selection and tolerate a certain rate of false negatives. In what follows, we illustrate for a specific setting how the non-Hermitian linear response results are affected by an incomplete post-selection, corresponding to a finite false negative rate β. Furthermore, we investigate a potential simplification of the protocol with engineered

dephasing, consisting in applying a scalar noise process acting globally an all ancillas instead of applying independent noise realizations on each ancilla individually.

XXZ Heisenberg model. We illustrate these aspects for an XXZ Heisenberg spin-1/2 model, which can be realized in Rydberg quantum simulators [193]. The Hamiltonian of this model is given by

$$H_{\mathrm{XXZ}} = \frac{1}{2}\sum_{i\neq j}\hbar J_{ij}\left(S_i^x S_j^x + S_i^y S_j^y + \Delta S_i^z S_j^z\right) + h_x\sum_j S_j^x + h_z\sum_j S_j^z\,, \tag{2.103}$$

where $\{S_j^x, S_j^y, S_j^z\} = \{\sigma_j^x, \sigma_j^y, \sigma_j^z\}/2$ are the spin-1/2 operators of spin j, defined in terms of Pauli matrices, J_{ij} are the interactions constants between the spins i and j, h_x and h_z are external fields in x and z direction, respectively, and Δ quantifies the anisotropy of the interaction in z direction. Due to the dipolar interactions between Rydberg atoms, the interactions are long ranged as $J_{ij} \propto r_{ij}^{-6}$, where r_{ij} is the distance between the spins i and j. We focus on the value $\Delta = -0.73$ of the anisotropy for consistency with the experiment in Ref. [193]. While the Rydberg atoms in this setup are disordered, we consider here for simplicity a linear chain with uniform spacing a, such that $J_{ij} = J/|i-j|^6$, and open boundary conditions, which can be realized in Rydberg experiments with arrays of optical tweezers [192].

2.5.3. The Role of False Negatives

The system is initialized in the product state $|\Psi_0\rangle = |{\rightarrow}\rangle^{\otimes N}$, corresponding to all spins initially pointing in x direction, where $|{\rightarrow}\rangle = (|{\uparrow}\rangle + |{\downarrow}\rangle)/\sqrt{2}$. At zero external field, it can take the system a long time to thermalize due to the long-range r^{-6} interaction. To accelerate the development of a stationary state, we choose the external fields as $h_x/\hbar J = -0.7$ and $h_z/\hbar J = -0.3$. Figure 2.12a shows the unperturbed evolution of the total magnetization in x and z direction, $\langle S_x\rangle = \sum_j \langle S_j^x\rangle$ and $\langle S_z\rangle = \sum_j \langle S_j^z\rangle$, for a system of $N = 12$ spins. After damped initial oscillations, both quantities reach approximately stationary values around times on the order of $Jt \approx 10$.

Our goal is to investigate the consequences of faulty projection on the correlation spectrum S_{BA} (an thus on the extracted FDRs) for the total magnetization in x direction, $B = A = S_x$. To this end, we use the non-Hermitian linear response protocol in Section 2.3.1, corresponding to a single step in the Zeno evolution. The coupling Hamiltonian reads

$$H_{\mathrm{cpl}} = \hbar\Omega\sum_j\left(|\mathrm{A}\rangle_j\langle{\rightarrow}|_j + |{\rightarrow}\rangle_j\langle\mathrm{A}|_j\right), \tag{2.104}$$

i.e., for each particle, the spin state $|{\rightarrow}\rangle$ is coherently coupled to the ancilla state $|\mathrm{A}\rangle$ with coupling strength Ω.

To mimic imperfect post-selection on realizations without ancilla occupancies, we compute the conditional expectation value with respect to the state in Eq. (2.102) at a finite false negative rate β (for simplicity, we neglect false positives as they do not contribute

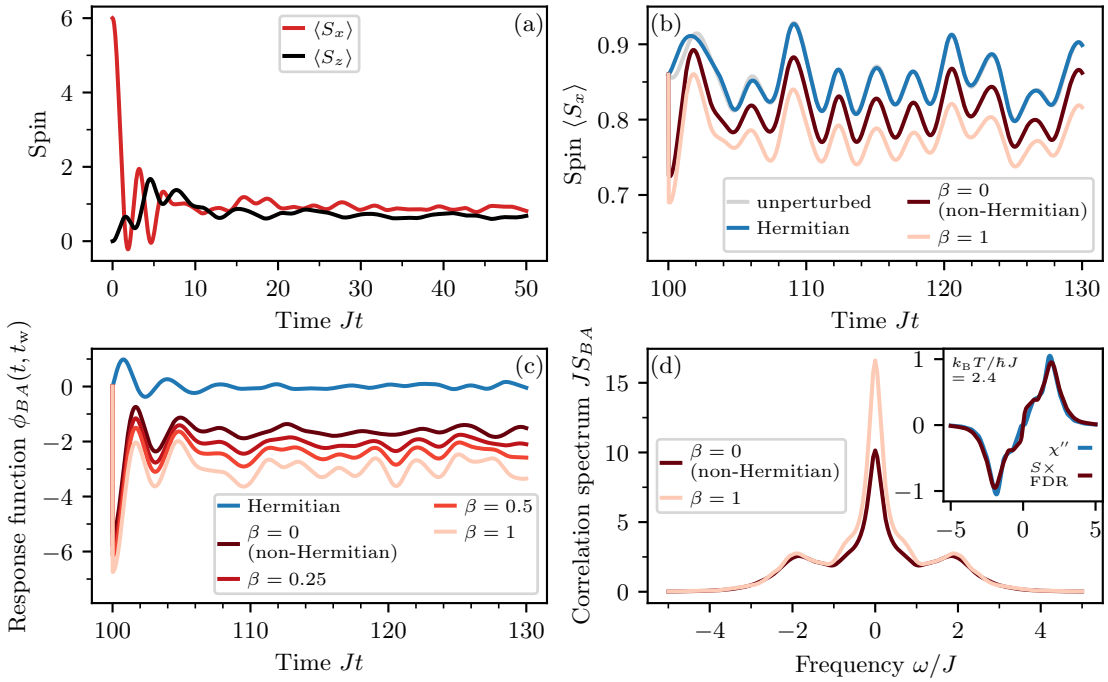

Figure 2.12.: Influence of faulty post-selection on the non-Hermitian linear response measurement of the unequal-time anti-commutator and the FDR. (a) Time evolution of the magnetization in an XXZ Heisenberg chain with initially all spins polarized in x direction. (b) Response of the total magnetization $B = S_x$ after applying a short system–ancilla coupling pulse at the waiting time $Jt_w = 100$ (red curves). A measurement with perfect post-selection on the absence of ancilla occupancies (false negative rate $\beta = 0$) realizes a purely non-Hermitian perturbation by the operator $A = P_{\rightarrow}$. The curve with $\beta = 1$ corresponds to a measurement without post-selection. The unperturbed evolution (grey) and the response to a Hermitian perturbation with $A = P_{\rightarrow}$ (blue) are shown for comparison. (c) Time trace of the response function extracted from (b), illustrating the ancilla-based measurement for several false negative rates β. (d) Correlation spectrum computed from the response functions in (c). The inset shows the FDR (1.83) with the fitted effective temperature T according to Eq. (2.26). The measurement without post-selection ($\beta = 1$) captures the qualitative behavior of both the response function (c) and the correlation spectrum (d).

a systematic error, setting $\alpha = 0$). In the present scenario, the projector on the empty-ancilla subspace reads $P = (|\uparrow\rangle\langle\uparrow| + |\downarrow\rangle\langle\downarrow|)^{\otimes N}$, while $Q = \mathbb{1} - P$ projects on the complementary subspace where at least one particle is detected in the ancilla state. Since we only probe system observables, which act trivially on the ancilla, coherences between the P and Q subspaces play no role when computing expectation values, such that the state in Eq. (2.102) can be replaced by $\rho' = (1 - \beta)P\rho P + \beta\rho$, where ρ is the (unprojected) state right after the coupling. Note that to leading order in the perturbation strength, only configurations where at most one of the particles is in the ancilla state contribute (see, for example, Eq. (3.17) in Section 3.1.2, where ancilla occupation probabilities are calculated up to next-to-leading order).

In case of perfect post-selection ($\beta = 0$), an analogous calculation as in Section 2.3.1 shows that the conditional expectation value of an observable B, post-selected on the empty-ancilla, is given by Eq. (2.43) with the perturbation operator $A = P_{\rightarrow}$, where $P_{\rightarrow} = \sum_j P_{\rightarrow}^{(j)} = \sum_j |{\rightarrow}\rangle_j\langle{\rightarrow}|_j$ is the sum of local projectors on the spin state $|{\rightarrow}\rangle$. Using $P_{\rightarrow}^{(j)} = (\mathbb{1} + 2S_j^x)/2$, we thus obtain

$$\langle B(t)\rangle_P = \langle B(t)\rangle_0 - s\big[\langle\{B(t), S_x(t_\mathrm{w})\}\rangle_0 - 2\langle B(t)\rangle_0\langle S_x(t_\mathrm{w})\rangle_0\big] + \mathcal{O}(s^2)\,, \tag{2.105}$$

where $s = (\Omega\delta t)^2/2$ and $S_x = \sum_j S_j^x$ is the total spin operator in x direction. By contrast, without post-selection ($\beta = 1$), the result reads

$$\begin{aligned}\langle B(t)\rangle = \langle B(t)\rangle_0 - s\Big[&\langle\{B(t), P_{\rightarrow}(t_\mathrm{w})\}\rangle_0 \\ &- 2\sum_j \big\langle \big(|{\rightarrow}\rangle_j\langle \mathrm{A}|_j\big)(t_\mathrm{w}) B(t) \big(|\mathrm{A}\rangle_j\langle{\rightarrow}|_j\big)(t_\mathrm{w})\big\rangle_0\Big] + \mathcal{O}(s^2)\,,\end{aligned} \tag{2.106}$$

which includes undesired contributions similar to recycling terms in Lindblad equations [cf. Eq. (2.45)].

Figure 2.12 shows how the undesired contributions in Eq. (2.106) manifest in practice for the particular scenario of probing FDRs in XXZ Heisenberg chains outlined above. In Fig. 2.12b, the response of the total magnetization in x direction ($B = S_x$) is shown at $Jt_\mathrm{w} = 100$ in the unperturbed case, for a Hermitian perturbation (probing the unequal-time commutator), as well as for the perturbation generated by coupling to the ancilla with and without post-selection. In all cases, the strength of the perturbation has been chosen as $s = 0.025$ with a duration $\delta t = 0.01$. The result for $\beta = 0$ reflects a perfect non-Hermitian perturbation, while $\beta = 1$ (no post-selection) is experimentally easier to realize. The corresponding response functions are shown in Fig. 2.12c, including intermediate values of β, which interpolate between the corner cases $\beta = 0$ and $\beta = 1$. While deviations are clearly visible, the qualitative behavior of the curves for $\beta = 0$ and $\beta = 1$ is similar. This is also reflected in the correlation spectrum depicted in Fig. 2.12d, where the protocol with $\beta = 1$ captures characteristic peaks around $\omega/J = 2$ even quantitatively, while deviations from the ideal result for $\beta = 0$ are apparent at small frequencies. The spectrum has been calculated using an exponential filter of characteristic frequency $\gamma/J = 0.2$. The inset in Fig. 2.12d shows that the system indeed fulfills the FDR in the stationary regime. For the specific scenario investigated, a measurement without post-selection is also capable of certifying the validity of the FDR since deviations in the correlation spectrum at small frequencies are irrelevant for probing FDRs.

It should be noted that the deviations for measurements with and without post-selection can be more severe in other scenarios, such that in general post-selection is required for an unbiased measurement. Yet, the above example illustrates that it is possible to identify scenarios where the difference is moderate, in which case also a measurement without post-selection can probe the validity (or the failure) of the FDR. This insight makes the proposed non-Hermitian linear response protocol attractive even to experiments where accurate post-selection is difficult to realize.

2.5.4. Local Versus Global Noise

We now investigate another question of practical relevance for an experimental realization of the non-Hermitian linear response scheme with engineered dephasing, presented in Section 2.3.3.

In case of a single ancilla, as considered in Section 2.3.3, engineered dephasing applied to the ancilla is described by the Hamiltonian $H_{\mathrm{A}}(t) = \hbar\sqrt{2\kappa}\xi(t)b^\dagger b$, giving rise to the stochastic von Neumann equation (2.68). The natural generalization of this scenario to multiple ancillas involves exposing each ancillary mode to a separate independent noise process [158]. For the Rydberg system considered here, this corresponds to the ancilla Hamiltonian

$$H_{\mathrm{A}}(t) = \sum_j \sqrt{2\kappa_j}\hbar\xi_j(t)P_{\mathrm{A}}^{(j)}\,, \tag{2.107}$$

where $P_{\mathrm{A}}^{(j)} = |\mathrm{A}\rangle_j\langle\mathrm{A}|_j$ is the local projector on the j-th ancilla, $\xi_j(t)$ represents uncorrelated Gaussian white noise with $\langle\!\langle \xi_j(t)\rangle\!\rangle = 0$ and $\langle\!\langle \xi_i(t)\xi_j(t')\rangle\!\rangle = \delta_{ij}\delta(t-t')$, and κ_j is the local dephasing rate. For a pure state $|\psi(t)\rangle$, time evolution is then governed by the stochastic Schrödinger equation in Stratonivich interpretation,

$$i\hbar\,\mathrm{d}|\psi(t)\rangle = \big[H_0 + H_{\mathrm{cpl}}(t)\big]|\psi(t)\rangle\,\mathrm{d}t + \sum_j \hbar\sqrt{2\kappa_j}P_{\mathrm{A}}^{(j)}|\psi(t)\rangle\circ\mathrm{d}W_j(t)\,, \tag{2.108}$$

where $W_j(t)$ is the j-th component of an N-dimensional Wiener process (defined in Appendix A.1.1). In analogy to the procedure in Section 2.3.3, we can derive a Lindblad master equation for the noise-averaged density operator $\sigma(t) = \langle\!\langle|\psi(t)\rangle\langle\psi(t)|\rangle\!\rangle$ using the methods for SDEs described in Appendix A.1. The result reads

$$\frac{\mathrm{d}}{\mathrm{d}t}\sigma = -\frac{i}{\hbar}\big[H_0 + H_{\mathrm{cpl}}(t), \sigma\big] - \sum_j \kappa_j\Big(\big\{L_j^\dagger L_j, \sigma\big\} - 2L_j\sigma L_j^\dagger\Big) \tag{2.109}$$

with Lindblad operators $L_j = P_{\mathrm{A}}^{(j)}$.

An enormous practical simplification with respect to the setup in Eq. (2.107) consists in applying only a single scalar noise process $\xi(t)$ globally to all ancillas. Engineering the corresponding noise Hamiltonian

$$H_{\mathrm{A}}(t) = \hbar\sqrt{2\kappa}\xi(t)\sum_j P_{\mathrm{A}}^{(j)} \tag{2.110}$$

then requires no single-site (or single-particle) addressing. This setting leads to a master equation with only a single Lindblad operator given by the sum of all local ancilla projectors, $L = \sum_j P_{\mathrm{A}}^{(j)}$.

It is clear that the settings in Eqs. (2.107) and (2.110) are not equivalent. Nonetheless, in the linear regime, where only single occupancies of the ancilla matter, the two variants give rise to the same evolution. In the non-Hermitian linear response context, we are interested in the limit where the dephasing rate is large compared to all other relevant

frequency scales. Using the same approximations as in Section 2.3.3, one derives the effective non-Hermitian Hamiltonian

$$H_{\mathrm{eff}}(t) = H_0 - iH_{PQ}(t)K^{-1}H_{QP}(t)\,, \tag{2.111}$$

governing the time evolution of the state $\sigma_{PP} = P\sigma P$ projected on the subspace without any ancilla occupancies. Here, $H_{PQ}(t) = PH_{\mathrm{cpl}}(t)Q$ and the operator K is given by

$$K = \begin{cases} Q\big(\sum_j \hbar\kappa_j L_j^\dagger L_j\big)Q & \text{(local noise)} \\ Q\,\hbar\kappa L^\dagger L\,Q & \text{(global noise)}\,. \end{cases} \tag{2.112}$$

Due to the projector P in Eq. (2.111), this operator only acts on states where exactly one particle is in the ancilla, state such that K can be replaced by a scalar factor $\hbar\kappa$ in both cases (assuming $\kappa_j \equiv \kappa$ for local noise). For the coupling Hamiltonian (2.113), the effective non-Hermitian Hamiltonian then becomes $H_{\mathrm{eff}} = H_0 - i\hbar\Omega^2 P_{\rightarrow}/\kappa$. Recall that one of the approximations made in the derivation of the effective non-Hermitian description in Eq. (2.78) is to neglect the population $\rho_{QQ} = Q\rho Q$ to leading order in Ω/κ. On the non-linear level, the operator K in Eq. (2.112) acts differently on states with multiple ancilla occupancies and therefore deviations between the local and global noise variants are expected when operating outside of the linear regime.

To confirm and illustrate the above predictions, we apply the engineered dephasing protocol to probing the non-Hermitian dynamical susceptibility (2.24) in the XXZ Heisenberg model (2.103), similarly to the numerical benchmark in Section 2.3.3. We consider a thermal state of $N = 6$ spins at temperature $k_{\mathrm{B}}T/\hbar J = 1.57$, chosen such that the mean energy matches that of a state with all spins polarized in x direction. All other model parameters are the same as in Fig. 2.12. Here, we probe unequal-time correlations of the total magnetization in z direction ($B = A = S_z = \sum_j S_j^z$), which can be realized by coupling the spin state $|{\uparrow}\rangle$ to the ancilla,

$$H_{\mathrm{cpl}} = \hbar\Omega \sum_j \big(|\mathrm{A}\rangle_j\langle{\uparrow}|_j + |{\uparrow}\rangle_j\langle\mathrm{A}|_j\big)\,. \tag{2.113}$$

The coupling is applied up to the final observation time $Jt_{\mathrm{f}} = 10$ at a strength $s = t_{\mathrm{f}}\Omega^2/\kappa = 0.05$ without modulation, i.e., we probe the static susceptibility ($\omega = 0$). To examine the differences between the local and global noise configurations in Eqs. (2.107) and (2.110), the master equation (2.109) has been solved for the two configurations (in the case of global noise, there is only a single Lindblad operator, as described above). The result is depicted in Fig. 2.13 for $\kappa/J = 10$ ($\kappa/J = 1$ is shown for comparison, although this value is not in the limit that yields the effective non-Hermitian Hamiltonian). Figure 2.13a shows the decrease of the projector as a function of time. The dotted line marks the prediction by Eq. (2.6) and can be used to gauge the extent of the linear regime. Figure 2.13b shows the unnormalized response of the observable $B = S_z$, while the susceptibility shown in Fig. 2.13d is obtained by normalizing this quantity. According to Eq. (2.79), the normalized response yields the time integral of the non-Hermitian response function $\phi_{BA}^{(\mathrm{NH})}$ over the shaded region in Fig. 2.13c, as indicated by

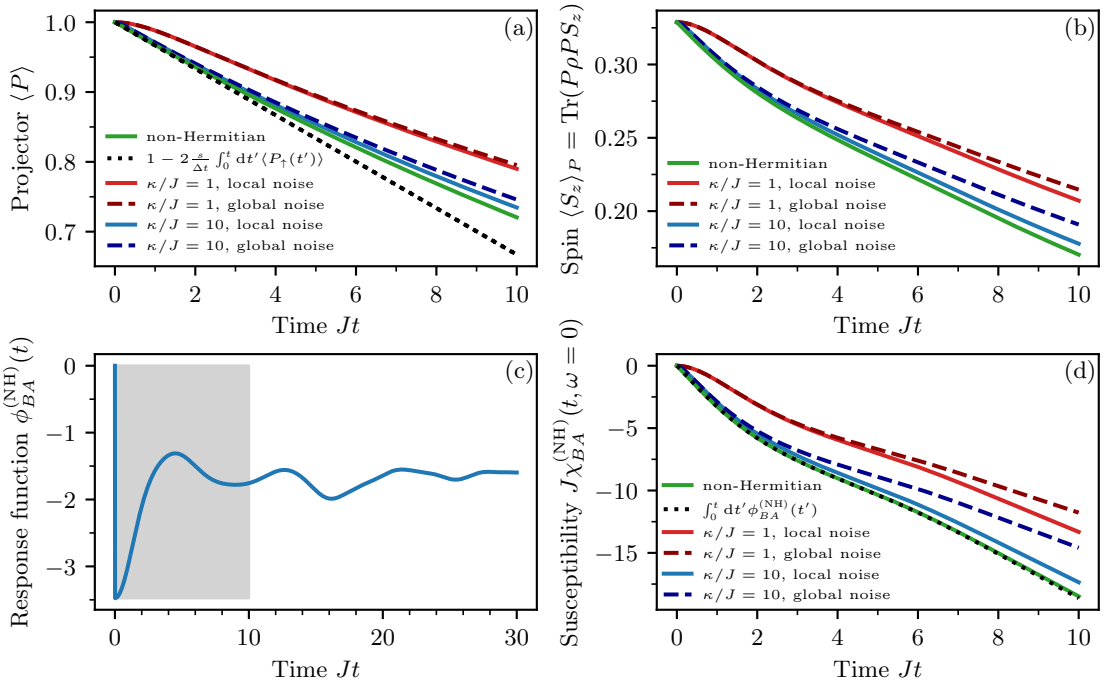

Figure 2.13.: Differences between local and global noise in the extraction of dynamical susceptibilities using engineered dephasing. (a) Decrease of the probability $\langle P \rangle$ to remain in the empty-ancilla subspace as a function of time. The green line shows the ideal result obtained directly from the effective non-Hermitian Hamiltonian. The dotted line marks the linear prediction by Eq. (2.6). (b) Unnormalized conditional expectation value of the total magnetization $B = S_z$. (c) Non-Hermitian response function $\phi_{BA}^{(\mathrm{NH})}$ for $B = A = S_z$ (exact result). (d) Static susceptibility, obtained by normalizing the expectation value in (b). The ideal result corresponds to the time integral over the shaded region of the response function in (c), as indicated by the dotted line. There is no visible difference between local and global noise in the linear regime, but on the non-linear level, the global noise scenario exhibits larger deviations from the desired non-Hermitian evolution.

the black dots in Fig. 2.13d. Deviations from the ideal non-Hermitian result, obtained directly from the effective non-Hermitian Hamiltonian $H_{\mathrm{eff}} = H_0 - i\hbar\Omega^2 P_\uparrow/\kappa$, become visible for times larger than $Jt \approx 3$, corresponding to a norm decrease of about 10 %. The onset of the deviations coincides with the onset of the non-linear regime. This confirms the above prediction that on the linear level, there is no difference between the local and global noise scenario, while deviations become apparent in the non-linear regime. Outside the linear regime, the scheme with local noise is closer to the non-Hermitian description. This can be explained by the increased sensitivity to correlations between particles in the ancilla if the noise acts globally. Furthermore, as can be seen in Fig. 2.13, the differences between the local and global setting grow with increasing dephasing rate κ.

As this analysis demonstrates, the simpler setup of engineering a single noise pro-

cess that globally acts on all ancillas yields accurate results when operating in the linear regime. This extends the scope of the engineered dephasing variant of the non-Hermitian linear response scheme to experimental setups where single-site addressing is not available.

2.6. Summary

In this chapter, we have introduced protocols based on non-Hermitian linear response to measure the elusive unequal-time anti-commutator as the missing piece for the direct observation of the fluctuation–dissipation relation (FDR) in quantum systems. The extraction of FDRs has been illustrated through numerical benchmark simulations at the experimentally motivated example of tracking thermalization in a Bose–Hubbard system after a quench. The non-Hermitian linear response framework is agnostic to specific platforms and implementations, and as such can be applied to any quantum many-body system. In particular, it also represents a simple and efficient way to numerically compute unequal-time anti-commutators, in analogy to the linear response protocols employed in Refs. [107, 118] to numerically extract unequal-time commutators. Higher orders in the response may be used to access nested unequal-time anti-commutators of increasing order. Furthermore, we have shown that common ancilla-based weak measurement protocols for dynamical correlations fit in the same framework, as these can be interpreted in the light of (non-)Hermitian linear response.

At the center of our discussion has been the design of specific ancilla-based schemes to realize the desired non-Hermitian perturbations in cold-atom systems. The basic variant of the scheme corresponds to a single step in the quantum Zeno evolution and consists of coupling to the ancilla, followed by a projection on the subspace where the ancilla remains unoccupied. This procedure realizes a delta-like effective non-Hermitian perturbation, suitable for mapping out the time trace of the unequal-time anti-commutator at a fixed waiting time. By iterating the Zeno evolution, a prolonged and possibly time-dependent non-Hermitian perturbation can be achieved, allowing one to directly probe susceptibilities in frequency space. The repeated measurements generating the Zeno effect can be substituted by strong engineered dephasing noise on the ancilla, such that only a single post-selected measurement at the final evolution time is required. The proposed realization of non-Hermitian linear response is feasible even when existing weak measurement protocols are difficult to engineer experimentally, and it excels in regimes where projective protocols fail as a consequence of their restriction to observables with two eigenvalues. While we have focused on lattice systems, the protocol can immediately be applied to continuous systems, e.g., via spatially focused laser beams, giving access to dynamical correlations of the field operator coarse-grained over a small region in space [69]. Moreover, our discussion of experimental perspectives for implementations in Rydberg quantum simulators has revealed that some experimental requirements, such as strict post-selection or engineering dephasing noise for each ancilla independently, may be relaxed under certain conditions. This significantly extends the feasibility of the method. The proposed realization of non-Hermitian linear response thus opens the

door to probing dynamical correlations and FDRs in quantum many-body systems for a broad range of observables, even beyond unequal-time density correlations.

3. Measuring Currents and Current Correlations

The discussion of the non-invasive current measurement scheme in this chapter is based on Ref. [194]. The figures and some parts of the text have been taken verbatim from that work, but the presentation has been adapted to better showcase the connections to non-Hermitian linear response discussed in Chapter 2. The application of the scheme to the measurement of chiral currents in bosonic ladders is a continuation of the work started in Janika Reichstetter's Bachelor's thesis [2]. See List of Publications for a statement of contributions.

In the previous chapter, we have explored ancilla-based schemes exploiting the quantum Zeno effect to realize effective non-Hermitian perturbations in quantum many-body systems. As demonstrated at the example of optical-lattice setups, measuring the induced non-Hermitian linear response enables the detection of quantities which are in general not immediately accessible through standard projective measurements, e.g., unequal-time anti-commutators. In this chapter, we follow a related approach to devise a handle on another observable that is inherently difficult to access in analog quantum simulators: the current operator.

While quantum simulators of condensed matter systems, e.g., based on cold atoms or trapped ions, not only allow one to engineer and manipulate a wide range of model Hamiltonians, but also to observe their dynamics at a microscopic resolution and in real time [6, 13–17, 71–74, 78, 195–197], possibilities to directly detect currents are sparse. In actual solid state systems, currents are comparatively easy to measure by connecting wires to the sample [198, 199], which has enabled milestone discoveries such as the integer and fractional quantum Hall effects [200–203]. For ultracold atoms or trapped ions, such a coupling to the outside world would destroy the high-vacuum sample. It is nevertheless possible to measure transport properties by tracking the evolution of individual particles or collective excitations [40, 182, 204–218], by tomography after quenching an optical lattice [180, 219–222], or by employing reservoir regions with different chemical potentials [223, 224]. In contrast, the direct measurement of currents requires additional experimental overhead, such as tuning interactions to zero [180] or coupling a synthetic dimension to a cavity [225]. Thus, it remains highly challenging to measure currents in quantum devices.

This chapter is devoted to novel ancilla-based protocols for the direct measurement of currents and current correlations [194]. The scheme relies on a setup similar to that employed in Fig. 2.7b for the realization of non-Hermitian linear response in optical

lattices, where two lattice sites are coherently coupled to a central ancilla. The key to gain access to the current operator is to engineer the phases of the couplings in an appropriate way. A short coupling pulse then maps the current between the two sites under investigation to the population of the ancilla, which can be read out using standard detection techniques. This method works for interacting bosons and fermions alike, both in and out of equilibrium, and can easily be extended to other platforms.

We first develop a non-invasive variant of the protocol, which is directly inspired from the non-Hermitian linear response scenario discussed in the previous chapter. As elucidated in Section 2.4.1, a non-Hermitian linear response can always be realized via an ancilla-based weak measurement. Keeping this connection in mind, we will in what follows adopt a weak measurement point of view. The central idea of this type of measurement is to weakly couple the system to an ancilla, on which suitable measurements are performed to extract information about the system. In our case, the system–ancilla coupling is engineered in such a way that a projective measurement of the ancilla population gives access to the current operator. Such a weak (or non-invasive) measurement has the advantage that measurement back action is reduced and the quantum state remains largely intact [163, 188], which enables, for example, the detection of temporal correlations (see discussion in Section 2.4.1). Furthermore, weak measurements permit the simultaneous readout of operators that are incompatible according to the Heisenberg uncertainty principle [226, 227], which turns out to be beneficial when measuring global currents.

After introducing the general technique for the non-invasive measurement of currents and current correlations, including a discussion of potential experimental error sources and strategies how to mitigate them, we unfold various applications of this method. Our first benchmark example is the Harper–Hofstadter model for interacting bosons on an optical-lattice ladder, which mimics the Meissner effect in type-II superconductors exposed to an external magnetic field [181, 228–244]. As demonstrated by numerical benchmark simulations, the non-invasive current measurement scheme reveals the characteristic current patterns of the Meissner and the vortex phases (see Fig. 3.1c), as well as the transition to a Mott-insulating phase. As a second benchmark, the technique is applied to the detection of chiral long-range order in frustrated bosons on spatially anisotropic triangular lattices, which host rich 1D and 2D Néel as well as subtle chiral phases [245–248]. The latter cannot be revealed by the current itself as it vanishes on average, but loop current correlations are sensitive to the chirality [249] and can be accessed by means of the proposed scheme. Moreover, we discuss possible implementations in trapped-ion quantum simulators, enabling, for example, the measurement of spin currents.

A practical challenge for the non-invasive current measurement scheme — as for any linear-response-type protocol where information about the system is extracted following a weak perturbation — is to achieve a sufficiently high signal-to-noise ratio. Although typically a good compromise between measurement accuracy and signal strength can be found (see numerical benchmarks in Section 3.2.1), it may in some cases be necessary to improve the signal-to-noise ratio even further, which usually comes at the price of systematic deviations due to non-linearities. However, it turns out that the non-invasive

protocol for measuring currents can be turned into a projective measurement by replacing the weak system–ancilla coupling with a π-pulse. In the last section of this chapter, we discuss how this projective variant enables the detection of currents and current correlations at a substantially increased signal-to-noise ratio.

3.1. Non-Invasive Protocol

We consider a general system described by the tight-binding Hamiltonian

$$H_0 = -\sum_{\ell \neq \ell'} \hbar J_{\ell\ell'} a_\ell^\dagger a_{\ell'} + V\,, \tag{3.1}$$

where a_ℓ ($a_\ell^\dagger$) denotes the bosonic or fermionic annihilation (creation) operator at local mode ℓ, which may represent lattice sites or internal states, and V contains any density–density interaction. We allow for complex hopping amplitudes $J_{\ell\ell'} = J_{\ell'\ell}^* = |J_{\ell\ell'}|\mathrm{e}^{i\phi_{\ell\ell'}}$ involving Peierls phases $\phi_{\ell\ell'}$, as is common in models with synthetic gauge fields [71, 74, 250]. For concreteness, we focus the following discussion on cold atoms in optical lattices, but the same concept can also be applied to other quantum simulation platforms, as will be exemplified in Section 3.2.3 for trapped ions.

It is our goal to measure expectation values involving the current operator from local mode ℓ_1 to ℓ_2,

$$j_{\ell_1\ell_2} = -i(J_{\ell_1\ell_2} a_{\ell_1}^\dagger a_{\ell_2} - J_{\ell_1\ell_2}^* a_{\ell_2}^\dagger a_{\ell_1})\,, \tag{3.2}$$

whose form follows by combining the Heisenberg equation of motion

$$\frac{\mathrm{d}}{\mathrm{d}t} n_{\ell_1} = \frac{i}{\hbar}[H_0, n_{\ell_1}] \tag{3.3}$$

with the continuity equation

$$\frac{\mathrm{d}}{\mathrm{d}t} n_{\ell_1} + \sum_{\ell_2 \neq \ell_1} j_{\ell_1\ell_2} = 0\,, \tag{3.4}$$

expressing local conservation of the particle number (density) $n_{\ell_1} = a_{\ell_1}^\dagger a_{\ell_1}$.

3.1.1. Non-Invasive Measurement of Currents

The non-invasive protocol for measuring currents is inspired from the non-Hermitian linear response scenario described in Section 2.1. The basic idea is as follows. Let us consider the unperturbed Hamiltonian H_0 subject to a static anti-Hermitian perturbation $H_1 = -i\hbar s A/2\delta t$, switched on during a short time interval δt. According to Eq. (2.6), the norm of a state ρ_0 evolving under the total Hamiltonian $H_0 + H_1$ decreases, to linear order in the perturbation strength s, as

$$\mathrm{Tr}[\rho(\delta t)] = 1 - s\langle A\rangle_0 + \mathcal{O}(s^2)\,. \tag{3.5}$$

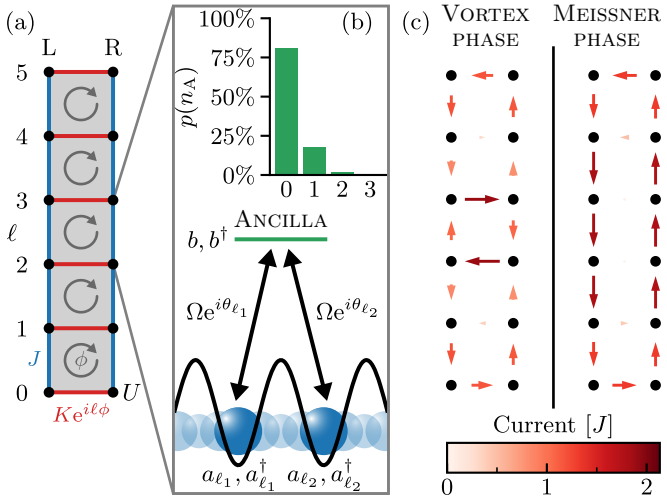

Figure 3.1.: Schematic of the non-invasive protocol for measuring currents. (a) The protocol is illustrated for interacting bosons on a Harper–Hofstadter optical-lattice ladder with on-site interaction U, real intra-leg tunneling J, and complex inter-leg tunneling $Ke^{i\ell\phi}$, generating a synthetic magnetic flux ϕ per plaquette. (b) A short pulse of strength Ω coherently couples two sites ℓ_1 and ℓ_2 to an empty ancillary mode. Using an appropriate choice of the phases, the current from site ℓ_1 to ℓ_2 can be extracted by measuring the probability of not populating the ancilla. (c) The scheme reveals the current characteristic of the vortex phase as well as the chiral current running along the system boundary in the Meissner phase, illustrated, respectively, for $K/J = 1.25$ and $K/J = 2.5$, with $\phi = 2\pi/3$ and $U/J = 1$.

Thus, it is possible to extract the expectation value of the operator A with respect to the unperturbed state ρ_0 by measuring the decay of the norm in response to the non-Hermitian perturbation H_1. In order to turn this idea into a practicable scheme for measuring currents, it remains to engineer an effective non-Hermitian perturbation such that the operator A is sensitive to the current, as well as to give physical meaning to the decay of the norm of a state.

Both problems can readily be solved using the tools developed in Section 2.3.1 for realizing non-Hermitian linear response based on the Zeno effect by coupling to an ancilla. In this setting, the decay of the norm corresponds to a leakage of probability from the subspace without any particles in the ancilla to a complementary subspace with non-vanishing ancilla population. In order to realize an effective non-Hermitian perturbation sensitive to the current operator, we consider a coupling scheme similar to that in Fig. 2.7b, where two modes are coupled simultaneously to an ancilla. As shown in Section 2.3.1, choosing a coherent coupling without relative phases gives rise to a non-Hermitian perturbation by the hopping operator (in the absence of Peierls phases). Here, in order to access the current operator between two modes ℓ_1 and ℓ_2, we consider instead a coupling Hamiltonian with phases θ_{ℓ_1} and θ_{ℓ_2},

$$H_{\mathrm{cpl}} = \hbar\Omega\left[b^\dagger\left(e^{i\theta_{\ell_1}}a_{\ell_1} + e^{i\theta_{\ell_2}}a_{\ell_2}\right) + \left(e^{-i\theta_{\ell_1}}a^\dagger_{\ell_1} + e^{-i\theta_{\ell_2}}a^\dagger_{\ell_2}\right)b\right], \tag{3.6}$$

where the operator $b^\dagger$ (b) creates (annihilates) a particle in the ancilla, modeled here

as a single bosonic or fermionic mode, and Ω is the coupling strength. The Λ configuration described by this coupling Hamiltonian is depicted in Fig. 3.1, where the non-invasive current measurement protocol is illustrated at the example of a Harper–Hofstadter optical-lattice ladder (see Section 3.2.1). Experimentally, the ancilla can conveniently be realized as an additional internal level of the atoms, for which detuning or polarization of the optical-lattice lasers are chosen such that it is trapped midway between the two sites under investigation — a common setup for laser-assisted tunneling [71, 74, 178, 181, 231–235]. Thus, realizing the system–ancilla coupling is on the same level of difficulty as, e.g., engineering the Peierls phases of a Harper–Hofstadter Hamiltonian [181, 231–235]. Alternatively, the ancilla may also correspond to an off-resonant site in an optical superlattice, where transitions between higher and lower sites can be generated via microwave pulses [251].

The protocol for the non-invasive measurement of currents resembles to the single step in the Zeno evolution for realizing non-Hermitian linear response in time domain (see Section 2.3.1). Let ρ_0 denote the unperturbed quantum state of interest, which may be the ground state of the Hamiltonian (3.1), a thermal state, or any other state, e.g., obtained after some unitary evolution. The coupling is applied as a rectangular pulse (or arbitrarily shaped pulse with equivalent pulse area) of duration δt much shorter than the characteristic time scales of the Hamiltonian (3.1). As before, system and ancilla should be in a product state before the coupling and we assume the ancilla to be initially empty and to have no internal dynamics[1]. Instead of post-selecting on the absence of particles in the ancilla and continuing time evolution as in the protocol for measuring the two-time anti-commutator, the observable of interest for the measurement of currents is the ancilla occupancy itself. More precisely, we consider the probability of not detecting any particles in the ancilla after the coupling. According to Eq. (2.38a), with the replacement $a \to \alpha_{\ell_1\ell_2} = \mathrm{e}^{i\theta_{\ell_1}} a_{\ell_1} + \mathrm{e}^{i\theta_{\ell_2}} a_{\ell_2}$, to leading order in the effective coupling strength[2] $s = (\Omega\Delta t)^2$, this probability is given by

$$p_{\ell_1\ell_2}(0) = 1 - s\left\langle \alpha^\dagger_{\ell_1\ell_2}\alpha_{\ell_1\ell_2}\right\rangle_0 + \mathcal{O}(s^2) \tag{3.7}$$

with

$$\alpha^\dagger_{\ell_1\ell_2}\alpha_{\ell_1\ell_2} = n_{\ell_1} + n_{\ell_2} + \mathrm{e}^{i(\theta_{\ell_2}-\theta_{\ell_1})} a^\dagger_{\ell_1} a_{\ell_2} + \mathrm{e}^{-i(\theta_{\ell_2}-\theta_{\ell_1})} a^\dagger_{\ell_2} a_{\ell_1}\,. \tag{3.8}$$

Here, $\langle\cdots\rangle_0$ denotes the expectation value with respect to the unperturbed state ρ_0 of the target system. For the choice

$$\theta_{\ell_2} - \theta_{\ell_1} = \phi_{\ell_1\ell_2} - \frac{\pi}{2}\,, \tag{3.9}$$

[1] In the relevant regime, interactions between particles in the ancilla can safely be neglected for two reasons: first, for measuring currents, we are interested in the linear regime where only a single particle is transferred to the ancilla, and second, even in the non-linear regime, which is of interest for measuring correlations, it is usually possible to make the pulse duration δt sufficiently short such that interactions and other internal dynamics of the ancilla are negligible on this time scale.

[2] For conciseness of the formulas, we do not include a factor of $1/2$ in the definition of the effective coupling strength s in this chapter, as opposed to the conventions in Section 2.3.

where $\phi_{\ell_1\ell_2} = \arg(J_{\ell_1\ell_2})$ is the Peierls phase associated with the hopping amplitude $J_{\ell_1\ell_2}$ in the Hamiltonian (3.1), the last two terms in Eq. (3.8) yield the current operator (3.2) and we obtain

$$p_{\ell_1\ell_2}(0) = 1 - s\left\langle n_{\ell_1} + n_{\ell_2} + \frac{j_{\ell_1\ell_2}}{|J_{\ell_1\ell_2}|}\right\rangle_0 + \mathcal{O}(s^2)\,. \tag{3.10}$$

This equation tells us that the leakage of atoms out of the system is determined by the densities at the involved modes and the current between them. Consequently, a measurement of this decrease of probability in the linear regime gives access to the expectation value of the current operator. In the light of the discussion in Section 2.4.1, this non-invasive measurement of the current can equivalently be interpreted in an ancilla-free way as the linear response of the projector on the empty-ancilla subspace ($B = P_0$) to a suitably engineered anti-Hermitian perturbation by the operator $A = n_{\ell_1} + n_{\ell_2} + j_{\ell_1\ell_2}/|J_{\ell_1\ell_2}|$.

The probability in Eq. (3.10), i.e., the fraction of experimental runs where no atoms are found in the ancilla, can be measured, e.g., with a quantum gas microscope [18, 19, 207, 213], though other methods exist to resolve occupation probabilities for different sites of a superlattice [135]. Since in the linear regime only single occupancies of the ancilla contribute, it is sufficient to be able to distinguish an empty ancilla from one with non-vanishing population. In the simplest case of a uniform system, the contribution of the densities to Eq. (3.10) merely yields a constant offset, while otherwise it can be accounted for via a separate standard measurement. As an alternative, one can conduct an independent ancilla-based measurement of the probability $p_{\ell_2\ell_1}(0)$. This exchange of the indices ℓ_1 and ℓ_2 does not affect the densities in Eq. (3.10), but reverses the sign of the current. Thus, it is possible to extract the current according to

$$\left\langle j_{\ell_1\ell_2}\right\rangle = \frac{|J_{\ell_1\ell_2}|}{2}\frac{\partial}{\partial s}\left[p_{\ell_1\ell_2}(0) - p_{\ell_2\ell_1}(0)\right]\Big|_{s=0}\,. \tag{3.11}$$

Most studies of transport phenomena monitor the density and then invoke the continuity equation to infer the current [40, 182, 204–218]. Those few proposals to directly access the current operator (3.2) are either plagued by strong measurement back action [225] or are most suited for non-interacting systems [180, 181] because magnetic control to turn off interactions via Feshbach resonances is slow. Conversely, the proposed non-invasive protocol achieves a direct measurement of the current even in the presence of interactions and significantly reduces back action in the linear regime due to the weakness of the coupling (see Section 3.1.3).

Finally, it is worth emphasizing that the freedom to adjust the phase difference $\theta_{\ell_2} - \theta_{\ell_1}$ in Eq. (3.7) enables access to arbitrary quadratures of the operator $a^\dagger_{\ell_1} a_{\ell_2}$. For example, the choice $\theta_{\ell_1} = \theta_{\ell_2}$ yields the correlator $\langle a^\dagger_{\ell_1} a_{\ell_2} + a^\dagger_{\ell_2} a_{\ell_1}\rangle$ (see Section 2.3.1), which can be useful, e.g., for probing superfluidity [57].

3.1.2. Extension to Current Correlations

The ability to resolve the ancilla occupation probabilities to higher orders in the effective coupling s gives access to successively higher moments of the current operator (3.2) In

what follows, we derive the relevant formulas up to quadratic order in s and discuss how such measurements can be used to extract current variances as well as spatial current correlations. While possibilities to measure variances and correlations for spatially close-lying links have been discussed in Ref. [180], precise control of the required optical triple-well potentials still remains elusive to modern experiments. As we will see, the technique described below permits the measurement of even long-range current correlations using the same experimental resources as for current expectation values.

General derivation

We consider again the general system–ancilla coupling Hamiltonian already introduced in Eq. (2.46),

$$H_{\mathrm{cpl}} = \sum_{m=1}^{M} \hbar\Omega_m \left(b_m^\dagger \alpha_m + \alpha_m^\dagger b_m \right), \tag{3.12}$$

where an arbitrary number of system modes is coherently coupled to one or several of a total of M bosonic or fermionic ancillary modes. That is, the linear combination of system modes $\alpha_m = \sum_\ell \lambda_{m\ell} a_\ell$ with complex coefficients $\lambda_{m\ell}$ is coupled to the mode b_m of the m-th ancilla. The Λ configuration described by Eq. (3.6) and depicted in Fig. 3.1b is recovered for $M = 1$ if only two coefficients $\lambda_{1\ell_1}$ and $\lambda_{1\ell_2}$ are chosen different from zero with appropriate phases.

We assume all ancillas to be initially in their respective vacuum states, such that when the coupling is turned on, the combined state of system and ancilla is given by the product state $\rho = \rho_0 \otimes |0\cdots 0\rangle\langle 0\cdots 0|$ (see Section 3.2.3 for generalizations to mixed initial states of the ancilla). As before, the coupling is applied as a short pulse of duration δt, which we assume to be sufficiently short compared to all other relevant time scales. It is then permissible to assume that the system evolves solely under the coupling Hamiltonian (3.12) during the coupling period, $\rho(\delta t) = \mathrm{e}^{-iH_{\mathrm{cpl}}\delta t}\rho \mathrm{e}^{iH_{\mathrm{cpl}}\delta t}$.

We are interested in the joint probability $P(n_1, \ldots, n_M)$ of finding n_1 particles in the first ancilla, n_2 particles in the second ancilla, and so on. This probability can be expressed with the help of the projector $P_{n_1\ldots n_M} = \mathbb{1} \otimes |n_1 \cdots n_M\rangle\langle n_1 \cdots n_M|$ as $P(n_1, \ldots, n_M) = \mathrm{Tr}[P_{n_1\ldots n_M}\rho(\delta t)]$. If the coupling is sufficiently weak, we can expand the time evolution operator to approximate this quantity perturbatively, yielding

$$\begin{aligned} P(n_1, \ldots, n_M) = \delta_{n_1 0}\cdots\delta_{n_M 0} &- \frac{1}{2}\delta t^2 \,\mathrm{Tr}\left[P_{n_1\ldots n_M}\left(H_{\mathrm{cpl}}^2\rho + \rho H_{\mathrm{cpl}}^2 - 2H_{\mathrm{cpl}}\rho H_{\mathrm{cpl}}\right)\right] \\ &+ \frac{1}{24}\delta t^4 \,\mathrm{Tr}\Big[P_{n_1\ldots n_M}\Big(H_{\mathrm{cpl}}^4\rho + \rho H_{\mathrm{cpl}}^4 + 6H_{\mathrm{cpl}}^2\rho H_{\mathrm{cpl}}^2 \\ &\qquad - 4H_{\mathrm{cpl}}^3\rho H_{\mathrm{cpl}} - 4H_{\mathrm{cpl}}\rho H_{\mathrm{cpl}}^3\Big)\Big] + \mathcal{O}(\Delta t^6)\,. \end{aligned} \tag{3.13}$$

Note that since $\mathrm{Tr}(P_{n_1\ldots n_M} H_{\mathrm{cpl}}^p \rho H_{\mathrm{cpl}}^q) = 0$ if $p + q$ is odd, only even orders in Δt contribute. Up to quartic order in Δt, the probability that more than two particles are found in ancillary modes vanishes. In what follows, we therefore focus on the probability $P_0 = \mathrm{Tr}[P_{0\ldots 0}\rho(\delta t)]$ of not populating any ancilla, the probability $P_1^{(m)} = \mathrm{Tr}[b_m^\dagger P_{0\ldots 0} b_m \rho(\delta t)]$

of finding a single particle in the m-th ancilla (while all others are empty), the probability $P_2^{(m_1,m_2)} = \mathrm{Tr}[b_{m_1}^\dagger b_{m_2}^\dagger P_{0\ldots0} b_{m_2} b_{m_1} \rho(\delta t)]$ of detecting one particle in two distinct ancillas m_1 and m_2 each, and the probability $P_2^{(m)} = \mathrm{Tr}[(b_m^\dagger)^2 P_{0\ldots0} b_m^2 \rho(\delta t)]/2$ of a double occupancy of the m-th ancilla (which can be non-zero for bosons only).

For bosons, the annihilation and creation operators satisfy canonical commutation relations,

$$[c_i, d_j] = [c_i^\dagger, d_j^\dagger] = 0\,, \qquad [c_i, d_j^\dagger] = \delta_{cd}\delta_{ij}\,, \tag{3.14}$$

while for fermions, they fulfill canonical anti-commutation relations,

$$\{c_i, d_j\} = \{c_i^\dagger, d_j^\dagger\} = 0\,, \qquad \{c_i, d_j^\dagger\} = \delta_{cd}\delta_{ij}\,, \tag{3.15}$$

where $c, d \in \{a, b\}$. In the special case of hard-core bosons, where repulsive on-site interactions are infinitely strong, the second relation in Eq. (3.14) has to be replaced by

$$[c_i, d_j^\dagger] = \delta_{cd}\delta_{ij}(1 - 2c_i^\dagger c_i)\,, \tag{3.16}$$

i.e., annihilation and creation operators anti-commute on site, prohibiting multiple occupancies of the same mode [252].

After some algebra, using the above (anti-)commutation relations, we find

$$\begin{aligned} P_0 &= 1 - \sum_{m=1}^{M} s_m \left\langle \alpha_m^\dagger \alpha_m \right\rangle \\ &\quad + \sum_{m,k=1}^{M} s_m s_k \left\langle \frac{1}{3}\alpha_m^\dagger \alpha_m \alpha_k^\dagger \alpha_k + \frac{1}{6}\alpha_m^\dagger \alpha_k^\dagger \alpha_k \alpha_m \right\rangle + \mathcal{O}(s^3)\,, \end{aligned} \tag{3.17a}$$

$$\begin{aligned} P_1^{(m)} &= s_m \left\langle \alpha_m^\dagger \alpha_m \right\rangle \\ &\quad - s_m \sum_{k=1}^{M} s_k \left\langle \frac{1}{6}\{\alpha_m^\dagger \alpha_m, \alpha_k^\dagger \alpha_k\} + \frac{2}{3}\alpha_m^\dagger \alpha_k^\dagger \alpha_k \alpha_m \right\rangle + \mathcal{O}(s^3)\,, \end{aligned} \tag{3.17b}$$

$$P_2^{(m_1,m_2)} = s_{m_1} s_{m_2} \left\langle \alpha_{m_1}^\dagger \alpha_{m_2}^\dagger \alpha_{m_2} \alpha_{m_1} \right\rangle + \mathcal{O}(s^3)\,, \tag{3.17c}$$

$$P_2^{(m)} = \frac{1}{2} s_m^2 \langle (\alpha_m^\dagger)^2 \alpha_m^2 \rangle + \mathcal{O}(s^3)\,. \tag{3.17d}$$

Here, $s_m = (\Omega_m \Delta t)^2$ and $\langle \cdots \rangle = \mathrm{Tr}(\cdots \rho_0)$ denotes the expectation value with respect to the unperturbed system state ρ_0. Note that for fermions, the expectation values $\langle \alpha_m^\dagger \alpha_k^\dagger \alpha_k \alpha_m \rangle$ vanish for $m = k$ due to the anti-commutation relations (3.15), in accordance with the Pauli exclusion principle. The same applies to hard-core bosons as a result of Eq. (3.16). It is easy to verify that the probabilities in Eq. (3.17) correctly sum to unity,

$$P_0 + \sum_m P_1^{(m)} + \sum_{m_1<m_2} P_2^{(m_1,m_2)} + \sum_m P_2^{(m)} = 1 + \mathcal{O}(s^3). \tag{3.18}$$

Up to linear order in s, Eq. (3.17a) represents a generalization of Eq. (3.7) to an arbitrary number of system modes coupled to one or more ancillas. In Section 3.2, we

illustrate how this result can be applied to extract global currents as well as loop currents around plaquettes. In what follows, we discuss the extraction of current variances as well as spatial current correlations from a measurement of the probabilities (3.17) resolved to quadratic order in s.

Current Variances

We are interested in the variance of the current between two sites ℓ_1 and ℓ_2,

$$\Delta j^2_{\ell_1\ell_2} = \left\langle j^2_{\ell_1\ell_2} \right\rangle - \left\langle j_{\ell_1\ell_2} \right\rangle^2 . \tag{3.19}$$

This quantity has been used, e.g., to characterize the Mott-insulator–superfluid transition [180], as well as to reveal many-body multi-valued Lissajous figures [253] or transitions in the Aubry–André–Harper model [254].

We first note that by using the (anti-)commutation relations (3.14) to (3.16), the square of the current operator (3.2) can be written as

$$j^2_{\ell_1\ell_2} = -J^2_{\ell_1\ell_2}(a^\dagger_{\ell_1} a_{\ell_2})^2 - (J^*_{\ell_1\ell_2})^2(a^\dagger_{\ell_2} a_{\ell_1})^2 + |J_{\ell_1\ell_2}|^2\big(n_{\ell_1} + n_{\ell_2} \pm 2n_{\ell_1} n_{\ell_2}\big), \tag{3.20}$$

where the upper sign applies to (soft-core) bosons, while the lower sign is valid for fermions and hard-core bosons. In the latter case, the first two terms do not contribute since multiple occupancies are forbidden, and the second moment of the current operator reduces to $\langle j^2_{\ell_1\ell_2}\rangle = |J_{\ell_1\ell_2}|^2\langle n_{\ell_1} + n_{\ell_2} - 2n_{\ell_1} n_{\ell_2}\rangle$. The density correlations in this expression are typically easy to measure in many experiments using standard techniques, which is why we focus the following discussion in this subsection on the non-trivial case of (soft-core) bosons.

Apart from the ability to resolve the probabilities in Eq. (3.17) to quadratic order in s, measuring the variance of the current (3.19) requires no additional experimental overhead because the same setup as for the current expectation value can be used (see Fig. 3.1b). For the special case of a single ancilla ($M = 1$), the general expressions in Eq. (3.17) simplify to

$$p(0) = 1 - s\langle\alpha^\dagger\alpha\rangle + s^2\left\langle \frac{1}{3}(\alpha^\dagger\alpha)^2 + \frac{1}{6}(\alpha^\dagger)^2\alpha^2 \right\rangle , \tag{3.21a}$$

$$p(1) = s\langle\alpha^\dagger\alpha\rangle - s^2\left\langle \frac{1}{3}(\alpha^\dagger\alpha)^2 + \frac{2}{3}(\alpha^\dagger)^2\alpha^2 \right\rangle , \tag{3.21b}$$

$$p(2) = \frac{1}{2}s^2\langle(\alpha^\dagger)^2\alpha^2\rangle . \tag{3.21c}$$

(For conciseness of the formulas, here and in what follows we implicitly consider the expressions for the probabilities as perturbative approximations valid up to second order in s, unless stated otherwise. Furthermore, we omit the subscripts ℓ_1 and ℓ_2 where there is no ambiguity.)

We choose the phases as in Eq. (3.9), such that $(\alpha^\dagger\alpha)_{\ell_1\ell_2} = n_{\ell_1} + n_{\ell_2} + j_{\ell_1\ell_2}/|J_{\ell_1\ell_2}|$. The relevant quantity in Eq. (3.21) for extracting the variance of the current (3.19) is

$$(\alpha^\dagger\alpha)^2_{\ell_1\ell_2} = \big(n_{\ell_1} + n_{\ell_2}\big)^2 + \frac{1}{|J_{\ell_1\ell_2}|}\big\{n_{\ell_1} + n_{\ell_2}, j_{\ell_1\ell_2}\big\} + \frac{j^2_{\ell_1\ell_2}}{|J_{\ell_1\ell_2}|^2} . \tag{3.22}$$

The contribution from the $\langle(\alpha^\dagger)^2\alpha^2\rangle$ term in Eq. (3.21a) can be accounted for via an independent measurement of one of the probabilities $p(1)$ or $p(2)$. It is then possible to eliminate this contribution by forming suitable linear combinations, e.g.,

$$p(0) - \frac{p(2)}{3} = 1 - s\langle\alpha^\dagger\alpha\rangle + \frac{1}{3}s^2\langle(\alpha^\dagger\alpha)^2\rangle\,. \tag{3.23}$$

Alternatively, Eq. (3.21a) can be simplified using the commutation relations (3.14). For the coupling setup under consideration, we have $[\alpha, \alpha^\dagger] = 2$, yielding

$$p(0) = 1 - s\langle\alpha^\dagger\alpha\rangle + s^2\left\langle\frac{1}{2}(\alpha^\dagger\alpha)^2 - \frac{1}{3}\alpha^\dagger\alpha\right\rangle, \tag{3.24a}$$

$$p(1) = s\langle\alpha^\dagger\alpha\rangle - s^2\left\langle(\alpha^\dagger\alpha)^2 - \frac{4}{3}\alpha^\dagger\alpha\right\rangle, \tag{3.24b}$$

$$p(2) = s^2\left\langle\frac{1}{2}(\alpha^\dagger\alpha)^2 - \alpha^\dagger\alpha\right\rangle. \tag{3.24c}$$

The quantity $\langle(\alpha^\dagger\alpha)^2\rangle$ can thus be obtained from the s^2 term of either of the above probabilites if the value of $\langle\alpha^\dagger\alpha\rangle$, corresponding to the linear coefficient of $p(0)$ or $p(1)$, is known.

In order to isolate the second moment of the current operator $\langle j^2_{\ell_1\ell_2}\rangle$ from Eq. (3.22), knowledge of the other two terms is required. The density correlator $\langle(n_{\ell_1} + n_{\ell_2})^2\rangle$ is typically directly accessible, for instance, in quantum gas microscopes [18, 19]. The contribution due to the density–current anti-commutator can be eliminated by conducting an additional ancilla-based measurement with the indices ℓ_1 and ℓ_2 exchanged. Since the densities in Eq. (3.22) are symmetric under this exchange, while the current is anti-symmetric, we have

$$\frac{1}{2}\left[(\alpha^\dagger\alpha)^2_{\ell_1\ell_2} + (\alpha^\dagger\alpha)^2_{\ell_2\ell_1}\right] = \left(n_{\ell_1} + n_{\ell_2}\right)^2 + \frac{j^2_{\ell_1\ell_2}}{|J_{\ell_1\ell_2}|^2}\,. \tag{3.25}$$

Alternatively, the anti-commutator $\langle\{n_{\ell_1} + n_{\ell_2}, j_{\ell_1\ell_2}\}\rangle$ can be obtained according to Eq. (2.43) as the conditional expectation value of the observable $B = n_{\ell_1} + n_{\ell_2}$, given that after the coupling no particles have been detected in the ancilla.

Spatial Current Correlations

Measuring the probabilities in Eq. (3.17) to quadratic order in s also gives access to current correlations. In what follows, we discuss this scenario for correlations $\langle j_{\ell_1\ell_2} j_{\ell_3\ell_4}\rangle$ of the current operators $j_{\ell_1\ell_2}$ and $j_{\ell_3\ell_4}$ between two pairs of modes (ℓ_1, ℓ_2) and (ℓ_3, ℓ_4), each coupled to a different ancilla. The coupling Hamiltonian (3.12) then reads

$$H_{\mathrm{cpl}} = \hbar\Omega_1\left(b_1^\dagger\alpha_1 + \alpha_1^\dagger b_1\right) + \hbar\Omega_2\left(b_2^\dagger\alpha_2 + \alpha_2^\dagger b_2\right) \tag{3.26}$$

with $\alpha_1 = \mathrm{e}^{i\theta_{1\ell_1}} a_{\ell_1} + \mathrm{e}^{i\theta_{1\ell_2}} a_{\ell_2}$ and $\alpha_2 = \mathrm{e}^{i\theta_{2\ell_3}} a_{\ell_3} + \mathrm{e}^{i\theta_{2\ell_4}} a_{\ell_4}$. For each pair of modes, the phases $\theta_{m\ell}$ are chosen according to Eq. (3.9) such that $\alpha_1^\dagger\alpha_1 = n_{\ell_1} + n_{\ell_2} + j_{\ell_1\ell_2}/|J_{\ell_1\ell_2}|$ and

$\alpha_2^\dagger\alpha_2 = n_{\ell_3}+n_{\ell_4}+j_{\ell_3\ell_4}/|J_{\ell_3\ell_4}|$. Note that the measurement of spatial current correlations is non-trivial also for fermions and hard-core bosons, unlike the measurement of current variances discussed above.

We first discuss the case where the modes ℓ_j with $j = 1, \ldots, 4$ are all distinct. Then, the operators α_1 and α_2 (anti-)commute for bosons (fermions), and Eq. (3.17a) simplifies to

$$p_{\ell_1\ell_2,\ell_3\ell_4}(0,0) = 1 + \big[p_{\ell_1\ell_2}(0) - 1\big] + \big[p_{\ell_3\ell_4}(0) - 1\big] + s_1 s_2 \langle \alpha_1^\dagger\alpha_1\alpha_2^\dagger\alpha_2\rangle \,. \tag{3.27}$$

Here, the probabilities $p_{\ell\ell'}(0)$ are given by Eq. (3.17a) for $M = 1$, corresponding to the scenario of coupling a pair of modes (ℓ, ℓ') to a single ancilla. The cross term

$$\begin{aligned}\alpha_1^\dagger\alpha_1\alpha_2^\dagger\alpha_2 = {} & \big(n_{\ell_1} + n_{\ell_2}\big)\big(n_{\ell_3} + n_{\ell_4}\big) \\ & + \frac{j_{\ell_1\ell_2} j_{\ell_3\ell_4}}{|J_{\ell_1\ell_2} J_{\ell_3\ell_4}|} + \frac{1}{|J_{\ell_3\ell_4}|}\big(n_{\ell_1} + n_{\ell_2}\big) j_{\ell_3\ell_4} + \frac{1}{|J_{\ell_1\ell_2}|} j_{\ell_1\ell_2}\big(n_{\ell_3} + n_{\ell_4}\big)\end{aligned} \tag{3.28}$$

contains the desired current correlator. To isolate it, one can pursue similar strategies as for the current variance discussed above. That is, one can measure the surrounding density correlations and density–current correlations independently, where the latter can be obtained as conditional expectation values. As an alternative, due to the symmetries of the densities and the currents with respect to exchanging the indices, the combination

$$\frac{1}{4}\big[p_{\ell_1\ell_2,\ell_3\ell_4} - p_{\ell_2\ell_1,\ell_3\ell_4} - p_{\ell_1\ell_2,\ell_4\ell_3} + p_{\ell_2\ell_1,\ell_4\ell_3}\big](0,0) = s_1 s_2 \big\langle j_{\ell_1\ell_2} j_{\ell_3\ell_4}\big\rangle \tag{3.29}$$

gives direct access to the current correlator.

If not all coupled modes are distinct, the procedure is more involved due to the non-commutativity of the associated operators. We elucidate this circumstance for current correlations between two adjacent sites, corresponding to $\ell_2 = \ell_3$ and $\ell_1 \neq \ell_4$. Then, applying the (anti-)commutation relations $[\alpha_1, \alpha_2^\dagger] = \mathrm{e}^{i(\theta_{1\ell_2} - \theta_{2\ell_2})}$ ($\{\alpha_1, \alpha_2^\dagger\} = \mathrm{e}^{i(\theta_{1\ell_2} - \theta_{2\ell_2})}$) for bosons (fermions) to Eq. (3.17a), we find

$$\begin{aligned}p_{\ell_1\ell_2,\ell_2\ell_4}(0,0) = {} & 1 + \big[p_{\ell_1\ell_2}(0) - 1\big] + \big[p_{\ell_2\ell_4}(0) - 1\big] \\ & + s_1 s_2 \bigg(\frac{1}{2}\langle\{\alpha_1^\dagger\alpha_1, \alpha_2^\dagger\alpha_2\}\rangle - \frac{1}{6} R_{\ell_1\ell_2,\ell_2\ell_4}\bigg) \,.\end{aligned} \tag{3.30}$$

with

$$\begin{aligned}R_{\ell_1\ell_2,\ell_2\ell_4} &= \langle \mathrm{e}^{i(\theta_{1\ell_2} - \theta_{2\ell_2})}\alpha_1^\dagger\alpha_2 + \text{h.c.}\rangle \\ &= \frac{\big\langle j_{\ell_1\ell_2}\big\rangle}{|J_{\ell_1\ell_2}|} + 2\big\langle n_{\ell_2}\big\rangle + \frac{\big\langle j_{\ell_2\ell_4}\big\rangle}{|J_{\ell_2\ell_4}|} - \langle \mathrm{e}^{i(\phi_{\ell_1\ell_2} + \phi_{\ell_2\ell_4})} a_{\ell_1}^\dagger a_{\ell_4} + \text{h.c.}\rangle \,.\end{aligned} \tag{3.31}$$

(For hard-core bosons, $\alpha_1^\dagger\alpha_2$ and $a_{\ell_1}^\dagger a_{\ell_4}$ are to be replaced in the above expression for $R_{\ell_1\ell_2,\ell_2\ell_4}$ by $\alpha_1^\dagger(1-2n_{\ell_2})\alpha_2$ and $a_{\ell_1}^\dagger(1-2n_{\ell_2})a_{\ell_4}$, respectively.) The last term in $R_{\ell_1\ell_2,\ell_2\ell_4}$ can in principle be obtained by directly coupling the sites ℓ_1 and ℓ_4 to a single ancilla

with appropriately chosen phases. However, it may be more practicable to eliminate this contribution all together by considering instead the combination

$$p_{\ell_1\ell_2,\ell_3\ell_4}(0,0) - \frac{1}{3}p_{\ell_1\ell_2,\ell_3\ell_4}(1,1) \\ = 1 + \left[p_{\ell_1\ell_2}(0) - 1\right] + \left[p_{\ell_3\ell_4}(0) - 1\right] + \frac{1}{3}s_1 s_2 \langle\{\alpha_1^\dagger\alpha_1, \alpha_2^\dagger\alpha_2\}\rangle \,. \quad (3.32)$$

The last term

$$\{\alpha_1^\dagger\alpha_1, \alpha_2^\dagger\alpha_2\} = \left\{n_{\ell_1} + n_{\ell_2}, n_{\ell_2} + n_{\ell_4}\right\} + \frac{\left\{j_{\ell_1\ell_2}, j_{\ell_2\ell_4}\right\}}{|J_{\ell_1\ell_2}J_{\ell_2\ell_4}|} \\ + \frac{1}{|J_{\ell_2\ell_4}|}\left\{n_{\ell_1} + n_{\ell_2}, j_{\ell_2\ell_4}\right\} + \frac{1}{|J_{\ell_1\ell_2}|}\left\{n_{\ell_2} + n_{\ell_4}, j_{\ell_1\ell_2}\right\} \quad (3.33)$$

then contains the desired current correlator $\langle\{j_{\ell_1\ell_2}, j_{\ell_2\ell_4}\}\rangle$, which can be isolated in a similar way as discussed before. Note that compared to Eq. (3.28), the anti-commutator appears here since the operators $j_{\ell_1\ell_2}$ and $j_{\ell_2\ell_4}$ do not commute. The ability to simultaneously measure observables that are incompatible according to the Heisenberg uncertainty principle is a typical feature of non-invasive measurement protocols [226, 227].

3.1.3. Measurement Back Action

In this subsection, we assess the non-invasiveness of the presented current measurement scheme. In general, it is not possible to extract information from a quantum system without disturbing it [188, 255]. This disturbance of the quantum state through the measurement process, known as measurement back action, is significantly reduced in ancilla-based protocols with respect to standard projective measurements if the system–ancilla coupling is weak. However, the reduced back action comes at the price of a reduced signal-to-noise ratio, which in practice requires a compromise between these two effects, which nevertheless in the proposed scheme is experimentally feasible.

Fidelity

To understand the back action caused by the system–ancilla coupling and the subsequent measurement of the ancilla population, we quantify its impact via the fidelity [3] of the state before and after the measurement. The fidelity of two density operators ρ and σ is defined as

$$F(\rho,\sigma) = \left(\mathrm{Tr}\left[\sqrt{\sqrt{\rho}\sigma\sqrt{\rho}}\right]\right)^2, \quad (3.34)$$

which reduces to $F(\rho,\sigma) = \langle\psi|\sigma|\psi\rangle$ if ρ is a pure state, $\rho = |\psi\rangle\langle\psi|$. To simplify the discussion, we consider here the case of a single ancilla ($M = 1$).

According to Eq. (2.40), the post-measurement states, conditioned on the outcome that n particles are detected in the ancilla, read (after tracing out the ancilla)

$$\rho(\delta t \mid 0) = \rho_0 - \frac{1}{2}s(\{\alpha^\dagger\alpha, \rho_0\} - 2\langle\alpha^\dagger\alpha\rangle\rho_0) + \mathcal{O}(s^2)\,, \tag{3.35a}$$

$$\rho(\delta t \mid 1) = \frac{\alpha\rho_0\alpha^\dagger}{\langle\alpha^\dagger\alpha\rangle} + \mathcal{O}(s)\,. \tag{3.35b}$$

To leading order in the effective coupling strength $s = (\Omega\delta t)^2$, higher ancilla occupancies do not contribute.

By virtue of Eq. (2.41), the unconditional state is recovered by averaging over all possible measurement outcomes as

$$\rho'(\delta t) = \mathrm{Tr}_\mathrm{A}[\rho(\delta t)] = \sum_n P(n)\rho(\delta t \mid n) = \rho_0 - \frac{1}{2}s(\{\alpha^\dagger\alpha, \rho_0\} - 2\alpha\rho_0\alpha^\dagger) + \mathcal{O}(s^2)\,. \tag{3.36}$$

Intuitively, it is clear that in realizations where a particle is transferred to the ancilla, as described by the conditional state $\rho(\delta t \mid 1)$, the disturbance of the state is somewhat strong. For instance, consider a pure state $\rho_0 = |\psi_0\rangle\langle\psi_0|$ with a fixed number of particles. Then, the fidelity vanishes (to all orders), $F[\rho_0, \rho(\delta t \mid 1)] = 0$, i.e., the initial state and the state after loosing one particle to the ancilla have zero overlap.

By contrast, if no particles are detected in the ancilla, which gives rise to the conditional state $\rho(\delta t \mid 0)$, the fidelity for $\rho_0 = |\psi_0\rangle\langle\psi_0|$ reads

$$F[\rho_0, \rho(\delta t \mid 0)] = 1 - \frac{1}{4}s^2\Big(\langle(\alpha^\dagger\alpha)^2\rangle - \langle\alpha^\dagger\alpha\rangle^2\Big) + \mathcal{O}(s^3), \tag{3.37}$$

where the expectation values are taken with respect to the initial state $|\psi_0\rangle$. Thus, the overlap decreases quadratically with s unless the variance of the operator $\alpha^\dagger\alpha$ vanishes. This means that, as quantified by the stringent measure of the fidelity, realizations where no particles are transferred to the ancilla are practically not disturbed if the measurement operates in the linear regime. This justifies referring to the scheme as "non-invasive".

The unconditional state $\rho'(\delta t)$ shows a different behavior: the fidelity decreases linearly with the coupling strength s, reflecting the uncertainty whether or not a particle has been transferred to the ancilla. For a pure state $\rho_0 = |\psi_0\rangle\langle\psi_0|$ with fixed particle number, the fidelity reads

$$F[\rho_0, \rho'(\delta t)] = 1 - s\langle\alpha^\dagger\alpha\rangle + \mathcal{O}(s^2)\,, \tag{3.38}$$

which, to linear order, is the same expression as Eq. (3.17a), i.e., the probability of not detecting any particles in the ancilla.

We conclude our discussion of the fidelity by deriving a perturbative formula for general mixed states ρ_0. To this end, we write $\rho = \rho_0 + s\delta\rho$ and evaluate Eq. (3.34) using the spectral decomposition $\rho_0 = \sum_\lambda \lambda|\lambda\rangle\langle\lambda|$, yielding

$$\sqrt{F}(\rho_0, \rho) = \mathrm{Tr}\sqrt{\sum_\lambda \lambda^2|\lambda\rangle\langle\lambda| + s\sum_{\lambda,\lambda'}\sqrt{\lambda\lambda'}\langle\lambda|\delta\rho|\lambda'\rangle|\lambda\rangle\langle\lambda'|}\,. \tag{3.39}$$

After diagonalizing the matrix under the square root as $\sum_\eta \eta|\eta\rangle\langle\eta|$, where the eigenvalues $\eta = \lambda^2 + s\lambda\langle\lambda|\delta\rho|\lambda\rangle$ are obtained from first order perturbation theory, we arrive at

$$\sqrt{F}(\rho_0, \rho) = \sum_\eta \sqrt{\eta} = \sum_\lambda \lambda + \frac{1}{2} s \sum_{\lambda > \epsilon_s} \langle\lambda|\delta\rho|\lambda\rangle + \mathcal{O}(s^2)\,. \tag{3.40}$$

The last expression is obtained from a Taylor expansion of the square root and the cutoff ϵ_s excludes eigenvalues λ on the order of s. Using the normalization $\sum_\lambda \lambda = 1$ and taking the square of the last expression, we finally obtain the fidelity to leading order in s as

$$F(\rho_0, \rho) = 1 + s \sum_{\lambda > \epsilon_s} \langle\lambda|\delta\rho|\lambda\rangle + \mathcal{O}(s^2)\,. \tag{3.41}$$

It is easy to verify that this formula is consistent with the results for pure states given above. Furthermore, plugging in the unconditional state $\rho = \rho'(\delta t)$ from Eq. (3.36), we find

$$F[\rho_0, \rho'(\delta t)] = 1 - s\left(\langle A^\dagger A\rangle - \sum_{\lambda > \epsilon_s} \langle\lambda|A\rho_0 A^\dagger|\lambda\rangle\right) + \mathcal{O}(s^2)\,, \tag{3.42}$$

which, as anticipated, decreases linearly with s.

Dynamics

To further characterize the measurement back action of our scheme, we briefly discuss how the measurement affects the dynamics of the state. To this end, we consider the expectation value of an observable B with respect to the post-measurement states Eq. (3.35) after a unitary evolution under the Hamiltonian $\mathcal{H}$ for a time t. The results, conditioned on the absence or presence of a particle in the ancilla, are given, respectively, by Eqs. (2.43) and (2.44) (with $A = \alpha^\dagger\alpha$, $t_\mathrm{w} = 0$, and the replacement $s \to s/2$).

Thus, if realizations are post-selected on the condition that no particles are detected in the ancilla, the post-measurement state exhibits the same dynamics as the initial state plus a small contribution on the order of s given by the unequal-time anticommutator $\{B(t), \alpha^\dagger(0)\alpha(0)\}$. This contribution represents the non-Hermitian linear response used in Section 2.3 to measure dynamical correlations and FDRs. In the context of the non-invasive current measurement scheme, this term reflects the measurement back action. If the measurement is post-selected instead on the condition that a particle is detected in the ancilla, the subsequent dynamics corresponds, to leading order, to that of a state with one particle in the mode α annihilated. Finally the expectation value with respect to the unconditional state in Eq. (3.36) (no post-selection) receives contributions from both scenarios, and the result is given by Eq. (2.45).

As these discussions demonstrate, the current measurement protocol is non-invasive in the sense that measurement back action is significantly reduced with respect to standard projective measurements. In fact, the back action can be made arbitrarily small by reducing the strength of the coupling at the cost of a lower signal-to-noise ratio, in line with the rule "no information gain without disturbance" [255]. While we have focused our

discussion on the linear regime, it is clear that the disturbance and thus the measurement back action is more dramatic in the non-linear regime. In practice, it is important to find a good compromise between measurement back action and signal-to-noise ratio, as the numerical benchmarks in Section 3.2 illustrate.

3.1.4. Error Sources and Error Mitigation

An inherent difficulty typical of non-invasive measurement protocols is the low signal-to-noise ratio. This is because these protocols rely on the assumption that the coupling between system and ancilla is weak. Only in this regime, the linear terms in Eq. (3.17), relevant for measuring expectation values of currents, constitute the dominant signal. Thus, it can be challenging for an experiment, on the one hand, to make the coupling sufficiently weak to access the linear regime, and, on the other hand, to obtain a reasonably strong signal. Nevertheless, both requirements can be balanced in realistic situations, as we discuss now in more detail.

Increasing the coupling strength beyond the linear regime leads to a systematic deviation of the measured values and causes a stronger measurement back action, as discussed in Section 3.1.3. As can be seen in Eqs. (3.17a) and (3.17b), the linear and the quadratic terms have opposite signs. Thus, the magnitude of the linear slope is typically underestimated in a linear fit, which leads to a systematic underestimation (overestimation) of the magnitudes of positive (negative) currents (see Fig. 3.3d). The accuracy of the measurement may therefore be improved by combining measurements in positive and negative flow direction. For bosons, the range of the linear regime can in general self-consistently be assessed using the condition that at most a single particle is detected in the ancilla, as higher occupancies can only stem from non-linear processes.

In the bosonic case, it is possible to mitigate the error due to non-linearities using knowledge about higher occupation probabilites. To eliminate the leading order error term in Eq. (3.7), we exploit the fact that the quantities $\langle(\alpha^\dagger\alpha)^2\rangle$ and $\langle\alpha^\dagger\alpha\rangle$ appear with different coefficients in the s^2 terms of the probabilities (3.24). This can be achieved by considering the combinations $p(1)+2p(2)$ or $2-2p(0)-p(1)$, yielding

$$\tilde{p}(0) \equiv 1 - \frac{p(1)+2p(2)}{1-2s/3} = 1 - s\langle A^\dagger A\rangle + \mathcal{O}(s^3)\,. \tag{3.43}$$

This quantity exhibits a significantly extended linear regime, allowing one to operate at higher signal-to-noise ratios, which ultimately leads to a more accurate measurement (see Fig. 3.2).

Apart from the errors due to non-linearities, typical experiments may faultily detect ancilla occupancies. Let α and β denote the rates of false positives and negatives of ancilla occupation, respectively (for simplicity, we do not distinguish different false negative probabilities). Then, instead of Eq. (3.10), one obtains the modified result $p'(0) = (1-\alpha)p(0) + \beta p(n>0)$. Assuming that α and β do not depend on s, this amounts to

$$p'(0) = 1 - \alpha - (1-\alpha-\beta)s\langle\alpha^\dagger\alpha\rangle + \mathcal{O}(s^2)\,, \tag{3.44}$$

i.e., the faulty detection leads to an irrelevant offset due to α, but also to a modified slope by the factor $(1-\alpha-\beta)$. If estimates for α and β are available, these systematic deviations can in principle be corrected for.

Finally, a potential source of experimental errors consists in adjusting the phase difference $\theta_2-\theta_1$ of the system–ancilla coupling. Assume a deviation by an angle $\delta\theta$ from the ideal value $\theta_0=\phi_{\ell_1\ell_2}-\pi/2$ given by Eq. (3.9). Inserting $\theta_2-\theta_1=\theta_0+\delta\theta$ into Eq. (3.8), we find that the deviation results in a measurement of the perturbed operator

$$\begin{aligned}(\alpha^\dagger\alpha)_{\ell_1\ell_2} &= n_{\ell_1}+n_{\ell_2}+\cos(\delta\theta)\frac{j_{\ell_1\ell_2}}{|J_{\ell_1\ell_2}|}+\sin(\delta\theta)\frac{c_{\ell_1\ell_2}}{|J_{\ell_1\ell_2}|}\\ &= n_{\ell_1}+n_{\ell_2}+\frac{j_{\ell_1\ell_2}}{|J_{\ell_1\ell_2}|}+\delta\theta\frac{c_{\ell_1\ell_2}}{|J_{\ell_1\ell_2}|}+\mathcal{O}(\delta\theta^2)\end{aligned} \tag{3.45}$$

with the correlator $c_{\ell_1\ell_2}=J_{\ell_1\ell_2}a^\dagger_{\ell_1}a_{\ell_2}+J^*_{\ell_1\ell_2}a^\dagger_{\ell_2}a_{\ell_1}$. This shows that an erroneous adjustment of the coupling phases leads to a linear deviation of the measured value. Thus, the error behaves in a controlled way and no excessive fine tuning of the coupling phases is required.

3.2. Applications

3.2.1. Chiral Currents in Bosonic Ladders

We first benchmark the proposed measurement scheme at the example of a Harper–Hofstadter model [228–230], which has successfully been realized experimentally in optical lattice setups [181, 231–235]. These and related systems host rich phase diagrams involving transitions between superfluid phases with persistent currents, Laughlin states, as well as (chiral) Mott-insulating and spin liquid phases [236–244].

Here, we focus on interacting bosons on a two-leg ladder in presence of an artificial magnetic field, as depicted in Fig. 3.1a. Denoting sites as $\ell=(\ell_x,\ell_y)$ with ladder legs $\ell_x\in\{\mathrm{L},\mathrm{R}\}$ and rungs $\ell_y\in\{0,\dots,L-1\}$, this model is described by the Hamiltonian (3.1) with real hopping amplitudes along legs, $J_{(\ell_x,\ell_y),(\ell_x,\ell_y+1)}\equiv J$, and complex hopping amplitudes across rungs, $J_{(\mathrm{L},\ell_y),(\mathrm{R},\ell_y)}\equiv K\mathrm{e}^{-i\phi\ell_y}$. This way, each lattice plaquette is pierced by an effective magnetic flux ϕ, which we choose here as $\phi=2\pi/3$. Moreover, we consider on-site interactions at strength U, i.e., we choose the interaction part of the Hamiltonian (3.1) as

$$V=\frac{\hbar U}{2}\sum_\ell n_\ell(n_\ell-1)\,. \tag{3.46}$$

The numerical benchmarks have been obtained using exact diagonalization on a ladder of length $L=6$ with $N=12$ particles (unit filling) and open boundary conditions. We focus on current detection across the ground state phase diagram, although the scheme is equally applicable to mixed states, e.g., at finite temperatures, as well as out of equilibrium.

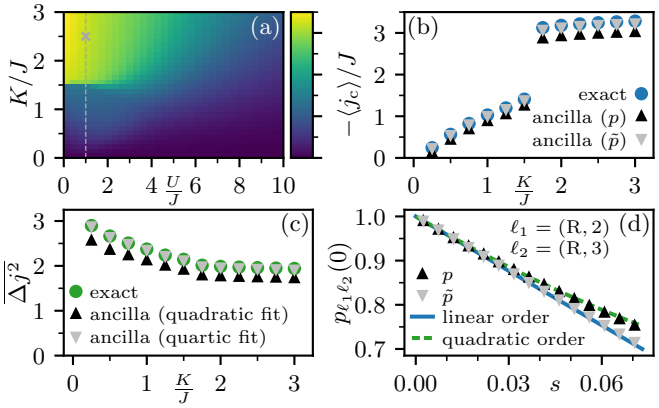

Figure 3.2.: Numerical benchmark of the non-invasive current measurement scheme. (a) The chiral current $\langle j_c \rangle$ acts as an order parameter to distinguish the vortex, Meissner, and Mott-insulating phases. (b) Cross section of the chiral current at $U/J = 1$ (grey dashed line in panel a), in comparison with the values extracted from linear fits to the ancilla occupation probabilities $p(0)$ and $\tilde{p}(0)$. (c) Mean current variance $\overline{\Delta j^2}$ for $U/J = 1$, compared with a simulated measurement involving quadratic and quartic fits to $p(0)$. (d) Probability $p_{\ell_1 \ell_2}(0)$ of not detecting any particles in the ancilla as a function of the effective coupling strength s. The current is probed in the Meissner phase in positive flow direction for the same configuration as in Fig. 3.1 ($K/J = 2.5$ and $U/J = 1$, marked by the grey cross in panel a). The continuous and dashed lines show the predictions from perturbation theory to linear and quadratic order in s, respectively.

To characterize the ground state phases, we use the chiral current

$$j_c = j_L - j_R \tag{3.47}$$

as an order parameter, where

$$j_{\ell_x} = \frac{1}{L-1} \sum_{\ell_y=0}^{L-2} j_{(\ell_x, \ell_y), (\ell_x, \ell_y+1)} \tag{3.48}$$

denotes the average current along the ladder leg ℓ_x [181]. Its behavior across the phase diagram, as resulting from exact diagonalization, is depicted in Fig. 3.2a. At small K/J and U/J, the model hosts a vortex phase, indicated by a small value of $\langle j_c \rangle$ and currents circulating around plaquettes in regular distances (see Fig. 3.1c). Upon increasing K/J, the system undergoes a quantum phase transition to the Meissner phase, characterized by a large chiral current $\langle j_c \rangle$ along the ladder legs. This current mimics the expulsion of an external magnetic field, analogous to the Meissner effect in type-II superconductors. Although the vortex–Meissner phase transition is continuous [238], the chiral current in our case exhibits a jump (see Fig. 3.2b) due to finite-size effects. At large U/J, the system enters a Mott-insulating regime, where any currents are suppressed.

As an additional benchmark observable, we use the mean current variance

$$\overline{\Delta j^2} = \frac{1}{N_{\text{link}}} \sum_{\langle \ell, \ell' \rangle} \frac{\Delta j^2_{\ell\ell'}}{|J_{\ell\ell'}|^2}\,, \tag{3.49}$$

averaged over all $N_{\text{link}} = 3L - 2$ links between nearest neighbors, where $\Delta j^2_{\ell\ell'}$ is the variance of the current between the sites ℓ and ℓ', as defined in Eq. (3.19). As can be seen in Fig. 3.2c, this quantity gradually decreases in the vortex phase as the tunneling K/J across the ladder rungs becomes stronger, until it saturates in the Meissner phase close to the value $\overline{\Delta j^2} = 2$ expected in the superfluid phase [180].

Numerical Benchmark of the Non-Invasive Current Measurement Scheme

To simulate the non-invasive measurement scheme, the full evolution of system plus ancilla under the Hamiltonian $H_0 + H_{\text{cpl}}$ during a fixed coupling time $J\delta t = 0.01$ has been computed for variable coupling strengths Ω. Figure 3.2d shows the probability $p_{\ell_1\ell_2}(0)$ as a function of $s = (\Omega \Delta t)^2$, where the coupling is set up for probing a local leg current in the Meissner phase in positive flow direction (cf. Fig. 3.1). For sufficiently small values of s, the result agrees well with the analytical approximations (3.17) to linear and quadratic order in s, while higher-order non-linear effects become relevant as s increases. This behavior reflects the trade-off between maximizing the signal-to-noise ratio (large s preferred) and minimizing the systematic errors due to non-linearities (small s preferred). For bosons, the linear regime can be significantly extended by resolving individual occupation numbers. For instance, the combination $\tilde{p}(0)$ in Eq. (3.43) agrees with $p(0)$ in Eq. (3.10) to linear order, while it is chosen such that the leading error term vanishes (see Section 3.1.4). As can be seen in Fig. 3.2d, this quantity allows one to extract the linear slope more reliably, enabling a higher signal-to-noise ratio.

In Fig. 3.2b, the chiral current obtained from a simulation of the measurement scheme is compared with the exact result. All constituent nearest-neighbor currents have been extracted in positive flow direction, where the system's response to the coupling is stronger (see discussion below). While in principle Eq. (3.10) allows for the extrapolation to $s = 0$ with arbitrary precision, in practice, a realistic signal-to-noise ratio requires a certain minimum fit range Δs (or equivalently Δp). Figure 3.2b shows the result for linear fits in the ranges $\Delta p = 6\,\%$ and $\Delta \tilde{p} = 20\,\%$ (the latter has also been used for Fig. 3.1c), which represents a satisfactory compromise between accuracy and signal strength.

Figure 3.2c shows a benchmark of the scheme for measuring the mean current variance $\overline{\Delta j^2}$ (see Section 3.1.2). This quantity has been obtained by extracting the local variance $\Delta j^2_{\ell_1\ell_2}$ of each nearest-neighbor current from the s^2 term of the probability (3.24a), assuming that the surrounding terms in that expression have been obtained separately. Moreover, the variance has been probed against the current's flow direction, as in this case the quadratic part of the probability is easier to resolve at small coupling strengths. In Fig. 3.2c, the variances have been extracted by fitting quadratic and quartic polynomials to the probabilities in the ranges $\Delta p = 6\,\%$ and $\Delta p = 20\,\%$,

respectively. While the quadratic fits yield reasonable estimates of the variances, fitting higher-order polynomials can produce more accurate results, provided the quality of the data is sufficient. The robustness of the non-invasive protocol against further potential error sources is discussed in Section 3.1.4.

Depending on the sign of the current, the system reacts more or less sensitively to the coherent coupling. This feature has the consequence that for positive currents, the effective perturbation strength s required to achieve a certain change of the ancilla occupation probability is much smaller than for negative currents. The performance of the scheme for measuring currents and their variances in positive and negative flow direction is analyzed in Fig. 3.3. For current expectation values, the scheme yields comparable results in either direction, allowing one to choose the configuration that best fits the experimental characteristics. In the case of current variances, the performance of the scheme varies depending on the direction in which the variance is probed. As for positive currents the quantity $\langle(\alpha^\dagger\alpha)^2\rangle$ is larger (see Fig. 3.3e), this quantity needs to be extracted more accurately to obtain the desired second moment of the current operator $\langle j^2_{\ell_1\ell_2}\rangle$ with a given precision than it is the case for negative currents. In addition, since the linear coefficient $\langle\alpha^\dagger\alpha\rangle$ is smaller for negative currents (see Fig. 3.3c), the quadratic regime is easier to resolve when probing the current in this direction (cf. Figs. 3.3a and 3.3b). For these reasons, it is preferable to probe the variance against the flow direction of the current (see Fig. 3.3f).

Global Measurement of the Chiral Current

So far, we have focused our discussion and benchmark examples on probing local current statistics, e.g., nearest-neighbor currents and their variances. Beyond these basic building blocks, the non-invasive scheme can immediately be extended to more general observables involving multiple local currents, e.g., currents through or into a given lattice site. In some situations, one is even interested in global currents, as is the case for the chiral current in the bosonic ladder system. Although global currents can be calculated from a summation of local ones, it can be more efficient to measure the global quantity of interest directly. Furthermore, in experiments without single-site addressing, only global quantities are typically accessible. Within the framework of our non-invasive measurement protocol, the sum of arbitrary local currents can be obtained directly by simultaneously coupling the relevant pairs of modes each to a distinct ancilla, located, for instance, at the intermediate sites of an optical superlattice. According to Eq. (3.17a), to linear order in s, the probability of not populating any ancilla then gives access to the desired sum of local currents, while the corresponding variance can be extracted from the quadratic order in s.

In what follows, we discuss a possible setup for the direct measurement of the chiral current in the bosonic ladder system using multiple ancillas. We consider a total of $M = 2L$ ancillas located midway between the system lattice sites on the ladder legs. They are labeled by the index $m = (m_x, m_y)$ with $m_x \in \{\mathrm{L}, \mathrm{R}\}$ and $m_y \in \{0, \dots, L-1\} + 1/2$, where we consider periodic boundary conditions for ease of notation. The ancilla $(m_x = \ell_x, m_y = l_y + 1/2)$ is then coupled to the lattice sites (l_x, l_y) and $(l_x, l_y + 1)$, and the

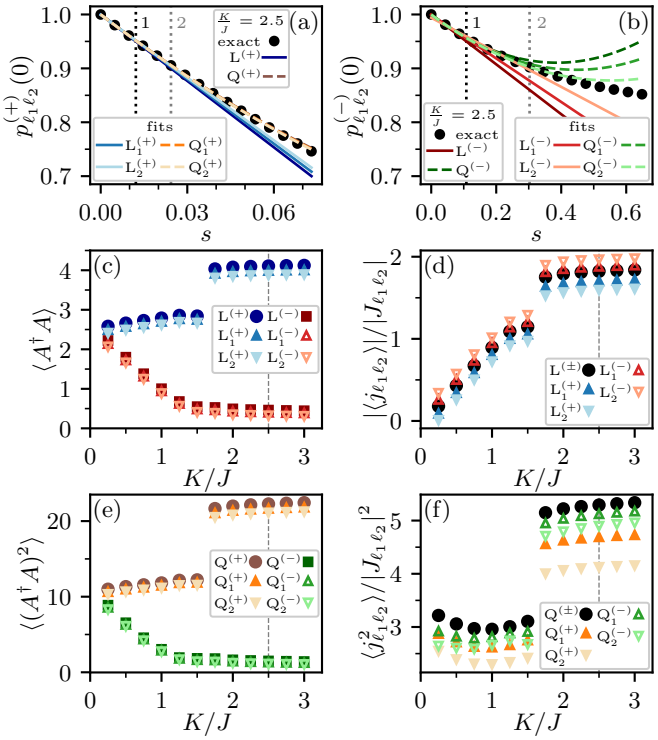

Figure 3.3.: Performance of the scheme for measuring currents and their variances in positive and negative flow direction. (a),(b) Probability $p^{(\pm)}_{\ell_1\ell_2}(0)$ of not detecting any particles in the ancilla as a function of the effective coupling strength $s = (\Omega\Delta t)^2$ for a bosonic ladder with rung hopping strength $K/J = 2.5$ (dashed vertical lines in central and lower panels), on-site interaction $U/J = 1$, and magnetic flux $\phi = 2\pi/3$. The lattice sites $\ell_1 = (\mathrm{R}, 2)$ and $\ell_2 = (\mathrm{R}, 3)$ are coupled such that the current is probed in positive (+) or negative (−) flow direction. The numerically computed probabilities are compared to the analytical prediction in Eq. (3.24a) to linear (L) and quadratic (Q) order in s. To extract the first and second moment of the current operator, we fit, respectively, linear and quadratic polynomials to $p^{(\pm)}_{\ell_1\ell_2}$ in the ranges $\Delta p = 5\,\%$ (1) and $\Delta p = 10\,\%$ (2), as marked by the dotted vertical lines. For negative currents (b), the system responds less strong to the coupling, making the linear and quadratic orders in s easier to distinguish than for positive currents (a). (c) The expectation value of the operator $\alpha^\dagger\alpha = n_{\ell_1} + n_{\ell_2} + j_{\ell_1\ell_2}/|J_{\ell_1\ell_2}|$ extracted from the linear fits ($\mathrm{L}_1^{(\pm)}$ and $\mathrm{L}_2^{(\pm)}$) tends to underestimate the exact result ($\mathrm{L}^{(\pm)}$). (The y-axis labels use the notation $A \equiv \alpha$.) (d) Currents computed from the values of $\langle\alpha^\dagger\alpha\rangle$ in (c). The magnitudes of the currents are systematically underestimated (overestimated) for measurements in positive (negative) flow direction. (e),(f) While the values of $\langle(\alpha^\dagger\alpha)^2\rangle$ (e) extracted from the quadratic fits ($\mathrm{Q}_1^{(\pm)}$ and $\mathrm{Q}_2^{(\pm)}$) deviate only little from the exact result ($\mathrm{Q}^{(\pm)}$), the derived second moments of the current operator $\langle j^2_{\ell_1\ell_2}\rangle$ (f) exhibit large errors for those values based on $p^{(+)}$. Consequently, $p^{(-)}$ is preferred for measuring current variances.

phases are chosen as in Eq. (3.9) such that

$$(\alpha^\dagger\alpha)_{(\mathrm{L},\ell_y+1/2)} = n_{(\mathrm{L},\ell_y)} + n_{(\mathrm{L},\ell_y+1)} + \frac{1}{J} j_{(\mathrm{L},\ell_y),(\mathrm{L},\ell_y+1)}\,, \tag{3.50a}$$

$$(\alpha^\dagger\alpha)_{(\mathrm{R},\ell_y+1/2)} = n_{(\mathrm{R},\ell_y)} + n_{(\mathrm{R},\ell_y+1)} - \frac{1}{J} j_{(\mathrm{R},\ell_y),(\mathrm{R},\ell_y+1)}\,. \tag{3.50b}$$

For simplicity, we assume the hopping amplitudes along the ladder legs to be of equal magnitude $J \equiv |J_{(l_x,l_y),(l_x,l_y\pm1)}|$, although spatial anisotropies in the hopping amplitudes can be accounted for by adjusting the relative magnitudes of the coefficients $\lambda_{m\ell}$ in Eq. (3.12) appropriately. This configuration then yields

$$\sum_m \alpha_m^\dagger \alpha_m = \frac{L}{J} j_\mathrm{c} + 2N\,, \tag{3.51}$$

where the chiral current operator for periodic boundary conditions reads

$$j_\mathrm{c} = \frac{1}{L}\sum_{l_y=0}^{L-1} \left[j_{(\mathrm{L},\ell_y),(\mathrm{L},\ell_y+1)} - j_{(\mathrm{R},\ell_y),(\mathrm{R},\ell_y+1)} \right] \tag{3.52}$$

and $N = \sum_\ell n_\ell$ is the total particle number operator, which reduces to a constant when working in a subspace with a fixed number of particles. The probability of not finding any particles in any ancilla (3.17a) thus becomes

$$P_0 = 1 - s\left\langle \frac{L}{J} j_\mathrm{c} + 2N \right\rangle + \mathcal{O}(s^2) \tag{3.53}$$

with $s \equiv s_m = (\Omega_m \delta t)^2$, giving access to the chiral current $\langle j_\mathrm{c}\rangle$.

By resolving this probability up to quadratic order in s, it is possible to also obtain the variance of the chiral current $\Delta j_\mathrm{c}^2 = \langle j_\mathrm{c}^2\rangle - \langle j_\mathrm{c}\rangle^2$. To eliminate the terms $\langle \alpha_m^\dagger \alpha_k^\dagger \alpha_k \alpha_m\rangle$ in Eq. (3.17a), it is convenient to consider the quantity $P_0 - P_2/3$, where

$$P_2 = \frac{1}{2}\sum_{m_1\neq m_2} P_2^{(m_1,m_2)} + \sum_m P_2^{(m)} \tag{3.54}$$

is the probability of finding two particles in ancillary modes all together. We then obtain, up to quadratic order in s, the result

$$\begin{aligned} P_0 - \frac{1}{3}P_2 &= 1 - s\sum_m \left\langle \alpha_m^\dagger \alpha_m \right\rangle + \frac{1}{3}s^2 \left\langle \Big(\sum_m \alpha_m^\dagger \alpha_m \Big)^2 \right\rangle \\ &= 1 - s\left\langle \frac{L}{J} j_\mathrm{c} + 2N \right\rangle + \frac{1}{3}s^2 \left\langle \left(\frac{L}{J} j_\mathrm{c} + 2N \right)^2 \right\rangle, \end{aligned} \tag{3.55}$$

from which the variance of the chiral current can be extracted in a similar way as described in Section 3.1.2. Such a global measurement using multiple ancillas can be much more efficient than measuring the constituent local currents and pairwise current correlations individually.

3.2.2. Chiral Loop Current Correlations Under Geometric Frustration

In our second benchmark example, we apply the non-invasive current measurement scheme to reveal chiral phases in frustrated quantum matter through loop current correlations. Specifically, we consider hard-core bosons on a spatially anisotropic triangular lattice at half filling, which exhibit a rich ground state phase diagram of 1D and 2D Néel as well as subtle chiral phases [245–248]. After introducing the model along with the chiral loop current correlation as the order parameter of the chiral phase, we discuss how to efficiently probe such loop current correlations, corroborated by numerical benchmarks.

Frustrated Hard-Core Bosons on a Spatially Anisotropic Triangular Lattice

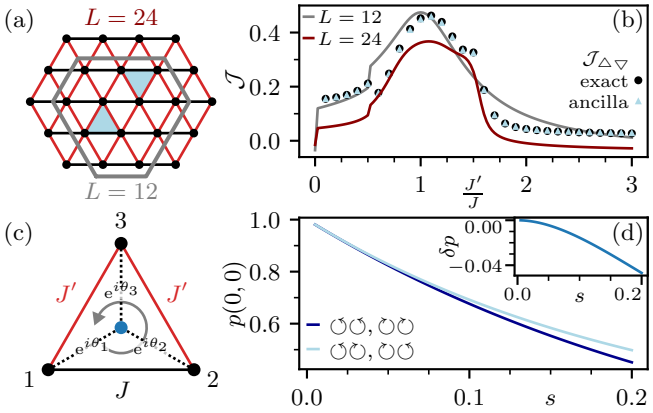

Figure 3.4.: Measurement scheme for loop current correlations revealing the chiral phase of frustrated bosons on a spatially anisotropic triangular lattice (a) with positive nearest-neighbor hopping amplitudes J (black bonds) and J' (red bonds). (b) The mean loop current correlation $\mathcal{J}$ is peaked around $J'/J = 1$, indicating long-range chiral order. (c) By coupling the three sites of a triangle to a central ancilla with properly chosen phases, loop current correlations can be probed efficiently with only two measurement configurations. (d) Probability of not detecting any particles in either ancilla for the pair of triangles $(\triangle, \triangledown)$ highlighted in (a) and different combinations of counter-clockwise ($\circlearrowleft$) and clockwise ($\circlearrowright$) directions of the probed loop currents ($L = 24$, $J'/J = 1$). The inset shows the difference δp of the two curves, which yields $\mathcal{J}_{\triangle\triangledown}$ plotted in (b).

We consider the Bose–Hubbard Hamiltonian describing ultracold atoms in optical lattices,

$$H_0 = \sum_{\langle \ell, \ell' \rangle} \hbar J_{\ell\ell'} a_\ell^\dagger a_{\ell'} + \frac{\hbar U}{2} \sum_\ell n_\ell (n_\ell - 1)\,, \tag{3.56}$$

where a_ℓ, $a_\ell^\dagger$, and n_ℓ are bosonic annihilation, creation, and number operators, respectively, and the sum in the first term runs over all pairs of nearest neighbors $\langle \ell, \ell' \rangle$. The model becomes frustrated if the hopping amplitudes are positive (anti-ferromagnetic), $J_{\ell\ell'} = |J_{\ell\ell'}|$. Note that in the notation of Eqs. (1.42) and (3.1), this situation corresponds to Peierls phases of $\phi_{\ell\ell'} = \pm\pi$, which can be realized employing the established

techniques for generating synthetic gauge fields [71, 74, 250]. In what follows, we focus on triangular lattices like those depicted in Fig. 3.4a, spanned by the primitive lattice vectors $\boldsymbol{\tau}_1 = (1,0)^T$ and $\boldsymbol{\tau}_2 = (1/2, \sqrt{3}/2)^T$ (the lattice constant is set to unity). We denote the (positive) hopping amplitude along the horizontal directions $\pm\boldsymbol{\tau}_1$ by J, and that along the diagonal directions $\pm\boldsymbol{\tau}_2$ and $\pm(\boldsymbol{\tau}_2 - \boldsymbol{\tau}_1)$ by J'. Furthermore, we consider the hard-core limit of infinitely strong on-site interactions $U \to \infty$ at half filling, $\langle n_\ell \rangle = 1/2$. The Hamiltonian (3.56) then maps to the spin-1/2 XY Hamiltonian with anti-ferromagnetic interactions on a spatially anisotropic triangular lattice, which hosts a rich phase diagram of 1D and 2D Néel, spiral, as well as candidate regions for extended spin-liquid phases [245–248].

Here, we are particularly interested in the spiral (or chiral) phase, which is characterized by long-range chirality correlations [245–249]. For a spin-1/2 system, the vector chirality is defined as

$$\kappa_\triangle = \frac{2}{3\sqrt{3}} \left[\boldsymbol{S}_{\ell_1} \times \boldsymbol{S}_{\ell_2} + \boldsymbol{S}_{\ell_2} \times \boldsymbol{S}_{\ell_3} + \boldsymbol{S}_{\ell_3} \times \boldsymbol{S}_{\ell_1} \right]_z , \tag{3.57}$$

where $\boldsymbol{S}_\ell = (S^x_\ell, S^y_\ell, S^z_\ell)^T$ is the vector of spin-1/2 operators at site ℓ and the indices (ℓ_1, ℓ_2, ℓ_3) label the corners of the triangular plaquette $\triangle$ in counter-clockwise direction. The normalization is chosen such that $\kappa_\triangle = \pm 1$ for the ground states of the classical anti-ferromagnetic XY model on a single triangle [256]. By means of the Holstein–Primakoff transformation [257], we can identify the spin raising and lowering operators $S^\pm_\ell = S^x_\ell \pm i S^y_\ell$, respectively, with the annihilation and creation operators a_ℓ and $a^\dagger_\ell$ of hard-core bosons. The vector chirality (3.57) then translates into the bosonic loop current operator around the plaquette [249],

$$\begin{aligned} \kappa_\triangle &= \frac{2}{3\sqrt{3}} \frac{1}{2} (-i) \left[S^-_{\ell_1} S^+_{\ell_2} + S^-_{\ell_2} S^+_{\ell_3} + S^-_{\ell_3} S^+_{\ell_1} - \text{h.c.} \right] \\ &= \frac{2}{3\sqrt{3}} \frac{1}{2} (-i) \left[a^\dagger_{\ell_1} a_{\ell_2} + a^\dagger_{\ell_2} a_{\ell_3} + a^\dagger_{\ell_3} a_{\ell_1} - \text{h.c.} \right] \\ &= -\frac{1}{3\sqrt{3}} \tilde{j}_\triangle \, . \end{aligned} \tag{3.58}$$

Here, the normalized loop current operator $\tilde{j}_\triangle$ is defined as the sum of the normalized current operators along the edges of the triangle in counter-clockwise direction (see Fig. 3.4c),

$$\tilde{j}_\triangle = \tilde{j}_{\ell_1 \ell_2} + \tilde{j}_{\ell_2 \ell_3} + \tilde{j}_{\ell_3 \ell_1} \, , \tag{3.59}$$

with $\tilde{j}_{\ell\ell'} = j_{\ell\ell'}/|J_{\ell\ell'}| = i(a^\dagger_\ell a_{\ell'} - a^\dagger_{\ell'} a_\ell)$ for the Hamiltonian (3.56).

Intuitively, the chiral phase is characterized by loop currents of alternating signs around triangles pointing upwards and downwards. However, the loop currents vanish on average and thus do not constitute a good order parameter. Instead, it has been shown that the long-range chiral order is revealed by the chirality correlation [245–249]. In the language of hard-core bosons, this order parameter corresponds to the chiral loop

current correlation [249], which we define for two triangles a and b as[3]

$$\mathcal{J}_{ab} = \frac{1}{3}\sigma_a\sigma_b\left\langle \tilde{j}_a\tilde{j}_b\right\rangle , \tag{3.60}$$

where $\sigma_a = +1$ ($\sigma_a = -1$) if the triangle a points upwards (downwards) [247]. The normalization is chosen as per usual convention[4] [245–247].

To reduce finite-size effects, we also define the mean loop current correlation

$$\mathcal{J} = \frac{1}{\mathcal{N}}{\sum_{a,b}}' \mathcal{J}_{ab}, \tag{3.61}$$

where $\mathcal{N}$ is a normalization corresponding to the number of terms in the sum which runs over all pairs of triangles that do not share a common edge. This definition reduces the effect of short-ranged correlations, which are typically suppressed in the thermodynamic limit, but may lead to artifacts in a system of finite size.

The mean loop current correlation, as obtained from exact diagonalization, is shown in Fig. 3.4b for two system sizes. This order parameter is clearly peaked around the isotropic point $J'/J = 1$, where chiral order is expected, and close to zero for small and large lattice anisotropies J'/J, where one expects 1D and 2D Néel order instead. Clearly, for finite lattices as in Fig. 3.4a, the order parameter is smooth as the system is rather far from the thermodynamic limit. To obtain sharper phase boundaries, one could approach the thermodynamic limit by finite-size scaling, which has been done, for example, in Ref. [247] for the XY model.

It is worth emphasizing that for the present model, the chirality cannot be revealed from simple expectation values of loop currents. In fact, any current vanishes on average in the ground state because the Hamiltonian (3.56) is real. In what follows, we show how the non-invasive measurement scheme can be extended to give access to loop current correlations capable of revealing the subtle chiral phases.

Non-Invasive Measurement of Loop Currents

Before turning to the measurement of loop current correlations as relevant for the present application, we first discuss an efficient way to measure expectation values of persistent loop currents around lattice plaquettes, arising, e.g., as a consequence of chiral symmetry breaking in frustrated systems [245–248, 259, 260]. While such loop currents can in principle be accessed by measuring nearest-neighbor currents across the individual links forming a plaquette, the required number of measurements can be reduced by coupling all sites of the plaquette simultaneously to the same ancilla.

[3]Note that the operator $\tilde{j}_a\tilde{j}_b$ is Hermitian only if $\tilde{j}_a$ and $\tilde{j}_b$ commute, which is the case if the two triangles do not share any common vertices or edges, as relevant for the long-range chiral loop current correlations we are interested in here. To ensure that the loop current correlation (3.60) is real for any pair of triangles, one could replace $\langle\tilde{j}_a\tilde{j}_b\rangle$ with the symmetrized correlator $\langle\{\tilde{j}_a,\tilde{j}_b\}\rangle/2$.

[4]The normalization of the order parameter (3.60) is chosen such that its maximum value is unity, which follows from the theoretical maximum of the chirality corrlation $\langle\kappa_\triangle^2\rangle_{\max} = 1/9$, yielding $\mathcal{J}_{\max} = \langle\tilde{j}_\triangle^2\rangle_{\max}/3 = 9\langle\kappa_\triangle^2\rangle_{\max} = 1$. This value is realized, e.g., in the ground state of a fully frustrated quantum Heisenberg anti-ferromagnet on a triangular plaquette [258].

Here, we illustrate this principle for a single triangular plaquette as depicted in Fig. 3.4c. The corresponding loop current operator is given by

$$j_{\triangle} = j_{12} + j_{23} + j_{31}\,, \tag{3.62}$$

where we allow for arbitrary hopping amplitudes and Peierls phases of the involved nearest-neighbor currents $j_{\ell\ell'}$.

The three lattice sites forming a plaquette are coupled to a central ancilla via the coupling operator

$$\alpha = r_1 \mathrm{e}^{i\theta_1} a_1 + r_2 \mathrm{e}^{i\theta_2} a_2 + r_3 \mathrm{e}^{i\theta_3} a_3\,. \tag{3.63}$$

To account for spatial anisotropies in the hopping amplitudes, we choose the magnitudes of the couplings according to

$$r_1 = \sqrt{\frac{\zeta_{12}\zeta_{31}}{\zeta_{23}}}\,, \quad r_2 = \sqrt{\frac{\zeta_{12}\zeta_{23}}{\zeta_{31}}}\,, \quad r_3 = \sqrt{\frac{\zeta_{23}\zeta_{31}}{\zeta_{12}}}\,, \tag{3.64}$$

where $\zeta_{\ell\ell'} = |J_{\ell\ell'}|/J$ denotes the magnitude of the hopping amplitude $J_{\ell\ell'}$, relative to some arbitrary energy scale $J > 0$. To obtain the correct Peierls phases $\phi_{\ell\ell'} = \arg(J_{\ell\ell'})$ of the currents, the coupling phases should be chosen as

$$\theta_2 - \theta_1 = \phi_{12} - \vartheta_1 \pmod{2\pi}\,, \tag{3.65a}$$
$$\theta_3 - \theta_2 = \phi_{23} - \vartheta_2 \pmod{2\pi}\,, \tag{3.65b}$$
$$\theta_1 - \theta_3 = \phi_{31} - \vartheta_3 \pmod{2\pi}\,. \tag{3.65c}$$

However, by summing these equations, one can see that the angles ϑ_1, ϑ_2, and ϑ_3 cannot be chosen arbitrarily, but they must satisfy the constraint

$$\vartheta_1 + \vartheta_2 + \vartheta_3 \pmod{2\pi} = \Phi, \tag{3.66}$$

where $\Phi = \phi_{12} + \phi_{23} + \phi_{31} \pmod{2\pi}$ is the effective magnetic flux through the plaquette. We then obtain

$$\begin{aligned}\alpha^\dagger\alpha = {} & r_1^2 n_1 + r_2^2 n_2 + r_3^2 n_3 + \frac{1}{J}[\cos(\vartheta_1)c_{12} + \cos(\vartheta_2)c_{23} + \cos(\vartheta_3)c_{31}] \\ & + \frac{1}{J}[\sin(\vartheta_1)j_{12} + \sin(\vartheta_2)j_{23} + \sin(\vartheta_3)j_{31}],\end{aligned} \tag{3.67}$$

where $c_{\ell\ell'} = J_{\ell\ell'} a_\ell^\dagger a_{\ell'} + J_{\ell\ell'}^* a_{\ell'}^\dagger a_\ell$ denotes the correlator between the sites ℓ and ℓ'.

The last term in Eq. (3.67) becomes proportional to the loop current operator (3.62) if $\sin(\vartheta_1) = \sin(\vartheta_2) = \sin(\vartheta_3)$, which is most conveniently achieved by choosing the same value ϑ for all angles ϑ_i. The constraint (3.66) then enforces

$$\vartheta = \frac{\Phi + 2\pi k}{3} \tag{3.68}$$

with $k \in \mathbb{Z}$ and Eq. (3.67) simplifies to

$$\alpha^\dagger\alpha = n_{\triangle} + \frac{1}{J}\cos(\vartheta)c_{\triangle} + \frac{1}{J}\sin(\vartheta)j_{\triangle}\,, \tag{3.69}$$

where $n_\triangle = r_1^2 n_1 + r_2^2 n_2 + r_3^2 n_3$ and $c_\triangle = c_{12} + c_{23} + c_{31}$.

For the special value $\Phi = \pm\pi/2$ of the magnetic flux, the choice $k = \mp 1$ in Eq. (3.68) yields $\vartheta = \mp\pi/2$, such that the coefficient of $c_\triangle$ in Eq. (3.69) vanishes. Thus, if the density $\langle n_\triangle \rangle$ is known, the loop current $\langle j_\triangle \rangle$ can be extracted from only a single measurement configuration.

For general values of the magnetic flux Φ, it is possible to deduce the loop current from two measurement configurations (provided the density $\langle n_\triangle \rangle$ is known). Given the measured values $\langle \alpha^\dagger \alpha \rangle^{(k_1)}$ and $\langle \alpha^\dagger \alpha \rangle^{(k_2)}$ for two different angles $\vartheta^{(k_1)}$ and $\vartheta^{(k_2)}$ chosen in accordance with Eq. (3.68) (where $k_1 - k_2$ is not a multiple of 3), Eq. (3.69) yields two equations with unknowns $\langle c_\triangle \rangle$ and $\langle j_\triangle \rangle$, which can readily be solved for the desired expectation value of the loop current. For example, in case of a fully frustrated triangular plaquette with $\Phi = \pi$, the choices $k_1 = 0$ and $k_2 = -1$, corresponding to $\vartheta = \pm\pi/3$, yield $\langle \alpha^\dagger \alpha \rangle^{(\pm)} = \langle n_\triangle \rangle + \langle c_\triangle \rangle / 2J \pm \sqrt{3} \langle j_\triangle \rangle / 2J$. These two configurations can be thought of as probing the loop current in positive and negative flow direction, respectively. The expectation value of the loop current can then be isolated by taking the difference of the two results.

All in all, coupling the three sites of a triangular plaquette simultaneously to a central ancilla has the advantage of reducing the number of measurement configurations from three, corresponding to separate measurements of the relevant nearest-neighbor currents, to at most two. This concept can also be applied to other plaquette geometries.

Non-Invasive Measurement of Loop Current Correlations

We now extend the above approach to the measurement of loop current correlations on a triangular lattice, revealing the chiral phase of frustrated bosons as illustrated in Fig. 3.4.

To begin with, we note that the loop current correlation can be written as

$$\left\langle \tilde{j}_a \tilde{j}_b \right\rangle = \sum_{(\ell_1,\ell_2)\in a} \sum_{(\ell_3,\ell_4)\in b} \left\langle \tilde{j}_{\ell_1\ell_2} \tilde{j}_{\ell_3\ell_4} \right\rangle, \tag{3.70}$$

where the sums run over all pairs of sites forming the edges of the triangles a and b. Recall that the tilde denotes the normalized (loop) current operator as defined in Eq. (3.59). The spatial current correlation $\langle \tilde{j}_{\ell_1\ell_2} \tilde{j}_{\ell_3\ell_4} \rangle$ can be accessed in the same way as detailed in Section 3.1.2. One disadvantage of this procedure is that the measurement of the current correlation for all relevant pairs of links may be somewhat tedious.

Alternatively, it can be more efficient to access the loop current operator directly by coupling the three sites forming a triangle simultaneously to a central ancilla, as discussed above. Analogously to Eq. (3.63), the corresponding coupling operator in the coupling Hamiltonian (3.12) is given by

$$\alpha_m = \mathrm{e}^{\theta_{m,1}} a_{m,1} + \mathrm{e}^{\theta_{m,2}} a_{m,2} + \mathrm{e}^{\theta_{m,3}} a_{m,3}\,, \tag{3.71}$$

where $m \in \{a, b\}$ labels both the ancillas and the triangles. According to Eqs. (3.65) to (3.67), choosing the phases as $\theta_{m,i+1} - \theta_{m,i} = \pm 2\pi/3$, where the index $i \in \{1, 2, 3\}$

enumerates the sites within a triangle (wrapping around), yields

$$\alpha_m^\dagger \alpha_m = n_m + \frac{1}{2}\tilde{c}_m \pm \frac{\sqrt{3}}{2}\tilde{j}_m \,. \tag{3.72}$$

Here, $n_m = n_{m,1} + n_{m,2} + n_{m,3}$ and $\tilde{c}_m = \tilde{c}_{m,12} + \tilde{c}_{m,23} + \tilde{c}_{m,31}$ with the correlators $\tilde{c}_{m,ij} = -(a_{m,i}^\dagger a_{m,j} + a_{m,j}^\dagger a_{m,i})$. For simplicity, we focus in what follows on the case where the triangles have no common vertices or edges, as is most relevant for characterizing long-range chiral loop current correlations.

The probability of not detecting any particles in either of the two ancillas is then, in analogy to Eq. (3.27), given by

$$p(0,0) = 1 + [p_a(0) - 1] + [p_b(0) - 1] + s^2 \left\langle \alpha_a^\dagger \alpha_a \alpha_b^\dagger \alpha_b \right\rangle + \mathcal{O}(s^3)\,, \tag{3.73}$$

where $p_m(0)$ is the probability of not detecting any particles in the ancilla if the coupling was applied only to triangle m, given by Eq. (3.17a) for $M = 1$. Note that the hard-core constraint also applies to the ancilla, although this is not necessary for the protocol to work.

The correlator $\langle \alpha_a^\dagger \alpha_a \alpha_b^\dagger \alpha_b \rangle$ in Eq. (3.73) contains the desired loop current correlation $\langle \tilde{j}_a \tilde{j}_b \rangle$ appearing in Eq. (3.60). To isolate it, one could extract the coefficient of the s^2 term in Eq. (3.73) and separately measure all surrounding terms appearing in $\alpha_a^\dagger \alpha_a \alpha_b^\dagger \alpha_b$ as well as in $p_a(0)$ and $p_b(0)$. However, there is a more efficient way to achieve this goal. According to Eq. (3.72), by flipping the signs of the phases $\theta_{m,i}$, we have the freedom to probe the loop current in counter-clockwise ($\circlearrowleft$) or clockwise ($\circlearrowright$) direction for each triangle individually. This admits the four combinations $\{\circlearrowleft\circlearrowleft, \circlearrowleft\circlearrowright, \circlearrowright\circlearrowleft, \circlearrowright\circlearrowright\}$. In analogy to Eq. (3.29), by noting that the operators n_m and c_m do not change their signs upon flipping the phases $\theta_{m,i}$, we can access the loop current correlation through the combination

$$\frac{p_{\circlearrowleft\circlearrowleft} - p_{\circlearrowleft\circlearrowright} - p_{\circlearrowright\circlearrowleft} + p_{\circlearrowright\circlearrowright}}{4} = \frac{3}{4} s^2 \left\langle \tilde{j}_a \tilde{j}_b \right\rangle + \mathcal{O}(s^3). \tag{3.74}$$

Since the Hamiltonian (3.56) is real, its ground state can be chosen to have real coefficients. For this reason, ground state expectation values of loop currents vanish identically, $\langle j_m \rangle_0 = 0$, as do the correlations $\langle n_m \tilde{j}_{m'} \rangle_0$ and $\langle c_m \tilde{j}_{m'} \rangle_0$. This implies $p_{\circlearrowleft\circlearrowleft} = p_{\circlearrowright\circlearrowright}$ and $p_{\circlearrowleft\circlearrowright} = p_{\circlearrowright\circlearrowleft}$, which allows one to isolate the loop current correlation in the ground state from only two measurement configurations according to

$$p_{\circlearrowleft\circlearrowleft} - p_{\circlearrowleft\circlearrowright} = \frac{3}{2} s^2 \left\langle \tilde{j}_a \tilde{j}_b \right\rangle_0 + \mathcal{O}(s^3). \tag{3.75}$$

In Fig. 3.4d, we show the probabilities of not detecting any particles in either ancilla for loop currents probed in equal ($p_{\circlearrowleft\circlearrowleft}$) and opposite ($p_{\circlearrowleft\circlearrowright}$) directions around the pair of triangles ($\triangle, \triangledown$) marked in Fig. 3.4a. Their difference, shown in the inset, is proportional to the loop current correlation according to Eq. (3.75), whose values can reliably be extracted with a quartic fit (see Fig. 3.4b). As this numerical benchmark demonstrates, the protocol discussed above provides an efficient way to access chiral

loop current correlations capable of revealing long-range chiral order in frustrated quantum matter. Although it may be challenging for present-day experiments to achieve the required resolution, such a measurement represents an attractive intermediate target in the endeavor of creating full-fledged quantum simulators.

3.2.3. Spin Currents in Trapped-Ion Systems

As a third application, we discuss how to implement the non-invasive current measurement protocol in trapped-ion platforms. To this end, we first specify the class of Hamiltonians as well as the type of currents we intend to investigate. We then present a possible implementation of the measurement scheme, where a collective vibrational mode plays the role of the ancilla. Unlike in our previous discussion, where we have assumed the ancilla to be empty, we consider the ancillary collective mode to be thermally occupied, which is a common scenario in trapped-ion systems. We present a generalization of the measurement scheme adapted to this setup, and discuss how to harness standard tools of trapped-ion experiments in order to measure the desired currents in these systems.

Spin Hamiltonian and Current Operator

Trapped-ion quantum simulation experiments enable controlled studies of interacting systems of spins [195–197] as well as bosons [261, 262]. Though the proposed measurement scheme is general, we focus here on quantum simulation experiments for spin-1/2 degrees of freedom, which in trapped ions can be represented by two internal electronic states. By coupling to the collective vibrational modes of the ion crystal, it is possible to engineer generic spin Hamiltonians of Heisenberg type [263], in particular also those with isotropic spin–spin interaction in x- and y-direction [182, 208]. The corresponding Hamiltonian is given by

$$H_0 = -\sum_{\ell \neq \ell'} \hbar J_{\ell\ell'} S_\ell^+ S_{\ell'}^- + V \,. \tag{3.76}$$

Here, $S_\ell^\pm = S_\ell^x \pm i S_\ell^y$ are the spin raising and lowering operators at site ℓ, defined in terms of the local spin-1/2 operators S_ℓ^α with $\alpha \in \{x, y, z\}$, and $J_{\ell\ell'} = J_{\ell'\ell}^*$ are the (possibly complex [250]) interaction constants in x- and y-direction. Furthermore, the term V represents a possible spin interaction in z-direction, which can be engineered using additional phononic modes [263]. Important special cases of the Hamiltonian (3.76) include the XY model ($J_{\ell\ell'} = J_{\ell\ell'}^*$ and $V = 0$) or the XXZ model ($J_{\ell\ell'} = J_{\ell\ell'}^*$ and $V = -\sum_{\ell\ell'} \hbar J_{\ell\ell'}^z S_\ell^z S_{\ell'}^z$), both of which are ubiquitous in many areas of physics and constitute paradigm models for strongly correlated materials [81, 264, 265]. By virtue of the Holstein–Primakoff transformation [257], this Hamiltonian maps to the one in Eq. (3.1) in the limit of hard-core bosons, by identifying the operators $S_\ell^+ = a_l$, $S_\ell^- = a_l^\dagger$, and $S_\ell^z = 1/2 - n_\ell$. In this mapping, the spin states $|\uparrow\rangle$ and $|\downarrow\rangle$ correspond to the bosonic vacuum $|0\rangle$ and the single excited state $|1\rangle$, respectively.

An important property of the Hamiltonian (3.76) is the conservation of the total

magnetization in z-direction, giving rise to the local continuity equation

$$\frac{\mathrm{d}}{\mathrm{d}t}S_\ell^z + \sum_{\ell' \neq \ell} j_{\ell\ell'} = 0\,, \tag{3.77}$$

where $j_{\ell\ell'}$ is the spin current operator from site ℓ to ℓ'. As in the case of soft-core bosons discussed in Section 3.1, the form of the current operator can be derived by comparing Eq. (3.77) to the Heisenberg equation of motion

$$\frac{\mathrm{d}}{\mathrm{d}t}S_\ell^z = \frac{i}{\hbar}[H_0, S_\ell^z]\,. \tag{3.78}$$

Using the commutation relations

$$[S_\ell^z, S_{\ell'}^\pm] = \pm\delta_{\ell\ell'}S_\ell^\pm\,, \tag{3.79a}$$
$$[S_\ell^+, S_{\ell'}^-] = 2\delta_{\ell\ell'}S_\ell^z\,, \tag{3.79b}$$

we find

$$j_{\ell\ell'} = -i(J_{\ell\ell'}S_\ell^+S_{\ell'}^- - J_{\ell\ell'}^*S_{\ell'}^+S_\ell^-)\,, \tag{3.80}$$

in complete analogy to Eq. (3.2).

Measurement Protocol

The basic idea for the implementation of the current measurement scheme in a trapped-ion system is to use collective vibrational modes of the ion crystal as ancillas. Here, we consider the case of a single ancilla corresponding to a certain mode of an orthogonal set of phonon modes, e.g., the center-of-mass mode. As before, we represent the ancilla by the bosonic annihilation and creation operators b and $b^\dagger$. Through an appropriate choice of the laser detunings, the ions can be coupled to this specific mode via the red sideband Hamiltonian [266]

$$H_{\mathrm{cpl}} = \frac{1}{2}\sum_\ell \Omega_\ell^{\mathrm{R}}\eta_\ell(S_\ell^+ b\mathrm{e}^{-i\varphi_\ell} + S_\ell^- b^\dagger \mathrm{e}^{i\varphi_\ell})\,. \tag{3.81}$$

Here, Ω_ℓ^{R} is the (Raman) Rabi frequency, η_ℓ is the Lamb–Dicke parameter, and φ_ℓ is the phase of the coupling to the ℓ-th ion, respectively. This Hamiltonian has the same form as the general coupling Hamiltonian (3.12) with $\alpha = \sum_\ell \lambda_\ell S_\ell^-$ and $\lambda_\ell = \Omega_\ell^{\mathrm{R}}\eta_\ell \mathrm{e}^{i\varphi_\ell}/2\Omega$, where Ω is the overall strength of the coupling pulse in Eq. (3.12) ($M = 1$).

For an ancilla that is initially in its motional ground state, the results in Eq. (3.17) immediately carry over to the trapped-ion case. Such a situation can be achieved thanks to the efficient cooling of trapped-ion phonon modes [266–270]. In addition, phonon heating is typically much slower than the coherent coupling pulses we are interested in here [271]. Nevertheless, in practice it may be desirable to relax the requirement of cooling the relevant phonon modes exactly to their motional ground states. Therefore, we consider here the more general case of an ancilla that is initially in the mixed state

$$\rho_{\mathrm{A}} = \sum_{n=0}^{\infty} p_n |n\rangle\langle n|\,, \tag{3.82}$$

where p_n is the occupation probability of the n-th excited phonon state. The precise distribution p_n is unimportant for the following discussion, but we require it to be quasistationary within the coupling duration δt. This includes the common scenario of a thermal state, i.e., $p_n \equiv p_n(T) = \mathrm{e}^{-n\hbar\omega/k_\mathrm{B}T}/Z$, where ω is the frequency of the ancillary (center-of-mass) mode and $Z = (1 - e^{-\hbar\omega/k_\mathrm{B}T})^{-1}$ is the partition sum in a canonical ensemble at temperature T.

As before, we assume that when the coupling is turned on, the total state of system plus ancilla is given by a product state, $\rho = \rho_0 \otimes \rho_\mathrm{A}$. Proceeding in an analogous way as in Section 3.1.2, we find that, to leading order in the effective coupling $s = (\Omega\Delta t)^2$, the probability of detecting n phonons in the ancilla reads

$$P(n) = p_n - s[(n+1)p_n - np_{n-1}]\langle\alpha^\dagger\alpha\rangle - s[np_n - (n+1)p_{n+1}]\langle\alpha\alpha^\dagger\rangle\,. \tag{3.83}$$

For a thermal state with $k_\mathrm{B}T \ll \hbar\omega$, implying $p_n \approx \delta_{n0}$, we recover the result in Eq. (3.7). According to Eq. (3.83), the expectation values $\langle\alpha^\dagger\alpha\rangle$ and $\langle\alpha\alpha^\dagger\rangle$ can be extracted by measuring how the phonon distribution has changed after the coupling with respect to the original (thermal) distribution. Counting the phonon population is a common tool in modern trapped-ion experiments [272–276].

To access the current (3.80) between two ions ℓ_1 and ℓ_2, we choose only those couplings in Eq. (3.81) corresponding to ℓ_1 and ℓ_2 different from zero, i.e.,

$$\alpha_{\ell_1\ell_2} = \mathrm{e}^{i\theta_{\ell_1}} S^-_{\ell_1} + \mathrm{e}^{i\theta_{\ell_2}} S^-_{\ell_2}\,. \tag{3.84}$$

The required single-site addressing is typically available in state-of-the art trapped-ion quantum-simulation experiments [182, 209]. The measurement scheme then gives access to the general combination

$$(\alpha^\dagger\alpha)_{\ell_1\ell_2} = S^+_{\ell_1}S^-_{\ell_1} + S^+_{\ell_2}S^-_{\ell_2} + \mathrm{e}^{i(\theta_{\ell_2}-\theta_{\ell_1})}S^+_{\ell_1}S^-_{\ell_2} + \mathrm{e}^{-i(\theta_{\ell_2}-\theta_{\ell_1})}S^+_{\ell_2}S^-_{\ell_1}\,. \tag{3.85}$$

By choosing the phases of the coupling such that $\theta_{\ell_2} - \theta_{\ell_1} = \phi_{\ell_1\ell_2} - \pi/2$, where $\phi_{\ell_1\ell_2} = \arg(J_{\ell_1\ell_2})$, and using $S^+_\ell S^-_\ell = S^z_\ell + 1/2$, we obtain

$$(\alpha^\dagger\alpha)_{\ell_1\ell_2} = \mathbb{1} + S^z_{\ell_1} + S^z_{\ell_2} + \frac{j_{\ell_1\ell_2}}{|J_{\ell_1\ell_2}|}\,. \tag{3.86}$$

For the coupling operator (3.84), the commutation relations (3.79) imply $[\alpha, \alpha^\dagger] = -2(S^z_{\ell_1} + S^z_{\ell_2})$, from which we conclude

$$(\alpha\alpha^\dagger)_{\ell_1\ell_2} = \mathbb{1} - S^z_{\ell_1} - S^z_{\ell_2} + \frac{j_{\ell_1\ell_2}}{|J_{\ell_1\ell_2}|}\,. \tag{3.87}$$

Inserting these expressions into Eq. (3.83), we arrive at

$$p_{\ell_1\ell_2}(n) = p_n - s\left[u_n\left(1 + \frac{\langle j_{\ell_1\ell_2}\rangle}{|J_{\ell_1\ell_2}|}\right) + v_n\left\langle S^z_{\ell_1} + S^z_{\ell_2}\right\rangle\right] \tag{3.88}$$

with $u_n = (2n+1)p_n - np_{n-1} - (n+1)p_{n+1}$ and $v_n = p_n - np_{n-1} + (n+1)p_{n+1}$. As discussed in Section 3.1.1, the quantity $\langle S^z_{\ell_1} + S^z_{\ell_2} \rangle$ required to isolate the desired current $\langle j_{\ell_1 \ell_2} \rangle$ can be obtained in a separate standard measurement, or its contribution can be eliminated by considering the anti-symmetric combination

$$\frac{1}{2}\big[p_{\ell_1\ell_2}(n) - p_{\ell_2\ell_1}(n)\big] = p_n - s u_n \frac{\big\langle j_{\ell_1\ell_2} \big\rangle}{|J_{\ell_1\ell_2}|} \,. \tag{3.89}$$

As these discussions show, the method works for general initial mixed ancilla states that are diagonal in the occupation basis of the ancilla. This feature may even be exploited to optimize the obtained signal. The proposed trapped-ion implementation of the non-invasive measurement scheme can immediately be extended to global currents, current variances, as well as spatial current correlations, following similar ideas as presented in Section 3.1.2.

3.3. Projective Protocol

In Section 3.1, we have approached the problem of measuring currents in analog quantum simulators from a weak measurement (or non-Hermitian linear response) point of view and developed a versatile non-invasive scheme with a wide range of potential applications, as exemplified in Section 3.2. Yet, since the scheme is based on weak system–ancilla couplings, it can be challenging for experiments to achieve a sufficiently high signal-to-noise ratio without leaving the linear regime (see discussion in Section 3.1.4). In this case, it can be advantageous to resort to projective protocols, which rely on standard projective von Neumann measurements [89, 90] and therefore typically achieve a higher signal-to-noise ratio than weak measurements [163]. As we will see in the course of this section, a direct projective measurement of the current can be realized based on the same setup as the non-invasive scheme in Fig. 3.1, but with the weak system–ancilla coupling replaced by a π-pulse. The resulting protocol admits an instructive interpretation using the concept of dark and bright states [106]: the coherent coupling is engineered in such a way that the bright mode which couples to the light field becomes sensitive to the desired current. The population of this bright mode is then transferred to the ancilla, where it can be read out via standard projective measurements.

In what follows, we work out the mathematical framework for the projective current measurement scheme in detail. It is instructive to first illustrate the basic idea for an atomic 3-level system, before treating the many-body case. In this context, we discuss how the projective protocol gives access to expectation values of currents, current variances, as well as spatial current correlations. In particular, the projective technique immediately applies to the scenarios presented in Section 3.2. Moreover, we elucidate the relations between the projective and the non-invasive variant and discuss the mutual benefits and drawbacks of these methods.

3.3.1. Illustrative Example: Three-Level System

As described in Section 3.1, the non-invasive scheme can be interpreted as probing the leakage of probability from the system to the ancilla in response to a suitably engineered coherent perturbation. For the projective scheme, where the system–ancilla coupling no longer operates in the linear regime, an alternative interpretation in terms of dark and bright states turns out to be more natural and also provides a complementary view on the non-invasive scheme. The projective protocol and the connection to dark and bright states are best illustrated at the simplest non-trivial example of an atomic three-level system.

To this end, we consider a three-level system in Λ configuration, whose Hilbert space is spanned by the states $\{|1\rangle, |2\rangle, |\mathrm{A}\rangle\}$. The two-level subsystem spanned by $\{|1\rangle, |2\rangle\}$ represents the target system, whose properties are probed using the ancilla state $|\mathrm{A}\rangle$.

In this example, we are interested in the probability current between the states $|1\rangle$ and $|2\rangle$. To define this quantity, we first ignore the ancilla and consider only the two-level subsystem. We assume its dynamics to be governed, in a suitable reference frame, by the Hamiltonian

$$H_0 = \frac{\hbar\Delta}{2}(|1\rangle\langle 1| - |2\rangle\langle 2|) + \frac{\hbar}{2}(\Omega_\mathrm{R}|1\rangle\langle 2| + \Omega_\mathrm{R}^*|2\rangle\langle 1|) \tag{3.90}$$

with detuning Δ and (complex) Rabi frequency Ω_R. From the Schrödinger equation

$$i\hbar\frac{\mathrm{d}}{\mathrm{d}t}|\psi(t)\rangle = H_0|\psi(t)\rangle \tag{3.91}$$

for the state $|\psi(t)\rangle = c_1(t)|1\rangle + c_2(t)|2\rangle$, it is easy to derive the continuity equation $\partial_t|c_1|^2 + j_{12} = 0$, which allows one to identify the probability current

$$j_{12} = \frac{i}{2}(\Omega_\mathrm{R}c_1^*c_2 - \Omega_\mathrm{R}^*c_1c_2^*)\,. \tag{3.92}$$

In order to probe this quantity, the states $|1\rangle$ and $|2\rangle$ are coupled resonantly to the ancilla (cf. Fig. 3.1b), as described by the coupling Hamiltonian

$$H_\mathrm{cpl} = \hbar\Omega_1|\mathrm{A}\rangle\langle 1| + \hbar\Omega_1^*|1\rangle\langle\mathrm{A}| + \hbar\Omega_2|\mathrm{A}\rangle\langle 2| + \hbar\Omega_2^*|2\rangle\langle\mathrm{A}|\,. \tag{3.93}$$

For any given configuration of the (complex) couplings Ω_1 and Ω_2, there is an associated dark and bright state [106], given by

$$|\mathrm{D}\rangle = \frac{1}{\tilde{\Omega}}(-\Omega_2|1\rangle + \Omega_1|2\rangle)\,, \qquad |\mathrm{B}\rangle = \frac{1}{\tilde{\Omega}}(\Omega_1^*|1\rangle + \Omega_2^*|2\rangle)\,, \tag{3.94}$$

with $\tilde{\Omega} = \sqrt{|\Omega_1|^2 + |\Omega_2|^2}$. It is easy to verify that these states form an orthonormal basis of the two-level subsystem, and the change of basis is given by

$$|1\rangle = \frac{1}{\tilde{\Omega}}(-\Omega_2^*|\mathrm{D}\rangle + \Omega_1|\mathrm{B}\rangle)\,, \qquad |2\rangle = \frac{1}{\tilde{\Omega}}(\Omega_1^*|\mathrm{D}\rangle + \Omega_2|\mathrm{B}\rangle)\,. \tag{3.95}$$

Expressing the coupling Hamiltonian in the basis of dark and bright states, the dark state decouples from the light field, such that effectively only the bright state is coupled to the ancilla,

$$H_{\mathrm{cpl}} = \hbar\tilde{\Omega}(|\mathrm{A}\rangle\langle\mathrm{B}| + |\mathrm{B}\rangle\langle A|)\,. \tag{3.96}$$

Let us now consider an arbitrary state $|\psi_0\rangle = c_1|1\rangle + c_2|2\rangle$ with no overlap to the ancilla state, whose momentary probability current j_{12} we intend to probe. For instance, $|\psi_0\rangle$ may be the result of some unitary evolution in the two-level subsystem under the unperturbed Hamiltonian H_0. By means of Eq. (3.95), we can express this state equivalently as $|\psi_0\rangle = c_{\mathrm{D}}|\mathrm{D}\rangle + c_{\mathrm{B}}|\mathrm{B}\rangle$ with coefficients $c_{\mathrm{D}} = (-c_1\Omega_2^* + c_2\Omega_1^*)/\tilde{\Omega}$ and $c_{\mathrm{B}} = (c_1\Omega_1 + c_2\Omega_2)/\tilde{\Omega}$.

We assume the duration δt of the system–ancilla coupling to be sufficiently short such that we can ignore the evolution under H_0 during the coupling, i.e., the measurement takes an instantaneous snapshot of the state $|\psi_0\rangle$. The time evolution solely under H_{cpl} can then be calculated exactly, yielding

$$|\psi(\delta t)\rangle = \mathrm{e}^{-iH_{\mathrm{cpl}}\delta t/\hbar}|\psi_0\rangle = c_{\mathrm{D}}|\mathrm{D}\rangle + \cos(\tilde{\Omega}\delta t)c_{\mathrm{B}}|\mathrm{B}\rangle - i\sin(\tilde{\Omega}\delta t)c_{\mathrm{B}}|A\rangle\,. \tag{3.97}$$

During the coupling, the population of the ancilla changes as

$$\left|\langle\mathrm{A}|\psi(\delta t)\rangle\right|^2 = \sin^2(\tilde{\Omega}\delta t)\left|c_{\mathrm{B}}\right|^2. \tag{3.98}$$

Thus, a pulse of duration $\tilde{\Omega}\delta t = \pi/2$ ("π-pulse") maps the total population of the bright state,

$$\left|c_{\mathrm{B}}\right|^2 = \frac{1}{\tilde{\Omega}^2}(|c_1|^2|\Omega_1|^2 + |c_2|^2|\Omega_2|^2 + c_1^*c_2\Omega_1^*\Omega_2 + c_1c_2^*\Omega_1\Omega_2^*)\,, \tag{3.99}$$

to the population of the ancilla, which can then be read out using standard projective measurements. Crucially, an appropriate choice of the phases of the couplings Ω_1 and Ω_2 gives access to the probability current j_{12} defined in Eq. (3.92): choosing $\Omega_1 = \Omega$ and $\Omega_2 = \Omega\mathrm{e}^{i\varphi}$, we obtain

$$\left|c_{\mathrm{B}}\right|^2 = \frac{1}{2}(1 + \mathrm{e}^{i\varphi}c_1^*c_2 + \mathrm{e}^{-i\varphi}c_1c_2^*)\,, \tag{3.100}$$

which indeed yields the current as $\left|c_{\mathrm{B}}\right|^2 = 1/2 + j_{12}/|\Omega_{\mathrm{R}}|$ for $\varphi = \arg(\Omega_{\mathrm{R}}) + \pi/2$.

By contrast, in the non-invasive variant of the scheme, the coupling is applied only weakly, corresponding to the leading-order expansion of Eq. (3.98), $|\langle\mathrm{A}|\psi(\delta t)\rangle|^2 = s|c_{\mathrm{B}}|^2 + \mathcal{O}(s^2)$ with $s = (\tilde{\Omega}\delta t)^2$. Consequently, at the cost of a reduced signal strength compared to the π-pulse, the state is only slightly perturbed by the measurement: the post-measurement state for realizations where the system has not been detected in the ancilla state is given by $|\psi(\delta t\,|\,\{\mathrm{D},\mathrm{B}\})\rangle = |\psi_0\rangle - s(c_{\mathrm{B}}|\mathrm{B}\rangle - |c_{\mathrm{B}}|^2|\psi_0\rangle)/2 + \mathcal{O}(s^2)$, which has unit overlap with the initial state $|\psi_0\rangle$ up to quadratic order in s, in line with the general results in Section 3.1.3.

3.3.2. Projective Measurement of Currents

Having gained intuition at the illustrative example of a single-particle three-level system, we now formulate the projective current measurement protocol for many-body systems.

Connection to Dark and Bright States

To carry the picture of dark and bright states over to the many-body case, we consider the second-quantized coupling Hamiltonian

$$H_{\mathrm{cpl}} = \sum_{i,j} \langle i|h_{\mathrm{cpl}}|j\rangle a_i^\dagger a_j \,, \tag{3.101}$$

where h_{cpl} is the single-particle coupling Hamiltonian and the summation runs over the single-particle basis states $\{|1\rangle, |2\rangle, |\mathrm{A}\rangle\}$. Here, a_1 ($a_1^\dagger$), a_2 ($a_2^\dagger$), and $b \equiv a_{\mathrm{A}}$ ($b^\dagger \equiv a_{\mathrm{A}}^\dagger$) are the annihilation (creation) operators associated with the states $|1\rangle$, $|2\rangle$, and the ancilla state $|\mathrm{A}\rangle$, respectively. Inserting the single-particle coupling Hamiltonian (3.93), yields

$$\begin{aligned} H_{\mathrm{cpl}} &= \langle A|h_{\mathrm{cpl}}|1\rangle b^\dagger a_1 + \langle 1|h_{\mathrm{cpl}}|A\rangle a_1^\dagger b + \langle A|h_{\mathrm{cpl}}|2\rangle b^\dagger a_2 + \langle 2|h_{\mathrm{cpl}}|A\rangle a_2^\dagger b \\ &= \Omega_1 b^\dagger a_1 + \Omega_1^* a_1^\dagger b + \Omega_2 b^\dagger a_2 + \Omega_2^* a_2^\dagger b \,. \end{aligned} \tag{3.102}$$

By means of Eq. (3.95), we can equivalently express this Hamiltonian with respect to the basis of dark and bright states as

$$\begin{aligned} H_{\mathrm{cpl}} &= \langle A|h_{\mathrm{cpl}}|\mathrm{D}\rangle b^\dagger a_{\mathrm{D}} + \langle \mathrm{D}|h_{\mathrm{cpl}}|A\rangle a_{\mathrm{D}}^\dagger b + \langle A|h_{\mathrm{cpl}}|\mathrm{B}\rangle b^\dagger a_{\mathrm{B}} + \langle \mathrm{B}|h_{\mathrm{cpl}}|A\rangle a_{\mathrm{B}}^\dagger b \\ &= \tilde{\Omega}\big(b^\dagger a_{\mathrm{B}} + a_{\mathrm{B}}^\dagger b\big) \,, \end{aligned} \tag{3.103}$$

where we have identified the dark and bright modes

$$a_{\mathrm{D}} = \frac{1}{\tilde{\Omega}}(-\Omega_2^* a_1 + \Omega_1^* a_2) \,, \qquad a_{\mathrm{B}} = \frac{1}{\tilde{\Omega}}(\Omega_1 a_1 + \Omega_2 a_2) \,, \tag{3.104}$$

and used the fact that according to Eq. (3.96) the matrix elements $\langle A|h_{\mathrm{cpl}}|\mathrm{D}\rangle$ vanish since the dark state decouples from the light field.

A comparison between Eqs. (3.6) and (3.103) reveals that the coupling scheme in Fig. 3.1b actually corresponds to coupling the bright mode a_{B} in Eq. (3.104) with $\Omega_1 = \Omega \mathrm{e}^{i\theta_1}$ and $\Omega_2 = \Omega \mathrm{e}^{i\theta_2}$ to the ancilla mode b. The choice of the phases in Eq. (3.9) corresponds to engineering the bright mode such that it involves becomes sensitive to the desired current. The current operator can then be accessed by transferring population from the bright mode to the ancilla, either just a small fraction (non-invasive scheme) or the total population (projective scheme), followed by a standard measurement of the ancilla occupancy.

Derivation of the Projective Scheme

We now develop the mathematical framework of the projective protocol for measuring currents. To this end, we consider the coupling Hamilton (3.103), corresponding to the scheme depicted in Fig. 3.1b. We assume that we can neglect the unperturbed evolution of system and ancilla during the coupling period, which is permissible if the coupling pulse is sufficiently short as compared to the characteristic time scales of the unperturbed dynamics.

The evolution of the bright mode $a_{\mathrm{B}}(t)$ and the ancilla mode $b(t)$ under the coupling Hamilton (3.103) can be computed in the Heisenberg picture by solving the Heisenberg equations of motion

$$\dot{a}_{\mathrm{B}}(t) = -\frac{i}{\hbar}\big[a_{\mathrm{B}}(t), H_{\mathrm{cpl}}\big] = -i\tilde{\Omega} b(t)\,, \tag{3.105a}$$

$$\dot{b}(t) = -\frac{i}{\hbar}\big[b(t), H_{\mathrm{cpl}}\big] \quad = -i\tilde{\Omega} a_{\mathrm{B}}(t)\,, \tag{3.105b}$$

with initial conditions $a_{\mathrm{B}}(0) = a_{\mathrm{B}}$ and $b(0) = b$. Combining these two equations, we obtain decoupled equations of harmonic oscillator type for both the bright mode and the ancilla mode,

$$\ddot{a}_{\mathrm{B}}(t) + \tilde{\Omega}^2 a_{\mathrm{B}}(t) = 0\,, \tag{3.106a}$$

$$\ddot{b}(t) + \tilde{\Omega}^2 b(t) \quad = 0\,, \tag{3.106b}$$

whose solutions are given by

$$a_{\mathrm{B}}(t) = a_{\mathrm{B}}\cos(\tilde{\Omega}t) - ib\sin(\tilde{\Omega}t)\,, \tag{3.107a}$$

$$b(t) = b\cos(\tilde{\Omega}t) - ia_{\mathrm{B}}\sin(\tilde{\Omega}t)\,. \tag{3.107b}$$

We are interested in the evolution of the number (density) operator $n_{\mathrm{A}}(t) = b^\dagger(t)b(t)$ of the ancilla mode, as this is the relevant experimentally accessible observable. Using the result in Eq. (3.107b), we find

$$n_{\mathrm{A}}(t) = \cos^2(\tilde{\Omega}t)b^\dagger b + \sin^2(\tilde{\Omega}t)a_{\mathrm{B}}^\dagger a_{\mathrm{B}} - i\cos(\tilde{\Omega}t)\sin(\tilde{\Omega}t)\Big(b^\dagger a_{\mathrm{B}} - a_{\mathrm{B}}^\dagger b\Big)\,. \tag{3.108}$$

As before, we assume system and ancilla to be in a product state before the coupling, $\rho = \rho_0 \otimes \rho_{\mathrm{A}}$. Choosing the duration of the coupling pulse as $\tilde{\Omega}t = \pi/2$, the expectation value of the ancilla population after the coupling corresponds to the population of the bright mode in the unperturbed state ρ_0,

$$\left\langle n_{\mathrm{A}}\left(t = \frac{\pi}{2\tilde{\Omega}}\right)\right\rangle = \left\langle a_{\mathrm{B}}^\dagger a_{\mathrm{B}}\right\rangle_0 \tag{3.109}$$

with

$$\begin{aligned} a_{\mathrm{B}}^\dagger a_{\mathrm{B}} &= \frac{1}{\tilde{\Omega}^2}\Big(|\Omega_1|^2 n_1 + |\Omega_2|^2 n_2 + \Omega_1^*\Omega_2 a_1^\dagger a_2 + \Omega_1\Omega_2^* a_2^\dagger a_1\Big) \\ &= \frac{1}{2}\Big(n_1 + n_2 + \mathrm{e}^{i(\theta_2-\theta_1)}a_1^\dagger a_2 + \mathrm{e}^{-i(\theta_2-\theta_1)}a_2^\dagger a_1\Big)\,, \end{aligned} \tag{3.110}$$

where we have specialized to $\Omega_1 = \Omega\mathrm{e}^{i\theta_1}$ and $\Omega_2 = \Omega\mathrm{e}^{i\theta_2}$. If we identify the modes a_1 and a_2 with the local modes a_{ℓ_1} and a_{ℓ_2} of a many-body system with Hamiltonian (3.1), we can access the corresponding current operator $a_{\mathrm{B}}^\dagger a_{\mathrm{B}}$ defined in Eq. (3.2) by choosing the coupling phases as in Eq. (3.9), such that[5]

$$a_{\mathrm{B}}^\dagger a_{\mathrm{B}} = \frac{1}{2}\left(n_{\ell_1} + n_{\ell_2} + \frac{j_{\ell_1\ell_2}}{|J_{\ell_1\ell_2}|}\right). \tag{3.111}$$

[5]The factor 1/2 between Eqs. (3.8) and (3.110) stems from the different normalization of the modes $\alpha_{\ell_1\ell_2}$ in Eq. (3.8) and a_{B} defined in Eq. (3.104). For $\Omega_1 = \Omega\mathrm{e}^{i\theta_{\ell_1}}$ and $\Omega_2 = \Omega\mathrm{e}^{i\theta_{\ell_2}}$, we have $\alpha_{\ell_1\ell_2} = \sqrt{2}a_{\mathrm{B}}$.

As Eq. (3.109) illustrates, the outlined scheme corresponds to a projective measurement of the bright mode population. Since the entire population is measured projectively, the signal-to-noise ratio is significantly improved as compared to the non-invasive measurement of the same quantity according to Eq. (3.10).

In practice, measuring the time trace of $\langle n_{\mathrm{A}}(t)\rangle$ and deducing the quantity $\langle a_{\mathrm{B}}^\dagger a_{\mathrm{B}}\rangle$ from the resulting oscillations can yield more accurate results than a single π-pulse as in Eq. (3.109), which is sensitive to a precise calibration of the pulse area. A measurement of $\langle n_{\mathrm{A}}(t)\rangle$ is viable as long as the coupling time t is short compared to the characteristic time scales of the unperturbed dynamics. Note that the expectation value of the last term in Eq. (3.108) vanishes in the common situation where the initial ancilla state ρ_{A} is diagonal in the Fock basis, e.g., if the ancilla is initially empty or in a thermal state.

In a similar vein, the projective scheme can be used to efficiently measure loop currents around plaquettes by coupling the sites forming a plaquette simultaneously to a central ancilla (see Fig. 3.4c). For a triangular plaquette, this amounts to the choice $a_{\mathrm{B}} = \tilde{\Omega}^{-1}(\Omega_1 a_1 + \Omega_2 a_2 + \Omega_3 a_3)$ with $\tilde{\Omega} = \sqrt{|\Omega_1|^2 + |\Omega_2|^2 + |\Omega_3|^2}$ and choosing the coupling phases as explained in Section 3.2.2, which allows one to obtain the loop current from only two measurement configurations.

Non-Invasive Limit of the Projective Protocol

It is instructive to examine the limit of weak coupling strengths, in which the projective scheme becomes non-invasive. On the one hand, for an initially empty ancilla, the expectation value of Eq. (3.110) can be expanded as

$$\langle n_{\mathrm{A}}(t)\rangle = \sin^2(\tilde{\Omega}t)\left\langle a_{\mathrm{B}}^\dagger a_{\mathrm{B}}\right\rangle = \left[(\tilde{\Omega}t)^2 - \frac{1}{3}(\tilde{\Omega}t)^4 + \mathcal{O}\big((\tilde{\Omega}t)^6\big)\right]\left\langle a_{\mathrm{B}}^\dagger a_{\mathrm{B}}\right\rangle . \tag{3.112}$$

On the other hand, we can express this quantity in terms of the ancilla occupation probabilities, calculated in Eq. (3.17) up to next-to-leading order in the coupling. For a single bosonic ancilla, Eq. (3.24) yields[6]

$$\langle n_{\mathrm{A}}\rangle = \sum_{n=0}^{\infty} np(n) = p(1) + 2p(2) + \ldots = \left[s - \frac{2}{3}s^2 + \mathcal{O}(s^3)\right]\langle \alpha^\dagger\alpha\rangle . \tag{3.113}$$

As expected, the two results in Eqs. (3.112) and (3.113) match since $\alpha^\dagger\alpha = 2a_{\mathrm{B}}a_{\mathrm{B}}$ and $s = (\Omega t)^2 = (\tilde{\Omega}t)^2/2$. This shows that in the limit of weak couplings, the projective scheme for measuring currents becomes equivalent to the non-invasive one in Section 3.1.1: a measurement of the expectation value $\langle n_{\mathrm{A}}\rangle$ corresponds to a measurement of the ancilla occupation probability $p(1)$ or the combination $p(1)+2p(2)$ [cf. Eq. (3.43)] up to linear or quadratic order in s, respectively.

[6] In the fermionic case, we have $\langle n_{\mathrm{A}}\rangle = p(1)$ and the expression in Eq. (3.113) is directly obtained from Eq. (3.21b) by noting that $(\alpha^\dagger\alpha)^2 = 2\alpha^\dagger\alpha$ and $(\alpha^\dagger)^2 = \alpha^2 = 0$.

Projective Measurement of Neighboring Currents

In Section 3.2.1, we have discussed how the non-invasive scheme can be set up for the efficient measurement of global currents using multiple ancillas. Remarkably, even currents across adjacent links can be measured simultaneously this way despite the fact that the respective current operators do not commute. The ability to access such incompatible observables is an important asset of weak over projective measurements [226, 227]. However, the non-commutativity does affect the measurement beyond the linear regime, in fact, already at the quadratic level, as we have seen in the context of spatial correlations between neighboring currents (see Section 3.1.2). This is particularly true for projective measurements, which are clearly non-perturbative.

To illustrate the consequences for the projective current measurement protocol, we apply the projective scheme to probe the current across two adjacent links of a bosonic lattice system. That is, we consider a system described by the tight-binding Hamiltonian (3.1) and focus on a subsystem of three lattice sites ℓ_1, ℓ_2, and ℓ_3. Our goal is to probe the current $j_{\ell_1\ell_2} + j_{\ell_2\ell_3}$ through the lattice site ℓ_2 by coupling simultaneously to two ancillas located midway between the pairs of sites (ℓ_1, ℓ_2) and (ℓ_2, ℓ_3), respectively. The corresponding coupling Hamiltonian reads

$$H_{\mathrm{cpl}} = \Omega\big(b_1^\dagger \alpha_1 + \alpha_1^\dagger b_1\big) + \Omega\big(b_2^\dagger \alpha_2 + \alpha_2^\dagger b_2\big) \tag{3.114}$$

with

$$\alpha_1 = \mathrm{e}^{i\theta_{\ell_1}} a_{\ell_1} + \mathrm{e}^{i\theta_{\ell_2,1}} a_{\ell_2}\,, \qquad \alpha_2 = \mathrm{e}^{i\theta_{\ell_2,2}} a_{\ell_2} + \mathrm{e}^{i\theta_{\ell_3}} a_{\ell_3}\,. \tag{3.115}$$

Note that both α_1 and α_2 involve the mode a_{ℓ_2}, which implies the non-trivial commutation relations $[\alpha_1, \alpha_2^\dagger] = \mathrm{e}^{i\phi}$ and $[\alpha_2, \alpha_1^\dagger] = \mathrm{e}^{-i\phi}$ with $\phi = \theta_{\ell_2,1} - \theta_{\ell_2,2}$.

The Heisenberg equations of motion for the ancilla modes can be cast in the form

$$\ddot{\boldsymbol{b}}(t) = -\Omega^2 \begin{pmatrix} 2 & \mathrm{e}^{i\phi} \\ \mathrm{e}^{-i\phi} & 2 \end{pmatrix} \boldsymbol{b}(t) \tag{3.116}$$

with $\boldsymbol{b}(t) = [b_1(t), b_2(t)]^\top$ and initial conditions $\boldsymbol{b}(0) = (b_1, b_2)^\top$, $\dot{\boldsymbol{b}}(0) = -i\Omega(\alpha_1, \alpha_2)^\top$. The fact that these equations do not decouple is a direct consequence of the non-commutativity of the operators α_1 and $\alpha_2^\dagger$. The resulting coupled equations (3.116) can be solved by diagonalizing the coefficient matrix. The solution is given by

$$\begin{aligned} b_1(t) = {} & \frac{1}{2}(b_1 - \mathrm{e}^{i\phi} b_2)\cos(\Omega t) - \frac{i}{2}(\alpha_1 - \mathrm{e}^{i\phi}\alpha_2)\sin(\Omega t) \\ & + \frac{1}{2}(b_1 + \mathrm{e}^{i\phi} b_2)\cos\big(\sqrt{3}\Omega t\big) - \frac{i}{2\sqrt{3}}(\alpha_1 + \mathrm{e}^{i\phi}\alpha_2)\sin\big(\sqrt{3}\Omega t\big)\,, \end{aligned} \tag{3.117}$$

while $b_2(t)$ is obtained by exchanging $1 \leftrightarrow 2$ and replacing $\phi \to -\phi$. If the ancilla is empty before the coupling, the expectation value of the ancilla population evolves in

time as

$$\begin{aligned}\left\langle b_1^\dagger(t)b_1(t)\right\rangle = \frac{1}{4}\left\langle \alpha_1^\dagger\alpha_1 + \alpha_2^\dagger\alpha_2 - \left(\mathrm{e}^{i\phi}\alpha_1^\dagger\alpha_2 + \text{h.c.}\right)\right\rangle \sin^2(\Omega t) \\ + \frac{1}{12}\left\langle \alpha_1^\dagger\alpha_1 + \alpha_2^\dagger\alpha_2 + \left(\mathrm{e}^{i\phi}\alpha_1^\dagger\alpha_2 + \text{h.c.}\right)\right\rangle \sin^2\left(\sqrt{3}\Omega t\right) \\ + \frac{1}{2\sqrt{3}}\left\langle \alpha_1^\dagger\alpha_1 - \alpha_2^\dagger\alpha_2\right\rangle \sin(\Omega t)\sin\left(\sqrt{3}\Omega t\right).\end{aligned} \tag{3.118}$$

Again, the corresponding expression for $\langle b_2^\dagger(t)b_2(t)\rangle$ is obtained by exchanging $1 \leftrightarrow 2$ and replacing $\phi \to -\phi$.

For an appropriate choice of the coupling phases, the current $\langle j_{\ell_1\ell_2} + j_{\ell_2\ell_3}\rangle$ can be extracted from the combination $\langle \alpha_1^\dagger\alpha_1 + \alpha_2^\dagger\alpha_2\rangle$. In the present example, this quantity can be isolated from Eq. (3.118) using two specific pulse widths, one with $\sqrt{3}\Omega t = \pi$, isolating the first term, and the other one with $\Omega t = \pi$, isolating the second term. However, there is apparently no advantage in coupling to two ancillas simultaneously as the quantities $\langle \alpha_1^\dagger\alpha_1\rangle$ and $\langle \alpha_2^\dagger\alpha_2\rangle$ could also simply be extracted from two individual local measurements.

The problem with the outlined approach is that it does not scale well. If we were to probe a current across a long chain of sites by coupling in sequence to ancillas located midway on the links, we would end up with a fully coupled system and the analogous expression to Eq. (3.118) for the ancilla population would take a complex form involving frequency components of all normal modes, rendering the isolation of the desired global current impracticable. A possible solution is to spare every other link such that only commuting observables are probed simultaneously in a single configuration. A repetition of the measurement for the remaining links then yields the full information on the global current.

By contrast, in case of the non-invasive scheme, the modes do not couple on the linear level despite their non-commutativity. This can be seen by expanding Eq. (3.118) to leading order in the coupling strength, yielding $\langle b_1^\dagger(t)b_1(t)\rangle = (\Omega t)^2\langle \alpha_1^\dagger\alpha_1\rangle$ and $\langle b_2^\dagger(t)b_2(t)\rangle = (\Omega t)^2\langle \alpha_2^\dagger\alpha_2\rangle$, in agreement with the results in Eq. (3.17). Thus, the possibility to efficiently access global currents in a single measurement configuration represents a main advantage of the non-invasive scheme.

3.3.3. Extension to Current Correlations

The projective protocol not only enables the measurement of expectation values of currents, but it is also well suited to extract current variances as well as spatial current correlations. Since the protocol maps the populations of suitably engineered bright modes to ancillas, current statistics can be accessed by measuring variances and correlations of the ancilla populations using standard density detection.

Current Variances

In Section 3.1.2, we have explained how the second moment of the current operator $\langle j_{\ell_1\ell_2}^2\rangle$ (and thus the variance of the current) between two modes ℓ_1 and ℓ_2 can be extracted

from a measurement of $\langle(\alpha^\dagger\alpha)^2_{\ell_1\ell_2}\rangle$, as given by Eq. (3.22). In the non-invasive scheme, this quantity can be obtained by resolving the ancilla occupation probabilities up to quadratic order in the coupling strength. Yet, it can be challenging for experiments to achieve the required accuracy due to the low signal-to-noise ratio. We now describe how the projective variant of the protocol can be harnessed to access the quantity $(\alpha^\dagger\alpha)^2_{\ell_1\ell_2}$ at a significantly higher signal-to-noise ratio.

To this end, we consider the square of the Heisenberg operator (3.108) describing the time evolution of the ancilla population during the coupling. If the ancilla is initially in the vacuum state, the second moment of the ancilla population reads

$$\langle n_\mathrm{A}^2(t)\rangle = \sin^4(\Omega t)\langle(\alpha^\dagger\alpha)^2\rangle + \cos^2(\Omega t)\sin^2(\Omega t)\langle\alpha^\dagger\alpha\rangle\,, \tag{3.119}$$

where we have substituted $\tilde{\Omega}\to\Omega$ and $a_\mathrm{B}\to\alpha = \mathrm{e}^{i\theta_{\ell_1}}a_{\ell_1} + \mathrm{e}^{i\theta_{\ell_2}}a_{\ell_2}$. The second term reflects a contribution from the (anti-)commutation relation $[b,b^\dagger]=1$ ($\{b,b^\dagger\}=1$) of the bosonic (fermionic[7]) ancilla mode. Thus, at times $\Omega t=(2k+1)\pi/2$, we have $\langle n_\mathrm{A}^2\rangle = \langle(\alpha^\dagger\alpha)^2\rangle$ and consequently the variance of the ancilla population corresponds to the variance of the desired operator $(\alpha^\dagger\alpha)^2$. From this quantity, the variance of the current can be extracted as explained in Section 3.1.2, e.g., by combining two measurements with the indices ℓ_1 and ℓ_2 exchanged according to Eq. (3.25).

The consistency of Eq. (3.119) with the perturbative results in Eq. (3.17) can directly be verified by considering the limit of weak coupling strengths. In the bosonic case, Eq. (3.24) yields

$$\langle n_\mathrm{A}^2\rangle = \sum_{n=0}^{\infty} n^2 p(n) = p(1) + 4p(2) + \ldots = s\langle\alpha^\dagger\alpha\rangle + s^2\left(\langle(\alpha^\dagger\alpha)^2\rangle - \frac{8}{3}\langle\alpha^\dagger\alpha\rangle\right) + \mathcal{O}(s^3)\,, \tag{3.120}$$

which coincides with the first two terms of the Taylor expansion of Eq. (3.119) for small $s=(\Omega t)^2$.

3.3.4. Spatial Current Correlations

The projective scheme enables the measurement of spatial current correlations $\langle j_{\ell_1\ell_2} j_{\ell_3\ell_4}\rangle$ using the same setup as in the non-invasive variant discussed in Section 3.1.2: each pair of modes (ℓ_1,ℓ_2) and (ℓ_3,ℓ_4) is coupled to a distinct ancilla, as described by the coupling Hamiltonian (2.31). Here, we focus on the situation where all modes ℓ_j are distinct. If this is not the case, the non-commutativity of the relevant modes leads to a fully coupled system with additional contributions from the normal modes as in Eq. (3.117), which complicates the extraction of the desired current correlator by far. The case where all modes are distinct is also the relevant scenario for probing long-range current correlations, which, for example, can reveal chiral long-range order in frustrated quantum matter as discussed in Section 3.2.2. Proceeding as in Section 3.3.2, we can solve the

[7] Recall that for fermions the square of the current operator takes a simple form and the current variance can directly be measured via density detection, as discussed below Eq. (3.20).

Heisenberg equations of motion for each ancilla independently, yielding

$$n_{\mathrm{A},m}(t) = \cos^2(\Omega_m t) b_m^\dagger b_m + \sin^2(\Omega_m t)\alpha_m^\dagger \alpha_m - i\cos(\Omega_m t)\sin(\Omega_m t)\left(b_m^\dagger \alpha_m - \alpha_m^\dagger b_m\right), \tag{3.121}$$

where the ancilla labeled by $m = 1, 2$ is coupled to the modes (ℓ_1, ℓ_2) and (ℓ_3, ℓ_4), respectively. Assuming both ancillas to be initially empty, the equal-time correlator of the two ancilla densities is given by

$$\left\langle n_{\mathrm{A},1}(t) n_{\mathrm{A},2}(t)\right\rangle = \sin^2(\Omega_1 t)\sin^2(\Omega_2 t)\left\langle \alpha_1^\dagger \alpha_1 \alpha_2^\dagger \alpha_2\right\rangle . \tag{3.122}$$

From a measurement of this quantity, the desired current correlator can be extracted as described in Section 3.1.2.

3.4. Summary

In this chapter, we have introduced non-invasive as well as projective schemes for the ancilla-based measurement of currents and current correlations in analog quantum simulators. In the non-invasive variant, the system–ancilla coupling is weak and the current can be extracted from a measurement of the probability of not populating the ancilla during the coupling. The projective variant of the scheme corresponds to a projective measurement of a suitably engineered bright mode, whose population is transferred to the ancilla in a π-pulse and can be read out using standard density detection. The experimental tools for engineering the appropriate phases of the system–ancilla coupling are readily available, e.g., in state-of-the-art optical lattice setups [71, 74, 178, 181, 231–235]. The non-invasive scheme has the advantage of perturbing the quantum state only marginally, which comes at the price of a lower signal-to-noise ratio as compared to the projective scheme. Furthermore, the non-invasive variant enables the efficient simultaneous measurement of neighboring currents, not possible in the projective case due to the non-commutativity of the involved operators. We have benchmarked the non-invasive protocol numerically for probing chiral currents of interacting bosons on a Harper–Hofstadter optical-lattice ladder, demonstrating its experimental feasibility. In addition, we have illustrated an application of the scheme for measuring chiral loop current correlations revealing chiral phases of frustrated quantum matter. Moreover, we have discussed possible implementations in trapped-ion systems, demonstrating the high flexibility of the method. Promising targets include currents and current correlations in chiral Mott insulators [236, 237, 243], chiral spin liquids [241], and fractional or anomalous Hall states [239, 277, 278], loop currents arising in vortex lattices [279, 280] and frustrated states of matter [259, 260], persistent currents in ring-shaped optical lattices [281–284], as well as local Chern markers [221, 285]. The protocol thus enables the characterization of strongly correlated phases of matter on a variety of analog quantum simulation platforms.

4. Dynamical Probes of Supersolidity in Spin–Orbit-Coupled Bose Gases

This chapter is based on Ref. [286]. Some figures and parts of the text have been taken verbatim from that work, while the presentation has been supplemented by a number of additional results obtained in the course of the project. See List of Publications for a statement of contributions.

Spin–orbit coupling has a deep influence on the structure of matter. For example, the coupling between spin and orbital angular momentum gives rise to a splitting of electronic energy levels in atoms, resulting in the fine or hyperfine structure of atomic spectral lines [287]. Moreover, spin–orbit coupling can modify the band structure of solids via the Rashba [288] and Dresselhaus [289] effect. With the advent of spin–orbit-coupled Bose–Einstein condensates (SOC BECs), a novel platform for studying the physics of spin–orbit coupling has become available [290]. Despite being entirely synthetic, the unprecedented level of experimental control over ultracold quantum gases allows one to study fundamental effects of spin–orbit coupling that are relevant also for other spin–orbit-coupled platforms and beyond.

Arguably, one of the most intriguing phenomena that can be studied in SOC BECs is supersolidity [32–34]. This exotic state of matter arises from the spontaneous breaking of both $U(1)$ phase symmetry as well as translational invariance. The former leads to superfluidity, characterized by irrotational and dissipationless flows, while the latter yields a crystalline structure. Supersolids have first been studied in the context of solid helium, where experiments aiming to reveal the superfluid properties of this system have, however, been inconclusive [35, 36]. More recently, the platform of ultracold quantum gases has been established as a promising playground for exploring supersolidity. Experimental evidence of typical supersolid features, e.g., the combination of long-range phase coherence and a spatial modulation of the density, has been reported in a variety of setups, including Bose–Einstein condensates inside optical resonators [37], spin–orbit-coupled configurations [38, 39], as well as quantum gases with long-range dipolar interactions [40–42].

In SOC BECs, supersolidity becomes manifest in the form of stripes in the density profile. However, since the distance between stripes is typically on the order of the optical wavelength, a direct resolution of the density modulation by optical means is challenging. Another fundamental hallmark of supersolidity can be deduced from Goldstone's theorem [43–45]: for every continuous symmetry that is spontaneously broken, there exists a gapless excitation called Goldstone mode (or Nambu–Goldstone mode). Thus, the

spontaneous breaking of translational invariance in a supersolid implies the emergence of additional Goldstone modes as compared to ordinary superfluids. In a uniform SOC BECs, the Goldstone mode associated with broken translational symmetry corresponds to a rigid translation of the stripes, which costs zero energy. Experimental signatures of such low-energy Goldstone modes have been observed inside optical resonators [291] and in harmonically trapped dipolar gases [292–295], while no experimental observation in spin–orbit-coupled configurations has been reported so far.

In this chapter, we explore signatures of supersolidity in harmonically trapped SOC BECs and develop protocols for their experimental observation. We consider two experimentally relevant configurations, one with symmetric intraspecies interactions, as typically found in ^{87}Rb [290], and the other one with highly asymmetric intraspecies interactions, which have recently become available in experiments on ^{39}K by means of Feshbach resonances [296]. We first investigate equilibrium properties such as density profiles or the static polarizability of these configurations with a particular emphasis on effects that arise due to the asymmetry of intraspecies interactions. Then, we discuss how Goldstone modes as dynamical probes of supersolidity can be accessed experimentally. In particular, a Goldstone mode of spin nature is revealed by a beating effect in the breathing oscillation, generated by a sudden change of the trap frequency, in analogy to a similar procedure followed in dipolar supersolids [292]. In addition, we point out experimentally accessible signatures of the zero-frequency Goldstone mode associated with the translation of the stripes and show that this mode can directly be excited via a uniform spin perturbation.

4.1. Spin–Orbit-Coupled Bose–Einstein Condensates

Spin–orbit coupling in a binary mixture of quantum gases can be realized via a Raman coupling of two internal states, generated by a pair of intersecting lasers [290]. Such a Raman transition involves a momentum transfer between the light field and the atoms due to the absorption and emission of photons. In contrast to simple microwave or radio frequency couplings, this momentum recoil cannot be neglected. In a suitable frame of reference, the system is described by the single-particle Hamiltonian [297]

$$H_{\mathrm{SOC}} = \frac{1}{2m}(\boldsymbol{p} - \hbar \boldsymbol{k}_0 \sigma_z)^2 + \frac{\Omega}{2}\sigma_x + \frac{\delta}{2}\sigma_z + V_{\mathrm{ext}}(\boldsymbol{x}), \tag{4.1}$$

where m is the mass, $\boldsymbol{x}$ and $\boldsymbol{p}$ denote position and momentum, respectively, σ_x and σ_z are Pauli matrices, and $V_{\mathrm{ext}}(\boldsymbol{x})$ is an external potential. The parameters relevant for spin–orbit coupling comprise the Raman wave vector $\boldsymbol{k}_0$, describing the momentum transfer due to the Raman lasers, the strength of the Raman coupling Ω, as well as the detuning δ from the Raman resonance. Throughout this chapter, we assume the Raman wave vector to be oriented in x direction, $\boldsymbol{k}_0 = k_0 \hat{\boldsymbol{e}}_x$. A peculiarity of the Hamiltonian (4.1) is the fact that it features equal contributions of Rashba [288] and Dresselhaus [289] spin–orbit couplings.

In uniform matter ($V(\boldsymbol{x}) = 0$), the single-particle dispersion relation of the Hamiltonian (4.1) contains two bands given by [297]

$$\epsilon_{\pm}(\boldsymbol{p}) = \frac{\boldsymbol{p}^2}{2m} + E_{\mathrm{r}} \pm \sqrt{\left(\frac{\hbar k_0 p_x}{m} - \frac{\delta}{2}\right)^2 + \frac{\Omega^2}{4}}\,, \tag{4.2}$$

where $E_{\mathrm{r}} = \hbar^2 k_0^2/2m$ is the recoil energy. At $\delta = 0$, the lower band exhibits two degenerate minima for $\Omega < 4E_{\mathrm{r}}$, located at non-zero momenta

$$\boldsymbol{p}_{\pm} = \pm\hbar k_0 \hat{\boldsymbol{e}}_x \sqrt{1 - \left(\frac{\Omega}{4E_{\mathrm{r}}}\right)^2}\,. \tag{4.3}$$

For $\Omega \geq 4E_{\mathrm{r}}$, the two minima merge into a single minimum at $\boldsymbol{p} = 0$. The disappearance of the double-minimum structure at $\Omega = 4E_{\mathrm{r}}$ is associated with a divergence of the effective mass $(m^*)^{-1} = \partial^2\epsilon/\partial p_x^2$ of a particle moving along the x direction and gives rise to a second-order phase transition between the so-called plane-wave and single-minimum phase, as explained below.

Within mean-field Gross–Pitaevskii theory [57], the interacting many-body system is described by a two-component spinor $\boldsymbol{\Psi}(\boldsymbol{x}) = [\Psi_\uparrow(\boldsymbol{x}), \Psi_\downarrow(\boldsymbol{x})]^\top$, where $\Psi_\uparrow(\boldsymbol{x})$ and $\Psi_\downarrow(\boldsymbol{x})$ are the wave functions of the involved internal states. The use of the mean-field picture in the description of SOC BECs is justified since the quantum depletion of the condensate is typically small for realistic experimental parameters [298, 299]. The energy functional is given by

$$E = \int \mathrm{d}\boldsymbol{x}\left(\boldsymbol{\Psi}^\dagger H_{\mathrm{SOC}}\boldsymbol{\Psi} + \frac{1}{2}g_{\uparrow\uparrow}|\Psi_\uparrow|^4 + \frac{1}{2}g_{\downarrow\downarrow}|\Psi_\downarrow|^4 + g_{\uparrow\downarrow}|\Psi_\uparrow|^2|\Psi_\downarrow|^2\right), \tag{4.4}$$

where the interaction constants $g_{ij} = 4\pi\hbar^2 a_{ij}/m$ with $i, j \in \{\uparrow, \downarrow\}$ are determined by the s-wave scattering lengths a_{ij} for the respective spin channels. It is instructive to rewrite the interaction part of the energy functional (4.4) in terms of the particle density $n = |\Psi_\uparrow|^2 + |\Psi_\downarrow|^2$ and the spin density $s_z = |\Psi_\uparrow|^2 - |\Psi_\downarrow|^2$, yielding

$$E = \int \mathrm{d}\boldsymbol{r}\left(\boldsymbol{\Psi}^\dagger H_{\mathrm{SOC}}\boldsymbol{\Psi} + \frac{1}{2}g_{\mathrm{nn}}n^2 + \frac{1}{2}g_{\mathrm{ss}}s_z^2 + g_{\mathrm{ns}}ns_z\right). \tag{4.5}$$

Here, we have introduced the coupling constants

$$g_{\mathrm{nn}} = \frac{1}{4}(g_{\uparrow\uparrow} + g_{\downarrow\downarrow} + 2g_{\uparrow\downarrow})\,, \tag{4.6a}$$

$$g_{\mathrm{ss}} = \frac{1}{4}(g_{\uparrow\uparrow} + g_{\downarrow\downarrow} - 2g_{\uparrow\downarrow})\,, \tag{4.6b}$$

$$g_{\mathrm{ns}} = \frac{1}{4}(g_{\uparrow\uparrow} - g_{\downarrow\downarrow})\,, \tag{4.6c}$$

characterizing density–density, spin–spin, and density–spin interactions, respectively. The equations of motion can be derived by varying the action

$$S = \int \mathrm{d}t\, E[\Psi_\uparrow, \Psi_\downarrow] - i\hbar \int \mathrm{d}t\, \mathrm{d}\boldsymbol{x}\left(\Psi_\uparrow^*\partial_t\Psi_\downarrow + \Psi_\downarrow^*\partial_t\Psi_\downarrow\right) \tag{4.7}$$

with respect to $\Psi_\uparrow^*$ and $\Psi_\downarrow^*$, yielding the coupled time-dependent GPEs

$$i\hbar\frac{\partial}{\partial t}\Psi_\uparrow = \left[\frac{\hbar^2}{2m}(-i\nabla - \boldsymbol{k}_0)^2 + \frac{\delta}{2} + V_{\text{ext}}(\boldsymbol{x}) + g_{\uparrow\uparrow}\left|\Psi_\uparrow\right|^2 + g_{\uparrow\downarrow}\left|\Psi_\downarrow\right|^2\right]\Psi_\uparrow + \frac{\Omega}{2}\Psi_\downarrow\,, \tag{4.8a}$$

$$i\hbar\frac{\partial}{\partial t}\Psi_\downarrow = \left[\frac{\hbar^2}{2m}(-i\nabla + \boldsymbol{k}_0)^2 - \frac{\delta}{2} + V_{\text{ext}}(\boldsymbol{x}) + g_{\downarrow\downarrow}\left|\Psi_\downarrow\right|^2 + g_{\uparrow\downarrow}\left|\Psi_\uparrow\right|^2\right]\Psi_\downarrow + \frac{\Omega}{2}\Psi_\uparrow\,. \tag{4.8b}$$

Expectation values of an observable O can be computed as

$$\langle O(t)\rangle = \frac{1}{N}\int \mathrm{d}\boldsymbol{x}\, \boldsymbol{\Psi}^\dagger(\boldsymbol{x},t)\, O\, \boldsymbol{\Psi}(\boldsymbol{x},t) \tag{4.9}$$

or with respect to an individual spin component i as

$$\langle O(t)\rangle_i = \frac{1}{N_i}\int \mathrm{d}\boldsymbol{x}\, \Psi_i^*(\boldsymbol{x},t)\, O\, \Psi_i(\boldsymbol{x},t)\,, \tag{4.10}$$

where $N_i = \int \mathrm{d}\boldsymbol{x}\,|\Psi_i|^2$ is the number of particles in the respective component, while $N = N_\uparrow + N_\downarrow$ is the total number of particles in the system.

As one varies the strength of the Raman coupling Ω, the ground state of the system undergoes transitions between the following three characteristic phases [300, 301]. At small values of Ω, the system is in the stripe (or supersolid) phase, characterized by a periodic modulation of the density along the direction of the Raman wave vector. Intermediate values of Ω give rise to the plane wave phase, where the system condenses in one of the two minima (4.3) of the single-particle dispersion relation (4.2). For large Ω, the dispersion only has a single minimum at zero momentum, and the corresponding phase is therefore called the single-minimum phase. A comprehensive characterization of the mean-field phase diagram in uniform systems with symmetric intraspecies interaction can be found in Ref. [297].

In what follows, we study how static and dynamic properties vary across these phases in presence of a harmonic trapping potential given by Eq. (1.22). Throughout this chapter, we measure length mainly in units of the harmonic oscillator length in x direction, $a_x = \sqrt{\hbar/m\omega_x}$. A main focus will be put on the effects of asymmetry in the intraspecies interactions as well as on the identification of experimentally accessible signatures of supersolidity.

4.2. Equilibrium Properties of Harmonically Trapped Systems

In this section, we investigate the equilibrium properties of harmonically trapped SOC BECs. We first consider the behavior of the polarization and the ground state density profiles across the different phases as a function of the Raman coupling Ω. In this context, we will point out crucial effects of spin–orbit coupling as well as of asymmetric interactions, especially in comparison to coherently coupled BECs with negligible

momentum transfer. Furthermore, we study the behavior of the static magnetic polarizability as a function of Ω, which is deeply connected to dynamic properties of the system. This analysis will serve as a bridge to the next section, which is devoted to the study of collective excitations and Goldstone modes as dynamical probes of supersolidity.

Parameters	Symmetric configuration	Asymmetric configuration
Mass m	$87\,\mathrm{u}$ (^{87}Rb)	$39\,\mathrm{u}$ (^{39}K)
Interaction constants $(g_{\uparrow\uparrow}, g_{\uparrow\downarrow}, g_{\downarrow\downarrow})$	$\frac{1}{\sqrt{2\pi}a_z}\frac{4\pi\hbar^2}{m}(100, 60, 100)\,\mathrm{a_0}$	$\frac{4\pi\hbar^2}{m}(252.7, -6.3, 1.3)\,\mathrm{a_0}$ [296]
Trap frequencies $(\omega_x, \omega_y, \omega_z)$	$2\pi \times (50, 200, 2500)\,\mathrm{Hz}$	$2\pi \times (50, 200, 200)\,\mathrm{Hz}$
Dimensionality	quasi-2D	3D
Particle number N	10^4	10^5
Raman momentum transfer k_0	$k_0 = \sqrt{2}\pi/\lambda = 5.53\,\mu\mathrm{m}^{-1}$ $\lambda = 804.1\,\mathrm{nm}$ [290]	$k_0 = 2\pi/\lambda = 8.17\,\mu\mathrm{m}^{-1}$ $\lambda = 768.97\,\mathrm{nm}$ [296]
Recoil energy $E_\mathrm{r} = \hbar^2 k_0^2/2m$	$2\pi\hbar \times 1.773\,\mathrm{kHz}$	$2\pi\hbar \times 8.652\,\mathrm{kHz}$
Raman coupling Ω	$0 \ldots 6\,E_\mathrm{r}$	$0 \ldots 8\,E_\mathrm{r}$
Detuning δ	0	0

Table 4.1.: Physical parameters used for numerical simulations of spin–orbit-coupled Bose–Einstein condensates with symmetric and asymmetric intraspecies interactions. In the symmetric case, the interaction constants correspond to effective values in a quasi-2D system, obtained by reducing the spatial overlap of the two spin components and integrating out the tightly-confined z direction, as explained in Section 4.2.1. The parameters specified above have been used throughout this chapter unless explicitly stated otherwise.

4.2.1. Symmetric Intraspecies Interactions

We start by investigating SOC BECs with symmetric intraspecies interactions, which is also where the majority of previous works focuses on. Symmetric configurations are well realized, for example, in the $F = 1$ hyperfine structure manifold of ^{87}Rb, where interactions between the $|\uparrow\rangle = |F = 1, m_F = 0\rangle$ and $|\downarrow\rangle = |F = 1, m_F = -1\rangle$ states are characterized by the scattering lengths $a_{\uparrow\uparrow} = 101.41\,\mathrm{a_0}$ and $a_{\uparrow\downarrow} = a_{\downarrow\downarrow} = 100.94\,\mathrm{a_0}$ ($\mathrm{a_0}$ is the Bohr radius) [297]. Thus, in ^{87}Rb not only the intraspecies interactions constants $g_{\uparrow\uparrow}$ and $g_{\downarrow\downarrow}$ are close to each other, but also the interspecies interaction $g_{\uparrow\downarrow}$ is close to $g_{\uparrow\uparrow}$

and $g_{\downarrow\downarrow}$, corresponding to $g_{ss} \approx 0$ according to Eq. (4.6). This has the downside that the critical value of the Raman coupling below which the system enters the supersolid phase [300, 301],

$$\Omega_{\mathrm{c}} = 4E_{\mathrm{r}}\sqrt{\frac{2g_{\mathrm{ss}}}{g_{\mathrm{nn}} + 2g_{\mathrm{ss}}}}\,, \tag{4.11}$$

takes a small value. On top of that, in the limited range of Raman couplings where the stripe phase is available, the contrast of the stripes, which is proportional to Ω [297], is relatively low, which makes the observation of supersolid features quite difficult. It is therefore desirable to increase the value of Ω_{c} in order to limit the effects of magnetic fluctuations and to observe measurable consequences due to the presence of stripes.

This can be achieved by reducing the spatial overlap between the wave functions of the two spin components, for instance, with the help of a spin-dependent trapping potential separating the two components [302, 303], or using pseudo-spin orbital states in a superlattice potential [38]. Here, we follow the former approach, employing a tight harmonic confinement along the z direction with the minima of the potentials for the two spin components separated by a distance d,

$$V(z) = \frac{1}{2}m\omega_z^2\Big(z - \frac{d}{2}\sigma_z\Big)^2\,. \tag{4.12}$$

Then, provided that ω_z is sufficiently large such that the wave function in z direction can be approximated by the harmonic oscillator ground state (see discussion of low-dimensional systems in Section 1.1.1), integrating out the z direction yields a quasi-2D description with effective coupling constants [302]

$$\tilde{g}_{\uparrow\uparrow} = \frac{g_{\uparrow\uparrow}}{\sqrt{2\pi}a_z}, \quad \tilde{g}_{\downarrow\downarrow} = \frac{g_{\downarrow\downarrow}}{\sqrt{2\pi}a_z}, \quad \tilde{g}_{\uparrow\downarrow} = \mathrm{e}^{-d^2/2a_z^2}\frac{g_{\uparrow\downarrow}}{\sqrt{2\pi}a_z}\,. \tag{4.13}$$

Thus, the reduced spatial overlap between the wave functions of the two spin components leads to an effective reduction of the interspecies interaction constant $\tilde{g}_{\uparrow\downarrow}$. Consequently, $\tilde{g}_{ss}$ is effectively increased, which enhances the stripe phase according to Eq. (4.11). In addition, the quasi-2D description contains the effective Raman coupling $\tilde{\Omega} = \mathrm{e}^{-d^2/4a_z^2}\Omega$, which is reduced compared to its physical value Ω. Thus, when reporting Raman couplings for the symmetric configuration, we mean this effective coupling in the quasi-2D description.

In what follows, we consider a configuration with symmetric intraspecies scattering lengths $a_{\uparrow\uparrow} = a_{\downarrow\downarrow} = 100\,\mathrm{a_0}$ close to those of ^{87}Rb. Furthermore, we choose a tight harmonic confinement along the z direction with frequency $\omega_z = 2.5\,\mathrm{kHz}$ and adjust the separation d of the two spin components such that the effective 2D interspecies coupling becomes $\tilde{g}_{\uparrow\downarrow} = 0.6\,\tilde{g}_{\uparrow\uparrow}$. Other physical parameters are summarized in Table 4.1.

The following results have been obtained by numerically computing the ground state of the Gross–Pitaevskii energy functional (4.5). Traditionally, this can be achieved using the method of imaginary time evolution (also known as normalized gradient flow) [66, 304]. However, for the problem at hand, an adaptation of the more recently developed preconditioned non-linear conjugate gradient method [67] turns out to have superior convergence properties and has been used throughout.

Polarization

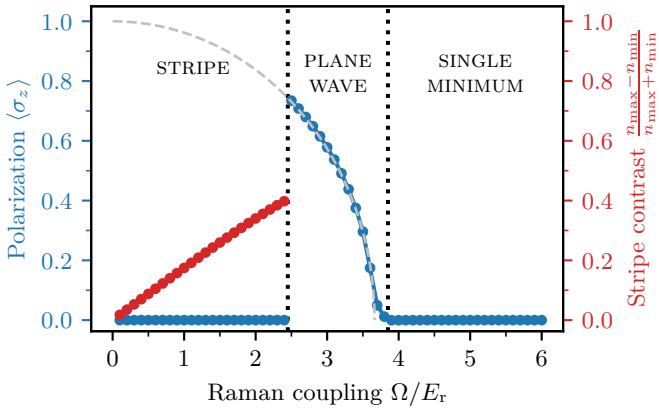

Figure 4.1.: Ground state polarization and contrast of the stripes in a harmonically trapped SOC BEC with symmetric intraspecies interactions, obtained by numerically minimizing the Gross–Pitaevskii energy functional (4.5). The vertical dotted lines mark the transitions from the stripe to the plane-wave phase at $\Omega_c \approx 2.4$ and from the plane-wave to the single-minimum phase at $\Omega_{\text{PW-SM}} \approx 3.8$, respectively. The dashed line corresponds to the prediction (4.14) for the polarization in the plane-wave phase of uniform systems with the fitted uniform density $\bar{n}a_x^2 \approx 242.8$. In the stripe phase, the polarization vanishes and the contrast of the stripes grows linearly with the Raman coupling Ω.

To get a first impression on the mean-field phase diagram, we consider the behavior of the polarization $\langle\sigma_z\rangle$ as a function of the Raman coupling Ω, shown in Fig. 4.1. Overall, the harmonically trapped system behaves similarly to the corresponding scenario in uniform matter, which has extensively been studied for symmetric configurations, e.g., in Refs. [297, 300, 301].

At large values of Ω, it is energetically favorable for the system to maximize the spatial overlap of the wave functions of the spin-up and spin-down components [cf. Eq. (4.5)]. Consequently, we find a vanishing polarization in the single-minimum phase. This behavior is completely analogous to that of coherently coupled BECs with negligible momentum transfer [57].

As we lower the Raman coupling, the system undergoes a second-order phase transition to the plane-wave phase, characterized by a non-vanishing polarization. The polarization therefore plays the role of the order parameter for this transition. At zero detuning, configurations with positive and negative polarizations have the same energy, but this degeneracy can be lifted by adding a small detuning as a bias. The transition from the plane-wave to the single-minimum phase is expected to occur at the Raman coupling $\Omega = 4E_r$, where the two minima (4.3) of the single-particle dispersion relation merge. Taking interaction effects into account, in uniform matter one finds that the order parameter in the plane-wave phase behaves like [300, 301]

$$\langle\sigma_z\rangle = \sqrt{1 - \left(\frac{\Omega}{\Omega_{\text{PW-SM}}}\right)^2}\,, \tag{4.14}$$

where the transition point $\Omega_{\text{PW–SM}} = 4(E_\text{r} - \bar{n}g_\text{ss}/2)$ is slightly shifted with respect to single-particle case. Here, $\bar{n}$ is the density in the uniform system. Treating this quantity as a fit parameter, the numerical data in Fig. 4.1 is well described by Eq. (4.14) for the value $\bar{n}a_x^2 = 242.8$. This corresponds to the critical Raman coupling $\Omega_{\text{PW–SM}}/E_\text{r} = 3.66$, which is not too far from the vertical dashed line on the right-hand side of Fig. 4.1 at $\Omega_{\text{PW–SM}} \approx 3.8$, marking the point where the polarization starts to differ significantly from zero as one lowers the Raman coupling coming from the single-minimum phase.

Once the Raman coupling reaches the critical value Ω_c for the transition to the stripe phase, the polarization jumps from a non-zero value in the plane-wave phase to zero in the stripe phase, reflecting the first-order nature of this transition. For our choice of parameters, Eq. (4.11) predicts the value $\Omega_\text{c}/E_\text{r} = 2.31$, which is close to the position $\Omega_\text{c} = 2.4$ (vertical dashed line on the left-hand side of Fig. 4.1) where the jump of the polarization occurs. Shifting this critical coupling to a larger value in order to observe appreciable effects due to the presence of stripes has been our main motivation of studying systems with reduced interspecies interactions $g_{\uparrow\downarrow}$.

Density Profiles

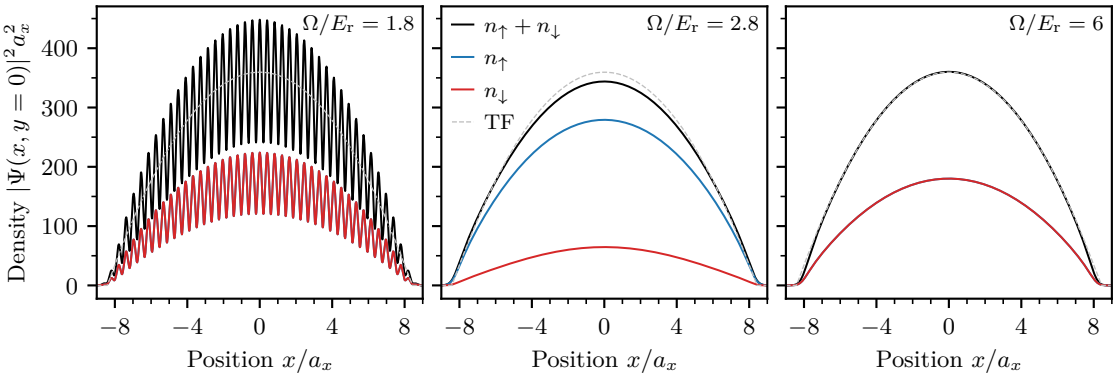

Figure 4.2.: Ground state density profiles for symmetric intraspecies interactions. The three panels represent typical profiles in the stripe phase ($\Omega/E_\text{r} = 1.8$), plane-wave phase ($\Omega/E_\text{r} = 2.8$), and single-minimum phase ($\Omega/E_\text{r} = 6$). The envelope of the total density in all three phases is close to a 2D Thomas–Fermi profile with effective interaction constant g_nn (grey dashed lines).

Figure 4.2 depicts characteristic density profiles in the stripe, plane-wave, and single-minimum phases. In the single-minimum phase ($\Omega/E_\text{r} = 6$), the wave functions of the two spin components overlap completely and the total density is well-described by a 2D Thomas–Fermi profile with interaction constant g_nn (see Eq. (1.24) as well as the corresponding discussion for the asymmetric configuration below). Apart from slight deviations due to the non-zero polarization, the total density in the plane-wave phase ($\Omega/E_\text{r} = 2.8$) is still close to the Thomas–Fermi prediction. In the stripe phase ($\Omega/E_\text{r} = 1.8$), the density profile exhibits the characteristic stripe pattern. The fact that the densities of the two spin components match exactly is a consequence of the symmetry of the intraspecies interactions and no longer holds in the asymmetric case,

as we will see below.

Phenomenologically, the stripe density profile can be approximated using the corresponding result for uniform systems [297] and replacing the uniform density $\bar{n}$ by a Thomas–Fermi envelope $n_{\mathrm{TF}}(\boldsymbol{x})$,

$$n(\boldsymbol{x}) = n_{\mathrm{TF}}(\boldsymbol{x})[1 + C\cos(2k_1 x + \phi)]\,. \tag{4.15}$$

Here, the wave number k_1 describes the periodicity of the stripes, ϕ is a phase, and the contrast C of the stripes is defined as

$$C = \frac{n_{\mathrm{max}} - n_{\mathrm{min}}}{n_{\mathrm{max}} + n_{\mathrm{min}}}\,. \tag{4.16}$$

As can be seen in Fig. 4.2, the same Thomas–Fermi profile describing the plane-wave and single-minimum phases corresponds to the envelope of the density profile in the stripe phase.

The red data points in Fig. 4.1 show the contrast of the stripes, extracted by fitting Eq. (4.15) to numerically computed ground state density profiles. It can be seen that the contrast of the stripes grows linearly with the Raman coupling, in agreement with the predictions for uniform systems with symmetric intraspecies interactions [297].

Polarizability

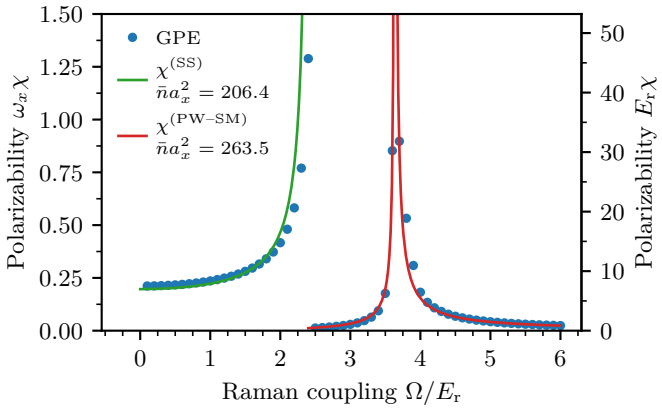

Figure 4.3.: Magnetic polarizability for symmetric intraspecies interactions. The polarizability diverges at the second-order phase transition between the plane-wave and single-minimum phase near $\Omega/E_\mathrm{r} \approx 3.65$. In the stripe phase, the polarizability is higher than in the bulk of the plane-wave and single-minimum phases and increases strongly as the transition to the plane-wave phase near $\Omega/E_\mathrm{r} = 2.4$ is approached. The continuous lines show fits of the analytical predictions according to Eq. (4.18) in the stripe phase and Eqs. (4.21) and (4.22) in the plane-wave and single-minimum phases, respectively, with the uniform density $\bar{n}$ taken as a fit parameter.

In Section 1.3.2, we have introduced the dynamical susceptibility as a key quantity that determines the linear response of a system to an external, possibly time-dependent perturbation. Here, we will be interested in the static susceptibility characterizing the

response of the polarization ($B = \sigma_z$) to a static perturbation by a magnetic field ($A = \sigma_z$). This quantity, which we will from now on also call the magnetic polarizability, is defined as [297]

$$\chi_{\mathrm{M}} = \lim_{h \to 0} \frac{\langle \sigma_z \rangle_h - \langle \sigma_z \rangle_{h=0}}{h} \,, \tag{4.17}$$

where $\langle \cdots \rangle_h$ denotes the expectation value with respect to the ground state in presence of the perturbation $H_1 = -h\sigma_z$ with a magnetic field h. Such a perturbation corresponds to an effective detuning and can therefore also be implemented optically by varying the detuning δ from the Raman resonance. The polarizability is deeply connected with dynamical properties like collective excitations. Using sum rule arguments (see Section 1.3.4), it is possible to derive a rigorous upper bound for the lowest energy mode [305], which we will use in the next section to infer the existence of the zero-frequency Goldstone mode associated with the translation of the stripes in the supersolid phase.

The polarizability of the symmetric SOC BEC configuration as a function of the Raman coupling Ω is depicted in Fig. 4.3. Similar results for symmetric intraspecies interactions in uniform and 1D harmonically trapped systems have been obtained in Ref. [305]. At the transition between the plane-wave and single-minimum phase near $\Omega/E_{\mathrm{r}} \approx 3.65$, the polarizability diverges, reflecting the second-order nature of this phase transition (the polarizability above and below the transition differ by a factor of two [305], as evident from the formulas given below). This divergence of the susceptibility has been confirmed experimentally by measuring collective dipole oscillations [306], whose frequency is strongly reduced close to the transition. In fact, a strong reduction of the frequency is expected for any hydrodynamic mode in x direction near the second-order transition where the polarizability diverges [297]. We will encounter such a behavior in the dispersion of the breathing (compression) mode in our analysis of collective excitations in Section 4.3.1 (see Fig. 4.7c).

The stripe phase is characterized by a significantly higher polarizability than in the bulk of the plane-wave and single-minimum phases. Close to the transition from the stripe to the plane-wave phase near $\Omega/E_{\mathrm{r}} = 2.4$, the polarizability is strongly peaked, before it jumps to a value close to zero in the plane-wave phase. The strongly enhanced polarizability in the stripe phase is a feature that may well be used to identify the supersolid phase in experiments.

For SOC BECs with symmetric intraspecies interactions, analytical predictions for the magnetic polarizability in uniform matter are available, which can be derived by means of a plane-wave variational ansatz for the ground state wave function [305]. For convenience, the relevant formulas are quoted below. In the supersolid (SS) phase, the prediction for the polarizability reads [307]

$$\chi_{\mathrm{M}}^{(\mathrm{SS})} = \frac{2E_{\mathrm{r}}\Omega^4 - 4(2E_{\mathrm{r}} + G_1)^2(4E_{\mathrm{r}} + G_1 + G_2)\Omega^2 + 16(2E_{\mathrm{r}} + G_1)^4(2E_{\mathrm{r}} + G_2)}{a_4\Omega^4 - a_2\Omega^2 + a_0} \tag{4.18}$$

with coefficients

$$a_0 = 32G_2(2E_\mathrm{r} + G_1)^4(2E_\mathrm{r} + G_2)\,, \tag{4.19a}$$
$$a_2 = 4(2E_\mathrm{r} + G_1)^2[(G_1 + 2G_2)(G_1 + G_2) + 2E_\mathrm{r}(G_1 + 4G_2)]\,, \tag{4.19b}$$
$$a_4 = 2E_\mathrm{r}(G_1 + 2G_2)\,, \tag{4.19c}$$

where $G_1 = \bar{n}g_\mathrm{nn}$ and $G_2 = \bar{n}g_\mathrm{ss}$ with the uniform density $\bar{n}$. Assuming weak couplings $G_1, G_2 \ll E_\mathrm{r}$, this rather involved expression simplifies to [305]

$$\chi_\mathrm{M}^{(\mathrm{SS})} = \frac{\Omega^2 - 16E_\mathrm{r}^2}{(G_1 + 2G_2)\Omega^2 - 32G_2E_\mathrm{r}}\,. \tag{4.20}$$

Finally, in the plane-wave (PW) and single-minimum (SM) phases, one finds, respectively, the predictions [305]

$$\chi_\mathrm{M}^{(\mathrm{PW})} = \frac{\Omega^2}{(2E_\mathrm{r} - 2G_2)[4(2E_\mathrm{r} - 2G_2)^2 - \Omega^2]}\,, \tag{4.21}$$
$$\chi_\mathrm{M}^{(\mathrm{SM})} = \frac{2}{\Omega - 2(2E_\mathrm{r} - 2G_2)}\,. \tag{4.22}$$

In Fig. 4.3, the above predictions for uniform systems have been fitted to the polarizability of the harmonically trapped system, computed by numerically solving the GPE. The only free parameter is the uniform density $\bar{n}$. The stripe phase has been fitted separately for values of the polarizability $\chi_\mathrm{M} < 0.45\,\omega_x^{-1} \approx 16\,E_\mathrm{r}^{-1}$ using the full expression (4.18), which turns out to describe the numerical data better than the simplified one in Eq. (4.20). Up to slight deviations close to the transitions, the analytical predictions are in good agreement with the numerical results.

4.2.2. Asymmetric Intraspecies Interactions

We now focus our attention on SOC BECs with highly asymmetric intraspecies interactions, $g_{\uparrow\uparrow} \gg g_{\downarrow\downarrow} \approx g_{\uparrow\downarrow}$, corresponding to $g_\mathrm{nn} \approx g_\mathrm{ss} \approx g_\mathrm{ns}$. Such configurations have recently become available in experiments on ^{39}K and represent a promising setting for studying supersolidity in spin–orbit-coupled systems [296]. Our main motivation is to explore how the strong polarization effects due to the asymmetric interactions influence the static and dynamic properties of this system, especially in the stripe phase. Specifically, we consider a set of scattering lengths given by $a_{\uparrow\uparrow} = 252.7\,\mathrm{a}_0$, $a_{\downarrow\downarrow} = 1.3\,\mathrm{a}_0$, and $a_{\uparrow\downarrow} = -6.3\,\mathrm{a}_0$, which can be realized in ^{39}K by using Feshbach resonances near a magnetic field of $B \approx 389\,\mathrm{G}$ [296]. These values are consistent with the stability criterion $g_{\uparrow\uparrow}g_{\downarrow\downarrow} > g_{\uparrow\downarrow}^2$ for binary quantum gas mixtures [57]. The full set of parameters can be found in Table 4.1. As an exception, the polarization and density profiles depicted in Figs. 4.5 and 4.6 have been computed for a different trap geometry, $(\omega_x, \omega_y, \omega_z) = 2\pi \times (138, 125, 59)\,\mathrm{Hz}$, and particle number $N = 1.4 \times 10^5$, corresponding to specific set of experimental parameters [296].

It should be noted that for sufficiently small differences of the interaction parameters, the effect of the asymmetry can be compensated by applying an appropriate detuning δ [297]. The ground state then exhibits the same properties as in the symmetric case. However, for the highly asymmetric configuration above ($g_{\uparrow\uparrow}/g_{\downarrow\downarrow} \approx 194$), an exact compensation is not possible in general. In what follows, we explore the consequences of the asymmetric intraspecies interactions for $\delta = 0$.

Polarization

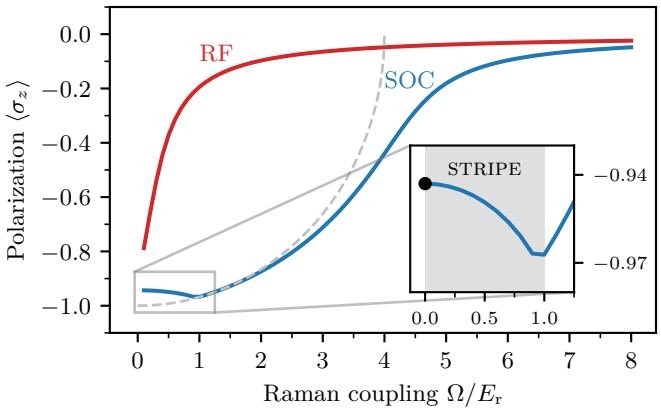

Figure 4.4.: Ground state polarization of a harmonically trapped SOC BEC with highly asymmetric intraspecies interactions. The polarization gradually decreases with as the Raman coupling Ω increases, indicating a smooth crossover between the plane-wave and single-minimum regimes. In the stripe phase, shown in the inset, the polarization remains large in magnitude, as opposed to the symmetric configuration (cf. Fig. 4.3). The black dot marks the analytical prediction by Eq. (4.26) at small Ω, $\langle\sigma_z\rangle \approx -0.943$. The behavior of the polarization is compared to that in systems with radio frequency (RF) coupling (red curve) as well as spin–orbit coupling with symmetric interactions (grey dashed line). Differing from the parameters given in Table 4.1, the experimental values $(\omega_x, \omega_y, \omega_z) = 2\pi \times (138, 125, 59)\,\mathrm{Hz}$ and $N = 1.4 \times 10^5$ [296] have been used in this figure.

Figure 4.4 shows the polarization of the SOC BEC configuration with asymmetric intraspecies interactions as a function of the Raman coupling Ω. At large values of Ω, the system can minimize its energy most efficiently by maximizing the overlap of the wave functions of the two spin components, which is why the polarization is close to zero in this regime. As Ω becomes smaller, the polarization gradually increases in magnitude. Unlike in the symmetric case (Fig. 4.1), there is no second-order phase transition, but rather a smooth crossover between the single-minimum and the plane-wave regime, the latter being characterized by a strong polarization. The direct comparison to an equivalent system with a simple radio frequency (RF) coupling, formally obtained by setting $k_0 = 0$ in Eq. (4.4), exposes the crucial polarization effects incurred by spin–orbit coupling: the presence of the spin-orbit term $\propto -k_0 p_x \sigma_z$ in the single-particle Hamiltonian (4.1) favors spin polarization and is responsible for the qualitatively different behavior of the polarization between RF and spin–orbit coupling, as evident from Fig. 4.4. As a

guide to the eye, the dashed line in this figure shows the prediction by Eq. (4.14) for $g_{\mathrm{ss}} = 0$, $\langle \sigma_z \rangle = -\sqrt{1-(\Omega/4E_{\mathrm{r}})^2}$, which reflects the behavior of systems like ^{87}Rb where all interaction constants are approximately equal. Clearly, in the asymmetric case, configurations with opposite polarizations are no longer energetically equivalent.

At the value $\Omega_{\mathrm{c}}/E_{\mathrm{r}} \approx 1$, a transition to the stripe phase occurs and the system slightly depolarizes as the Raman coupling decreases further. There are two crucial differences with respect to the stripe phase in the symmetric case. First, there is no jump in the order parameter, but the polarization behaves continuous at the transition to the stripe phase. This indicates that, as the transition is approached from the stripe phase, the contrast of the stripes is reduced, whereas in Fig. 4.1, the stripes reach there maximum contrast just before the transition. Second, as opposed to the symmetric case, where the polarization in the stripe phase vanishes, for highly asymmetric intraspecies interactions, the system remains strongly polarized even in the stripe phase.

A simple estimate of this effect can be obtained in uniform matter for $\Omega \to 0$ [308]. In this limit, the contribution of k_0 to the kinetic term in Eq. (4.5) can be transformed away by means of $\boldsymbol{\Psi} \to \mathrm{e}^{i\boldsymbol{k}_0 \boldsymbol{x} \sigma_z} \boldsymbol{\Psi}$. Then, in uniform matter, we can make the ansatz $\boldsymbol{\Psi} = \sqrt{\bar{n}}(C_\uparrow, C_\downarrow)^\top$, yielding the energy per particle

$$\epsilon = \frac{1}{2}\bar{n} g_{\mathrm{nn}} + \left(\frac{\delta}{2} + \bar{n} g_{\mathrm{ns}}\right) S + \frac{1}{2}\bar{n} g_{\mathrm{ss}} S^2 \tag{4.23}$$

with $S = |C_\uparrow|^2 - |C_\downarrow|^2$, subject to the normalization constraint $|C_\uparrow|^2 + |C_\downarrow|^2 = 1$. It is convenient to introduce a new variable θ via $C_\uparrow = \cos^2(\theta/2)$ and $C_\downarrow = \sin^2(\theta/2)$, such that $S = \cos(\theta)$. This quantity directly corresponds to the polarization, $\langle \sigma_z \rangle = s_z/n = \cos(\theta)$. Minimizing Eq. (4.23) at fixed uniform density $\bar{n}$ with respect to θ yields the condition

$$\left(\frac{\delta}{2} + \bar{n} g_{\mathrm{ns}}\right) \sin(\theta) + \bar{n} g_{\mathrm{ss}} \cos(\theta) \sin(\theta) = 0\,. \tag{4.24}$$

Thus, the minimum energy configuration corresponds to

$$\cos(\theta) = -\frac{\bar{n} g_{\mathrm{ns}} + \delta/2}{\bar{n} g_{\mathrm{ss}}}\,, \tag{4.25}$$

provided that $|\bar{n} g_{\mathrm{ns}} + \delta/2| \leq \bar{n}|g_{\mathrm{ss}}|$. If this stability condition is not satisfied, the energy minimum is instead given by $\sin(\theta) = 0$, corresponding to a fully polarized system. At $\delta = 0$, Eq. (4.25) yields the polarization

$$\langle \sigma_z \rangle = -\frac{g_{\mathrm{ns}}}{g_{\mathrm{ss}}} \tag{4.26}$$

and the stability condition is fulfilled if $g_{\uparrow\uparrow} > g_{\uparrow\downarrow}$ and $g_{\downarrow\downarrow} > g_{\uparrow\downarrow}$. For the asymmetric configuration under investigation, this prediction yields the value $\langle \sigma_z \rangle = -0.943$, which is in excellent agreement with the numerical results in Fig. 4.4 (black dot in the inset). As this simple estimate shows, the strong polarization in the stripe phase is a consequence of the highly asymmetric intraspecies interactions, which is in stark contrast to the symmetric case, where we have $g_{\mathrm{ns}} = 0$ and the polarization vanishes in the stripe phase (see Fig. 4.1).

Density Profiles

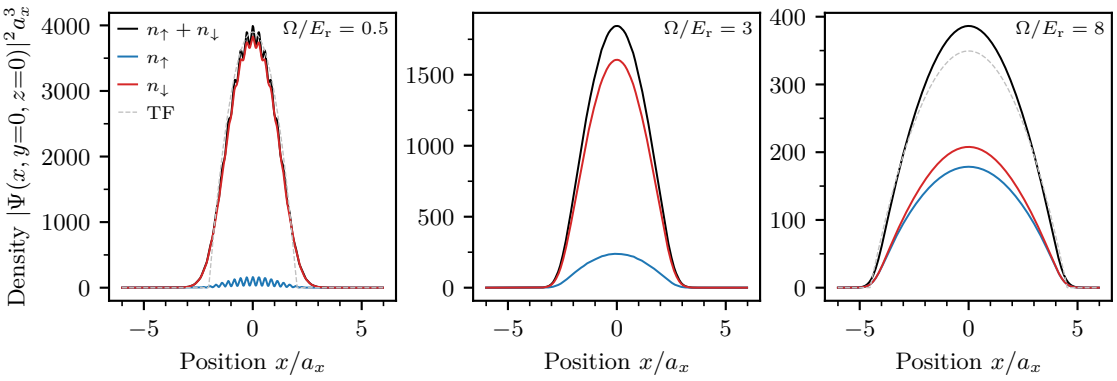

Figure 4.5.: Ground state density profiles for highly asymmetric intraspecies interactions. The three panels represent typical profiles in the stripe phase ($\Omega/E_\mathrm{r} = 0.5$), plane-wave phase ($\Omega/E_\mathrm{r} = 3$), and single-minimum phase ($\Omega/E_\mathrm{r} = 8$). The central density increases strongly as the Raman coupling is reduced, which is accompanied by a shrinking of the cloud radius. At small and large Ω, the total density is close to a Thomas–Fermi profile with effective interaction constants $g_\mathrm{nn} - g_\mathrm{ns}^2/g_\mathrm{ss}$ and g_nn, respectively (grey dashed lines). Differing from the parameters given in Table 4.1, the experimental values $(\omega_x, \omega_y, \omega_z) = 2\pi \times (138, 125, 59)\,\mathrm{Hz}$ and $N = 1.4 \times 10^5$ [296] have been used in this figure.

To gain a deeper understanding of the polarization effects due to highly asymmetric intraspecies interactions, we consider typical density profiles in the stripe ($\Omega/E_\mathrm{r} = 0.5$), plane-wave ($\Omega/E_\mathrm{r} = 3$), and single-minimum regimes ($\Omega/E_\mathrm{r} = 8$), as illustrated in Fig. 4.5. The stripe phase is characterized by a large polarization and fringes of high contrast in the minority component $\Psi_\uparrow$. The polarization remains large also in the plane-wave regime, and decreases only gradually at large Raman couplings as the system enters the single-minimum regime. A main difference with respect to the symmetric case in Fig. 4.2, where the total density is approximately the same across the phase diagram, is the strong increase of the central density at small and intermediate Raman couplings (note the different scales on the y axes in Fig. 4.5). The enhancement of the central density, dominated by the majority component $\Psi_\downarrow$, is accompanied by a shrinking of the cloud radius.

This effect can be estimated in a simple way for $\Omega \to 0$ [308]. In this limit, the contrast of the stripes is small and we can use the Thomas–Fermi approximation, which consists of neglecting the kinetic term in the energy functional (4.5). It is important to keep in mind, however, that the coherent coupling fixes the value of the polarization. To take this effect into account, we use the estimate for the polarization in Eq. (4.26) and substitute $s_z = -n g_\mathrm{ns}/g_\mathrm{ss}$, such that the energy functional becomes

$$E = \int \mathrm{d}\boldsymbol{x} \left[V(\boldsymbol{x}) n + \frac{1}{2} \left(g_\mathrm{nn} - \frac{g_\mathrm{ns}^2}{g_\mathrm{ss}} \right) n^2 \right]. \tag{4.27}$$

The total density in 3D is then described by a Thomas–Fermi profile with chemical potential (1.25), Thomas–Fermi radius (1.26), and an effective scattering length a_eff,

which, in the light of Eq. (4.27), is given by

$$\frac{4\pi\hbar^2}{m}a_{\mathrm{eff}} \equiv g_{\mathrm{eff}} = g_{\mathrm{nn}} - \frac{g_{\mathrm{ns}}^2}{g_{\mathrm{ss}}} = \frac{g_{\uparrow\uparrow}g_{\downarrow\downarrow} - g_{\uparrow\downarrow}^2}{g_{\uparrow\uparrow} + g_{\downarrow\downarrow} - 2g_{\uparrow\downarrow}}\,. \tag{4.28}$$

Thus, for a non-zero value of g_{ns}, the effective scattering length is reduced, which leads to a shrinking of the Thomas–Fermi radius $R_{\mathrm{TF}} \propto a_{\mathrm{eff}}^{1/5}$ as well as to an enhancement of the central density $n(0) = \mu_{\mathrm{TF}}/g_{\mathrm{eff}} \propto a_{\mathrm{eff}}^{-3/5}$. In Fig. 4.5, it can be seen that the density profile in the stripe phase is close to the Thomas–Fermi prediction obtained by this simple estimate (grey dashed line).

In the opposite limit of large Raman couplings Ω, the spin density s_z is instead small as the tendency of the two spin components to overlap dominates over the polarization favored by the asymmetric interaction and the spin–orbit term. According to the energy functional in Eq. (4.5), this suggests that the system mainly interacts via the total density n, characterized by the interaction constant g_{nn}. Consequently, it is reasonable to expect the density to be well approximated by a Thomas–Fermi profile with effective interaction constant $g_{\mathrm{eff}} = g_{\mathrm{nn}}$. Indeed, the density profile in Fig. 4.5 at $\Omega/E_{\mathrm{r}} = 8$ is close to this prediction (grey dashed line), and the agreement further improves for larger values of Ω. In contrast, the symmetric case in Fig. 4.2 is well described by a Thomas–Fermi profile with $g_{\mathrm{eff}} = g_{\mathrm{nn}}$ in both limits of small and large Raman couplings, which follows for $\Omega \to 0$ from Eq. (4.28) by noting that $g_{\mathrm{ns}} = 0$, and in the opposite limit by the same argument of a vanishing polarization due the large Raman coupling.

Polarizability

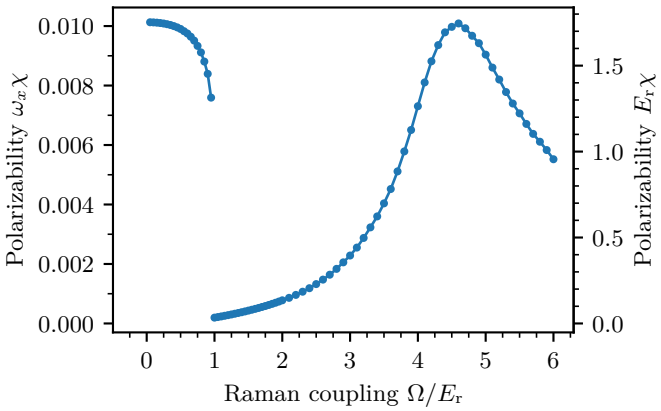

Figure 4.6.: Magnetic polarizability for highly asymmetric intraspecies interactions. The polarizability is peaked near the crossover between the plane-wave and single-minimum regimes around $\Omega/E_{\mathrm{r}} = 4$, but there is no divergence as in the symmetric case (cf. Fig. 4.3). In the stripe phase, the polarizability is higher than in the bulk of the other phases. As the critical Raman coupling $\Omega_{\mathrm{c}}/E_{\mathrm{r}} \approx 1$ is approached, the polarizability sharply drops, which is the opposite behavior as observed for symmetric intraspecies interactions.

To conclude our discussion of ground state properties of the asymmetric SOC BEC configuration, we consider the polarizability as a function of the Raman coupling Ω shown in Fig. 4.6. Obviously, there is no divergence of the polarizability at the crossover between the plane-wave and single-minimum regimes due to the absence of a proper phase transition, in line with the behavior of the polarization in Fig. 4.4. However, a remnant of this phase transition is still clearly visible in form of a peak near the Raman coupling $\Omega/E_\mathrm{r} = 4$, where the single-particle dispersion relation (4.2) changes from a double-minimum to a single-minimum structure.

As in the symmetric case, the stripe phase features a higher polarizability compared to the bulk of the plane-wave and single-minimum regimes. However, the polarizability in the stripe phase of the asymmetric configuration is more than one order of magnitude smaller than that of the symmetric configuration. Intuitively, this is a consequence of the strong polarization due to the asymmetric intraspecies interactions, which requires a stronger magnetic field to polarize the system even further. Yet, there is a key difference: at the transition from the stripe to the plane-wave regime near $\Omega/E_\mathrm{r} = 1$, there is a sharp drop of the polarizability, which is connected to the gradual disappearance of the stripes discussed in the context of Fig. 4.4. This is in stark contrast to the behavior of the symmetric configuration in Fig. 4.3, where the polarizability instead strongly increases and the stripes acquire their highest contrast just before the transition.

In principle, it is possible to understand the properties of the asymmetric configuration in uniform matter using a similar plane-wave ansatz for the ground state wave function as in Ref. [301]. However, due to the strongly enhanced central density at low and intermediate values of the Raman coupling (see Fig. 4.5), the relevant interaction constants are no longer small. Thus, the corresponding theory likely requires the inclusion of higher harmonics in the ansatz, such that the relevant equations become much more involved and must in general be solved numerically [307].

4.3. Probing Supersolidity by Exciting Golstone Modes

Having compared the equilibrium properties of SOC BECs with symmetric and asymmetric intraspecies interactions in the previous section, we now consider dynamic properties and study collective excitations. To this end, we consider the following linear response protocol. The system is initially prepared in the ground state in presence of a static perturbation of density or spin nature. At time $t = 0$, the perturbation is suddenly removed, which excites collective oscillations. The frequencies ω of these oscillations can then be extracted from sinusoidal fits to the time traces of the relevant observables. Repeating this procedure for different Raman couplings Ω yields the dispersion relation $\omega(\Omega)$, which allows us to study the hybridization of density and spin degrees of freedom in spin–orbit-coupled configurations and reveals characteristic signatures of supersolidity in the stripe phase. In order to simulate this protocol numerically, the time-dependent GPE (4.8) has been solved using a time-splitting Fourier pseudospectral method [309], while the same method for computing ground states as in the previous section has been employed.

More specifically, we consider breathing (monopole) oscillations, generated by suddenly changing the trap frequency. As we will see, the behavior of this excitation changes drastically at the transition to the supersolid phase. Above the critical Raman coupling, a single mode of hybridized density and spin nature is excited, while below it, a beating of two different frequencies can be observed, signaling the excitation of a Goldstone spin–dipole mode.

Furthermore, we explore experimentally accessible signatures of the zero-frequency Goldstone mode associated with the translational motion of the stripes. Indirect evidence for its existence can be gained from the behavior of the center-of-mass (dipole) mode in relation to the previously discussed polarizability when the transition to the stripe phase is crossed. In addition, it turns out that the zero-frequency Goldstone mode can also be excited directly by applying a uniform spin perturbation, which is accompanied by a characteristic locking of the polarization.

These effects can be observed in both configurations with symmetric and highly asymmetric intraspecies interactions, which therefore provide promising platforms for experimentally observing typical supersolid features in SOC BECs.

4.3.1. Goldstone Spin-Dipole Mode

A main feature that distinguishes spin–orbit-coupled configurations from other platforms for studying supersolidity is the existence of a non-trivial spin degree of freedom. The coupling between density and spin by the spin–orbit term in the Hamiltonian (4.1) leads to a mixture (or hybridization) of the corresponding degrees of freedom. For example, in the plane-wave and single-minimum phase, the position (or dipole) operator x excites the same mode as the spin operator σ_z, which follows from the locking of the relative phase of the spin wave functions in these phases [297, 310]. A similar hybridization mechanism exists between the operators x^2 and $x\sigma_z$, the former exciting the breathing (monopole) mode and the latter exciting the spin dipole mode, i.e., the oscillation of the two spin components relative to each other. In what follows, we exploit the hybridization of these modes and show that the character of the breathing oscillation changes qualitatively when crossing the transition to the supersolid phase. While above the transition only a single frequency is excited, corresponding to full hybridization, below it there is a beating of two frequencies. The newly emerging mode in the supersolid phase corresponds to a spin–dipole oscillation and its Goldstone nature derives from the fact that its frequency vanishes at the critical Raman coupling, such that it can be identified with a gapless Goldstone spin branch in uniform matter [311]. The appearance of a Goldstone mode of spin nature in the supersolid phase shows that the phenomenon of supersolidity becomes even richer in systems with non-trivial spin degree of freedom and motivates further studies of such configurations. In particular, the predicted beating effects represent an experimentally accessible signature of supersolidity in both systems with symmetric and asymmetric intraspecies interactions.

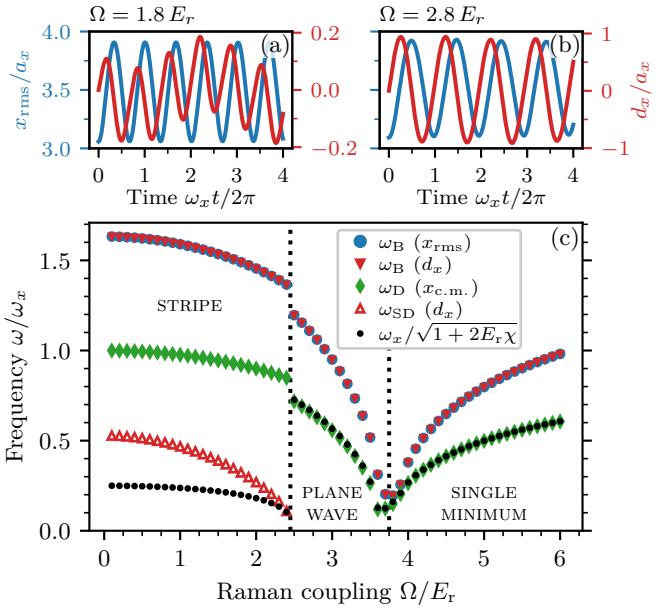

Figure 4.7.: Collective modes of a harmonically trapped SOC BEC with symmetric intraspecies interactions. (a),(b) Oscillations of the observables $x_{\mathrm{rms}} = \sqrt{\langle x^2 \rangle}$ and $d_x = \langle x \rangle_\uparrow - \langle x \rangle_\downarrow$ after suddenly removing the perturbation $H_1 = \lambda m \omega_x^2 x^2$ with $\lambda = 0.2$. In the stripe phase (a), a clear beating of two frequencies $\omega_{\mathrm{B}} \approx 1.49\,\omega_x$ and $\omega_{\mathrm{SD}} \approx 0.32\,\omega_x$ is visible in the observable d_x, which is absent in the plane-wave phase (b), where d_x oscillates only at a single frequency $\omega_{\mathrm{B}} \approx 1.02\,\omega_x$. (c) Dispersion $\omega(\Omega)$ of the breathing mode (B), the spin-dipole mode (SD), and the center-of-mass (dipole) mode (D), calculated for $\lambda \ll 1$. The breathing and the spin-dipole modes are fully hybridized above the critical coupling $\Omega_{\mathrm{c}} \approx 2.5\,E_{\mathrm{r}}$, while below Ω_{c}, a new Goldstone mode of spin nature appears. The dipole frequencies ω_{D} have been obtained from the center-of-mass oscillation $x_{\mathrm{c.m.}} = \langle x \rangle$ after a sudden shift of the trap center. For $\Omega > \Omega_{\mathrm{c}}$, they practically coincide with the bound $\omega_x/\sqrt{1 + 2E_{\mathrm{r}}\chi}$. The violation of this upper bound by ω_{D} for $\Omega < \Omega_{\mathrm{c}}$ implies the emergence of a new low-energy mode.

Symmetric Intraspecies Interactions

We first investigate the configuration with symmetric intraspecies interactions. As we are interested in probing collective excitations along the x axis, i.e., the axis of spin–orbit coupling, we have chosen an elongated trap in x direction (see parameters in Table 4.1). The elongated trap geometry is also advantageous for studying axial breathing oscillations excited by the operator x^2 as it avoids the simultaneous excitation of the quadrupole mode.

Figures 4.7a and 4.7b, shows the time dependence of the root-mean-square radius $x_{\mathrm{rms}} = \sqrt{\langle x^2 \rangle}$ and of the relative displacement $d_x = \langle x \rangle_\uparrow - \langle x \rangle_\downarrow$ of the two spin components after suddenly removing the static perturbation $H_1 = \lambda m \omega_x^2 x^2$, corresponding to a sudden decrease of the trapping frequency ω_x by a factor $\sqrt{1 + 2\lambda}$. Note that for an unpolarized system, the spin displacement d_x is linked to the expectation value of the operator $x\sigma_z$ via $d_x = 2\langle x\sigma_z \rangle$. Since the commutator $[x^2, H_{\mathrm{SOC}}]$ contains a term pro-

portional to $x\sigma_z$, one would expect, in general, to observe two collective oscillations of hybridized density and spin nature. For values of Ω larger than the critical coupling Ω_c, we find instead that the observables x_{rms} and d_x oscillate with one and the same frequency (see Fig. 4.7b). This is the consequence of the locking of the relative phase of the order parameters of the two spin components characterizing the low-frequency oscillations in the plane-wave and single-minimum phases [310].

When entering the stripe phase, the scenario changes drastically and we observe the appearance of a new oscillation of spin nature, revealed by the beating in the signal d_x (see Fig. 4.7a). This oscillation is the finite-size manifestation of the gapless Goldstone spin branch exhibited by the supersolid phase in uniform matter [311]. The beating reflects the fact that the two gapless branches are decoupled density and spin modes only in the limit of long wavelengths. An analogous effect has recently been identified in spin–orbit-coupled fluids of light in Kerr non-linear media [312].

The dispersion $\omega(\Omega)$ of the breathing and spin-dipole modes excited by the operator x^2 is shown in Fig. 4.7c. The observable $x_{rms} = \sqrt{\langle x^2 \rangle}$, associated with the density perturbation operator x^2, oscillates in all phases at a single frequency, the breathing frequency ω_B, which is the same frequency found in the d_x signal. However, as described above, in the stripe phase, the spin observable d_x contains a second frequency ω_{SD}, corresponding to the spin-dipole mode. Conversely, by applying a spin perturbation proportional to $x\sigma_z$, which amounts to a relative displacement of the two spin components, one finds that the observable d_x associated with the spin excitation operator $x\sigma_z$ oscillates at the single frequency ω_B in all phases, but a beating of ω_B and ω_{SD} occurs in the density observable x_{rms} when entering the stripe phase. The fact that the density operator x^2 and the spin operator $x\sigma_z$ excite the same modes is an expression of the hybridization of density and spin degrees of freedom in spin–orbit-coupled systems.

At small values of the Raman coupling Ω, the breathing frequency in Fig. 4.7c approaches the analytical prediction $\omega_B/\omega_x = \sqrt{8/3} \approx 1.63$ for the axial breathing mode in a 2D harmonic trap [57]. Furthermore, in the limit $\Omega \to 0$, the spin-dipole frequency can be calculated analytically within the formalism of two-fluid hydrodynamics [57]. One finds

$$\omega_{SD}^2(\Omega \to 0) = \omega_x^2 \frac{1 - (g_{ns}/g_{ss})^2}{g_{nn}/g_{ss} - (g_{ns}/g_{ss})^2}, \tag{4.29}$$

yielding the value $\omega_{SD} = 0.5\,\omega_x$ for the symmetric configuration under investigation, in agreement with Fig. 4.7c. The dispersion of the spin-dipole branch decreases as Ω approaches the transition at the critical value Ω_c and is expected to vanish at the spinodal point, corresponding to a value of Ω a little higher than Ω_c where the system develops a dynamic instability associated with the divergent behavior of the magnetic polarizability [305] (see Fig. 4.3). The decrease of ω_{SD} as a function of Ω is a crucial consequence of spin–orbit coupling and of the presence of stripes. By contrast, for a radio frequency or microwave coupling, the spin-dipole frequency increases with the coupling strength, quickly approaching the value Ω of the spin gapped branch [313].

In addition to the breathing and spin-dipole frequencies, Fig. 4.7c also shows the dispersion of the center-of-mass (dipole) mode, which can be excited by suddenly removing the perturbation $H_1 = -\lambda m \omega_x^2 a_x x$, corresponding to a shift of the harmonic trap by

a distance λa_x in x direction. Above Ω_c, the dipole operator x and the spin operator σ_z excite the same mode, similar to the case of the operators x^2 and $x\sigma_z$ discussed above. Both the breathing and the dipole frequencies decrease when approaching the transition to the single-minimum phase, where the effective mass increases, inducing sizable non-linear effects [305, 306]. These anharmonic properties make it difficult to observe stable harmonic oscillations at very low frequencies close to the second-order transition in experiments [306] and even in numerical simulations, where high spatial and temporal accuracy as well as weak perturbations are required to suppress the proliferation of instabilities. At the transition to the supersolid phase, both the breathing and the dipole frequencies exhibit a small jump, reflecting the first-order nature of the supersolid–superfluid transition. As we will see below, using sum rule arguments, the behavior of the dipole frequency and the high polarizability in the stripe phase provide indirect evidence for the zero-frequency Goldstone mode associated with the translation of the stripes.

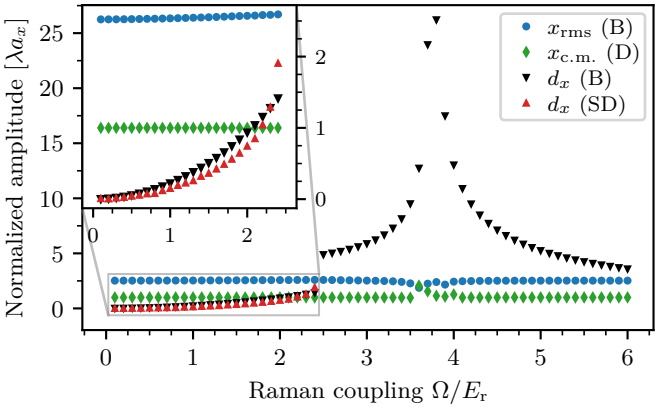

Figure 4.8.: Amplitudes of the collective modes in Fig. 4.7c for symmetric intraspecies interactions. They have been extracted in the linear regime and are normalized by the perturbation strength λ. The amplitudes of the spin-dipole observable d_x are strongly peaked around the second-order transition between the plane-wave and single-minimum phase. In the stripe phase (inset), the amplitudes of the frequency components ω_B and ω_{SD} in the beating signal d_x increase gradually with the Raman coupling.

Figure 4.8 shows the amplitudes of the oscillations corresponding to the frequencies in Fig. 4.7c, normalized with respect to the perturbation strength λ. The amplitudes of the breathing and dipole modes are approximately constant, with only small instabilities close to the second-order phase transition between the plane-wave and single-minimum phase. In the vicinity of this transition, the amplitude of the spin-dipole observable d_x is strongly peaked, which is linked to the divergence of the polarizability (cf. Fig. 4.3). In the stripe phase (shown in the inset of Fig. 4.8), the amplitudes of both frequency components in the beating signal d_x gradually increase with the Raman coupling and thus with the contrast of the stripes. The beating signal is strongest just before the transition to the plane-wave phase, where the two modes fully hybridize and the amplitude exhibits a discontinuity as typical for first-order phase transitions.

The frequencies and amplitudes of the collective excitations in Figs. 4.7c and 4.8 have been calculated for small perturbations in the regime of linear response. However, the beating effect in the supersolid phase is clearly visible also for larger perturbation strengths (cf. Fig. 4.7a) that are closer to the onset of the non-linear regime. We will analyze the impacts of non-linearities in more detail for the asymmetric configuration in the next section.

Finally, we remark that similar dispersion laws as in Fig. 4.7c have been obtained in Ref. [314] by solving the Bogoliubov equations for a spin–orbit-coupled mixture in one dimension. With respect to Ref. [314], the present approach explicitly exposes the beating effect between the spin-dipole excitation and the compression mode in the stripe phase, as well as the full hybridization of the two modes above Ω_c.

Asymmetric Intraspecies Interactions

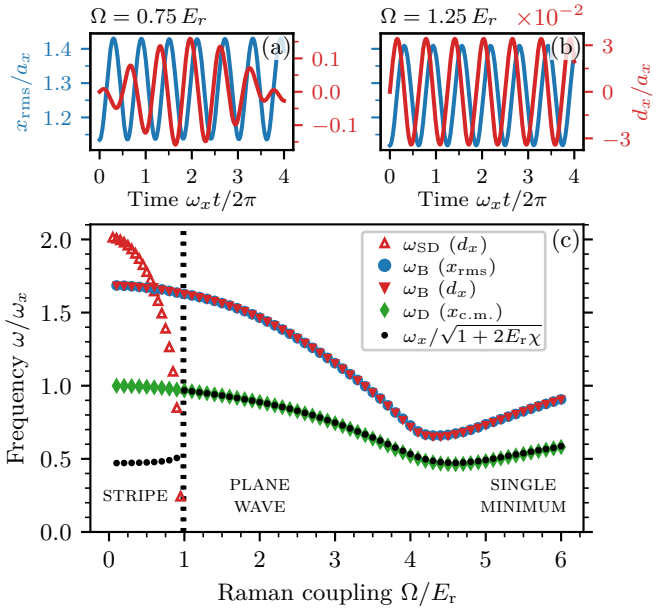

Figure 4.9.: Same as Fig. 4.7, but for highly asymmetric intraspecies interactions. The asymmetry leads to a smooth crossover between the plane-wave and the single-minimum regime. Nevertheless, in the stripe phase, the beating effects (a) and the additional frequencies (c) characteristic of the Goldstone spin-dipole mode are evident, while they are absent in the plane-wave phase (b).

We now investigate the analogous scenario for the configuration with highly asymmetric intraspecies interactions, as relevant for experiments on ^{39}K. As before, in order to probe collective excitations along the x axis, an elongated trap in x direction has been chosen (see parameters in Table 4.1), which also suppresses quadrupole oscillations excited by the operator x^2. Following the same procedure employed in the symmetric case, we consider the relative displacement d_x of the two components after a sudden

quench of the trapping frequency. The respective time traces are illustrated in Figs. 4.9a and 4.9b for a Raman coupling below and above the transition to the supersolid phase at $\Omega_c/E_r \approx 1$. Also in this case, we observe a clear beating effect, revealing the occurrence of a Goldstone mode of spin nature in the stripe phase. Because of the large polarization of the system, this mode mainly corresponds to the motion of the minority component $\Psi_\uparrow$, while the majority component $\Psi_\downarrow$ remains practically at rest, i.e., $d_x \approx \langle x \rangle_\uparrow$.

In Fig. 4.9c, the dispersion law of the resulting elementary excitations is shown as a function of the Raman coupling Ω, along with the dispersion of the center-of-mass mode excited by shifting the trap center. At $\Omega \to 0$, the spin-dipole frequency is larger than the center-of-mass frequency as a result of the negative interspecies interaction $g_{\uparrow\downarrow}$, in agreement with Eq. (4.29). Because of the asymmetry of the intraspecies interactions, the transition between the plane-wave and the single-minimum phase is less sharp than in the symmetric case and actually becomes a smooth crossover. Nonetheless, the qualitative features of the excitation spectrum are similar to the symmetric case. In particular, the beating effect in the observable d_x, signaling the emergence of a Goldstone spin-dipole mode below the critical coupling $\Omega_c/E_r \approx 1$, provides a clear experimental signature of the supersolid phase.

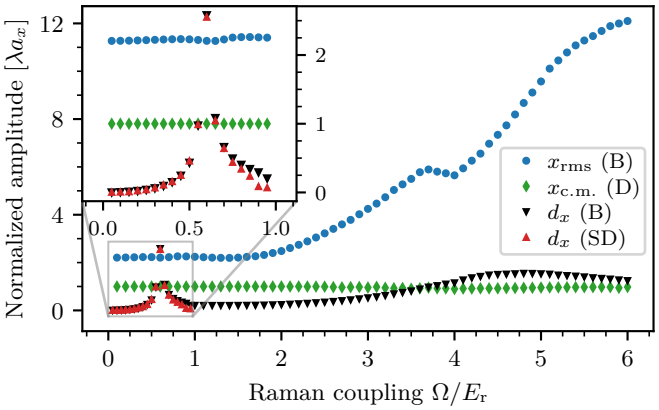

Figure 4.10.: Amplitudes of the collective modes in Fig. 4.9c for highly asymmetric intraspecies interactions. The gradual increase of the amplitude of the breathing oscillation in the observable x_{rms} reflects the growth of the cloud radius with increasing Raman coupling. A shallow peak in the amplitude of d_x around $\Omega/E_r = 4$ indicates the smooth crossover between the plane-wave and single-minimum regime. In the stripe phase (inset), the amplitudes of the frequency components ω_B and ω_{SD} in the beating signal d_x exhibit a peak where the stripes reach their maximum contrast.

The normalized oscillation amplitudes corresponding to the frequencies in Fig. 4.9c are shown in Fig. 4.10. Unlike in the symmetric case (see Fig. 4.8), the amplitude of the x_{rms} oscillation grows with increasing Raman coupling, which reflects the concomitant increase of the cloud radius (see Fig. 4.5). While for symmetric intraspecies interactions the amplitude of the signal d_x is strongly peaked at the transition between the plane-wave and single-minimum phase, the asymmetric configuration exhibits only a moderate increase of the amplitude in this region. Interestingly, the amplitudes of the frequency

components creating the beating signal d_x reach a maximum in the bulk of the stripe phase (see inset in Fig. 4.10). As mentioned before, in the system with asymmetric intraspecies interactions, the stripes disappear continuously as the transition to the plane-wave phase is approached and their contrast does not jump as in the symmetric case. Hence, the maximum amplitude in Fig. 4.10 is found at the Raman coupling where the stripes have their highest contrast. This shows that the beating effect and the appearance of the Goldstone spin–dipole mode are intrinsically connected with the presence of stripes.

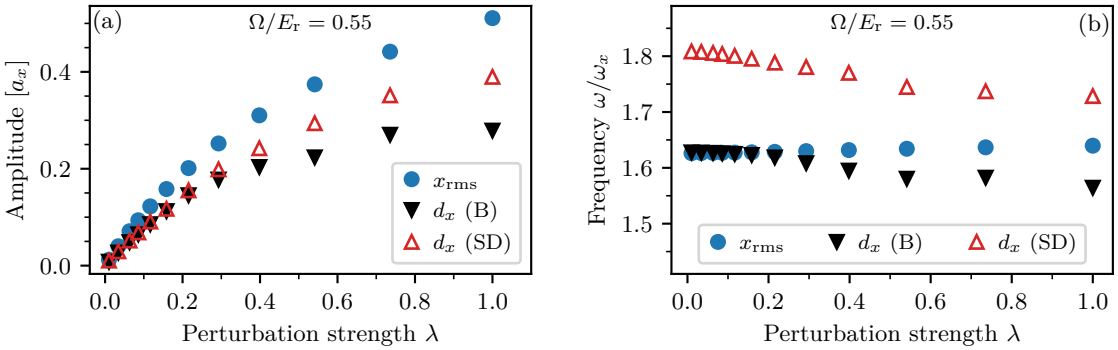

Figure 4.11.: Amplitudes of collective modes excited by the operator x^2 as a function of the perturbation strength λ for highly asymmetric intraspecies interactions. The Raman coupling $\Omega/E_\mathrm{r} = 0.55$ lies in the bulk of the stripe phase. As the perturbation strength extends into the non-linear regime, the frequencies ω_B and ω_SD in the signal d_x start deviating moderately, but the beating effect remains robust.

It is important to keep in mind that the frequencies and amplitudes in reported Figs. 4.9c and 4.10 have been computed for weak perturbations in the linear regime. However, experiments are often forced to apply stronger perturbations in order to obtain a sufficiently large signal-to-noise ratio. Thus, it is a relevant question whether the predicted beating effect in the supersolid phase survives in the non-linear regime typically probed in experiments. As our protocol of exciting collective modes is by no means restricted to the linear regime, we can answer this question by studying how the amplitudes and frequencies change as the perturbation strength λ is increased beyond the linear regime. This is illustrated in Fig. 4.11 for a fixed value of the Raman coupling in the stripe phase. For small perturbations, the amplitudes in Fig. 4.11a behave linearly and the frequencies in Fig. 4.11b are approximately constant. As the perturbation strength is increased into the non-linear regime, the frequencies slightly deviate, but the beating effect remains robust. This suggests that a measurement of the Goldstone spin–dipole mode is in reach for state-of-the-art experimental setups.

4.3.2. Zero-Frequency Goldstone mode

In the supersolid phase, one expects the emergence of the crystal Goldstone mode that corresponds, in uniform matter, to the rigid translation of stripes. In a harmonic trap, the frequency of this motion is not exactly zero, but still much smaller than the oscillator

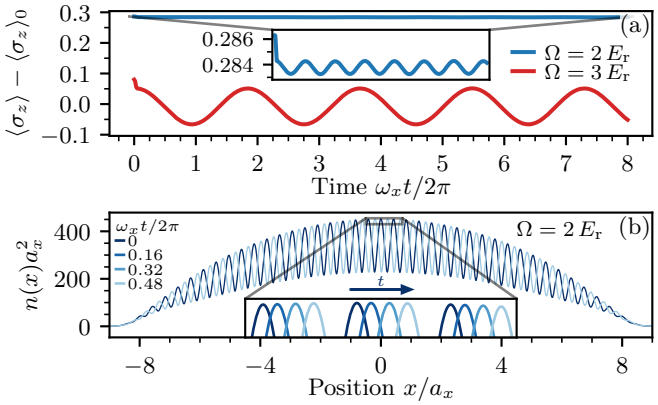

Figure 4.12.: Evidence for the zero-frequency Goldstone mode associated with the translation of the stripes in a SOC BEC with symmetric intraspecies interactions. (a) Time evolution of the polarization $\langle\sigma_z\rangle$ with respect to its equilibrium value $\langle\sigma_z\rangle_0$ after removing the perturbation $H_1 = -\lambda E_r \sigma_z$ with $\lambda = 0.02$ in the stripe phase ($\Omega = 2\,E_r$) and $\lambda = 0.1$ in the plane-wave phase ($\Omega = 3\,E_r$). In the latter case, the polarization oscillates around equilibrium at the dipole frequency $\omega_D \approx 0.55\,\omega_x$. By contrast, in the stripe phase, the polarization remains locked for a time much longer than $2\pi/\omega_x$, providing evidence for the zero-frequency Goldstone mode. The low-amplitude oscillations at the dipole frequency $\omega_D \approx 0.89\,\omega_x$ shown in the inset indicate a weak excitation of the center-of-mass mode. (b) Time evolution of the density profile $n(x)$ in the stripe phase for the same scenario as in (a), explicitly revealing the excitation of the translational motion of the stripes.

frequency ω_x. The existence of this "zero-frequency" Goldstone mode can be inferred employing a sum-rule argument (see Section 1.3.4). As shown in Ref. [305], a rigorous upper bound to the lowest-energy mode excited by the operator x is given by

$$\omega_{\text{min}} \leq \frac{\omega_x}{\sqrt{1 + 2E_r \chi_M}}\,, \tag{4.30}$$

where χ_M is the static magnetic polarizability defined in Eq. (4.17). As can be seen in Figs. 4.7c and 4.9c, this upper bound practically coincides with the center-of-mass frequency ω_D if $\Omega > \Omega_c$, while below Ω_c the calculated value of ω_D violates the bound due to the large value of χ_M, revealing the existence of a new low-frequency mode.

To shed light on the nature of this low-energy excitation, we consider a uniform spin perturbation $H_1 = -\lambda E_r \sigma_z$, causing a magnetic polarization of the system. After removing the perturbation[1], one would expect the polarization to oscillate around its equilibrium value, driven by the Raman coupling. Indeed, above Ω_c, after a short initial decrease reflecting the contribution of the high-frequency gapped spin branch to the static magnetic polarizability [310], the polarization oscillates at the center-of-mass frequency. This is shown in Fig. 4.12a for the system with symmetric intraspecies interactions. The fact that the spin operator excites the center-of-mass mode is a mani-

[1]To avoid the excitation of high-frequency modes on the order of the Raman coupling, the perturbation should be switched off smoothly within a time interval τ chosen such that $2\pi\hbar/\Omega \ll \tau \ll 2\pi/\omega_x$.

festation of the hybridization mechanism between the operators x and σ_z, similar to the one discussed above for x^2 and $x\sigma_z$.

In the stripe phase, we find instead that the polarization remains locked to its initial value throughout the simulation time, with a residual small-amplitude oscillation stemming from a weak excitation of the center-of-mass mode by the spin operator σ_z. In the numerical simulation, the locking of the polarization survives longer than 1000 times the oscillator time $2\pi/\omega_x$, confirming the anticipated low frequency of the Goldstone mode. Remarkably, releasing the spin perturbation has the effect of applying a boost to the stripes, causing their translation at a constant velocity, as illustrated in Fig. 4.12b. The translation of the stripes is practically independent of the center-of-mass motion, thereby providing direct evidence for the excitation of the zero-frequency Goldstone mode. By contrast, after suddenly shifting the trap center, corresponding to a perturbation by the dipole operator x, the center of mass oscillates around equilibrium both in the superfluid and in the supersolid phase (not shown). This shows that the zero-frequency Goldstone mode contributes only marginally to the static dipole polarizability, whereas its strong excitation by the operator σ_z implies that it constitutes the predominant contribution to the magnetic polarizability in the stripe phase.

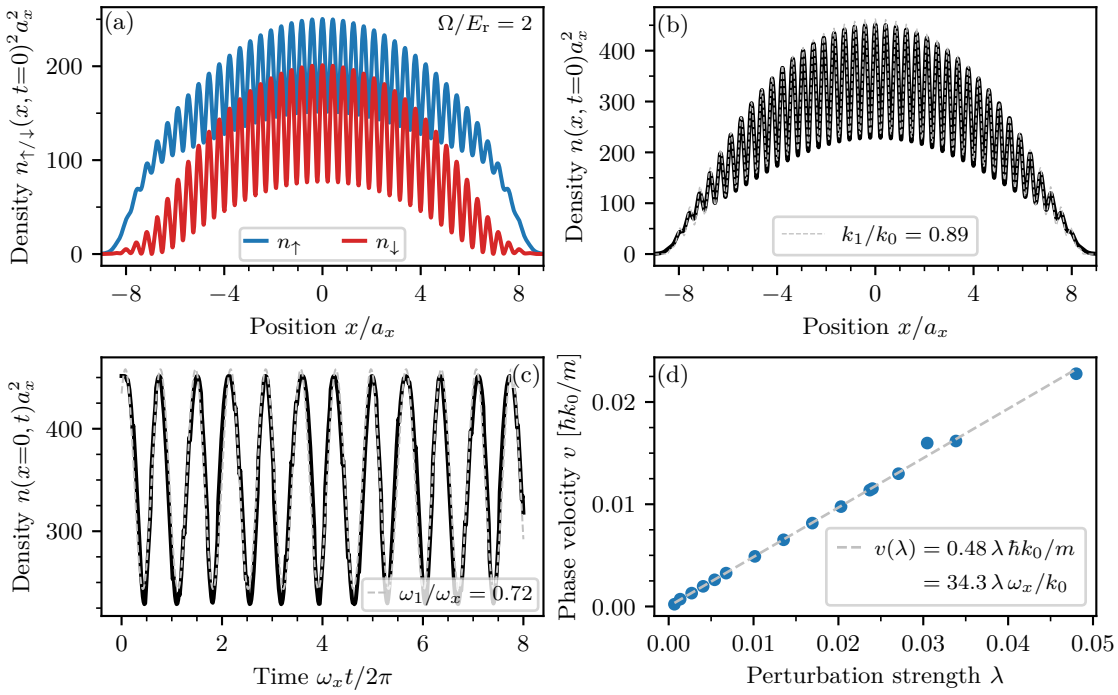

Figure 4.13.: Dependence of the phase velocity of the zero-frequency Goldstone mode on the perturbation strength for symmetric intraspecies interactions. (a) Ground state density profiles of the two spin components at $\Omega/E_r = 2$ after applying the perturbation $H_1 = -\lambda E_r \sigma_z$ with $\lambda \approx 0.024$. (b),(c) Fits of the density profile (4.31) to the total density at time $t = 0$ and position $x = 0$ in order to extract the wave number k_1 and the angular frequency ω_1 of the stripe motion, respectively. (d) The phase velocity $v = \omega_1/k_1$ of the stripes is proportional to the perturbation strength λ.

In Fig. 4.13, we analyze the dependence of the phase velocity of the stripe motion on the strength λ of the spin perturbation. The evolution of the total density can be described phenomenologically by a Thomas–Fermi profile, modulated by a running wave with wave number k_1 and frequency ω_1 [cf. Eq. (4.15)],

$$n(\boldsymbol{x}, t) = n_{\mathrm{TF}}(\boldsymbol{x})\{1 + C\cos[2(k_1 x - \omega_1 t + \phi)]\}\,. \tag{4.31}$$

Note that the angular frequency ω_1 of this running wave is not to be identified with the quasi-zero energy cost of the stripe motion. Figure 4.13a depicts a typical spin-polarized density profile after applying the uniform spin perturbation. The phase velocity $v = \omega_1/k_1$ of the stripes can be extracted by fitting Eq. (4.31) to the numerical data. At a fixed instance of time t, the fit yields the wave number k_1 (Fig. 4.13b), while at a fixed position x, the angular frequency ω_1 can be extracted (Fig. 4.13c). In Fig. 4.13d, the phase velocity $v = \omega_1/k_1$ obtained this way is plotted against the strength λ of the uniform spin perturbation, which reveals a linear relation. If the perturbation strength is increased further, the stripes eventually cease to exist and the system enters a highly spin-polarized state. Nonetheless, the linearity of the stripe velocity for a wide range of perturbation strengths is remarkable.

Let us conclude this section by summarizing the evidence for the zero-frequency Goldstone mode in the stripe phase. First, the violation of the sum rule bound (4.30) by the dipole mode due to the high polarizability implies the emergence of a new low-energy mode below the critical coupling Ω_{c}. Second, after polarizing the system by a uniform spin perturbation, the polarization, instead of undergoing harmonic oscillations at the dipole frequency, remains locked on all practically accessible time scales, which hints at the excitation of a mode of very low frequency. And third, the translational motion of the stripes at a velocity proportional to the perturbation strength is directly revealed by the time evolution of the density profile.

While we have demonstrated the possibility to excite the zero-frequency Goldstone mode for a SOC BEC with symmetric intraspecies interactions, the same procedure also works in the asymmetric case. In uniform matter, it has recently been understood analytically that the spin collective mode in the stripe phase corresponds to a translational motion of the fringes in the long-wavelength limit [315], corroborating the excitation mechanism for the crystal Goldstone mode identified in this section. The above results may thus guide the efforts towards an experimental detection of the zero-frequency Goldstone mode in spin–orbit-coupled configurations.

4.4. Summary

In this chapter, we have explored accessible signatures of supersolidity in harmonically trapped spin–orbit-coupled Bose–Einstein condensates. We have investigated equilibrium properties of configurations with symmetric as well as highly asymmetric intraspecies interactions, the latter being motivated by the recent availability of such configurations in experiments on ^{39}K [296]. The asymmetric configuration is characterized by sizable polarization effects even in the stripe phase and exhibits equilibrium

properties different from the symmetric case such as the increase of the central density and the concomitant shrinking of the cloud radius at small Raman couplings. One characteristic of the supersolid phase is the large value of the magnetic polarizability. As we have seen, the polarizability is also closely linked to dynamical properties, as it yields a rigorous upper bound for the lowest energy mode excited by the dipole operator, which can be derived using the general framework of sum rule theory. The violation of this upper bound by the dipole frequency provides indirect evidence for the existence of the zero-frequency Goldstone mode associated with the translational motion of the stripes. As illustrated through Gross–Pitaevskii simulations, this crystal Goldstone mode can directly be excited by suddenly releasing a uniform spin perturbation. Furthermore, we have shown that the emergence of a Goldstone spin-dipole mode in the supersolid phase is revealed by a beating effect in the breathing oscillation induced by suddenly changing the trap frequency. The approach of probing supersolidity by exciting Goldstone modes exposes the crucial hybridization phenomena of density and spin degrees of freedom in spin–orbit-coupled configurations, which makes the phenomenon of supersolidity even richer.

5. Analog Cosmological Reheating: From Parametric Instabilities to Universal Dynamics Far From Equilibrium

This chapter is based on Ref. [108]. The figures and parts of the text have been taken verbatim from that work, occasionally with minor modifications and additional explanations for a better embedding in the context of this thesis. See List of Publications for a statement of contributions. Parts of the results are also discussed in Aleksandr Chatrchyan's PhD thesis [1], with a focus on the cosmological perspective and using the methods of non-equilibrium quantum field theory.

In Chapter 2, we have developed measurement tools based on non-Hermitian linear response for probing fluctuation–dissipation relations, allowing one to monitor if and how isolated quantum systems return to thermal equilibrium after a quench. As we have seen, a Bose–Hubbard system quenched from a Mott-insulating initial state into the superfluid phase thermalizes on time scales on the order of the inverse coupling parameters in the Hamiltonian. However, there exists a wide range of far-from-equilibrium initial conditions for which quantum many-body systems first approach a so-called non-thermal fixed point (NTFP), in whose vicinity they spend a very long time before eventually approaching thermal equilibrium. Such a NTFP can be thought of as an attractor in a renormalization group sense and characterizes the far-from-equilibrium behavior of an entire universality class of physical systems across vastly different scales [51, 53, 54, 316–318]. In the vicinity of a NTFP, dynamics becomes universal and self-similar [52], which is associated with the onset of hydrodynamic behavior and leads to a significant reduction of complexity in the description of central dynamical properties [56]. Universality makes it possible to use table-top experiments, e.g., based on cold atoms, to study universal aspects in the non-equilibrium dynamics of systems that are challenging (or impossible) to access otherwise, such as the quark–gluon plasma explored in heavy-ion collisions or the early universe [51, 53–55].

In this chapter, we study far-from-equilibrium dynamics in a parametrically excited ultracold Bose gas, providing an analog of post-inflationary reheating dynamics in the early universe. According to the theory of cosmological inflation [319, 320], the early universe underwent an epoch of exponential expansion, during which its radius increased by some 60 e-folds or so with expansion times on the order of 10^{-34} sec [49]. This theory not only

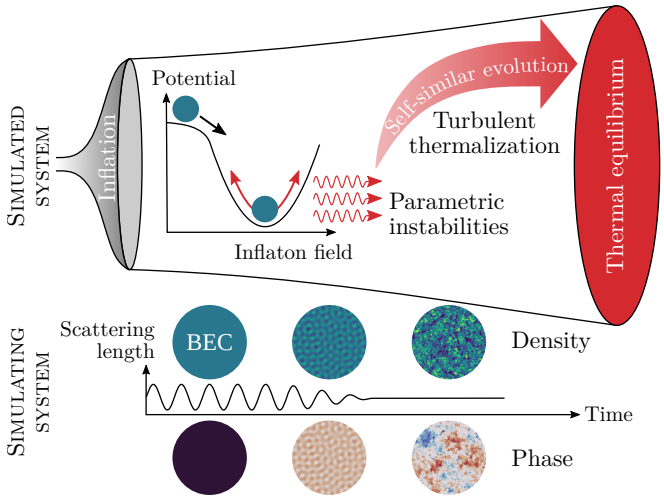

Figure 5.1.: Schematic illustration of post-inflationary reheating dynamics in the early universe and the simulation of an analogous process in an ultracold Bose gas. We consider a scenario where a single-component homogeneous "inflaton" field oscillates around the minimum of its potential, producing particles via parametric instabilities ("preheating"). Later, the system enters a turbulent state where energy is transported towards higher momenta in a self-similar way as the universe approaches thermal equilibrium ("reheating"). In the simulation, expanding spacetime as well as the oscillating inflaton field are mimicked in the non-relativistic limit by modulating the scattering length of a Bose–Einstein condensate (BEC), whose excitations play the role of particles produced by the decaying inflaton.

solves the horizon and flatness problem in cosmology [319, 320], but also explains the origin of density perturbations that seeded structure formation [321]. In typical models, inflation is driven by a scalar field known as the inflaton. Inflation leaves the universe in a super-cooled state with essentially all energy stored in the homogeneous (condensate) mode of the inflaton. The subsequent stage of cosmological reheating, which we are interested in here, involves the decay of the inflaton into lighter constituents, e.g., standard model particles. These decay products then thermalize, causing the universe to heat up and eventually approach thermal equilibrium at the reheating temperature, as required for Big Bang nucleosynthesis [50]. In a common scenario, the heating process is preceded by a so-called preheating stage of explosive particle production, driving the system far away from equilibrium into a turbulent state, where energy is transported self-similarly towards higher momenta in form of a direct cascade [51, 322, 323]. This regime of universal self-similar time evolution can be thought of as being governed by a NTFP, in whose vicinity the system remains for a long time before it eventually reaches thermal equilibrium.

It is our goal to gain a better understanding of the rich far-from-equilibrium dynamics underlying this turbulent thermalization scenario [51] by harnessing the capabilities of state-of-the-art analog quantum simulators. To this end, we design an experimental protocol for quantum-simulating salient aspects of cosmological reheating dynamics in an ultracold Bose gas. The basic setup is depicted in Fig. 5.1. An atomic BEC plays

the role of the inflaton field after inflation and excitations on top of the condensate are identified with particles produced by the decaying inflaton. Both expanding spacetime as well as the background oscillating inflaton field, which drives preheating by inducing parametric resonances, are mimicked in the non-relativistic limit by a modulation of the condensate scattering length, which can be realized via Feshbach resonances [58]. As will be illustrated by means of classical–statistical (or truncated Wigner) simulations [324–327], this "analog reheating" scenario gives access to the well-known stages of far-from-equilibrium reheating [323], including the preheating phase of parametric amplification of quantum fluctuations ("analog preheating") as well as the later stage of turbulent thermalization [51].

Analog gravity is a thriving field aiming at investigating aspects of the physics of curved spacetime in non-relativistic systems [48]. On the platform of cold atoms, such an analogy can be established by engineering emergent curved spacetimes for low-energy excitations on top of BECs, e.g., by manipulating external potentials [328–330] or interactions [330–334]. Based on such setups, a variety of scenarios for simulating particle production and (post-)inflationary dynamics have been investigated both theoretically and experimentally [329, 331–341]. A main challenge for the quantum simulation of cosmological reheating remains the incorporation of non-linear effects into these frameworks, as the mappings to curved spacetime are typically restricted to the linear regime. In the analog (p)reheating scenario presented below, we mimic particle production in Bose gases by inducing parametric instabilities [342–348] and put particular emphasis on the less understood non-linear stages of reheating dynamics, including secondary excitations [322, 339, 349] as well as the turbulent regime of universal self-similar time evolution [51].

Universal dynamics far from equilibrium has been observed experimentally in spinor and tunnel-coupled Bose gases in form of inverse cascades transporting conserved quantities towards lower momenta [317, 318]. Bidirectional universal scaling, involving additionally a direct cascade transporting energy towards higher momenta, have been studied numerically in 1D spinor Bose gases [350] and have been realized experimentally in isolated 3D Bose gases following a cooling quench [351]. Below, we show that the analog reheating scenario of parametrically exciting a scalar BECs constitutes a complementary route into the regime of self-similar dynamics far from equilibrium and allows one to study the direct energy cascade in both driven and isolated systems, as well as a recently predicted prescaling regime of partial universality [55, 56], characterized by time-dependent scaling exponents which slowly relax to their universal values. The proposed setup thus enables the observation of salient features of far-from-equilibrium dynamics, which are of great relevance far beyond the cosmological context.

5.1. Cosmological Reheating in the Early Universe

Before addressing the task of quantum-simulating post-inflationary reheating dynamics in an ultracold Bose gas, we briefly review the cosmological target model.

The inflaton is commonly modeled as a relativistic real scalar field $\phi(x)$ in curved

spacetime with the action [49]

$$S = \int \mathrm{d}^{d+1}x \sqrt{-g}\left[\frac{1}{2}g^{\mu\nu}\partial_\mu\phi\partial_\nu\phi - V(\phi)\right], \tag{5.1}$$

where V is the potential, $g_{\mu\nu}$ is the metric tensor, g its determinant, and d the number of spatial dimensions[1]. The expansion of the universe is well described by the flat Friedmann–Lemaître–Robertson–Walker (FLRW) metric [49]

$$\mathrm{d}s^2 = g_{\mu\nu}\,\mathrm{d}x^\mu\,\mathrm{d}x^\nu = c^2\,\mathrm{d}\tau^2 - a^2(\tau)\,\mathrm{d}\boldsymbol{x}^2\,, \tag{5.2}$$

where c is the speed of light and τ denotes the cosmic time. The cosmic scale factor $a(\tau)$ grows with time in an expanding universe and relates the comoving distance $\boldsymbol{x}$ to the proper distance $\boldsymbol{r}(\tau) = a(\tau)\boldsymbol{x}$. The FLRW metric describes a homogeneous and isotropic universe that is Minkowskian at each time slice, in accordance with the cosmological principle [49].

The classical equations of motion for the inflaton field can be obtained from Eq. (5.1) using the principle of least action. For the FLRW metric (5.2), one obtains

$$\frac{1}{c^2}\ddot{\phi} + \frac{1}{c^2}dH\dot{\phi} - \frac{\nabla^2}{a^2}\phi + V'(\phi) = 0\,, \tag{5.3}$$

where

$$H(t) = \frac{\dot{a}(t)}{a(t)} \tag{5.4}$$

is the Hubble parameter. Here, we use the dot to represent the derivative with respect to the cosmic time τ, while $(\cdots)'$ denotes the derivative with respect to the field ϕ. There are two main effects induced by the expansion as compared to scalar fields in static spacetime. First, the "Hubble friction" term proportional to the Hubble parameter H expresses the dilution of the field due to the expansion. Second, the presence of the scale factor a in the spatial derivative term describes the redshift of momenta in the co-moving frame [49].

5.1.1. Inflation

In what follows, we briefly outline the basic mechanism behind the widespread "slow-rollover" scenario of cosmic inflation, which is sometimes also refereed to as "new inflation" [352, 353].

In a flat FLRW universe (and in absence of the cosmological constant), the Friedmann equation determines the expansion rate as [49]

$$H^2 = \frac{8\pi G}{3}\rho_\phi\,, \tag{5.5}$$

where G is the gravitational constant and ρ_ϕ is the mass density associated with the inflaton field ϕ.

[1]The cosmologically relevant case is $d = 3$. For later purposes, we keep d general nonetheless.

For the description of inflation, only the zero-momentum (condensate) mode of the inflaton field plays a role, any spatial inhomogeneities are rapidly red-shifted away [49]. We can therefore safely neglect any spatial derivative terms in Eq. (5.3) during the inflationary epoch, which amounts to taking $\phi(\tau, \boldsymbol{x}) \equiv \phi(\tau)$ to be a homogeneous field. The canonical energy–momentum tensor $T^{\mu\nu} = \partial^\mu\phi\partial^\nu\phi - g^{\mu\nu}\mathcal{L}$, where $\mathcal{L}$ is the Lagrangian density corresponding to the action (5.1) ($S = \int \mathrm{d}^4x\,\sqrt{-g}\mathcal{L}$), then takes the form of a perfect fluid with energy density $\epsilon_\phi = c^2\rho_\phi$ and pressure p_ϕ given by [49]

$$\epsilon_\phi = \frac{1}{c^2}\frac{1}{2}\dot{\phi}^2 + V(\phi)\,, \tag{5.6a}$$

$$p_\phi = \frac{1}{c^2}\frac{1}{2}\dot{\phi}^2 - V(\phi)\,. \tag{5.6b}$$

The typical setting is to consider the inflaton field ϕ initially to be displaced from the minimum of its potential. Inflationary expansion is obtained if the potential is sufficiently flat, such that the field "slowly rolls down" its potential landscape towards the minimum [49]. In this slow-roll regime, one has $\ddot{\phi} \approx 0$ and the kinetic energy of the inflaton field $\dot{\phi}^2/2c^2$ is much smaller than the potential energy $V(\phi)$. Consequently, the energy density ϵ_ϕ in Eq. (5.6a) is approximately constant and the system is characterized by a negative pressure $p_\phi \approx -\epsilon_\phi$ [95]. Moreover, using $\rho_\phi = \epsilon_\phi/c^2 = \text{const}$, the Friedmann equation (5.5) yields $H = \dot{a}/a = \text{const}$, which implies an exponential growth of the scale factor,

$$a(t) = \mathrm{e}^{Ht}a(0)\,. \tag{5.7}$$

The inflationary expansion of the universe is accompanied by a dramatic drop in temperature as $T \propto \mathrm{e}^{-Ht}$, which is sometimes referred to as "super-cooling" [49]. Inflation ends when ϕ reaches the bottom of its potential and starts undergoing rapid coherent oscillations around the minimum, which marks the beginning of the reheating phase (see Fig. 5.1).

5.1.2. Reheating and Preheating

At the end of inflation, the universe is in a super-cooled state with practically all energy contained in the condensate mode of the inflaton field ϕ. This sets the initial condition for the reheating process, which we are interested in here. During reheating, the inflaton decays and the decay products thermalize at the reheating temperature T_f, involving a massive increase in entropy with respect to the state before inflation ($S \propto a^3(t_\mathrm{f})T_\mathrm{f}^3$, where t_f is the reheating time) [49].

Preheating

We focus on the scenario where reheating is preceded by a preheating stage of explosive particle production. To this end, we consider a generic potential with quartic self-interactions,

$$V(\phi) = \frac{m^2c^2}{2\hbar^2}\phi^2 + \frac{\lambda}{4!}\phi^4\,, \tag{5.8}$$

where m is the mass and λ a quartic coupling. A common mechanism for preheating is the parametric amplification of quantum fluctuations in the presence of the effective potential induced by the inflaton [322, 349]. This effect can most conveniently be understood by linearizing the fluctuations of the inflaton field around its homogeneous background, $\phi(\tau, \boldsymbol{x}) = \phi_0(\tau) + \delta\phi(\tau, \boldsymbol{x})$, and inserting it in Eq. (5.3). The resulting equation describes damped oscillations of the background field around the minimum of the potential (see Fig. 5.1),

$$\frac{1}{c^2}\ddot{\phi}_0 + \frac{1}{c^2} dH \dot{\phi}_0 + \frac{m^2 c^2}{\hbar^2}\phi_0 + \frac{\lambda}{6}\phi_0^3 = 0\,. \tag{5.9}$$

The equations of motion for the fluctuations, dropping all terms of quadratic or higher order in $\delta\phi$, read in Fourier space

$$\delta\ddot{\phi}_{\boldsymbol{p}} + dH\delta\dot{\phi}_{\boldsymbol{p}} + \omega_{\boldsymbol{p}}^2(\phi_0, \tau)\delta\phi_{\boldsymbol{p}} = 0 \tag{5.10}$$

with

$$\omega_{\boldsymbol{p}}^2(\phi_0, \tau) = \frac{c^2\boldsymbol{p}^2}{\hbar^2 a^2(\tau)} + \frac{m^2c^4}{\hbar^2} + \frac{\lambda c^2}{2}\phi_0^2 \tag{5.11}$$

and the Fourier transform $\delta\phi_{\boldsymbol{p}}(\tau) = \int \mathrm{d}^d x\, \delta\phi(\tau, \boldsymbol{x}) \mathrm{e}^{-i\boldsymbol{p}\boldsymbol{x}/\hbar}$. Equation (5.10) describes a collection of parametric oscillators for each momentum mode $\boldsymbol{p}$, driven by the background oscillations of $\phi_0(\tau)$. Modes within certain instability bands satisfy resonance conditions, which leads to an exponential growth of occupancies, corresponding to particle production [349, 354]. The growth of fluctuations eventually invalidates the linearized approach of Eq. (5.10). Note that in more realistic models, couplings of the inflaton to other bosonic fields can lead, in a similar way, to a production of those degrees of freedom via parametric resonances as well [322]. Here, we focus on the simplest scenario corresponding to a decay of the inflaton solely into its own quanta of excitation, as has been studied in Ref. [51].

Reheating

Particle spectra formed during preheating are highly non-thermal with large occupation numbers at low momenta. As a consequence, the system is driven far away from equilibrium into a turbulent state, characterized by a local transport of conserved quantities in momentum space that leads to universal self-similar time evolution [51]. Typically, an inverse cascade transports particles towards lower momenta, while a direct cascade transports energy towards higher momenta. The latter constitutes a key process in the context of turbulent thermalization [51]. At early times, this transport is driven, i.e., the oscillating inflaton acts as a source injecting energy into the system at resonant momenta. Eventually, the inflaton decays, marking the transition from driven to free turbulence. The system remains in the turbulent state for a long time, until the occupancy of characteristic momenta eventually becomes comparable to the vacuum expectation value given by the "quantum half". In this final stage, which is dominated by quantum fluctuations, the system relaxes to thermal equilibrium at the reheating temperature, completing the reheating process [51, 323].

5.2. Expanding Spacetime in Bose Gases

Our goal is to observe reheating-like dynamics in an ultracold Bose gas in analogy to reheating in the early universe. As a first step, we discuss an approach for incorporating expansion in non-relativistic Bose gases. Note that since we are interested in post-inflationary dynamics, we do not target the exponential expansion during inflation, but typical expansion schemes in standard cosmology, e.g., power-law expansions $a(t) \propto t^\nu$, where $\nu = 1/2$ ($\nu = 2/3$) in a radiation-dominated (matter-dominated) universe [49].

A Bose gas is described by a non-relativistic complex field operator $\hat{\Psi}$ subject to the Hamiltonian (1.2). The most straightforward approach to incorporate expansion in a trapped Bose gas is to physically expand the trap geometry [328, 330]. For example, in the experiment of Ref. [329], preheating-like dynamics has been observed after rapidly expanding a ring-shaped trap. While this approach is simple and direct in principle, there are practical limitations such as the restriction to short times or small expansion velocities due to a finite optical imaging system.

Here, we follow an alternative approach, motivated by taking the non-relativistic limit of the relativistic equations of motion (5.3) for the inflaton field ϕ. To this end, we factor out the fast oscillations due to the mass term in Eq. (5.3) from the canonically quantized inflaton field $\hat{\phi}(\tau, \boldsymbol{x})$, defining a slowly varying complex field $\hat{\psi}(\tau, \boldsymbol{x})$ via the relation

$$\hat{\phi} = \frac{\hbar}{\sqrt{2mc}} \left[\hat{\psi} \mathrm{e}^{-imc^2\tau/\hbar} + \mathrm{h.c.} \right] . \tag{5.12}$$

As shown in Appendix A of Ref. [108], provided typical momenta, expansion velocities, and field values are small, this new field evolves according to [355]

$$i\hbar\dot{\hat{\psi}} = \left(-\frac{\hbar^2}{2m}\frac{\nabla^2}{a^2} - i\hbar\frac{d}{2}H + g\hat{\psi}^\dagger\hat{\psi} \right)\hat{\psi} \tag{5.13}$$

with coupling $g = \lambda\hbar^4/8m^2c$. Equation (5.13) is reminiscent of the Heisenberg equations of motion of an ultracold Bose gas (1.6) in absence of an external trapping potential. The kinetic term is proportional to a^{-2}, which describes the redshift of momenta in the co-moving frame, and the dilution of the system due to the expansion is expressed by a non-Hermitian term causing the norm of the field to decay. Remarkably, this formulation allows one to simulate expansion without physically expanding the trap by associating physical distances with the co-moving distances of an expanding system. The required non-Hermitian Hamiltonian describing an effective decrease of the norm can in principle be realized experimentally using the same methods as presented in Section 2.3. However, apart from the technical overhead and the challenge of engineering the modified kinetic term, e.g., via a time-dependent effective mass, this approach has the practical drawback that the decreasing atomic density leads to an ever diminishing signal-to-noise ratio.

To arrive at a more practicable formulation, we introduce a new time variable, the laboratory time t, as well as a rescaled field operator $\hat{\Psi}$ via the relations

$$\mathrm{d}t = \frac{\mathrm{d}\tau}{a^2} , \qquad \hat{\Psi} = \hat{\psi} a^{d/2} . \tag{5.14}$$

This procedure is analogous to the transformation to conformal variables, well-known in quantum field theory on curved spacetime [356]. Equation (5.13) then takes the standard form of the equations of motion for a non-relativistic bosonic field (1.6),

$$i\hbar\frac{\partial\hat{\Psi}}{\partial t} = \left(-\frac{\hbar^2\nabla^2}{2m} + g_{\mathrm{eff}}(t)\hat{\Psi}^\dagger\hat{\Psi}\right)\hat{\Psi}\,, \tag{5.15}$$

with the time-dependent effective coupling

$$g_{\mathrm{eff}}(t) = g a^{2-d}(t)\,. \tag{5.16}$$

Equations (5.15) and (5.16) describe a Bose gas in an expanding spacetime, where the expansion enters only in the time dependence of the interaction term via the scale factor $a(t)$. In cold-atom experiments where a broad Feshbach resonance is available to tune the interactions, this approach may be the preferred way of studying a broad range of expansion scenarios.

The above scheme may be compared to common scenarios in analog gravity, where time-dependent atomic interactions have been used to engineer an emergent expanding spacetime for linear excitations on top of the condensate [330–332]. However, the mapping to an expanding relativistic system within the analog gravity framework typically breaks down on the non-linear level. By contrast, in the approach presented above, the relation between Eqs. (5.3) and (5.15) holds even on the non-linear level since the derivation does not rely on any linearization. This formulation is therefore well suited for simulating reheating-like dynamics, where non-linear effects are essential. On the downside, the correspondence to Eq. (5.3) is restricted to the non-relativistic limit and therefore not capable of capturing relativistic effects, such as the resonant amplification of fluctuations during the preheating stage. As discussed in the next section, we can nonetheless mimic an analogous process in the non-relativistic system by periodically modulating the interaction.

Scale Invariance and Expansion in 2D

For $d = 2$, the effective coupling in Eq. (5.16) becomes independent of the scale factor $a(t)$. This is a consequence of a dynamical symmetry in 2D Bose gases known as scale invariance [357]. While quantum anomalies in strongly interacting systems can lead to violations of scale invariance [358, 359], this property has been well tested experimentally in the weakly interacting regime [360, 361]. Thus, if scale invariance holds, the equations of motion are the same as in the case of a static spacetime. The nature of the expansion, encoded in the scale factor $a(t)$, then only enters the transformation back to the original temporal and spatial coordinates as well as field variables. This makes the simulation in two spatial dimensions particularly efficient, since the evolution of a single experiment can conveniently be mapped to arbitrary expanding spacetimes in a post-processing step. For this reason, we will focus on weakly interacting 2D Bose gases in the remainder of this chapter. Although our universe is clearly not 2D, this geometry captures most of the essential physics of reheating dynamics, as demonstrated in the following sections.

5.3. Analog Preheating: Mimicking Preheating Dynamics in Bose Gases via Parametric Instabilities

We are now in a position to develop a scenario that enables the quantum simulation of the characteristic stages of (p)reheating dynamics (as outlined in Section 5.1) in an ultracold Bose gas. This scenario, which we will refer to as "analog reheating", is depicted in Fig. 5.1 and consists of two main stages: an early preheating-like phase, where particle production is mimicked by inducing parametric instabilities in a Bose–Einstein condensate ("analog preheating"), and the subsequent regime of turbulent thermalization, characterized by universal self-similar time evolution. This section is devoted to the analog preheating scenario, which we will study both analytically and by means of classical–statistical simulations.

As described in Section 5.1.1, inflation leaves the universe in a super-cooled state with essentially all energy contained in the zero-momentum mode of the inflaton. This suggests taking a uniform BEC as the initial state for the analog implementation of the reheating process in an ultracold Bose gas. (Possible implications of the presence of an external trapping potential are discussed in Section 5.5.) Time evolution is governed by Eq. (5.15), which, as discussed in Section 5.2, describes the non-relativistic limit of the inflaton dynamics in expanding spacetime. It is tempting to search for a direct analog of the oscillations performed by the homogeneous part of the inflaton according to Eq. (5.9), which could trigger parametric instabilities in the condensate. However, this effect is not present in a single-component Bose gas in its ground state.

In fact, the absence of parametric resonances is a consequence of the non-relativistic limit considered in Section 5.2. To re-introduce parametric instabilities in the non-relativistic model, we add a periodic modulation of the coupling according to[2]

$$g(t) = g_0[1 + r\sin(\omega t)]\,, \tag{5.17}$$

where g_0 is a positive offset value, r is the amplitude of the modulation and ω is its frequency. This replacement can be motivated by the structure of the relativistic equations for the fluctuations of the inflaton field (5.10). The modulation of the dispersion (5.11), which induces parametric resonances, occurs due to the coherent oscillations of the homogeneous background field ϕ_0 in the term proportional to the quartic coupling λ. On the linear level, it makes formally no difference whether this modulation arises from the time-dependence of ϕ_0 or λ. Since in a non-relativistic cold-atom BEC the magnitude of the field does not oscillate, an analogous mechanism of parametric resonance can be realized in the simulating system by a modulation of the interaction g (which according to Eq. (5.13) is proportional to λ).

[2]Note that here we have used the laboratory time t in the argument of the sine function instead of the cosmic time τ, which, when expressed in terms of the laboratory time t, results in oscillations with increasing frequency. This substitution is based on the simplifying assumption that the expansion is insignificant during the duration of the modulation, in which case the relation between both time variables becomes linear and the corresponding proportionality constant can be absorbed in the modulation frequency.

It should be said that this procedure does not map one-to-one to the parametric resonance scenario described by Eq. (5.10) (see Appendix B of Ref. [108] for a detailed discussion). For instance, the modulation frequency ω is non-relativistic in the simulating system, while according to Eq. (5.9), the inflaton oscillates at relativistic frequencies $\omega_{\mathrm{rel}} \simeq mc^2/\hbar$ on the scale given by its rest mass. Furthermore, in contrast to the post-inflationary setting, where the produced particles back-react on the inflaton, the modulation of the coupling is imposed externally through Eq. (5.17). Switching off the modulation thus corresponds to the decay of the inflaton, which constitutes a free parameter in the model.

Despite these differences, modulating the interaction as described above suffices to generate the desired parametric resonance phenomena in the Bose gas [342–348], analogous to the ones taking place in the preheating stage of most inflationary models [322, 349]. This is demonstrated in detail in what follows.

5.3.1. Numerical Study of Preheating Dynamics

We illustrate the analog preheating scenario by means of numerical simulations based on Eq. (5.15) for a 2D Bose gas, where due to scale invariance the expansion does not explicitly enter the dynamics. (Nonetheless, we keep the number of spatial dimensions d in all formulas general.) Equation (5.15) then formally corresponds to a Bose gas in static spacetime, while arbitrary expansion schemes $a(t)$, which enter the back transformation to the original time and field variables according to Eq. (5.14), can be considered in post-processing (see discussion at the end of Section 5.4.3).

As a main observable in the study of parametric instabilities and turbulent thermalization, we consider the single-particle momentum distribution $f(t, \boldsymbol{p})$ defined in Eq. (1.8). Importantly, this quantity can be experimentally accessed in time-of-flight measurements (see Section 5.5 for further discussions).

We evaluate the quantum expectation value in Eq. (1.8) by means of classical–statistical (or truncated Wigner) simulations [324–327]. This method takes into account quantum fluctuations by stochastically sampling classical field configurations from the Wigner distribution of the initial state. Each realization is propagated deterministically according to the GPE and quantum mechanical observables are obtained as statistical averages over multiple realizations. In the present case, the initial state corresponds to a spatially homogeneous BEC, and for each realization, all non-zero momentum modes are populated with vacuum noise corresponding to an average occupancy of half a particle per mode. This mimics quantum fluctuations acting as a seed for parametric instabilities. It is important to note that this approach goes beyond a mean-field description, which fails to capture parametric resonance since the occupancies of all excited modes are exactly zero. Further details about the simulation method can be found in Appendix B.

In what follows, we express length and time in units of the characteristic scales $x_0 = \hbar/\sqrt{mn_0g_0}$ and $t_0 = \hbar/n_0g_0$, respectively, where $n_0 = N/V$ is the homogeneous particle density in a system of N particles in a volume V. Momenta are given either in units of the lowest non-zero momentum $p_L = 2\pi\hbar/L$ or in units of the characteristic momentum $p_\xi = 2\pi\hbar/\xi$ corresponding to the healing length $\xi = \hbar/\sqrt{2mn_0g_0}$. According

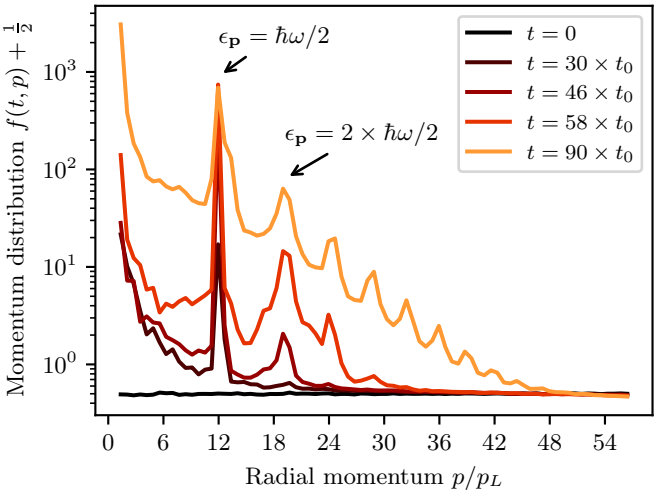

Figure 5.2.: Radially averaged momentum distribution $f(t,p)$ as a function of the radial momentum $p = |\boldsymbol{p}|$ at different times t, demonstrating preheating dynamics. The coupling is modulated with relative strength $r = 0.25$ at a frequency ω, chosen such that the resonance condition $\epsilon_{p_{\text{res}}} = \hbar\omega/2$ for the momentum $p_{\text{res}} = 12 \times p_L$ with $p_L = 2\pi\hbar/L$ is fulfilled [see discussion below Eq. (5.19)]. At early times $t \lesssim 30 \times t_0$, a single narrow resonance can be observed around p_{res}. At later times, a broad resonance band emerges with peaks at higher harmonics of the modulation frequency. These secondary resonances are due to non-linear interactions, as discussed in Section 5.3.3. See the video[3] in the Supplemental Material of Ref. [108] for a qualitative illustration of the dynamics of a single realization.

to Eq. (1.29), in a quasi-2D Bose gas, the interaction strength $g_0 = \tilde{g}\hbar^2/m$ is characterized by the dimensionless parameter $\tilde{g} = \sqrt{8\pi}a_s/a_{\text{HO}}$, where a_s is the s-wave scattering length and a_{HO} is the oscillator length of the harmonic potential in the strongly confined direction. If not stated otherwise, we consider a uniform quasi-2D system of $N = 10^6$ weakly interacting particles with coupling $\tilde{g} = 2.5 \times 10^{-3}$ in a square box with periodic boundary conditions. This choice of parameters fixes the box length as $L/x_0 = 50$. Moreover, in this isotropic setting, the momentum distribution depends only on the magnitude $p = |\boldsymbol{p}|$ of the momentum, $f(t,\boldsymbol{p}) \equiv f(t,p)$.

Figure 5.2 shows the radially averaged momentum distribution of a parametrically excited system described by Eq. (5.15). The interaction is modulated according to Eq. (5.17) with $r = 0.25$, and the modulation frequency ω is chosen as the resonance frequency of the momentum $|p_{\text{res}}| = 12 \times p_L$, as discussed below Eq. (5.19). In this simulation, the noise cutoff has been chosen as $p_\Lambda = p_\xi \approx 70.7 \times p_L$, which is smaller than the lattice cutoff, but sufficiently large to not affect the dynamics at early times. To gain a qualitative impression of the induced preheating dynamics, see the video[3] in the Supplemental Material of Ref. [108], illustrating the evolution of both the density and the phase of a single realization.

[3] A video illustrating the preheating dynamics of the density and the phase of a single realization can be found in the Supplemental Material of Ref. [108] or in the section "ancillary files" on the arXiv page of that article.

At early times, $t \lesssim 30 \times t_0$, in Fig. 5.2, we observe a single narrow resonance around the resonance momentum p_{res} satisfying the resonance condition $\epsilon_{p_{\mathrm{res}}} = \hbar\omega/2$ (see Section 5.3.2). Due to particle number conservation, the growing occupancy of the resonant momentum causes the condensate to decay, mimicking particle production from the decaying inflaton in the early universe. At later times, secondary resonances at higher harmonics of the modulation frequency appear as a result of non-linear interactions among the produced quasi-particles.

In addition to the narrow resonance peaks, a transient growth of fluctuations at low momenta occurs at early times before the primary peak becomes visible. This growth can be interpreted as a consequence of the fact that the sampled initial state corresponds to the ground state of an ideal Bose gas. At $t = 0$, the system is effectively quenched to a finite interaction, producing a power law in the momentum distribution proportional to p^{-1} at low momenta (see Appendix B). This early-time behavior has, however, no influence on the preheating dynamics we are interested in here.

Below, we provide analytical insights into both the linear regime of parametric resonance as well as the non-linear regime of secondary excitations.

5.3.2. Parametric Resonance in the Linear Regime

Parametric instabilities play a crucial role in many modern experiments with BECs [342–344, 346, 347] and the concept has evolved into a promising tool for state preparation [348]. The underlying process can conveniently be understood by adopting a semi-classical point of view. To this end, we consider the GPE (1.14) with $V_{\mathrm{ext}}(\boldsymbol{x}) = 0$ for the condensate wave function $\Psi(t, \boldsymbol{x})$. It is instructive to work in the Madelung representation, $\Psi(t, \boldsymbol{x}) = \sqrt{n(t, \boldsymbol{x})}\exp[i\theta(t, \boldsymbol{x})]$, which allows us to express the GPE (1.14) in form of the hydrodynamic equations (1.15). To obtain some intuition about the early stages of the evolution, we express both the density and the phase in terms of a homogeneous background with fluctuations on top of it, $n(t, \boldsymbol{x}) = n_0(t) + n_1(t, \boldsymbol{x})$ and $\theta(t, \boldsymbol{x}) = \theta_0(t) + \theta_1(t, \boldsymbol{x})$. Linearizing Eq. (1.15) with respect to the fluctuations yields the equations $\partial_t n_0 = 0$ and $\partial_t \theta_0 = -g(t)n_0/\hbar$ for the background condensate. For the fluctuations, we obtain

$$\partial_t n_1 = -\frac{\hbar n_0}{m}\nabla^2\theta_1\,, \tag{5.18a}$$

$$\hbar\partial_t\theta_1 = -g(t)n_1 + \frac{\hbar^2}{4mn_0}\nabla^2 n_1\,. \tag{5.18b}$$

Taking the time derivative and inserting the resulting equations into each other, fluctuations of the density and the phase decouple to linear order. Transforming to momentum space, $n_{1\,\boldsymbol{p}}(t) = \int \mathrm{d}^d x\, n_1(t, \boldsymbol{x})\mathrm{e}^{-i\boldsymbol{p}\boldsymbol{x}/\hbar}$ and similarly for the phase, the linearized equations can be expressed as

$$\partial_t^2 n_{1\,\boldsymbol{p}} + \omega_{\boldsymbol{p}}^2(t) n_{1\,\boldsymbol{p}} = 0\,, \tag{5.19a}$$

$$\partial_t^2\theta_{1\,\boldsymbol{p}} + \frac{2n_0\partial_t g(t)}{2n_0 g(t) + \epsilon_{\boldsymbol{p},0}}\partial_t\theta_{1\,\boldsymbol{p}} + \omega_{\boldsymbol{p}}^2(t)\theta_{1\,\boldsymbol{p}} = 0\,, \tag{5.19b}$$

where

$$\hbar^2\omega_{\boldsymbol{p}}^2(t) = \epsilon_{\boldsymbol{p},0}\big[\epsilon_{\boldsymbol{p},0} + 2n_0 g(t)\big] \tag{5.20}$$

is a time-dependent form of the Bogoliubov dispersion relation (1.38) with the free-particle dispersion relation $\epsilon_{\boldsymbol{p},0} = \boldsymbol{p}^2/2m$. Equation (5.19) describes a collection of parametric oscillators for each momentum mode $\boldsymbol{p}$, which are undamped for the density and damped for the phase. The structure is similar to the relativistic equations for the inflaton fluctuations (5.10) describing the linear stage of cosmological preheating.

The equation for the density fluctuations (5.19a) can be rewritten in the form

$$\frac{\partial^2 n_{1\,\boldsymbol{p}}(s)}{\partial s^2} + \big[A_{\boldsymbol{p}} - 2q_{\boldsymbol{p}}\cos(2s)\big]n_{1\,\boldsymbol{p}}(s) = 0 \tag{5.21a}$$

with parameters

$$A_{\boldsymbol{p}} = \frac{\epsilon_{\boldsymbol{p}}^2}{(\hbar\omega/2)^2} \quad \text{and} \quad q_{\boldsymbol{p}} = \frac{r\epsilon_{\boldsymbol{p},0}n_0 g_0}{(\hbar\omega/2)^2}\,, \tag{5.21b}$$

where $s = \omega t/2 + \pi/4$ is a dimensionless time variable and $\epsilon_{\boldsymbol{p}}^2 = \epsilon_{\boldsymbol{p},0}(\epsilon_{\boldsymbol{p},0} + 2n_0 g_0)$ denotes the Bogoliubov dispersion relation. Equation (5.21) is the standard form of Mathieu's equation [362]. Importantly, this equation admits solutions which can be expressed as the product of an oscillatory function and an exponentially growing prefactor $\propto \mathrm{e}^{\zeta_{\boldsymbol{p}}t}$, describing parametric resonance [349, 354]. The condition for exact resonance is given by $A_{\boldsymbol{p}} = 1$, or equivalently $\epsilon_{\boldsymbol{p}} = \hbar\omega/2$. That is, resonance occurs for those momentum modes $\boldsymbol{p}_{\mathrm{res}}$ whose energy equals half a quantum of energy $\hbar\omega/2$ injected in the system through the modulation.

The growth rate $\zeta_{\boldsymbol{p}}$ of unstable modes can be estimated for small modulation amplitudes $q_{\boldsymbol{p}} \ll 1$ using perturbation theory [363]. To leading order, it is given by

$$\zeta_{\boldsymbol{p}} = \frac{\omega}{4}\sqrt{q_{\boldsymbol{p}}^2 - (A_{\boldsymbol{p}} - 1)^2}\,. \tag{5.22}$$

Thus, there is an entire range of modes around $\boldsymbol{p}_{\mathrm{res}}$ which experience a positive growth rate and thus undergo parametric resonance. The width of this instability band is delimited by the modes satisfying $A_{\boldsymbol{p}} = 1 \pm q_{\boldsymbol{p}}$ and increases with the amplitude r of the modulation. At the resonant momentum $\boldsymbol{p}_{\mathrm{res}}$, Eq. (5.22) reduces to

$$\zeta_{\boldsymbol{p}_{\mathrm{res}}} = r\omega\Big(\frac{n_0 g_0}{\hbar\omega}\Big)^2\left(\sqrt{1 + \left(\frac{\hbar\omega}{2n_0 g_0}\right)^2} - 1\right). \tag{5.23}$$

For $\hbar\omega \ll n_0 g_0$, this rate simplifies to $\zeta_{\boldsymbol{p}_{\mathrm{res}}} \approx r\omega/8$. In this regime, the Bogoliubov dispersion becomes linear, $\epsilon_{\boldsymbol{p}} \approx c_{\mathrm{s}}|\boldsymbol{p}|$ with the speed of sound $c_{\mathrm{s}} = \sqrt{n_0 g_0/m}$, and the produced quasi-particles have the character of sound waves. In the opposite limit, $\hbar\omega \gg n_0 g_0$, particles with quadratic dispersion $\epsilon_{\boldsymbol{p}} \approx n_0 g_0 + \boldsymbol{p}^2/2m$ are produced.

Comparison to numerical results. In Fig. 5.2, parametric resonance is clearly visible as a pronounced peak at the momentum satisfying the resonance condition. Likewise, the excitation of a single dominant wave length in the linear stage of the dynamics is qualitatively confirmed in the evolution of both the density and the phase of a single realization, as can be seen in the video[3] in the Supplemental Material of Ref. [108] as well as in the snapshots[4] shown in the central panels in the lower part of Fig. 5.1. It is worthwhile emphasizing that parametric instabilities can be triggered only if the initial occupancy is non-zero. This seed is not contained in the mean field analysis presented in this subsection, but is added in the simulation in form of vacuum noise according to the truncated Wigner prescription.

The linearized equations (5.18) are helpful to get an intuitive analytical understanding for the early stages of the dynamics and describe the emergence of the primary resonant peak in Fig. 5.2. However, as a result of the exponential growth of occupancies, this approach fails to describe the later stages where non-linear effects play a fundamental role. These non-linearities are taken into account in the numerical simulations, which are based on the full GPE (1.14), and include secondary excitations outside the resonance band, as shown in Fig. 5.2. These will be discussed further below.

5.3.3. Secondary Instabilities

We now discuss secondary instabilities arising from non-linear interactions of the produced quasi-particles [339, 349]. By expanding the hydrodynamic equations (1.15) to quadratic order in the fluctuations, it can be shown that modes which are stable on the linear level experience an effective forcing, which leads to an exponential growth of mode occupancies for momenta $p \lesssim 2p_{\mathrm{res}}$ proportional to $\mathrm{e}^{2\zeta_{p_{\mathrm{res}}} t}$, where the growth rate $\zeta_{\boldsymbol{p}_{\mathrm{res}}}$ is given by Eq. (5.23) [108]. Furthermore, modes which additional satisfy the resonance condition $\epsilon_{\boldsymbol{p}} \approx 2\epsilon_{\boldsymbol{p}_{\mathrm{res}}}$ are resonantly amplified and therefore strongest enhanced [108].

These features of secondary instabilities are captured by the classical–statistical simulations shown in Fig. 5.2. In particular, one can observe both the narrow peak and the broad band in the distribution function between $t/t_0 = 46$ and $t/t_0 = 58$. Similar peaks at higher multiples of the resonance frequency appear at later times due to higher-order corrections to Eq. (1.15).

Analysis of growth rates. Figure 5.3 depicts the time evolution of the occupancies corresponding to the primary and secondary resonances annotated in Fig. 5.2. The growth of the secondary resonance marks the onset of the non-linear regime where the quasi-particles produced in the primary resonance start to interact, and the linear picture presented in Section 5.3.2 breaks down.

Before comparing the numerically extracted growth rates to analytical predictions, we first relate the momentum distribution $f(t, \boldsymbol{p})$ to the hydrodynamic density and phase

[4]Since n_1 and θ_1 are conjugate variables, they are phase shifted such that the density fluctuations reach their maximum when the phase fluctuations cross zero, and vice versa. To create a better visual impression, the central snapshot of the phase in Fig. 5.1 has been shifted forward in time by a quarter of an oscillation period until the phase fluctuations reach their next maximum.

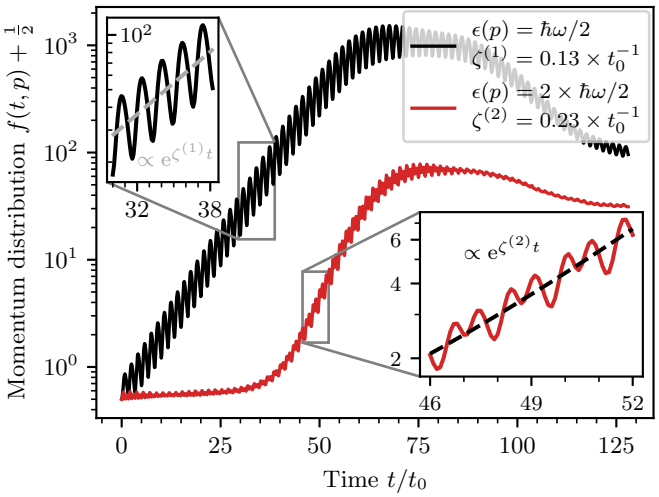

Figure 5.3.: Radially averaged momentum distribution $f(t,p)$ as a function of time t showing the exponential growth of the primary and secondary resonances corresponding to the annotated peaks in Fig. 5.2. The growth rates have been extracted by fitting a straight line to the quantity $\ln f(t,p)$, as shown in the insets. The result for the primary resonance, $\zeta^{(1)}_{\mathrm{num}} t_0 = 0.13$, agrees well with the analytical prediction $2\zeta^{(1)}_{\mathrm{pert}} t_0 = 0.15$ obtained from Eq. (5.23). The growth of the secondary instability starts later, but its rate $\zeta^{(2)}_{\mathrm{num}} t_0 = 0.23$ is approximately twice as large as the one of the primary resonance, as expected from the discussion in Section 5.3.3. The exponential growth stops when the number of excited atoms becomes comparable to the number of condensate atoms.

variables. On the mean-field level, linear fluctuations of the condensate wave function, expressed as $\Psi(t,\boldsymbol{x}) = \Psi_0(t) + \Psi_1(t,\boldsymbol{x})$, are related to linear density and phase fluctuations via $\Psi_1(t,\boldsymbol{x})/\Psi_0(t) = n_1(t,\boldsymbol{x})/2n_0 + i\theta_1(t,\boldsymbol{x})$. The momentum distribution on the linear level then corresponds to

$$\left|\Psi_{1\boldsymbol{p}}\right|^2 = n_0 \left[\frac{n_{1\boldsymbol{p}}^2}{(2n_0)^2} + \theta_{1\boldsymbol{p}}^2 \right]. \tag{5.24}$$

Therefore, a parametric resonance where the density and phase fluctuations grow as $n_{1\boldsymbol{p}} \propto \theta_{1\boldsymbol{p}} \propto e^{\zeta_{\boldsymbol{p}} t}$ results in a growth of the momentum distribution as $f(t,\boldsymbol{p}) \propto e^{2\zeta_{\boldsymbol{p}} t}$.

The oscillations of the occupancies in Fig. 5.3 can be understood from the linearized parametric oscillator equations (5.19). Recall that the latter admit oscillatory solutions with exponentially growing amplitudes. However, being conjugate variables, the oscillations of n_1 and θ_1 are shifted in phase by approximately $\pi/2$. According to Eq. (5.24), the momentum distribution thus corresponds to the sum of two phase-shifted oscillating functions with slightly different initial amplitudes. This results in the residual oscillations on top of the exponential growth observed in Fig. 5.3. As expected, the oscillation frequency of the primary resonance agrees with the modulation frequency, while the oscillations of the secondary resonance additionally contain frequency components corresponding to twice the modulation frequency, reflecting the interactions between the resonantly produced quasi-particles.

The growth rate of the primary resonance $\zeta^{(1)}_{\mathrm{num}} t_0 = 0.13$ has been extracted by fitting an exponential function to the numerical data, as shown in the insets of Fig. 5.3. The result is close to the analytical prediction (5.23) obtained from perturbation theory, $2\zeta^{(1)}_{\mathrm{pert}} t_0 = 0.15$. The secondary resonance at $2\epsilon_{\boldsymbol{p}_{\mathrm{res}}}$ grows at a rate $\zeta^{(2)}_{\mathrm{num}} t_0 = 0.23$, which is indeed approximately twice the growth rate of the primary resonance.

The perturbative regime ends when $n_1/n_0 \approx 1$, i.e., when the number of excited atoms becomes comparable to the number of condensate atoms. At this point, the exponential growth stops and turbulent dynamics sets in. A typical snapshot[3] of the density and the phase of a single realization after the onset of turbulence is shown in the right panels in the lower part of Fig. 5.1. In the next section, we analyze the turbulent dynamics quantitatively in momentum space.

5.4. Analog Reheating: Turbulent Thermalization in Bose Gases

This section is devoted to the turbulent thermalization stage of the analog reheating scenario (see Fig. 5.1). Turbulent dynamics is accompanied by the emergence of self-similarity and universality. This is reflected by a power-law behavior of the momentum distribution within a certain inertial range of momenta. One well-known example within the theory of weak wave turbulence is the prediction of a stationary direct cascade with a universal power-law distribution $f(p) \propto p^{-d}$ [364]. More generally, self-similarity in far-from-equilibrium systems can become manifest in their time evolution. In such a scenario the evolution of the distribution function can be expressed as

$$f(t, \boldsymbol{p}) = s^{\alpha} f_{\mathrm{S}}(s^{\beta} \boldsymbol{p}) \,, \tag{5.25}$$

where $s = t/t_{\mathrm{ref}}$ and t_{ref} is an arbitrary reference time. The scaling hypothesis (5.25) constitutes a significant reduction of complexity as it allows one to describe a relevant part of the dynamics by simply rescaling a single-variable scaling function f_{S}, as determined by the scaling exponents α and β. Remarkably, in many far-from-equilibrium scenarios, both the exponents as well as the scaling form of the distribution are universal, which means they are insensitive to microscopic details as well as initial conditions, and depend only on a few macroscopic system parameters like dimensionality, symmetry or the number of field components [51, 53–55, 365]. As a result, if universality holds, physical systems with vastly differing energy scales can behave quantitatively the same. This makes ultracold Bose gases a particularly promising target for simulating universal aspects of far-from-equilibrium dynamics like that of the inflaton in the early universe. Universal self-similar time evolution reflects the system being in the vicinity of a non-thermal fixed point, which acts as an attractor on the way towards thermal equilibrium [52, 366, 367].

In this section, we demonstrate, corroborated by classical–statistical simulations, that the salient features of the turbulent thermalization scenario of cosmological reheating (see Section 5.1.2) can be observed in an ultracold Bose gas within the proposed analog reheating setup. We first study the regimes of driven and free turbulence separately,

before considering a transient prescaling regime, where the universal shape of the scaling function is maintained, but the scaling exponents change over time. The numerically extracted scaling exponents in the universal regimes turn out to agree well with analytical predictions from kinetic theory. Finally, we discuss the relaxation to thermal equilibrium, which is, however, not captured by classical–statistical simulations as it is dominated by quantum fluctuations. We conclude this section with a discussion of how expansion may prevent the system from thermalizing, building a bridge to Section 5.2.

5.4.1. Driven Versus Free Turbulence

In order to drive the system into a turbulent state, we follow the protocol presented in Section 5.3 of parametrically exciting a homogeneous BEC. Here, our focus lies on the later stages of the non-linear dynamics after the proliferation of secondary instabilities, when a smooth distribution in form of a power law has formed. We distinguish the regime of driven turbulence, realized by continuously modulating the interaction according to Eq. (5.17), and free turbulence, developed if the modulation is switched off shortly after the primary resonance has saturated. In our analogy to reheating in the early universe, the former case corresponds to the situation where the inflaton possesses enough energy to drive turbulence for a long time, while in the latter case, the inflaton runs out of energy rather quickly at around the same time when turbulence sets in.

To maximize the inertial range where self-similar scaling can be observed, it is desirable to inject energy at momentum scales close to the lowest momenta supported by the system, where occupancies can become large. To this end, we consider a modulation of the interaction with a relative amplitude $r = 1$ at frequency ω chosen such that the resonant momentum becomes $p_{\mathrm{res}} = 3 \times 2\pi\hbar/L$ (see Section 5.3.2).

The left and right panels of Fig. 5.4 show a comparison of the direct cascades emerging in the regimes of driven and free turbulence, respectively. All parameters for both simulations are identical, with the exception that in Fig. 5.4a, the interaction is modulated continuously, while in Fig. 5.4b, the modulation is switched off smoothly within two modulation periods $2\pi/\omega \approx 8.2\, t_0$ at time $t/t_0 = 80$, roughly corresponding to the time when the primary resonance saturates[5]. In the latter case, energy is conserved already at the onset of turbulence and the driven regime is skipped. In both scenarios, the momentum distribution takes a scaling form corresponding to a power law close to $f(t, p) \propto p^{-2}$, which is indicated by a dotted line as a guide to the eye. A power law proportional to p^{-d} is characteristic for weak wave turbulence [364, 368, 369] and has been observed experimentally in Ref. [370].

Moreover, as can be seen in Fig. 5.4, the distributions in the two regimes exhibit self-similar time evolution in different ways. In the case of driven turbulence, Fig. 5.4a, the front of the cascade evolves self-similarly, leaving behind a stationary distribution. Stationary turbulence arises in the theory of weak wave turbulence as a stationary solution of the scattering integral. However, such a configuration necessarily requires the

[5]The differences between switching off the modulation suddenly or smoothly within a few modulation periods are insignificant.

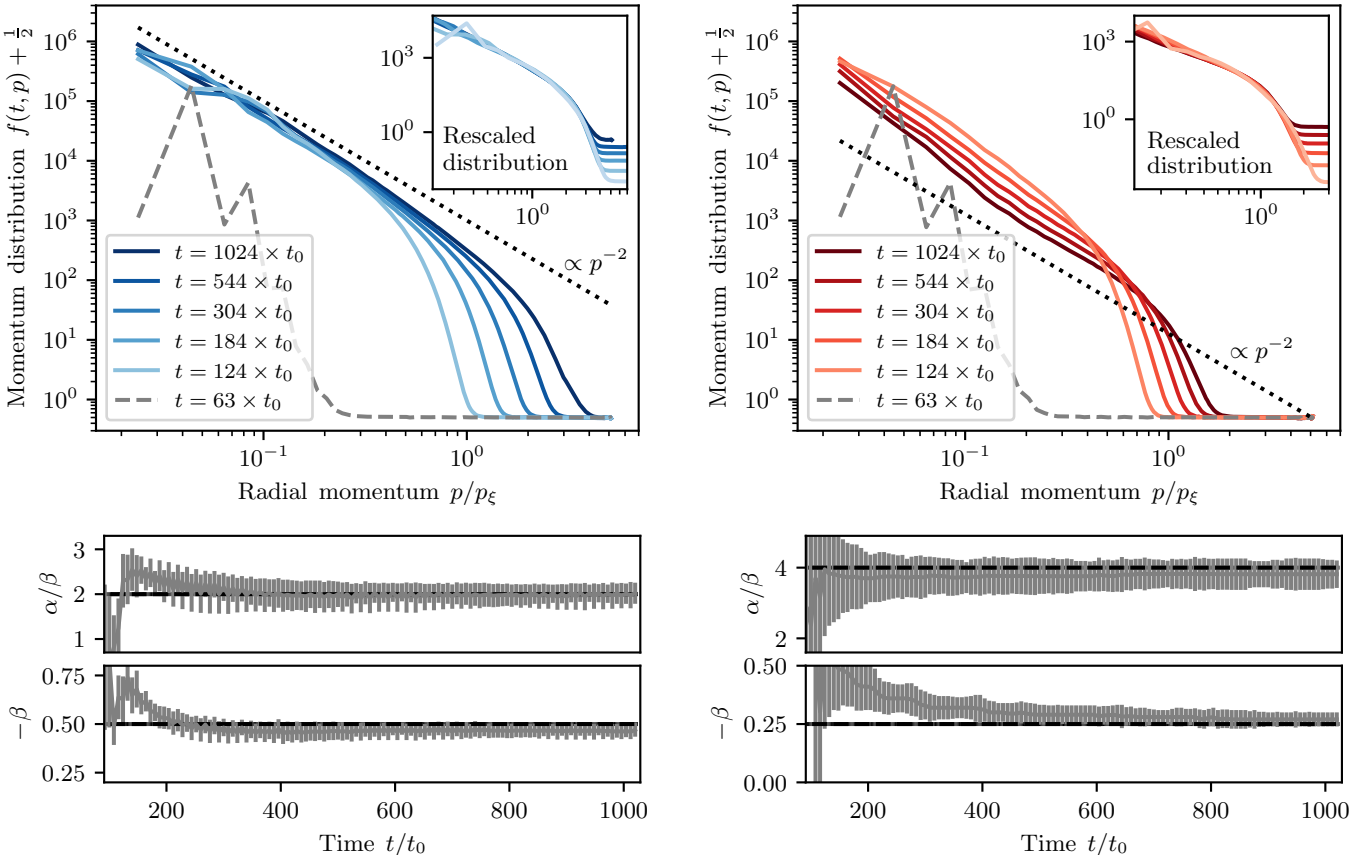

(a) Direct cascade with continuous modulation.

(b) Direct cascade after switching off the modulation.

Figure 5.4.: Self-similar time evolution of the momentum distribution in form of a direct energy cascade for driven turbulence (a) and free turbulence (b). Energy is injected at low momenta by modulating the scattering length according to Eq. (5.17) with a relative amplitude $r = 1$ at a frequency ω chosen such that $\hbar\omega/2 = \epsilon_{p_{\mathrm{res}}}$ with $p_{\mathrm{res}} = 3 \times 2\pi\hbar/L$. In the case of continuous modulation (a), a stationary distribution with a power law close to p^{-2} develops, whose front is evolving self-similarly. If the driving is switched off once the primary resonance has saturated, corresponding here to $t = 80 \times t_0$ (b), energy is propagated in a self-similar way to higher momenta, but the distribution at a given momentum decreases with time, reflecting energy conservation. A power law proportional to p^{-2} is shown in form of a dotted line as a guide to the eye. The insets show the distributions rescaled according to Eq. (5.25) using the numerically extracted scaling exponents displayed below the respective distributions [108].

existence of at least a source and a sink for energy to be injected and dissipated, respectively [364]. In the present case, the energy source is provided by the modulation of the interaction. In fact, the rate of energy injection into the system is approximately constant in this stationary regime, as expected for driven turbulence [51]. Since energy is transported locally in momentum space, unoccupied higher momentum modes play the role of an energy sink [51]. This allows for the build-up of a stationary distribution,

although the model lacks a mechanism of dissipation. By contrast, the distribution in the case of free turbulence, Fig. 5.4b, is not stationary, but decreases as a function of time for a given momentum, reflecting energy conservation.

To quantify the self-similar time evolution, the scaling exponents α and β defined in Eq. (5.25) have been extracted from the numerical data at different times using a maximum likelihood technique [108]. In the turbulent stage of the dynamics, the exponents are approximately constant at late times, as shown in the lower part of Fig. 5.4. The observed slow relaxation of the exponents at early times in Fig. 5.4b can be interpreted as prescaling (see Section 5.4.2). At the latest simulated times, the exponents take the values

$$\alpha_{\text{driven}} = -0.95 \pm 0.17, \quad \beta_{\text{driven}} = -0.46 \pm 0.06\,, \tag{5.26}$$

for driven turbulence, and

$$\alpha_{\text{free}} = -1.05 \pm 0.11, \quad \beta_{\text{free}} = -0.27 \pm 0.03\,, \tag{5.27}$$

for free turbulence, respectively. Rescaling the distribution according to Eq. (5.25) with the extracted exponents (see Ref. [108] for technical details), all data points collapse to a single universal scaling function $f_{\text{S}}(p)$, as shown in the insets of Fig. 5.4. The exponent β describes the speed of energy propagation towards higher momenta, which is higher for the driven cascade than for the free cascade.

The above values of the exponents are insensitive to the details of how the far-from-equilibrium state is approached. In particular, one observes the same exponents starting from an initial state with a highly occupied narrow window of momenta on top of a condensate background. Such an initial state is similar to the state of the system at the end of the preheating stage, when a certain momentum mode is overpopulated as a consequence of parametric resonance.

The slow power-law dynamics of the direct cascade can be challenging to capture with classical–statistical simulations for experimentally realistic configurations, since this method is known to be prone to instabilities caused by the vacuum noise [327]. These instabilities manifest themselves in a decay of the "quantum half" and the generation of spurious quantum pressure, resulting in an unphysical dependence of the results on the ultraviolet (UV) cutoff [371]. Classical–statistical simulations are therefore restricted to large occupancies and weak couplings, where these inevitable deficiencies are mitigated via a separation of scales. To simulate reheating dynamics in the turbulent regime, the particle number has therefore been increased and the coupling reduced such that the validity of the classical–statistical approximation can be ensured. Further details can be found in Appendix B.3, where we also assess the range of accessible coupling strengths for the present setup. In Section 5.5, we discuss how the above numerical results relate to realistic experimental conditions.

Comparison to Analytical Predictions

Let us now compare the numerically extracted scaling exponents in Eqs. (5.26) and (5.27) with analytical predictions.

One relation between the exponents α and β follows from the scaling of the total energy. To see this, we assume a self-similar time evolution according to Eq. (5.25) as well as a power-law scaling of the dispersion relation, $\epsilon_{\boldsymbol{p}} \propto |\boldsymbol{p}|^z$, where $z \approx 2$ in the particle regime of the Bogoliubov dispersion. Then, the total kinetic energy scales as

$$E(t) = V \int \frac{\mathrm{d}^d p}{(2\pi\hbar)^d}\, \epsilon_{\boldsymbol{p}} f(t, \boldsymbol{p}) = \left(\frac{t}{t_{\mathrm{ref}}}\right)^{\alpha-(d+z)\beta} E(t_{\mathrm{ref}})\,. \tag{5.28}$$

In the case of free turbulence, energy is conserved across the cascade, $E = \mathrm{const}$, while in the case of driven turbulence, it grows linearly with time, $E \propto t$. This implies the relation

$$\alpha = \gamma + (d + z)\beta\,, \tag{5.29}$$

where $\gamma = 1$ in the driven regime and $\gamma = 0$ in the absence of driving. For $d = 2$ and $z = 2$, Eq. (5.29) yields $\alpha = 1+4\beta$ for driven turbulence and $\alpha/\beta = 4$ for free turbulence, in agreement with the numerical results in Eqs. (5.26) and (5.27), respectively.

Another relation between the scaling exponents can be obtained from the scaling of scattering integrals in Boltzmann-type equations within kinetic theory [54, 364, 368]. In the scaling regime $f(t, p) \gg 1$, the direct cascade can still be treated perturbatively (in contrast to the inverse cascade, where occupancies are typically orders of magnitude higher), allowing one to derive the relation [54, 108]

$$(l - 2)\alpha = [(l - 2)d - 2]\beta - 1\,. \tag{5.30}$$

Here, $l = 4$ ($l = 3$) if $2 \leftrightarrow 2$ ($2 \leftrightarrow 1$) scattering dominates. Combining this result with Eq. (5.29) yields [108]

$$\beta = -\frac{-1 - (l - 2)\gamma}{(l - 2)z + 2}\,. \tag{5.31}$$

For driven turbulence, $\gamma = 1$, and a quadratic dispersion, $z = 2$, both scattering types lead to $\beta = -1/2$, in agreement with the numerical result in Eq. (5.26). In case of free turbulence, $\gamma = 0$, the prediction from perturbative kinetic theory yields $\beta = -1/6$ for $2 \leftrightarrow 2$ scattering and $\beta = -1/4$ for $2 \leftrightarrow 1$ scattering. The latter is closer to the value in Eq. (5.27) found at late times in the numerical simulations. By contrast, in the experiment reported in Ref. [351], where, instead of parametrically driving a pure condensate out of equilibrium, a cooling quench has been applied to an initially uncondensed Bose gas, a scaling exponent closer to the $2 \leftrightarrow 2$ scattering solution, $\beta = -1/6$, has been observed. Deviations from the predicted scaling can in general be induced by a non-quadratic scaling of the dispersion relation $\epsilon_{\boldsymbol{p}}$ or by the time dependence of the number of atoms in the condensate [108].

5.4.2. Prescaling

So far, we have investigated the two limiting cases where turbulence is either driven or free. Now, we address the transient regime corresponding to the somewhat more realistic situation where, in the beginning, turbulence is driven by the inflaton oscillations, but at some point goes over to free turbulence when the inflaton has decayed.

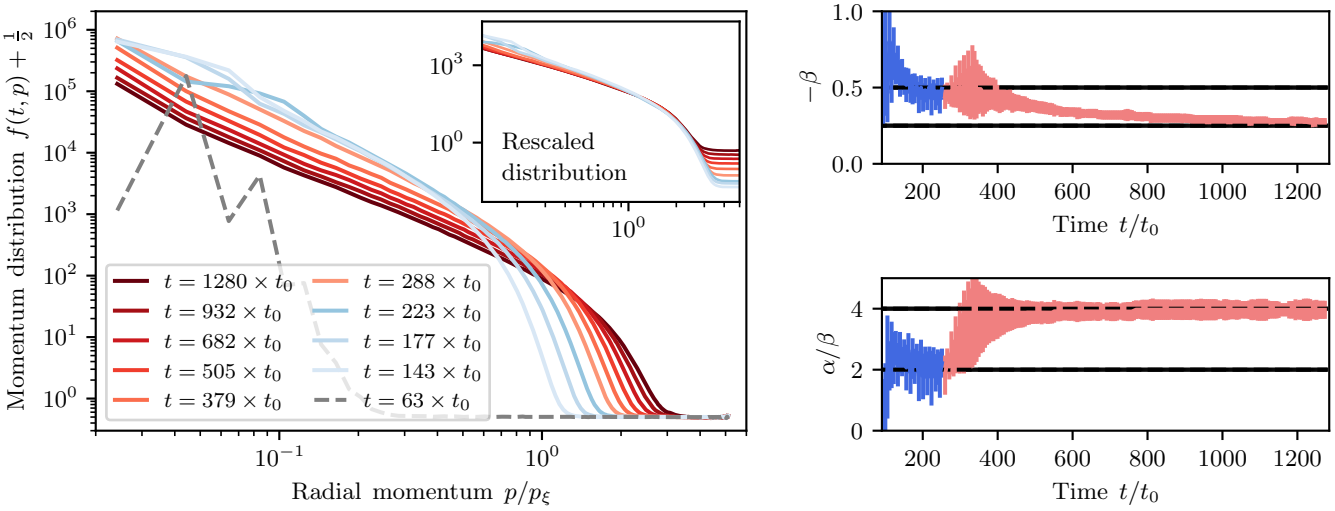

Figure 5.5.: Prescaling at the transition from driven to free turbulence. The simulation parameters are identical to those in Fig. 5.4, but the modulation is switched off suddenly at a later time $t/t_0 = 256$. Before this time (blue curves), turbulence is driven and both the momentum distribution as well as the scaling exponents α and β are the same as in Fig. 5.4a. After switching off the modulation (red curves), the ratio α/β quickly changes to the one expected for free turbulence, reflecting energy conservation. The exponent β gradually changes towards the value obtained for free turbulence in Fig. 5.4b, reducing the speed of energy transport in the cascade. Although the scaling exponents still change in time, the distribution has already attained its universal scaling form. This important hallmark of prescaling is indicated in the inset, where all data points collapse to a single curve after rescaling according to Eq. (5.25) with the extracted time-dependent scaling exponents $\alpha(t)$ and $\beta(t)$ [108].

This scenario is illustrated in Fig. 5.5. Up to the time $t/t_0 = 256$, the direct cascade is driven (blue curves), as in Fig. 5.4a. At this time, the modulation is switched off, mimicking the decay of the inflaton. We then observe a slowing down of the speed of energy propagation and the distribution decreases in time for a given momentum (red curves), reminiscent of the direct cascade of free turbulence shown in Fig. 5.4b.

On the right-hand side of Fig. 5.5, the numerically extracted scaling exponents are shown as a function of time. After switching off the modulation, the exponent β slowly evolves from a value close to the one reported in Eq. (5.26) for driven turbulence to a value close to the one reported in Eq. (5.27) for free turbulence. By contrast, the ratio α/β changes rather quickly between these two regimes. This behavior is expected since this ratio is fixed by energy conservation [see Eq. (5.29)], which is enforced instantaneously after switching off the modulation. Surprisingly, the self-similar scaling form of the distribution is approximately preserved during the transition, which is clearly visible in the inset of Fig. 5.5, where the distributions, rescaled according to Eq. (5.25) with the time-dependent scaling exponents, fall on top of each other.

Recently, such a situation, where the system's dynamics is governed by a universal scaling function much before the corresponding exponents have attained their universal values, has been studied in the context of heavy-ion collisions [56] This phenomenon,

termed prescaling, is closely related to the emergence of a far-from-equilibrium hydrodynamic behavior, as it allows one to describe the dynamics in terms of few slowly changing parameters [56]. A different type of prescaling, where certain correlation functions already scale with their universal exponents at early times while others do so only at much later times, has been studied numerically in three-component Bose gases [55]. The above results indicate that prescaling, as defined in Ref. [56], can be observed during the transition from driven to free turbulence[6], opening up new paths to studying this phenomenon experimentally.

Analysis of Prescaling Using the Method of Moments

To gain a deeper understanding of the phenomenon of prescaling, we conduct a complementary scaling analysis based on the method of moments [56]. The maximum likelihood technique used to extract the scaling exponents in Figs. 5.4 and 5.5 locally compares the distributions at two reference times t_1 and $t_2 > t_1$ [108]. By iterating over all times t_1, time-dependent scaling exponents are obtained that best collapse the pairs of distributions $f(t_1, \boldsymbol{p})$ and $f(t_2, \boldsymbol{p})$ on top of each other. By contrast, the method introduced in Ref. [56] relies on the moments as global properties of the distribution and allows one to extract instantaneous scaling exponents $\alpha(t)$ and $\beta(t)$ that do not depend on a reference time. In what follows, we briefly outline the method of moments, following Ref. [56], and then apply it to the prescaling scenario discussed above.

Method of moments. The n-th moment of the distribution $f(t, \boldsymbol{p})$ is defined as

$$M_{(n)}(t) = V \int \frac{\mathrm{d}^d p}{(2\pi\hbar)^d} \left(\frac{p}{p_0}\right)^n f(t, \boldsymbol{p})\,, \tag{5.32}$$

where V is the volume, $p = |\boldsymbol{p}|$, and p_0 is an arbitrary momentum scale to make the moment dimensionless. Note that in an isotropic system, as considered here, the distribution in fact depends only on the magnitude of the momentum, $f(t, \boldsymbol{p}) = f(t, p)$. For each moment $M_{(n)}$, the integrand is peaked around a certain characteristic momentum whose scaling properties are probed. In particular, the zeroth moment is the total particle number and the second moment is proportional to the total kinetic energy for a system with quadratic dispersion.

The most straightforward way of introducing time-dependent scaling exponents $\alpha(t)$ and $\beta(t)$ is to make the replacements $\alpha \to \alpha(t)$ and $\beta \to \beta(t)$ in the scaling ansatz Eq. (5.25), such that the latter reads $f(t, \boldsymbol{p}) = s^{\alpha(t)} f_{\mathrm{S}}\big(s^{\beta(t)} \boldsymbol{p}\big)$ with $s = t/t_{\mathrm{ref}}$. However, the exponents defined in this way depend on the reference time t_{ref}. To lift this dependency, it is advantageous to define $\alpha(t)$ and $\beta(t)$ instead in terms of the scaling functions

$$s_\alpha(t) = \exp\left[\int_{t_{\mathrm{ref}}}^{t} \alpha(t') \frac{\mathrm{d}t'}{t'}\right] \tag{5.33}$$

[6] A much shorter and less pronounced stage of prescaling occurs also in the scenario shown in Fig. 5.4b, where the modulation is switched off much earlier, at $t/t_0 = 80$.

and $s_\beta(t)$ defined in an analogous way. The scaling ansatz in Eq. (5.25) then generalizes to

$$f(t,\boldsymbol{p}) = s_\alpha(t) f_{\mathrm{S}}\big[s_\beta(t)\boldsymbol{p}\big]\,. \tag{5.34}$$

For constant exponents α and β, the power-law scaling of Eq. (5.25) is recovered.

Inserting the above scaling ansatz into Eq. (5.32), it is straightforward to derive that the moments scale with time as

$$M_{(n)}(t) = s_\alpha(t) s_\beta^{d+n}(t) M_{(n)}(t_{\mathrm{ref}})\,. \tag{5.35}$$

Given a pair of moments $M_{(n_1)}(t)$ and $M_{(n_2)}(t)$ with $n_1 \neq n_2$, it is thus possible to express the scaling functions $s_\alpha(t)$ and $s_\beta(t)$ in terms of these moments,

$$s_\alpha(t) = \left[\frac{M_{(n_1)}^{d+n_2}(t)/M_{(n_1)}^{d+n_2}(t_{\mathrm{ref}})}{M_{(n_2)}^{d+n_1}(t)/M_{(n_2)}^{d+n_1}(t_{\mathrm{ref}})}\right]^{1/(n_2-n_1)}, \tag{5.36a}$$

$$s_\beta(t) = \left[\frac{M_{(n_1)}(t)/M_{(n_1)}(t_{\mathrm{ref}})}{M_{(n_2)}(t)/M_{(n_2)}(t_{\mathrm{ref}})}\right]^{1/(n_2-n_1)}, \tag{5.36b}$$

which allows one to access the scaling exponents as

$$\alpha(t) = \frac{1}{n_2-n_1}\frac{\mathrm{d}}{\mathrm{d}\ln t}\ln\frac{M_{(n_1)}^{d+n_2}(t)}{M_{(n_2)}^{d+n_1}(t)}\,, \tag{5.37a}$$

$$\beta(t) = \frac{1}{n_2-n_1}\frac{\mathrm{d}}{\mathrm{d}\ln t}\ln\frac{M_{(n_1)}(t)}{M_{(n_2)}(t)}\,. \tag{5.37b}$$

Note that the dependency on the reference time t_{ref} drops out as a consequence of the derivatives.

Prescaling analysis. Since each moment condenses the information about the distribution into a single number, it is necessary to examine many different moments, each sensitive to a different characteristic momentum, to certify that a given distribution scales as a whole. Figures 5.6 and 5.7 show the scaling functions and time-dependent scaling exponents, respectively, extracted using the method of moments outlined above for all possible combinations of moments $1 \leq n_1 < n_2 \leq 4$. We exclude the zeroth moment from our analysis since the associated particle number conservation is incompatible with the energy-conserving direct cascade. All simulation parameters are the same as in Fig. 5.5, with the exception that the modulation is switched off at a later time, $t = 56 \times 2\pi/\omega \approx 458.6\,t_0$, allowing one to better distinguish the regimes of driven and free turbulence. The classical–statistical simulation presented in Figs. 5.6 and 5.7 has been conducted on a spatial grid of 768×768 grid points to increase the UV resolution and the data have been averaged over 100 runs. To reduce numerical errors of the calculated moments due to instabilities near the UV cutoff, the integral in Eq. (5.32) has been restricted to absolute momenta $|\boldsymbol{p}| \leq 3 \times p_\xi$ ($|\boldsymbol{p}| \leq \pi\hbar/\Delta x$, where Δx is the lattice

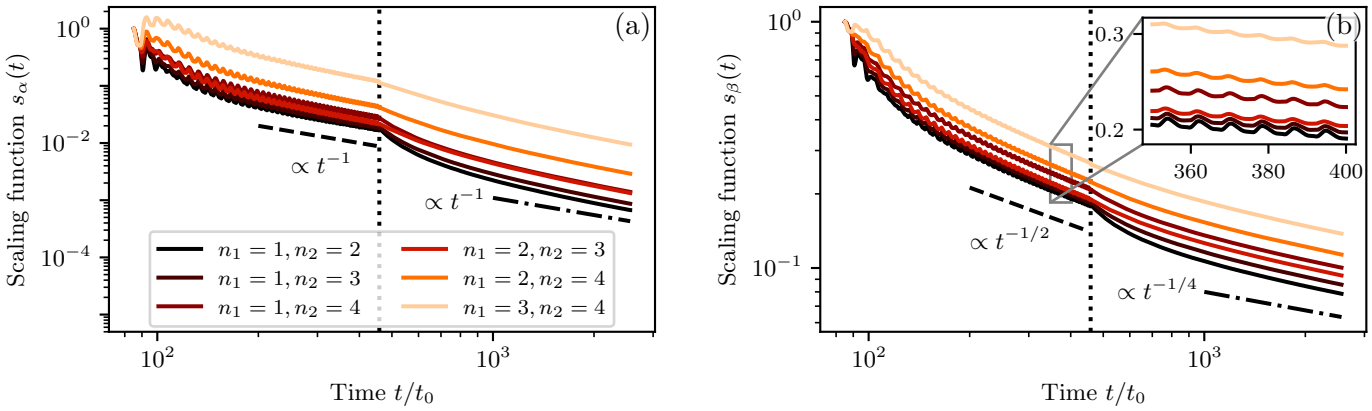

Figure 5.6.: Scaling functions $s_\alpha(t)$ (a) and $s_\beta(t)$ (b) with respect to the reference time $t_{\mathrm{ref}}/t_0 = 85$, extracted from the moments of orders $1 \leq n_1 < n_2 \leq 4$. The vertical dotted line marks the time $t/t_0 \approx 458.6$ when the modulation is switched off instantaneously. Before this point, the oscillatory behavior of the moments is directly reflected in the evolution of the scaling functions. As driven turbulence develops, their time averages approach power laws with exponents close to the predictions from kinetic theory, $\alpha_{\mathrm{driven}} = -1$ and $\beta_{\mathrm{driven}} = -1/2$ (dashed lines). After the modulation is switched off, the scaling functions exhibit a kink and the oscillations vanish. In the subsequent evolution, the scaling functions extracted from different moments evolve asynchronously, until they adopt a power-law behavior again for times $t/t_0 \gtrsim 1000$ with exponents close to the predictions from kinetic theory in the regime of free turbulence, $\alpha_{\mathrm{free}} = -1$ and $\beta_{\mathrm{free}} = -1/4$ (dashed-dotted lines). The system evolves self-similarly where all curves have the same slope, as analyzed in Fig. 5.7.

spacing) before (after) switching off the modulation. In addition, the origin of time has been shifted as $t \to t - 63\,t_0$ to improve the scaling analysis at early times [108].

Figure 5.6 shows the scaling functions $s_\alpha(t)$ and $s_\beta(t)$ with respect to the reference time $t_{\mathrm{ref}}/t_0 = 85$. As turbulence develops, the scaling functions approach power laws $s_\alpha(t) \propto (t/t_{\mathrm{ref}})^\alpha$ and $s_\beta(t) \propto (t/t_{\mathrm{ref}})^\beta$. In the driven regime, before switching off the modulation, the corresponding exponents are close to the analytical predictions from kinetic theory, $\alpha_{\mathrm{driven}} = -1$ and $\beta_{\mathrm{driven}} = -1/2$ (see Section 5.4.1). At the time when the modulation is switched off instantaneously, the scaling functions exhibit a kink and continue evolving asynchronously for some time. This indicates that the shape of the distribution is not preserved exactly, but slightly readjusts during the transition from driven to free turbulence. The changes in the shape of the distribution are more pronounced at lower momenta, which is reflected by the fact that those curves in Fig. 5.6 extracted from lower moments react stronger at the transition. Despite these local adjustments, it is remarkable that the global scaling form of the distribution is approximately preserved during the transition from driven to free turbulence, as can also be seen in Fig. 5.5. For $t/t_0 \gtrsim 1000$, the scaling functions again approach a power law with exponents close to the analytical predictions for free turbulence, $\alpha_{\mathrm{free}} = -1$ and $\beta_{\mathrm{free}} = -1/4$. In the region where the scaling functions extracted from different combinations of moments all evolve in parallel, the distribution scales self-similarly as a whole. To certify that the distribution also exhibits prescaling, i.e., a self-similar evolution with time-dependent

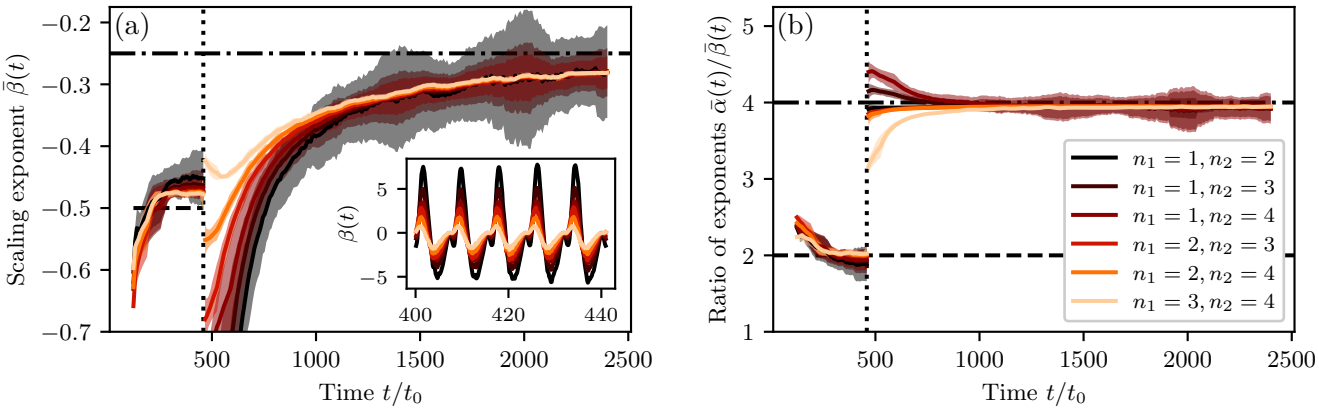

Figure 5.7.: Time-averaged scaling exponents $\bar{\beta}(t)$ (a) and $\bar{\alpha}(t)/\bar{\beta}(t)$ (b), extracted from the moments of orders $1 \leq n_1 < n_2 \leq 4$. The data have been smoothed using simple moving means and the shaded regions show the corresponding moving standard deviations. The vertical dotted line represents the time when the modulation is switched off. Before this point, in the regime of driven turbulence, the exponents are approximately constant and close to the analytical predictions from kinetic theory, $\beta_{\text{driven}} = -1/2$ and $\alpha_{\text{driven}}/\beta_{\text{driven}} = 2$ (dashed lines). After the modulation is stopped, the exponents jump discontinuously and the exponents extracted from different combinations of moments exhibit discrepancies. For $t/t_0 \gtrsim 1000$, they converge and continue evolving as a single curve, certifying the existence of a prescaling regime of self-similar time evolution. The exponent $\beta(t)$ gradually approaches the universal value $\beta_{\text{free}} = -1/4$ [dashed-dotted line in panel (a)] predicted from kinetic theory in the regime of free turbulence, while the ratio of the exponents quickly adjusts to the prediction $\alpha_{\text{free}}/\beta_{\text{free}} = 4$ [dashed-dotted line in panel (b)], reflecting energy conservation. The inset in panel (a) shows the instantaneous exponent $\beta(t)$ in the driven regime, which strongly oscillates due to the modulation.

scaling exponents, we analyze the change of the scaling functions as quantified by the exponents $\alpha(t)$ and $\beta(t)$ in what follows.

In the driven regime, the scaling functions oscillate in time, as indicated in the inset of Fig. 5.6b. These oscillations originate from the modulated interaction, which causes the distribution and therefore the moments to oscillate in time (cf. Fig. 5.3). As a result, the instantaneous scaling exponents $\alpha(t)$ and $\beta(t)$, which are derivatives of the scaling functions according to Eq. (5.37), exhibit the strong oscillatory behavior shown for $\beta(t)$ in the inset of Fig. 5.7a. To connect with the results in Fig. 5.5 obtained using the maximum likelihood technique [108], it is convenient to consider instead the time-averaged exponents $\bar{\alpha}(t)$ and $\bar{\beta}(t)$, defined as

$$\bar{\beta}(t) = \frac{1}{\ln(1 + T/t)} \int_t^{t+T} \beta(t') \frac{\mathrm{d}t'}{t'} \,, \tag{5.38}$$

and analogously for $\bar{\alpha}(t)$, where $T = 2\pi/\omega$ is the modulation period. After switching off the modulation, the oscillations of the moments vanish and the time-averaging of the exponents is not required any more.

Figures 5.7a and 5.7b show the quantities $\bar{\beta}(t)$ and $\bar{\alpha}(t)/\bar{\beta}(t)$, respectively, as a function of time. The derivatives in Eq. (5.37) are sensitive to small fluctuations in the data due to

statistical uncertainties, resulting in a large spread of the data points. This is especially true where moments of lower orders are involved since they probe the distribution at smaller momenta with a lower density of states. To better visualize the trend of the exponents, the data have been smoothed by calculating simple moving means (separately in the regimes of driven and free turbulence) using a window size of 8 (16) periods involving 512 (1024) data points for $n_1 > 1$ ($n_1 = 1$). The shaded regions represent the corresponding moving standard deviations.

Before the modulation is switched off, the system is in the state of driven turbulence. Indeed, for $t/t_0 \gtrsim 200$, both $\bar{\beta}(t)$ and $\bar{\alpha}(t)/\bar{\beta}(t)$ are approximately constant and for all considered moments close to the analytical predictions $\beta_{\text{driven}} = -1/2$ and $\alpha_{\text{driven}}/\beta_{\text{driven}} = 2$ (see Section 5.4.1). After suddenly switching off the modulation, the exponents jump discontinuously, reflecting the kink in the scaling functions in Fig. 5.6. Furthermore, there are discrepancies in the values of the exponents extracted from different combinations of moments after the modulation is stopped. As discussed above, this indicates a slight readjustment of the shape of the distribution, which is consistent with the behavior in Fig. 5.5, where the exponents exhibit large error bars in this regime. For times $t/t_0 \gtrsim 1000$, the exponents extracted from different moments converge to a single curve, certifying a self-similar evolution of the distribution as a whole. During this prescaling stage, the exponent $\bar{\beta}(t)$ evolves gradually towards the analytical prediction for free turbulence, $\beta_{\text{free}} = -1/4$. By contrast, the ratio $\bar{\alpha}(t)/\bar{\beta}(t)$ adjusts rather quickly to the value $\alpha_{\text{free}}/\beta_{\text{free}} = 4$, expressing energy conservation.

Thus, the analysis using the method of moments certifies the existence of a prescaling regime during the transition from driven to free turbulence, where the momentum distribution scales self-similarly with time-dependent scaling exponents approaching gradually their universal values.

5.4.3. Thermalization

As we have seen, on its way to thermal equilibrium the system takes a detour via a non-thermal fixed point, in the vicinity of which the dynamics is dominated by a turbulent transport of energy towards higher momenta. The self-similar dynamics of the direct cascade stops once the occupancy of the characteristic momentum dominating the kinetic energy budget becomes comparable to the expectation value of the vacuum noise given by the "quantum half". At this point, quantum fluctuations become dominant over statistical fluctuations [51] and the system is expected to relax to a Bose–Einstein distribution

$$f_{\text{BE}}(\boldsymbol{p}) = \frac{1}{\exp(\epsilon_{\boldsymbol{p}}/k_{\text{B}}T_{\text{f}}) - 1}\,, \tag{5.39}$$

where $\epsilon_{\boldsymbol{p}}$ is the dispersion relation, k_{B} is the Boltzmann constant and T_{f} is the reheating temperature.

The dominance of quantum fluctuations makes this final stage of the dynamics inaccessible to classical–statistical simulations. In contrast to the expected relaxation to a Bose–Einstein distribution, at sufficiently late times in the numerical simulation, the cascade stops being self-similar, slows down, and approaches a classical equilibrium

distribution [53] with a temperature $\widetilde{T}(\Lambda)$ that depends on the UV cutoff Λ and is determined by the equipartition theorem, $f_{\mathrm{cl,th}}(\boldsymbol{p})+1/2 \propto k_{\mathrm{B}}\widetilde{T}(\Lambda)/\epsilon_{\boldsymbol{p}}$ [108]. In particular, mode occupancies drop to unphysical values below the vacuum noise of 1/2.

Here, we resort to analytical estimates for the reheating time and the reheating temperature in our system based on the self-similar time evolution. Following Ref. [51], we neglect the final stage of quantum relaxation to a Bose–Einstein distribution and consider thermalization as complete once the occupancy of the characteristic momentum dominating the kinetic energy budget becomes on the order of unity. More precisely, we define the characteristic momentum $\bar{p}(t)$ as the momentum that maximizes the integrand in the expression (5.28) for the total kinetic energy. For an isotropic system with dispersion relation $\epsilon_{\boldsymbol{p}} \propto p^z$, where $p = |\boldsymbol{p}|$, the characteristic momentum is given by

$$\bar{p}(t) = \arg\max_{p} p^{d+z-1} f(t,p)\,. \tag{5.40}$$

If the scaling exponents as well as the momentum distribution at some reference time are known, the assumption of self-similar time evolution according to Eq. (5.25) is sufficient to predict the time t_{f} when the occupancy of the final characteristic momentum p_{f} will reach unity. The time t_{f} can be regarded as the best possible approximation to the reheating time obtainable from classical–statistical simulations. However, Eq. (5.25) is not directly applicable since the scaling exponents are not constant throughout the entire time evolution. In fact, they take different universal values in the regimes of driven and free turbulence, respectively, which are interpolated during a transient regime of prescaling. Importantly, as shown in Section 5.4.2, the universal scaling form of the distribution is preserved during prescaling, allowing us to describe the full evolution solely in terms of time-dependent scaling exponents.

To properly account for time-dependent exponents $\alpha(t)$ and $\beta(t)$, we use the generalized scaling law in Eq. (5.34), while the original power-law form (5.25) is recovered for constant exponents. This way, the evolution of the initial characteristic momentum scale for turbulence p_{i} is given by

$$\bar{p}(t) = \exp\left[-\int_{t_{\mathrm{i}}}^{t} \beta(t')\frac{\mathrm{d}t'}{t'}\right] p_{\mathrm{i}}\,, \tag{5.41}$$

where t_{i} denotes the time when turbulence sets in. While the exponent β determines the scaling of the characteristic momentum, the evolution of its occupancy is governed by the exponent α,

$$f(t,\bar{p}(t)) = \exp\left[\int_{t_{\mathrm{i}}}^{t} \alpha(t')\frac{\mathrm{d}t'}{t'}\right] f(t_{\mathrm{i}},p_{\mathrm{i}})\,. \tag{5.42}$$

By virtue of Eq. (5.42), it is in principle possible to compute the time t_{f} by solving $f(t_{\mathrm{f}},p_{\mathrm{f}}) = 1$, given full knowledge of the time dependence of the exponent α. It is instructive, however, to rewrite this formula using some simplifying approximations. To this end, we assume that α is approximately constant during the driven regime, taking its universal value α_{driven}, and that, after switching off the modulation at time t_{d}, the

relaxation to its universal value for free turbulence α_{free} occurs fast compared to the overall reheating time scale. We then recover power-law scaling for the occupancy of the final characteristic momentum,

$$f(t_{\mathrm{f}}, p_{\mathrm{f}}) \approx \left(\frac{t_{\mathrm{d}}}{t_{\mathrm{i}}}\right)^{\alpha_{\mathrm{driven}}} \left(\frac{t_{\mathrm{f}}}{t_{\mathrm{d}}}\right)^{\alpha_{\mathrm{free}}} f(t_{\mathrm{i}}, p_{\mathrm{i}})\,, \tag{5.43}$$

and it reaches unity at the time

$$t_{\mathrm{f}} = t_{\mathrm{d}} \left(\frac{t_{\mathrm{d}}}{t_{\mathrm{i}}}\right)^{-\alpha_{\mathrm{driven}}/\alpha_{\mathrm{free}}} [f(t_{\mathrm{i}}, p_{\mathrm{i}})]^{-1/\alpha_{\mathrm{free}}}\,. \tag{5.44}$$

Recall that a direct energy cascade is described by negative exponents α and β with large initial occupancies $f(t_{\mathrm{i}}, p_{\mathrm{i}})$, which decrease in time according to Eq. (5.43). Furthermore, the condition $t_{\mathrm{i}} \leq t_{\mathrm{d}} \leq t_{\mathrm{f}}$ requires $t_{\mathrm{d}} \leq t_{\mathrm{i}}[f(t_{\mathrm{i}}, p_{\mathrm{i}})]^{-1/\alpha_{\mathrm{driven}}}$. If the latter inequality is satisfied as an equality, the occupancy of the characteristic momentum reaches unity already during driven turbulence before switching off the modulation, such that $t_{\mathrm{f}} = t_{\mathrm{d}}$. Here, we focus on the situation where $t_{\mathrm{d}} < t_{\mathrm{f}}$ such that the system spends a dominant part of its evolution in the regime of free turbulence.

Using an analogous line of arguments, we can estimate the final characteristic momentum scale from Eq. (5.41) as

$$p_{\mathrm{f}} \approx \left(\frac{t_{\mathrm{d}}}{t_{\mathrm{i}}}\right)^{-\beta_{\mathrm{driven}}} \left(\frac{t_{\mathrm{f}}}{t_{\mathrm{d}}}\right)^{-\beta_{\mathrm{free}}} p_{\mathrm{i}} = \left(\frac{t_{\mathrm{d}}}{t_{\mathrm{i}}}\right)^{-\beta_{\mathrm{driven}}+\alpha_{\mathrm{driven}}/(d+z)} [f(t_{\mathrm{i}}, p_{\mathrm{i}})]^{1/(d+z)} p_{\mathrm{i}}\,, \tag{5.45}$$

where the second equality follows after inserting our estimate for the reheating time (5.44) and substituting the relation (5.29) between α_{free} and β_{free} imposed by energy conservation. The use of the latter identity makes the estimate (5.45) of the final characteristic momentum independent of the scaling exponents in the regime of free turbulence, reflecting the fact that p_{f} is closely connected to the total energy in the system [51], which is conserved after switching off the modulation. By contrast, the reheating time, according to Eq. (5.44), is sensitive to the values of the scaling exponents in both regimes, and, in particular, can be influenced by the non-universal behavior during prescaling.

Finally, we can obtain an order-of-magnitude estimate for the reheating temperature T_{f} in our system by identifying the latter with the typical kinetic energy of a particle with momentum p_{f}. For a dispersion relation of non-relativistic particles, this reads [108]

$$k_{\mathrm{B}} T_{\mathrm{f}} \sim \frac{p_{\mathrm{f}}^2}{2m}\,. \tag{5.46}$$

In order to complete the analogy to cosmological reheating, it is important to remember that the time variable t in the estimate for the reheating time (5.44) denotes the laboratory time and should be transformed back to the cosmic time τ by integrating the relation (5.14). Likewise, taking into account the redshift of momenta, the final characteristic momentum in Eq. (5.45) should be replaced as $p_{\mathrm{f}} \to p_{\mathrm{f}}/a(t_{\mathrm{f}})$ [cf. Eq. (5.13)]. For the estimate of the reheating temperature (5.46), this means $T_{\mathrm{f}} \to T_{\mathrm{f}}/a^2(t_{\mathrm{f}})$ [108].

Although Eqs. (5.44) to (5.46) are useful to estimate asymptotic quantities without requiring to simulate the dynamics up to the point where the system thermalizes, the outlined argumentation is based on the strong assumption that the neglected final stage of the dynamics, which is dominated by quantum fluctuations, does not have a significant impact on these estimates. The latter remains to be checked against physical reality, which can be provided by comparison to an experiment.

Thermalization Versus Expansion

A peculiarity of the transformation of the time variable in Eq. (5.14) is that for certain expansion scenarios, the cosmic time τ can become infinite within a finite laboratory time t. For example, in case of a power-law expansion $a(\tau) = (1 + H_0\tau/\nu)^\nu$ with initial conditions $a(0) = 1$ and $H(0) = H_0$, one finds that for $\nu > 1/2$, which includes the case of matter-dominated expansion ($\nu = 2/3$), the laboratory time corresponding to the asymptotic cosmic time $\tau = \infty$ takes the finite value $t(\tau = \infty) = \nu/(2\nu-1)H_0$ [108]. Consequently, thermalization in the simulated cosmological system can only occur if $t_\mathrm{f} < t(\tau = \infty)$, as otherwise the dynamics "freezes" and the system will never thermalize.

Recall that in two spatial dimensions, the fact that the scale factor $a(t)$ does not explicitly enter the evolution equation (5.15) allows one to consider arbitrary expansion scenarios in post-processing. This may be used to constrain the class of expansion schemes that are consistent with an asymptotic thermal state of the simulated cosmological system, which in the simulating cold-atom system is always reached [108].

By contrast, in three spatial dimensions, the interaction in Eq. (5.15) depends explicitly on the scale factor and decreases as $g \propto a^{-1}$, such that the simulating system may become effectively non-interacting due to the expansion already before reaching $t(\tau = \infty)$. In cosmology, such a behavior is known as freeze out, which occurs when interaction rates of particles fall below the expansion rate $H = \dot{a}/a$ of the universe and explains the relic abundances of certain species today [49].

5.5. Experimental Perspectives

In this section, we summarize the experimental requirements for observing the salient features of reheating dynamics discussed in this chapter.

The simulating system is a single-component BEC that is parametrically excited by modulating the interaction according to Eq. (5.17) around some positive offset value. This can be realized experimentally with the help of a Feshbach resonance, which allows one to tune the s-wave scattering length using an external magnetic field [58, 342, 344, 347, 348]. The interaction strength g_3D of a 3D Bose gas is related to the s-wave scattering length a_s via Eq. (1.4). While the analog reheating scenario is independent on dimensionality, for concreteness, we have focused here on 2D geometries, which may be realized through a tight confinement of the atomic gas in the vertical direction by a harmonic potential. In the quasi-2D regime, the effective interaction strength $g_\mathrm{2D} = \tilde{g}\hbar^2/m$ is characterized by the dimensionless parameter $\tilde{g} = \sqrt{8\pi}a_s/a_\mathrm{HO}$, where $a_\mathrm{HO} = \sqrt{\hbar/m\omega_\mathrm{HO}}$ is the oscillator length of the confining harmonic potential with

frequency ω_{HO} [see Eq. (1.29)]. Besides via Feshbach resonances, 2D Bose gases with tunable effective interactions can therefore alternatively be realized by changing the frequency of the harmonic trap [372].

The numerical simulations presented in this chapter have been conducted for the fixed value $N\tilde{g} = 2.5 \times 10^3$ of the product of the particle number N and the interaction strength $\tilde{g}$. This value is readily achievable in present-day experiments with uniform 2D Bose gases [361]. On the classical level, the parameters N and $\tilde{g}$ enter the equations of motion only via the product $N\tilde{g}$ (see Appendix B.2), but this no longer holds on the quantum level. In fact, even classical–statistical simulations are sensitive to the individual values of N and $\tilde{g}$ since they control the relative magnitude of mode occupancies with respect to quantum fluctuations mimicked in form of vacuum noise. As discussed in Appendix B, classical–statistical simulations are restricted to large occupancies and weak interactions, which is why the simulations of turbulent reheating dynamics in Section 5.4 have been conducted for a higher particle number than currently realizable in experiments. To estimate characteristic quantities for more realistic experimental setups, we rescale our numerical results to the reference parameters $N_{\mathrm{ref}} = 10^6$ and $\tilde{g}_{\mathrm{ref}} = 2.5 \times 10^{-3}$. Pure BECs with almost 10^6 atoms can be reached in state-of-the-art experimental setups, e.g., for ^{39}K [373–375], where a wide range of interactions is accessible through the broad Feshbach resonance at the magnetic flux $B = 560.7\,\mathrm{G}$ [376]. We emphasize that extrapolating weak coupling results to stronger couplings is *a priori* not justified. Yet, this procedure is often the only way to be consistent with experimental aspects and commonly used, e.g., in the context of quantum chromodynamics (QCD) [377]. In the field of ultracold atoms, a number of positive examples exist, where weak coupling expectations of non-equilibrium quantum dynamics have been found experimentally at strong couplings [46, 317].

For the above choice $N\tilde{g} = 2.5 \times 10^3$ and a 2D system of ^{39}K atoms in a square box of length $L = 50\,\mu\mathrm{m}$, one obtains the typical values $x_0 = 1\,\mu\mathrm{m}$ and $t_0 \approx 0.6\,\mathrm{ms}$ for the characteristic length and time scales $x_0 = \hbar/\sqrt{m n_0 g_0}$ and $t_0 = \hbar/n_0 g_0$, respectively. Here, g_0 is the offset value around which the interaction is modulated and $n_0 = N/L^2$ is the atomic density.

The analog reheating scenario can be subdivided into two distinct stages, namely, the early preheating-like stage, where occupancies of resonant momenta grow exponentially as a result of parametric instabilities, and the subsequent stage of turbulent thermalization, characterized by a self-similar transport of energy towards higher momenta. The time scales at which these phenomena can be observed depend on the choice of the modulation frequency ω and the relative modulation amplitude r in Eq. (5.17). The choice $r = 1$, i.e., modulating the scattering length with an amplitude close to its offset value, is efficient for rapidly driving the system out of equilibrium. (Note that the perturbative expression for the growth rate in Eq. (5.23) is no longer applicable in this case.) The direct cascade is observed best if occupancies of the initial characteristic momentum, where energy is injected in the system, are as high as possible. To this end, the modulation frequency ω should be chosen close to the frequency of the lowest non-zero momentum mode supported by the system, which is typically deep in the phonon regime where the Bogoliubov dispersion is linear. In the simulations of reheating dynamics presented

in Figs. 5.4 and 5.5, the modulation frequency has been chosen such that the primary resonance occurs at the momentum $p_{\mathrm{res}} = 3 \times 2\pi\hbar/L$, i.e., $\omega = 2\epsilon_{p_{\mathrm{res}}}/\hbar \approx 2\pi \times 199\,\mathrm{Hz}$ for the example parameters mentioned above. The onset of turbulence, marking the end of the preheating stage, occurs at around $t/t_0 \approx 80$, corresponding to roughly 10 oscillations of the scattering length. The subsequent turbulent scaling regime extends up to times of about $t_{\mathrm{f}}/t_0 \approx 1500$, which can be deduced from Figs. 5.4 and 5.5 with the help of Eq. (5.44) after rescaling the occupancies to the reference particle number $N = 10^6$ (cf. Appendix B.3). The estimated reheating time t_{f} is well within the reach of modern experiments, where typical lifetimes of BECs are on the order of a few seconds [374].

In our analysis, we have considered the momentum distribution $f(t, \boldsymbol{p}) = \langle \hat{\Psi}^\dagger_{\boldsymbol{p}}(t) \hat{\Psi}_{\boldsymbol{p}}(t) \rangle$ as the main observable. Experimentally, this quantity can be accessed in TOF measurements [60]. In the case of driven turbulence [cf. Fig. 5.4a], by virtue of Eq. (5.45), we find that the characteristic momentum at the reheating time t_{f} is roughly given by $p_f/p_\xi \approx 1.5$, which is on the order of the momentum corresponding to the healing length ξ. In general, this value depends on the duration of the regime of driven turbulence and tends to be smaller in the case of free turbulence [cf. Fig. 5.4b] or in the prescaling scenario [cf. Fig. 5.5], where less energy is injected into the system. It is a fortunate circumstance that higher momenta, which are increasingly populated as the direct cascade progresses, are typically easier to resolve in TOF measurements since they require a shorter expansion time. As an alternative means of detection, *in situ* images of the density profile may be used. In fact, all relevant signatures of both the parametric resonance and the turbulent cascade can be extracted from the quantity $\langle \hat{n}^\dagger_{\boldsymbol{p}}(t) \hat{n}_{\boldsymbol{p}}(t) \rangle$, where $\hat{n}_{\boldsymbol{p}}(t)$ is the Fourier transform of the operator $\hat{n}(t, \boldsymbol{x}) = \hat{\Psi}^\dagger(t, \boldsymbol{x}) \hat{\Psi}(t, \boldsymbol{x})$ describing the spatial density profile of the Bose gas.

Although we have put our main focus on uniform systems, nowadays available in many laboratories [372, 378], the characteristic features of the dynamics can be expected to be prevalent even in the presence of a harmonic trap. In general, such an external trapping potential couples different momenta and thereby changes the nature of Bogoliubov quasi-particles. However, within a local density approximation, a harmonically trapped BEC in the Thomas–Fermi regime can be regarded as locally uniform around the center [57]. Thus, while inhomogeneities of the trap may distort long-range correlations in the system, the dynamics on small scales or at large momenta, relevant for the direct cascade, remains unaffected. Separate GPE simulations of a harmonically trapped system confirm that this is indeed the case (not shown).

We conclude this section with some remarks on dimensionality. The observation of a turbulent cascade in a scalar BEC requires at least two spatial dimensions. This is owed to the fact that in a strictly 1D system, due to kinematic constraints, there can be no $2 \leftrightarrow 2$ scattering processes redistributing momenta. If, however, the system is elongated, but not as strongly confined in the transversal direction to be considered in the quasi-1D regime, turbulent energy transport sets in once transversal modes are excited. This is confirmed by separate simulations of a 3D system in an elongated periodic box (not shown).

Compared to the 3D case, the study of reheating dynamics in two dimensions is some-

what simpler for at least two reasons. First, as discussed in Section 5.2, the effective interaction in 2D is independent of the cosmic scale factor and there is no need to continuously adjust the scattering length according to the specific expansion model chosen. Second, an absorption image of an atomic cloud, taken after a TOF expansion or *in situ*, will always be a 2D projection on the plane transversal to the optical axis. In three dimensions, this means that the distribution is integrated along the optical axis, thereby mixing momenta of different magnitudes. As revealed separately by a simulation of a 3D system in a periodic box, the scaling is robust with respect to integrating the momentum distribution along one spatial dimension before performing the radial average. Thus, the scheme can readily be applied to experimentally investigate reheating dynamics in three dimensions, which is of fundamental interest from a cosmological point of view.

5.6. Summary

In this chapter, we have discussed how an ultracold Bose gas can be used for quantum-simulating the characteristic stages of far-from-equilibrium reheating dynamics in the early universe. The analogy builds on the identification of the inflaton field with an atomic Bose–Einstein condensate, while excitations on top of the condensate play the role of particles produced by the decaying inflaton. We have discussed how in the non-relativistic limit, expanding spacetime can be encoded in the time dependence of the atomic interaction, which can be controlled experimentally, e.g., via Feshbach resonances. In addition, the oscillations of the inflaton are mimicked by a periodic modulation of the interaction, which induces a resonant amplification of quantum fluctuations in analogy to preheating in the early universe. Following the proliferation of secondary instabilities due to non-linear effects, the system enters a turbulent state, characterized by a self-similar transport of energy towards higher momenta. The universal scaling exponents extracted from classical–statistical simulations of the analog reheating scenario agree with predictions from kinetic theory for both driven and free turbulence. The transition between these regimes, marked by the decay of the inflaton, is characterized by an extended prescaling regime of partial universality, where the scaling form of the distribution is approximately preserved, while the scaling exponents gradually relax to their universal values. The proposed implementation of analog reheating therefore opens the door to an experimental observation of this phenomenon and provides a setting for investigating universal far-from-equilibrium dynamics based on tools commonly available in modern experiments. In particular, the final stage of relaxation to thermal equilibrium is beyond the scope of classical–statistical simulations as it is dominated by quantum fluctuations, and as such represents a question that can more efficiently be answered in physical quantum simulators.

Conclusion

In this thesis, we have developed protocols and scenarios that enable analog quantum simulators to disclose previously elusive dynamics and correlations in quantum many-body systems. We have illustrated these schemes for a variety of relevant applications from the wide spectrum of the versatile platform of ultracold atoms, while extensions to other platforms are in most cases immediate. The presented numerical benchmark simulations demonstrate that the protocols as well as the physics they give access to are within the reach of state-of-the-art experimental setups. In what follows, we summarize the most important insights for the individual problems addressed in this thesis and give an outlook on future research directions.

In Chapter 2, we have developed protocols based on non-Hermitian linear response to measure the elusive unequal-time anti-commutator in quantum many-body systems. Combined with a standard (Hermitian) linear response measurement of the unequal-time commutator, this method allows one to independently probe both sides of the fluctuation–dissipation relation (FDR). The concept of non-Hermitian linear response is general and can be applied to any observable in any quantum system, irrespective of microscopic details like particle statistics or interactions. To realize effective non-Hermitian perturbations in cold-atom systems, we have introduced specific schemes that combine coupling to an ancilla with a post-selection on realizations where no particles are detected in the ancilla. By applying engineered dephasing noise to the ancilla, effective non-Hermitian dynamics can be generated for an extended period of time via the continuous quantum Zeno effect, which allows one to probe frequency-resolved responses. Moreover, the system–ancilla coupling can be generalized to give access to a wide range of observables beyond unequal-time density correlations. We have illustrated the framework for probing thermalization in isolated quantum systems through an independent measurement of both sides of the FDR. Besides certifying that a given quantum state is thermal, testing scenarios where the system fails to thermalize, e.g., due to integrability, localization, or scar states, represents an application of at least equal importance. In addition, the proposed methods of engineering effective non-Hermitian dynamics may not only be used for measuring dynamical correlations, but also for exploring the intriguing realm of non-Hermitian physics [137, 138].

The main challenges for an experimental implementation of the proposed non-Hermitian linear response schemes are rooted in the optimization of the signal-to-noise ratio in combination with the post-selection on the empty-ancilla subspace. On the one hand, a stronger perturbation is favorable to increase the strength of the measurement signal, on the other hand, the perturbation must be sufficiently weak to stay within the regime of linear response, such that errors due to non-linear effects are suppressed. As the numerical benchmarks in Chapter 2 demonstrate, a good compromise between these

objectives can be achieved within the capabilities of state-of-the-art experiments like quantum gas microscopes. In addition, we have examined potential challenges for experimental implementations of the non-Hermitian linear response scheme in Rydberg quantum simulators. As illustrated at the example of an XXZ Heisenberg spin model, a perfect post-selection on the absence of ancilla occupancies is not necessary in all cases and an accurate extraction of FDRs may still be possible despite systematic deviations due to false negatives. It should be noted, however, that it must be checked a priori, e.g., via numerical simulations, whether the requirement of post-selection can be relaxed for a particular application. Furthermore, we have shown that in case of multiple ancillas a single noise process acting globally on all ancillas may be used when operating in the linear regime. This represents an enormous practical simplification compared to engineering independent noise processes for each ancilla locally. These insights thus extend the scope of the protocols to experiments where single-site (or single-particle) addressing is not available and where accurate post-selection is difficult to achieve. While preliminary experimental results successfully demonstrate building blocks of the non-Hermitian linear response scheme for non-interacting systems [104], the next step will be to work on the realization of such measurements also in interacting many-body systems.

In Chapter 3, we have introduced ancilla-based schemes for the measurement of currents as well as current correlations. The protocol can be executed as a non-invasive measurement, involving only a marginal perturbation of the probed quantum state, or as a projective measurement yielding a higher signal-to-noise ratio. We have numerically benchmarked and illustrated the technique for probing chiral phases of quantum matter in optical-lattice setups, demonstrating its feasibility within the capabilities of modern experiments. The protocol can also flexibly be adapted to other platforms through a suitable choice of ancillas. For example, in a cavity setup [379], it is natural to represent the ancilla by the cavity mode, while in a trapped ion system, collective vibrational modes of the ion crystal may serve as ancillas. The method therefore enables the measurement of transport properties in a wide range of synthetic quantum systems simulating strongly correlated phases of matter. A promising extension consists in the combination of the non-invasive and the projective scheme in order to measure dynamical current correlations. In the light of our discussion in Chapter 2, this corresponds to a non-Hermitian linear response protocol for measuring unequal-time anti-commutators of currents. In combination with a standard linear response measurement of the corresponding unequal-time commutator, this enables probing FDRs for currents. In addition, unequal-time current correlations encode fundamental transport properties like conductivities [82]. In particular, the outlined scheme may enable the direct measurement of quantum Hall conductivities in Harper–Hofstadter optical-lattice models.

Chapter 4 has been devoted to the investigation of dynamical probes of supersolidity in spin–orbit-coupled Bose–Einstein condensates by exciting the Goldstone modes associated with the spontaneous breaking of translational invariance. We have demonstrated that a beating in the breathing oscillation, induced by a sudden change of the trap frequency, signals the emergence of a Goldstone mode of spin nature once the transition to the supersolid phase is crossed. This effect is a manifestation of the rich hybridization phenomena between density and spin degrees of freedom typical of spin–orbit-coupled

configurations. In addition, we have provided direct and indirect evidence for the existence of the crystal Goldstone mode associated with the translational motion of the stripes, which can be excited by suddenly releasing a uniform spin perturbation. The presented Gross–Pitaevskii simulations demonstrate that the predicted static and dynamic signatures of supersolidity are accessible under realistic experimental conditions in both configurations with symmetric and asymmetric intraspecies interactions, leaving the observation of these effects as a task for upcoming experiments. On the theory side, it will be interesting to extend the analysis of collective oscillations in the supersolid phase to transversal excitations like the scissors mode. In fact, there exists a hybridization mechanism between the quadrupole operator xy exciting the scissors mode and the transversal spin operator $y\sigma_z$ [380], similar to the hybridization of x^2 and $x\sigma_z$ underlying the beating effect discussed in Chapter 4. One may therefore expect to observe an analogous beating in the modes excited by the operators xy and $y\sigma_z$ below the transition to the supersolid phase. In addition, the transversal spin operator $y\sigma_z$ exhibits a nontrivial coupling to the angular momentum, enabling the excitation vortices for strong perturbations [381]. Thus, a promising future research direction is the exploration of transversal excitations in both linear and non-linear regimes in the supersolid phase.

In Chapter 5, we have developed a scenario for quantum-simulating aspects of cosmological reheating dynamics in an ultracold Bose gas. We have demonstrated by means of classical–statistical simulations that the dynamics of a parametrically driven atomic Bose–Einstein condensate undergoes the characteristic stages of far-from-equilibrium reheating, including a preheating phase of explosive particle production through parametric amplification of quantum fluctuations as well as the subsequent stage of turbulent thermalization. The turbulent dynamics is characterized by universal self-similar time evolution in form of a direct cascade transporting energy towards higher momenta. Owing to universality, the proposed setup enables the experimental investigation of far-from-equilibrium quantum dynamics relevant for a large class of physical systems at vastly different energy scale. In addition, the analog reheating scenario opens promising prospects of experimentally observing a prescaling regime of partial universality, which we have shown to emerge at the interface between driven and free turbulence. An experimental implementation is feasible regarding the technical capabilities of modern laboratories and motivated by the possibility to study aspects of the dynamics which are not captured by currently available analytical and numerical methods, such as the final relaxation to thermal equilibrium, which is dominated by quantum fluctuations. Cold-atom quantum simulators are quantum mechanical by nature and not restricted to weak couplings, enabling them to address these problems more efficiently.

While the proposed analog reheating scenario focuses on a generic single-field model of cosmological reheating, there is plenty of room for extensions to more realistic situations. For instance, in models involving a single scalar field, the inflaton decays only into its own quanta of excitation, whereas for consistency with standard cosmology, it should eventually decay into other forms matter, e.g., standard model particles. Such a production of different particle species and their subsequent thermalization dynamics could be simulated in multi-component Bose gases. Furthermore, future studies of analog reheating in three spatial dimensions, where in contrast to the investigated 2D setting

the cosmological scale factor explicitly enters the dynamics, have the potential to reveal effects arising from the competition between thermalization and expansion. While in the proposed implementation the parametric driving mimicking the inflaton oscillations is imposed externally, it is desirable to look for ways that provide a dynamical mechanism of back reaction of the produced excitations on the cause of their creation. A promising approach in this direction has been suggested in Ref. [341], where parametric resonances are triggered by a breathing oscillation of the condensate, allowing the produced quasiparticles to back-react on the oscillating condensate. It would be interesting to explore whether this scenario also enables access to the far-from-equilibrium turbulent thermalization scenario. As these discussions show, the proposed setup provides a solid base that can be extended to develop more complete analog models of cosmological reheating.

In conclusion, the methods and applications presented in this thesis provide a plethora of starting points to fork new lines of research from. These consist primarily in the experimental realization of the introduced techniques, but also in their conceptual refinement and extension to novel applications. We are currently at the threshold where quantum simulators start to unfold their true potential and the years to come are likely to witness new discoveries that today are unimaginable.

Acknowledgments

First of all, I would like to express my gratitude towards my main supervisor Philipp Hauke for his continuous support, inspiration, and motivation throughout my doctoral studies. Many results presented in this thesis would not have been possible if it were not for his brilliant ideas and competent advices across a remarkably wide range of physical disciplines. As a research group leader, he always maintained a friendly relationship to all group members, which made conducting research under his supervision an overall positive experience, in particular on the personal level. In addition, it was my great pleasure to have Markus K. Oberthaler and Jürgen Berges as supervisors before and after the beginning of my cotutelle, respectively, whose valuable inputs on our collaboration projects I appreciated a lot. I am also thankful to José R. Crespo López-Urrutia and Lauriane Chomaz for accepting the role of referees for my thesis and being part of the examination committee.

A special thanks also goes to all of my collaborators. I would like to thank Aleksandr Chatrchyan for a close and fruitful collaboration as well as for introducing me to the previously faraway topic of early universe dynamics, which raised my enthusiasm for analog cosmology. I am grateful to Sandro Stringari for sharing with me his immense expertise on the topics of supersolidity, spin–orbit-coupled Bose gases, and more, as well as for always being available when I needed advice. Furthermore, I would like to thank Giovanni I. Martone for his valuable inputs to our common research project and I regret not having met him in person so far. It was my pleasure to co-supervise Janika Reichstetter during her Bachelor's thesis and I would like to thank her for the continued commitment to the project, which resulted in a fruitful research output. Moreover, I am thankful to Andre Salzinger and the entire Rydberg team led by Matthias Weidemüller for ample enlightening discussions and their unbroken commitment to the experimental implementation of our ideas.

I would like to thank all people who helped me advance with my research through useful discussions, including Zoran Hadzibabic, Maurus Hans, Aleksas Mazeliauskas, Aleksandr N. Mikheev, Julius Mildenberger, Christian-Marcel Schmied, Marius Sparn, Daniel Spitz, Helmut Strobel, Malo Tarpin, Celia Viermann, Torsten V. Zache, Leticia Tarruell, Ramón Ramos, Martin Gärttner, Stefan Lannig, Asier Piñeiro Orioli, and Tilman Esslinger.

A big thanks goes to all people from my research group for the great time we spent together and for maintaining a group spirit despite being scattered across multiple continents during the pandemic. During my time in Heidelberg, I very much enjoyed being part of the Synthetic Quantum Systems collaboration, whose members I share unforgettable memories with. Splitting the time between the KIP and the ITP was not always easy, but I am grateful for also having been nicely integrated in the ITP community,

involving in particular the members of Jürgen Berges' group. Moreover, I am grateful to the people of the BEC Center in Trento for the warm welcome after my arrival there.

I would like to thank all of my friends and the people who accompanied me throughout my PhD studies (and before) for their continuous moral support and being there for me whenever I needed help. A particular thanks goes to Jan Philipp Eberle, Martin Klassen, Maximilian Galm, and Monika Elza Bancsina Mihaly for proofreading parts of my thesis.

Last but not least, it remains to express my infinite gratitude towards my father, who is sadly no longer with us, my mother, my sister, and the rest of my family for their unconditional love, support, and encouragement.

A. Numerical Methods for Stochastic Differential Equations

A.1. Introduction to Stochastic Differential Equations

Langevin's equation for Brownian motion (1.88) can be seen as the historic prototype of a stochastic differential equation (SDE) [382, 383]. Despite the elegance of Langevins's approach, the precise mathematical definition of the stochastic force acting on the Brownian particle, in Langevin's words, the "irregularity of the impacts of the surrounding molecules" [383], has long remained vague. This changed when K. Itô introduced a rigorous mathematical framework for the theory of stochastic integration, now known as Itô stochastic calculus [384]. Ever since, SDEs have been established as indispensable tools in a variety of fields as diverse as statistical physics, molecular biology, climate science, as well as mathematical finance [183, 184].

This appendix contains a brief introduction into the basic concepts and the mathematical foundations of SDEs, before discussing methods for their numerical solution. An emphasis will be put on numerical methods for linear SDEs, which can directly be applied to the solution of stochastic Schrödinger or von Neumann equations, as relevant for the application presented in Section 2.3.3. A comprehensive introduction to the field of SDEs can be found in Ref. [184], where the following overview is based on.

A.1.1. Markov Process

A stochastic process can be thought of as a time-dependent random variable $\boldsymbol{X}(t)$, which takes the values $\boldsymbol{x}_1, \ldots, \boldsymbol{x}_n$ at times $t_1, \ldots, t_n$. Such a system is completely described by the joint probability distribution $p(\boldsymbol{x}_1, t_1; \ldots; \boldsymbol{x}_n, t_n)$. Alternatively, we can consider the conditional probability $p(\boldsymbol{x}_n, t_n \,|\, \boldsymbol{x}_1, t_1; \ldots; \boldsymbol{x}_{n-1}, t_{n-1})$ of measuring the value $\boldsymbol{x}_n$ at time t_n, given the results of all previous measurements. In general, this quantity depends on the entire history of the stochastic process.

We call a process Markovian if the conditional probability depends only on the most recent condition,

$$p(\boldsymbol{x}_n, t_n \,|\, \boldsymbol{x}_1, t_1; \ldots; \boldsymbol{x}_{n-1}, t_{n-1}) = p(\boldsymbol{x}_n, t_n \,|\, \boldsymbol{x}_{n-1}, t_{n-1})\,, \tag{A.1}$$

where $t_1 \leq \ldots \leq t_n$. As a consequence, the joint probability distribution of the entire Markov process can be expressed as

$$p(\boldsymbol{x}_1, t_1; \ldots; \boldsymbol{x}_n, t_n) = p(\boldsymbol{x}_1, t_1) \prod_{i=2}^{n} p(\boldsymbol{x}_i, t_i \,|\, \boldsymbol{x}_{i-1}, t_{i-1})\,, \tag{A.2}$$

where $p(\boldsymbol{x}_1, t_1)$ describes the initial distribution. The sequence of outcomes $\boldsymbol{x}_1, \dots, \boldsymbol{x}_n$ then forms a so-called Markov chain, which is completely determined by the transition probability $p(\boldsymbol{x}_i, t_i \mid \boldsymbol{x}_{i-1}, t_{i-1})$ from the current outcome to the next.

In the context of SDEs, we are interested in Markov processes with continuous sample paths. The time evolution of the probability density is then described by the Fokker–Planck equation

$$\frac{\partial}{\partial t} p(\boldsymbol{x}, t) = -\sum_i \frac{\partial}{\partial x_i} [A_i(\boldsymbol{x}, t) p(\boldsymbol{x}, t)] + \frac{1}{2} \sum_{i,j} \frac{\partial^2}{\partial x_i \partial x_j} \left[B_{ij}(\boldsymbol{x}, t) p(\boldsymbol{x}, t) \right], \tag{A.3}$$

where $p(\boldsymbol{x}, t) \equiv p(\boldsymbol{x}, t \mid \boldsymbol{x}_0, t_0)$ with initial condition $p(\boldsymbol{x}, t_0) = p_0(\boldsymbol{x})$. The drift vector $\boldsymbol{A}(\boldsymbol{x}, t)$ and the diffusion matrix $B(\boldsymbol{x}, t)$ determine the Markov process completely. The significance of these quantities will become more transparent in the context of SDEs.

Wiener Process

The Wiener process, sometimes simply referred to as Brownian motion, is of fundamental importance in the theory of SDEs. It describes a diffusion process and can be thought of as the continuum limit of a random walk. The multivariate Wiener process $\boldsymbol{W}(t) = [W_1(t), \dots, W_d(t)]^\top$ can be defined via its conditional probability density $p(\boldsymbol{w}, t \mid \boldsymbol{w}_0, t_0)$, which satisfies the Fokker–Planck equation

$$\frac{\partial}{\partial t} p(\boldsymbol{w}, t \mid \boldsymbol{w}_0, t_0) = \frac{1}{2} \sum_i \frac{\partial^2}{\partial w_i^2} p(\boldsymbol{w}, t \mid \boldsymbol{w}_0, t_0) \tag{A.4}$$

with initial condition $p(\boldsymbol{w}, t_0 \mid \boldsymbol{w}_0, t_0) = \delta(\boldsymbol{w} - \boldsymbol{w}_0)$. The solution is given by the multivariate Gaussian distribution

$$p(\boldsymbol{w}, t \mid \boldsymbol{w}_0, t_0) = \frac{1}{[2\pi(t - t_0)]^{n/2}} \exp\left[-\frac{(\boldsymbol{w} - \boldsymbol{w}_0)^2}{2(t - t_0)} \right], \tag{A.5}$$

whose first and second moments read

$$\langle\!\langle \boldsymbol{W}(t) \rangle\!\rangle = \boldsymbol{w}_0 \,, \tag{A.6a}$$

$$\langle\!\langle [W_i(t) - w_{0i}][W_j(t) - w_{0j}] \rangle\!\rangle = \delta_{ij}(t - t_0) \,. \tag{A.6b}$$

Since the variance grows linearly with time, the Wiener process is characterized by highly irregular sample paths. Furthermore, the sample paths are continuous, but not differentiable. If we sample the Wiener process at discrete times $t_1, \dots, t_n$, then, by virtue of Eq. (A.2), the increments $\Delta W_i = W(t_i) - W(t_{i-1})$ are statistically independent,

$$p(w_0; \Delta w_1, \dots, \Delta w_n) = p(w_0, t_0) \prod_{i=1}^{n} \frac{1}{\sqrt{2\pi \Delta t_i}} \mathrm{e}^{-\Delta w_i^2 / 2\Delta t_i} \,, \tag{A.7}$$

where $\Delta t_i = t_i - t_{i-1}$. The statistical independence of the Wiener increments is crucial in the context of SDEs.

A.1.2. Stochastic Integration

In order to define SDEs, it is necessary to introduce the notion of stochastic integration, i.e., integration with respect to Brownian motion.

To this end, let $t_0 \leq t_1 \leq ... \leq t_n \equiv t$ be a partition of the interval $[t_0, t]$ into n subintervals. For a given sample path $W(t)$ of the Wiener process and an arbitrary function $G(t)$, we consider the partial sum

$$S_n = \sum_{i=1}^{n} G(\tau_i)[W(t_i) - W(t_{i-1})] \tag{A.8}$$

with intermediate points $\tau_i \in [t_{i-1}, t_i]$. If $W(t)$ were a function of bounded variation, we would recover the Riemann–Stieltjes integral in the limit $n \to \infty$ (for continuous G). As is well-known, the Riemann–Stieltjes integral is independent of the intermediate values τ_i. However, for the Wiener process $W(t)$, whose sample paths are *not* of bounded variation, it turns out that different choices of τ_i lead to different limits of S_n. The most common choices in the literature correspond to evaluating the function G at the left point of each subinterval ($\tau_i = t_{i-1}$) or in the middle of each subinterval [$\tau_i = (t_{i-1} + t_i)/2$], which lead to the Itô and Stratonovich definition of the stochastic integral, respectively.

Itô Stochastic Integral

The Itô stochastic integral of a function $G(t)$ with respect to the Wiener process $W(t)$ is defined as

$$\int_{t_0}^{t} G(t')\,\mathrm{d}W(t') = \lim_{n\to\infty} \sum_{i=1}^{n} G(t_{i-1})[W(t_i) - W(t_{i-1})]\,. \tag{A.9}$$

Here, convergence is to be understood in mean square, i.e., $\lim_{n\to\infty} \langle\!\langle (S_n - I)^2 \rangle\!\rangle = 0$, where I denotes the value of the Itô integral and S_n the n-th partial sum. Note that the integrand $G(t)$ is evaluated at the left boundary of each subinterval. This choice by Itô leads to a couple of useful properties.

It can be shown that the Itô integral exists if $G(t)$ is continuous and non-anticipating. A function G is called non-anticipating of t if $G(t)$ is statistically independent of $W(s) - W(t)$ for all $s > t$, i.e., if it is independent of the behavior of the Wiener process in the future of t. From the definition (A.9), it is then immediately clear that for such a function G the expectation value of the Itô stochastic integral vanishes,

$$\left\langle\!\!\left\langle \int_{t_0}^{t} G(t')\,\mathrm{d}W(t') \right\rangle\!\!\right\rangle = \int_{t_0}^{t} \langle\!\langle G(t') \rangle\!\rangle \langle\!\langle \mathrm{d}W(t') \rangle\!\rangle = 0\,. \tag{A.10}$$

Likewise, for two non-anticipating functions G and H, one finds the correlation formula

$$\left\langle\!\!\left\langle \int_{t_0}^{t} G(t')\,\mathrm{d}W(t') \int_{t_0}^{t} H(t'')\,\mathrm{d}W(t'') \right\rangle\!\!\right\rangle = \int_{t_0}^{t} \mathrm{d}t'\, \langle\!\langle G(t')H(t') \rangle\!\rangle\,. \tag{A.11}$$

In the physical literature, it is common to write the Wiener increments symbolically as $\mathrm{d}W(t) = \xi(t)\,\mathrm{d}t$, where $\xi(t)$ represents Gaussian white noise and formally plays the role of the "derivative" of the Wiener process (which rigorously does not exist though). The condition (A.11) is then implied by the requirement that the noise is delta-correlated, $\langle\!\langle \xi(t)\xi(t') \rangle\!\rangle = \delta(t-t')$. A useful rule for practical computations is encoded in the relation

$$\int_{t_0}^{t} G(t')[\mathrm{d}W(t')]^2 = \int_{t_0}^{t} \mathrm{d}t' G(t')\,, \tag{A.12}$$

which is often used in the form $\mathrm{d}W^2 = \mathrm{d}t$ when calculating differentials of non-anticipating functions (see Itô formula below).

Stratonovich Stochastic Integral

As noted above, Stratonovich's stochastic integral corresponds to choosing the intermediate points in Eq. (A.8) as the midpoints of each subinterval. In the context of SDEs, we will be dealing with Stratonovich integrals of functions of two variables in the form $G[x(t), t]$. For mathematical reasons of convergence, in this case the definition slightly differs from the naive expectation. The Stratonovich integral of a function $G[x(t), t]$ is defined as

$$\int_{t_0}^{t} G[x(t'), t'] \circ \mathrm{d}W(t') = \lim_{n\to\infty} \sum_{i=1}^{n} G\left[\frac{x(t_{i-1}) + x(t_i)}{2}, t_{i-1}\right][W(t_i) - W(t_{i-1})]\,. \tag{A.13}$$

Here, the limit again corresponds to the mean-square limit and the notation $\circ\,\mathrm{d}W$ is used to distinguish the Stratonovich integral from the Itô definition (A.9). For simpler integrands of the form $G[x(t), t] = x(t)$, the above definition is equivalent to evaluating the integrand at the midpoints of the subintervals $[t_{i-1}, t_i]$, provided the function $x(t)$ is sufficiently smooth such that $x[(t_{i-1} + t_i)/2] \approx [x(t_{i-1}) + x(t_i)]/2$.

The Stratonovich integral is constructed such that it obeys the rules of ordinary calculus. We will make this statement more precise in the context of SDEs. As a consequence of Stratonovich's definition, the mean and correlation formulas Eqs. (A.10) and (A.11) do not hold for Stratonovich integrals since the integrand and the Wiener increments are no longer statistically independent at equal times. Intuitively, the Stratonovich integral retains some memory about the Wiener process during a time step, while the Itô integral does not. From a physical point of few, the Stratonovich interpretation is thus often more natural since physical noise processes always have a finite correlation time (see Appendix A.2).

We now have all main ingredients at hand to introduce both the Itô and Stratonovich form of SDEs and discuss how these two interpretations are related.

A.1.3. Itô Stochastic Differential Equations

A stochastic process $x(t)$ obeys an Itô SDE, written as

$$\mathrm{d}x(t) = a[x(t), t]\,\mathrm{d}t + b[x(t), t]\,\mathrm{d}W(t)\,, \tag{A.14}$$

if it satisfies for all t and t_0 the integral equation

$$x(t) = x(t_0) + \int_{t_0}^{t} \mathrm{d}t'\, a[x(t'), t'] + \int_{t_0}^{t} \mathrm{d}W(t')\, b[x(t'), t']\,. \tag{A.15}$$

The drift coefficient $a[x(t), t]$ characterizes the deterministic part of the SDE, while the stochastic part is described by the diffusion coefficient $b[x(t), t]$. Existence and uniqueness of solutions to Eq. (A.14) can be shown similarly as in the theory of ordinary differential equations (ODEs) by assuming suitable Lipschitz and growth conditions for the coefficient functions. The solution $x(t)$ of an Itô SDE is also a Markov process. Crucially, $x(t)$ is a non-anticipating function, to which the rules in Appendix A.1.2 apply.

We can now derive Itô's formula for the change of variables, which is also known as the stochastic chain rule. To this end, we compute the differential of a function $f[x(t)]$:

$$\begin{aligned} \mathrm{d}f[x(t)] &= f[x(t) + \mathrm{d}x(t)] - f[x(t)] = f'[x(t)]\,\mathrm{d}x(t) + \frac{1}{2} f''[x(t)]\,\mathrm{d}x(t)^2 + \ldots \\ &= \left\{ a[x(t), t] f'[x(t)] + \frac{1}{2} b^2[x(t), t] f''[x(t)] \right\} \mathrm{d}t + b[x(t), t] f'[x(t)]\,\mathrm{d}W(t)\,. \end{aligned} \tag{A.16}$$

The last line follows by using the SDE (A.14) and the rule $\mathrm{d}W^2 = \mathrm{d}t$ [see Eq. (A.12)], as well as the fact that all other higher-order differentials $\mathrm{d}t^2$, $\mathrm{d}t\,\mathrm{d}W$, etc. vanish. The appearance of the second-order derivative as a consequence of $\mathrm{d}W^2 = \mathrm{d}t$ is what deeply distinguishes Itô calculus from ordinary calculus.

A system of Itô SDEs for a d-dimensional stochastic vector $\boldsymbol{x}(t)$ and an m-dimensional Wiener process $\boldsymbol{W}(t)$ can be written as

$$\mathrm{d}\boldsymbol{x}(t) = \boldsymbol{A}(\boldsymbol{x}, t)\,\mathrm{d}t + B(\boldsymbol{x}, t)\,\mathrm{d}\boldsymbol{W}(t)\,, \tag{A.17}$$

where $\boldsymbol{A}(\boldsymbol{x}, t)$ is the d-dimensional drift vector and $B(\boldsymbol{x}, t)$ is the diffusion matrix of dimensions $d \times m$. Then, using $\mathrm{d}W_i\,\mathrm{d}W_j = \delta_{ij}\,\mathrm{d}t$, the Itô formula generalizes to

$$\begin{aligned} \mathrm{d}f(\boldsymbol{x}) = &\left\{ \sum_i A_i(\boldsymbol{x}, t) \partial_i f(\boldsymbol{x}) + \frac{1}{2} \sum_{i,j} \left[B(\boldsymbol{x}, t) B^{\top}(\boldsymbol{x}, t) \right]_{ij} \partial_i \partial_j f(\boldsymbol{x}) \right\} \mathrm{d}t \\ &+ \sum_{i,j} B_{ij}(\boldsymbol{x}, t) \partial_i f(\boldsymbol{x})\,\mathrm{d}W_j(t)\,. \end{aligned} \tag{A.18}$$

This result can be used to establish a connection between SDEs and Fokker–Planck equations. The former describe the time evolution of individual realizations of a stochastic process $\boldsymbol{x}(t)$, while the latter determine the evolution of the corresponding conditional probability density $p(\boldsymbol{x}, t \mid \boldsymbol{x}_0, t)$. To see how these descriptions are connected, we consider the time evolution of the expectation value of an arbitrary function $f[\boldsymbol{x}(t)]$, which

can be expressed as

$$\begin{aligned}\frac{\mathrm{d}}{\mathrm{d}t}\langle\!\langle f[\boldsymbol{x}(t)]\rangle\!\rangle &= \int \mathrm{d}\boldsymbol{x}\, f(\boldsymbol{x})\frac{\partial}{\partial t}p(\boldsymbol{x},t\mid\boldsymbol{x}_0,t_0)\\ &= \int \mathrm{d}\boldsymbol{x}\left\{\sum_i A_i(\boldsymbol{x},t)\partial_i f(\boldsymbol{x}) + \frac{1}{2}\sum_{i,j}\bigl[B(\boldsymbol{x},t)B^\top(\boldsymbol{x},t)\bigr]_{ij}\partial_i\partial_j f(\boldsymbol{x})\right\}p(\boldsymbol{x},t\mid\boldsymbol{x}_0,t_0)\,.\end{aligned} \tag{A.19}$$

The first line uses the definition of the expectation value, while the second line is directly obtained by taking the expectation value of Itô's formula (A.18). Then, after integration by parts, assuming that the boundary terms vanish, we find that the conditional probability density must satisfy the Fokker–Planck equation

$$\frac{\partial}{\partial t}p(\boldsymbol{x},t) = -\sum_i \frac{\partial}{\partial x_i}[A_i(\boldsymbol{x},t)p(\boldsymbol{x},t)] + \frac{1}{2}\sum_{i,j}\frac{\partial^2}{\partial x_i\partial x_j}\Bigl\{\bigl[B(\boldsymbol{x},t)B^\top(\boldsymbol{x},t)\bigr]_{ij}p(\boldsymbol{x},t)\Bigr\}\,. \tag{A.20}$$

Thus, the Itô SDE (A.14) is completely equivalent to the Fokker–Planck equation (A.3) with drift vector $\boldsymbol{A}(\boldsymbol{x},t)$ and diffusion matrix $B(\boldsymbol{x},t)B^\top(\boldsymbol{x},t)$.

A.1.4. Stratonovich Stochastic Differential Equations

We have seen that the Itô SDE (A.14) is defined in terms of the corresponding integral equation (A.15) involving the Itô stochastic integral. Alternatively, we may also use the Stratonovich interpretation. That is, $\boldsymbol{x}(t)$ is a solution of the Stratonovich SDE

$$\mathrm{d}\boldsymbol{x}(t) = \underline{\boldsymbol{A}}(\boldsymbol{x},t)\,\mathrm{d}t + B(\boldsymbol{x},t)\circ\mathrm{d}\boldsymbol{W}(t) \tag{A.21}$$

if it satisfies for all t and t_0 the integral equation

$$\boldsymbol{x}(t) = \boldsymbol{x}(t_0) + \int_{t_0}^{t}\mathrm{d}t'\,\underline{\boldsymbol{A}}[\boldsymbol{x}(t'),t'] + \int_{t_0}^{t}B[\boldsymbol{x}(t'),t']\circ\mathrm{d}\boldsymbol{W}(t')\,, \tag{A.22}$$

where the underbar distinguishes the drift vector of a Stratonovich SDE from that of an Itô SDE and the circle in the stochastic part indicates the use of Stratonovich integration.

It can be shown that the Stratonovich SDE (A.21) is equivalent to the Itô SDE (A.17) with the same diffusion matrix $B(\boldsymbol{x},t)$, but a modified drift vector

$$A_i(\boldsymbol{x},t) = \underline{A}_i(\boldsymbol{x},t) + \frac{1}{2}\sum_{j=1}^{m}\sum_{k=1}^{d}B_{kj}(\boldsymbol{x},t)\partial_k B_{ij}(\boldsymbol{x},t)\,. \tag{A.23}$$

The extra contribution to the drift term is sometimes called a noise-induced drift. This formula permits the conversion between SDEs in Itô and Stratonovich form depending on which formulation is more convenient for a certain application. Remarkably, in the case of additive noise, where the diffusion matrix does not depend on the solution $\boldsymbol{x}(t)$,

$B(\boldsymbol{x},t) \equiv B(t)$, the Itô and Stratonovich interpretations give the same answer. According to Eq. (A.23), the difference between Itô and Stratonovich SDEs arises only for multiplicative noise, where B depends on the solution $\boldsymbol{x}(t)$.

The Fokker–Planck equation corresponding to the Stratonovich SDE (A.21) can be written in the form

$$\frac{\partial}{\partial t}p(\boldsymbol{x},t) = -\sum_i \frac{\partial}{\partial x_i}[A_i(\boldsymbol{x},t)p(\boldsymbol{x},t)] + \frac{1}{2}\sum_{i,j,k}\frac{\partial}{\partial x_i}\Big\{B_{ij}(\boldsymbol{x},t)\frac{\partial}{\partial x_k}\big[B_{kj}(\boldsymbol{x},t)p(\boldsymbol{x},t)\big]\Big\}. \tag{A.24}$$

Using the conversion formula between Itô and Stratonovich SDEs (A.23) as well as the Itô formula for the change of variables (A.18), it can be shown that in the Stratonovich case the same rules as in ordinary calculus apply.

When modeling real systems by SDEs, the natural question arises whether to choose the Itô or Stratonovich interpretation. While the "right" choice varies between different applications, physical systems where the stochastic description arises as the white-noise idealization of a noise process with finite correlation time are usually described by Stratonovich SDEs. One reason for this is that in most realistic physical systems the noise process actually corresponds to an effective description of a rapidly fluctuating, yet smoothly varying variable, e.g., an electric field. The "true" physical system naturally obeys ordinary calculus and so should the effective stochastic description, which requires the Stratonovich interpretation. In the next section, we will illustrate this at the example of a quantum mechanical two-level system subject to frequency noise.

A.2. Example: Qubit Subject to Frequency Noise

As an instructive example of relevance for the applications presented in Section 2.3.3, we consider a two-level quantum system (qubit) subject to frequency noise. We will show that for each noise realization, the system evolves unitarily under a stochastic Schrödinger equation in Stratonovich form, while the ensemble average over all noise realizations obeys a Lindblad master equation.

For concreteness, we take the qubit states to be the ground state $|g\rangle$ and excited state $|e\rangle$ of an atom. The Hamiltonian of a two-level atom coupled to a classical electric field $E(t) = E_0 \cos\phi(t)$ in the rotating wave approximation is given by

$$H(t) = \hbar\omega_0|e\rangle\langle e| + \frac{\hbar\Omega}{2}\big(\mathrm{e}^{i\phi(t)}|g\rangle\langle e| + \mathrm{e}^{-i\phi(t)}|e\rangle\langle g|\big), \tag{A.25}$$

where ω_0 is the atomic transition frequency, Ω is the Rabi frequency (proportional to E_0), and $\phi(t) = \int_{t_0}^{t} \mathrm{d}t'\,\omega(t')$ is the phase of the light field with instantaneous frequency $\omega(t)$.

We can transform a state $|\psi(t)\rangle$ to a rotating frame via a unitary transformation $U(t)$ as $|\psi_I(t)\rangle = U(t)|\psi(t)\rangle$. The interaction picture Hamiltonian is then given by $H_I = UHU^\dagger + i\hbar(\partial_t U)U^\dagger$. The choice

$$U(t) = \exp\big\{i\varphi_g(t)|g\rangle\langle g| + i\varphi_e(t)|e\rangle\langle e|\big\} \tag{A.26}$$

with

$$\varphi_g(t) = \frac{\omega_0(t-t_0) - \phi(t)}{2} \quad \text{and} \quad \varphi_e(t) = \frac{\omega_0(t-t_0) + \phi(t)}{2} \tag{A.27}$$

leads to

$$H_I(t) = \frac{\hbar\Delta(t)}{2}\sigma_z + \frac{\hbar\Omega}{2}\sigma_x\,, \tag{A.28}$$

where $\sigma_z = |g\rangle\langle g| - |e\rangle\langle e|$, $\sigma_x = |g\rangle\langle e| + |e\rangle\langle g|$, and $\Delta(t) = \dot{\phi}(t) - \omega_0$ is a time-dependent detuning.

Consider now a monochromatic laser field of frequency ω_L subject to Gaussian white noise $\xi(t)$ with $\langle\!\langle \xi(t) \rangle\!\rangle = 0$ and $\langle\!\langle \xi(t)\xi(t') \rangle\!\rangle = \delta(t-t')$, i.e., $\omega(t) = \omega_\mathrm{L} + \sqrt{\kappa}\xi(t)$. The noise process $\xi(t)$ may be considered as the white-noise idealization of a physical colored noise process with a spectrum that is approximately flat for all relevant frequency scales in the system. As will become clear further below, κ plays the role of a dephasing rate. The phase of the electric field then becomes

$$\phi(t) = \omega_\mathrm{L}(t-t_0) + \sqrt{\kappa}[W(t) - W(t_0)]\,, \tag{A.29}$$

where $W(t)$ is a Wiener process (Brownian motion). That is, the phase of the electric field performs a random walk subject to a constant drift determined by the carrier frequency ω_L.

The Schrödinger equation in the rotating frame thus becomes an SDE,

$$i\hbar\,\mathrm{d}|\psi(t)\rangle = H_0|\psi(t)\rangle\,\mathrm{d}t + \hbar\sqrt{\kappa}\sigma_z|\psi(t)\rangle \circ \mathrm{d}W(t)\,, \tag{A.30}$$

where $H_0 = \hbar\Delta\sigma_z/2 + \hbar\Omega\sigma_x/2$ is the deterministic Hamiltonian with detuning $\Delta = \omega_\mathrm{L} - \omega_0$. We will now argue that the Stratonovich interpretation is the correct one to use in this scenario.

Let us assume the Stratonovich interpretation for Eq. (A.30) and transform this equation to an Itô SDE via the Itô–Stratonovich conversion formula (A.23), yielding

$$\mathrm{d}|\psi(t)\rangle = \left(-\frac{i}{\hbar}H_0 - \frac{\kappa}{2}\sigma_z^2\right)|\psi(t)\rangle\,\mathrm{d}t + \hbar\sqrt{\kappa}\sigma_z|\psi(t)\rangle\,\mathrm{d}W(t)\,. \tag{A.31}$$

Since the solution to an Itô SDE is non-anticipating, the state $|\psi(t)\rangle$ and the Wiener increment $\mathrm{d}W(t)$ are uncorrelated at equal times. We may therefore take the noise average of the above equation,

$$\mathrm{d}\langle\!\langle |\psi(t)\rangle \rangle\!\rangle = \left(-\frac{i}{\hbar}H_0 - \frac{\kappa}{2}\sigma_z^2\right)\langle\!\langle |\psi(t)\rangle \rangle\!\rangle\,\mathrm{d}t\,, \tag{A.32}$$

with solution $\langle\!\langle |\psi(t)\rangle \rangle\!\rangle = \mathrm{e}^{-\kappa t/2}\mathrm{e}^{-iH_0t/\hbar}|\psi_0\rangle$. Although this average probability amplitude is not a physically useful observable, the exponential decay of this quantity reflects the dephasing of different realizations due to the frequency noise and is intuitively expected. In contrast, by interpreting Eq. (A.30) as an Itô SDE, we would obtain $\langle\!\langle |\psi(t)\rangle \rangle\!\rangle = \mathrm{e}^{-iH_0t/\hbar}|\psi_0\rangle$ and the effect of dephasing would be absent.

Physically relevant observables are generally quadratic in the state. To this end, we consider the time evolution of the expectation value of an observable O. By virtue of Itô's formula (A.16), using $\mathrm{d}W^2 = \mathrm{d}t$, one easily finds

$$\begin{aligned}\mathrm{d}\langle\psi(t)|O|\psi(t)\rangle &= (\mathrm{d}\langle\psi(t)|)O|\psi(t)\rangle + \langle\psi(t)|O(\mathrm{d}|\psi(t)\rangle) + (\mathrm{d}\langle\psi(t)|)O(\mathrm{d}|\psi(t)\rangle) \\ &= \langle\psi(t)|\Big(\frac{i}{\hbar}[H_0, O] + \kappa\Big[\sigma_z O\sigma_z - \frac{1}{2}\{\sigma_z^2, O\}\Big]\Big)|\psi(t)\rangle\,\mathrm{d}t \\ &\quad + \langle\psi(t)|(i\sqrt{\kappa}[\sigma_z, O])|\psi(t)\rangle\,\mathrm{d}W(t)\,.\end{aligned} \tag{A.33}$$

For $O = \mathbb{1}$, this equation describes the change of the norm of the state. In fact, we have $\mathrm{d}\langle\psi|\psi\rangle = 0$, i.e., the state evolves unitarily on the stochastic level. If we had not started from the Stratonovich interpretation, but used the Itô one, the anti-commutator term $\{\sigma_z^2, O\}$ would be missing in Eq. (A.33). We would then find $\mathrm{d}\langle\psi|\psi\rangle = \kappa\langle\psi|\psi\rangle\,\mathrm{d}t$, implying an unphysical exponential growth of the norm of the state. Consequently, demanding unitary time evolution for each stochastic realization requires the Stratonovich interpretation of Eq. (A.30).

After taking the ensemble average of Eq. (A.33), the deterministic part can be rewritten as

$$\mathrm{d}\,\mathrm{Tr}[O\rho(t)] = \mathrm{Tr}\Big(-\frac{i}{\hbar}[H_0, \rho(t)] + \kappa\Big[\sigma_z\rho(t)\sigma_z - \frac{1}{2}\{\sigma_z^2, \rho(t)\}\Big]\Big)\,, \tag{A.34}$$

where $\rho(t) = \langle\!\langle|\psi(t)\rangle\langle\psi(t)|\rangle\!\rangle$ is the noise-averaged density operator. Since the observable O is arbitrary, this implies that $\rho(t)$ obeys the Lindblad master equation

$$\dot{\rho}(t) = -\frac{i}{\hbar}[H_0, \rho(t)] + \kappa\Big(L\rho(t)L^\dagger - \frac{1}{2}\{L^\dagger L, \rho(t)\}\Big) \tag{A.35}$$

with the Hermitian Lindblad operator $L = L^\dagger = \sigma_z$. Of course, this result could have been directly obtained by applying the Itô formula to the stochastic density matrix $|\psi(t)\rangle\langle\psi(t)|$ and then taking the ensemble average.

A.3. Numerical Solution of Stochastic Differential Equations

There exists a vast number of accurate, robust, and efficient numerical methods for integrating ODEs [385]. Although many approaches can also be applied to their stochastic counterparts, the numerical solution of SDEs is in general much more demanding. In particular, higher-order general-purpose integrators for SDEs are difficult to construct and available schemes are often restricted to a certain class of problems with a special structure. In what follows, after briefly reviewing basic integration schemes for general SDEs, we will discuss higher-order Taylor methods as well as Magnus integrators for linear SDEs, relevant for the applications discussed in Chapter 2. A comprehensive overview of numerical methods for SDEs can be found in Ref. [183], where large parts of this section are based upon.

Weak and Strong Convergence

Before considering concrete schemes, we introduce the notion of weak and strong convergence of approximations to solutions of SDEs.

Strong convergence means that the approximation converges path-wise to the solution. Let $x(t)$ be the solution of an SDE (in either Ito or Stratonovich form) for a given sample path $W(t)$ of the Wiener process and denote by $y_{\Delta t}(t)$ a time discrete approximation of $x(t)$ with (maximum) time step size Δt. Then, the approximation $y_{\Delta t}(t)$ converges strongly with order $\gamma > 0$ to the solution $x(t)$ at time t if [183]

$$\langle\!\langle \| x(t) - y_{\Delta t}(t) \| \rangle\!\rangle = \mathcal{O}(\Delta t^{\gamma}) \,. \tag{A.36}$$

In the deterministic case, the left-hand side is known as the global truncation error.

In some applications, one is only interested in approximating the moments of the solution $\langle\!\langle x^p(t) \rangle\!\rangle$ rather than individual trajectories. In this case, the convergence conditions for a numerical approximation can be relaxed, which leads to the notion of weak convergence. The time discrete approximation $y_{\Delta t}(t)$ with (maximum) time step size Δt converges weakly with order $\beta > 0$ to the solution $x(t)$ at time t if [183]

$$\| \langle\!\langle g[x(t)] \rangle\!\rangle - \langle\!\langle g[y_{\Delta t}(t)] \rangle\!\rangle \| = \mathcal{O}(\Delta t^{\beta}) \,, \tag{A.37}$$

for all functions g within a suitable function space, which, for simplicity, we take as the space of all polynomials. Thus, weak convergence of a numerical approximation implies the convergence of all moments at weak order β.

Strong convergence at order γ implies weak convergence at order $\beta \geq \gamma$. In general, both the weak and strong convergence order of a numerical scheme for SDEs are less than or equal to the deterministic convergence order of its counterpart for ODEs.

A.3.1. Euler–Maruyama Scheme

The simplest scheme for integrating the Itô SDE (A.17) is obtained by discretizing the Itô stochastic integral in a straightforward way via the partial sums in the definition (A.9). This leads to the so-called Euler–Maruyama scheme (or simply Euler scheme), which for a d-dimensional system with an m-component Wiener process reads [183]

$$\boldsymbol{y}_{n+1} = \boldsymbol{y}_n + \boldsymbol{A}(\boldsymbol{y}_n, t_n)\Delta t_n + B(\boldsymbol{y}_n, t_n)\Delta \boldsymbol{W}_n \,. \tag{A.38}$$

Here, $\boldsymbol{y}_n = \boldsymbol{y}(t_n)$ represents the approximate solution at time t_n with given initial value $\boldsymbol{y}_0$, $\Delta t_n = t_{n+1} - t_n$ is the time step size (which from now on we assume to be the same for all time steps), and $\Delta \boldsymbol{W}_n = \boldsymbol{W}(t_{n+1}) - \boldsymbol{W}(t_n)$ is the vector of Wiener increments.

The Wiener increments can be sampled as independent Gaussian random variables of zero mean and variance Δt for each component and at each time step (see Appendix A.1.1). The sum of the Wiener increments then yields a discretized sample path of the Wiener process, $\boldsymbol{W}(t_n) = \sum_{i=1}^{n} \Delta \boldsymbol{W}_i$, with $\boldsymbol{W}(t_0) = 0$. To compare strong approximations at different time step sizes, e.g., for adaptive step size control, it is

often necessary to refine an existing Brownian path in a consistent way. This can be achieved by sampling the Wiener process at a finer step size to begin with or by sampling intermediate values according to

$$\boldsymbol{W}\left(t_{n+\frac{1}{2}}\right) = \boldsymbol{W}(t_n) + \frac{1}{2}\Delta\boldsymbol{W}_n + \frac{\sqrt{\Delta t}}{2}\boldsymbol{z}\,, \tag{A.39}$$

where $\boldsymbol{z}$ is a vector of independent standard Gaussian random variables [386].

It can be shown that the Euler scheme generally converges with strong order $\gamma = 0.5$ and weak order $\beta = 1$. The advantage of the Euler scheme is its simplicity and the fact that it works for any Itô SDE of any noise type. On the downside, due to the low order of convergence, the scheme is not very efficient, especially if accurate strong solutions are sought. In addition, as is well-known for ODEs, the explicit Euler scheme suffers from numerical stability issues for stiff problems, which can only be avoided by choosing a very small time step up to the point that computation becomes unfeasible.

A.3.2. Milstein Scheme

By virtue of stochastic Taylor expansion, it is possible to derive higher-order schemes. To this end, we consider the integral version of Itô's formula (A.18) in the multi-dimensional case [183],

$$f[\boldsymbol{x}(t),t] - f[\boldsymbol{x}(t_0),t_0] = \int_{t_0}^{t} \mathrm{d}t'\, L^0 f[\boldsymbol{x}(t'),t'] + \sum_{j=1}^{m}\int_{t_0}^{t} \mathrm{d}W^j(t)\, L^j f[\boldsymbol{x}(t'),t'] \tag{A.40}$$

with the definitions

$$L^0 = \frac{\partial}{\partial t} + \sum_{k=1}^{d} a\frac{\partial}{\partial x_k} + \frac{1}{2}\sum_{k,l=1}^{d}\sum_{j=1}^{m} b^{k,j}b^{l,j}\frac{\partial^2}{\partial x_k \partial x_l}\,, \tag{A.41a}$$

$$L^j = \sum_{k=1}^{d} b^{k,j}\frac{\partial}{\partial x_k}\,, \tag{A.41b}$$

where for brevity we have omitted the arguments of the coefficient functions[1] $a[\boldsymbol{x}(t),t]$ and $b[\boldsymbol{x}(t),t]$. The stochastic Taylor expansion of the solution to an Itô SDE follows by iteratively applying Itô's formula in the form (A.16) to the coefficient functions $a[\boldsymbol{x}(t),t]$ and $b[\boldsymbol{x}(t),t]$ in the intergral equation (A.15). Keeping only terms up to first order in $\Delta t = t - t_0$ (which includes single and double stochastic integrals since $\mathrm{d}W^2 = \mathrm{d}t$), we arrive at

$$x_t^k = x_{t_0}^k + a_{t_0}^k\int_{t_0}^{t}\mathrm{d}t' + \sum_{j=1}^{m} b_{t_0}^{k,j}\int_{t_0}^{t}\mathrm{d}W_{t'} + \sum_{j_1,j_2=1}^{m} L^{j_1}b_{t_0}^{k,j_2}\int_{t_0}^{t}\int_{t_0}^{t'}\mathrm{d}W_{t''}^{j_1}\,\mathrm{d}W_{t'}^{j_2} + \mathcal{O}(\Delta t^{3/2})\,, \tag{A.42}$$

[1] In this section, we use lower-case letters to denote the coefficient functions of SDEs for a consistent notation with Ref. [183].

where we have written time arguments as subscripts for conciseness. This Taylor expansion to first order in Δt immediately yields the famous Milstein scheme

$$y_{n+1}^k = y_n^k + a^k \Delta t + \sum_{j=1}^{m} b^{k,j} \Delta W^j + \sum_{j_1,j_2=1}^{m} L^{j_1} b^{k,j_2} I_{(j_1,j_2)} \,, \tag{A.43}$$

where $I_{(j_1,j_2)}$ denotes the double Itô integral appearing in Eq. (A.42). For $j_1 = j_2$, the double Itô integrals can generally be computed as [183]

$$I_{(j,j)} = \frac{1}{2}\left[(\Delta W^j)^2 - \Delta t\right] . \tag{A.44}$$

Unfortunately, for $j_1 \neq j_2$, the quantity $I_{(j_1,j_2)}$ cannot simply be expressed in terms of Wiener increments and must be approximated otherwise, e.g., using truncated Fourier series [183]. However, if the noise is commutative, i.e., if it fulfills the commutativity condition

$$L^{j_1} b^{k,j_2} = L^{j_2} b^{k,j_1} \,, \tag{A.45}$$

one can use the relation $I_{(j_1,j_2)} + I_{(j_2,j_1)} = \Delta W^{j_1} \Delta W^{j_2}$ [183] such that the Milstein scheme simplifies to

$$y_{n+1}^k = y_n^k + a^k \Delta t + \sum_{j=1}^{m} b^{k,j} \Delta W^j + \frac{1}{2} \sum_{j_1,j_2=1}^{m} L^{j_1} b^{k,j_2} \left(W^{j_1} \Delta W^{j_2} - \delta_{j_1 j_2} \Delta t \right) . \tag{A.46}$$

A similar procedure can be applied to derive Taylor schemes for Stratonovich SDEs. If $\boldsymbol{x}(t)$ is a solution to the Stratonovich SDE (A.21), the formula for the change of variable takes a similar form as in Eq. (A.40) [183],

$$f[\boldsymbol{x}(t), t] - f[\boldsymbol{x}(t_0), t_0] = \int_{t_0}^{t} \mathrm{d}t' \, \underline{L}^0 f[\boldsymbol{x}(t'), t'] + \sum_{j=1}^{m} \int_{t_0}^{t} \circ \, \mathrm{d}W^j(t) \, \underline{L}^j f[\boldsymbol{x}(t'), t'] \tag{A.47}$$

with

$$\underline{L}^0 = \frac{\partial}{\partial t} + \sum_{k=1}^{d} \underline{a} \frac{\partial}{\partial x_k} \,, \tag{A.48a}$$

$$\underline{L}^j = \sum_{k=1}^{d} b^{k,j} \frac{\partial}{\partial x_k} \,. \tag{A.48b}$$

The simpler structure of $\underline{L}^0$ as compared to the Itô case in Eq. (A.41a) reflects the fact that Stratonovich SDEs obey the rules of ordinary calculus. As a consequence, the Stratonovich Taylor expansion has fewer terms than the Itô Taylor expansion, which is an advantage for deriving numerical schemes.

The Milstein scheme for solving a general system of SDEs in Stratonovich form reads [183]

$$y_{n+1}^k = y_n^k + \underline{a}^k \Delta t + \sum_{j=1}^{m} b^{k,j} \Delta W^j + \sum_{j_1,j_2=1}^{m} L^{j_1} b^{k,j_2} J_{(j_1,j_2)} \,, \tag{A.49}$$

where $J_{(j_1,j_2)}$ denotes the double Stratonovich integral. For $j_1 = j_2$, we have $J_{(j,j)} = (\Delta W^j)^2/2$, while $j_1 \neq j_2$ requires some kind of approximation in general. For commutative noise, the Milstein scheme for Stratonovich SDEs simplifies to

$$y_{n+1}^k = y_n^k + \underline{a}^k \Delta t + \sum_{j=1}^{m} b^{k,j} \Delta W^j + \frac{1}{2} \sum_{j_1,j_2=1}^{m} L^{j_1} b^{k,j_2} W^{j_1} \Delta W^{j_2} \,. \tag{A.50}$$

The Milstein scheme has strong and weak order of convergence $\gamma = \beta = 1$. Higher order Taylor schemes can be constructed by computing the Taylor expansion in Eq. (A.42) to the desired order. A general formula can be found in Ref. [183]. Since the number of terms generally increases rapidly when going to higher orders, such schemes are mostly practical if the SDE has a certain simplifying structure. In addition, the multiple stochastic integrals arising in higher-order Taylor schemes cannot be computed analytically and generally require some kind of approximation, which increases the computational cost. Finally, implementing the Milstein scheme (or higher-order Taylor schemes) requires the explicit specification of derivatives of the coefficient functions, which can be inconvenient in practice. This can be remedied by approximating derivatives through finite differences, which leads to explicit or implicit Runge–Kutta schemes [183].

A.3.3. Magnus Integrators for Linear Stochastic Differential Equations

Linear SDEs are common in many applications. They arise, for instance, from the spatial discretization of partial differential equations describing many models in continuum mechanics [385]. Furthermore, the play an important role for diffusive unravelings of quantum master equation in the theory of open quantum systems [186]. In the engineered dephasing scenario discussed in Section 2.3.3, the dynamics is governed on a fundamental level by a linear stochastic Schrödinger or von Neumann equation. The purpose of this section is to discuss accurate and robust schemes for the numerical integration of such systems.

A general homogeneous linear Itô SDE for a d-dimensional stochastic process $x(t)$ and an m-component Wiener process takes the form

$$\mathrm{d}\boldsymbol{x}(t) = A(t)\boldsymbol{x}(t)\,\mathrm{d}t + \sum_{j=1}^{m} B^j(t)\boldsymbol{x}(t)\,\mathrm{d}W(t)\,, \tag{A.51}$$

where the $d \times d$ matrices $A(t)$ and $B^j(t)$ characterize the deterministic and stochastic evolution, respectively. If all of these matrices commute with each other at arbitrary times, the solution is given by [183]

$$\boldsymbol{x}(t) = \exp\left[\int_{t_0}^{t} \mathrm{d}t' \left[A(t') - \frac{1}{2}\sum_{j=1}^{m}(B^j)^2(t')\right] + \sum_{j=1}^{m}\int_{t_0}^{t} \mathrm{d}W^j(t')\, B^j(t')\right]\boldsymbol{x}(t_0)\,. \tag{A.52}$$

In the non-commutative case, however, there is no known explicit solution of Eq. (A.51) in general.

By means of Eq. (A.23), the linear Itô SDE can be transformed into the equivalent linear Stratonovich SDE

$$\mathrm{d}\boldsymbol{x}(t) = \underline{A}(t)\boldsymbol{x}(t)\,\mathrm{d}t + \sum_{j=1}^{m} B^j(t)\boldsymbol{x}(t) \circ \mathrm{d}W(t)\,, \tag{A.53}$$

where the Stratonovich drift term is related to that of the equivalent Itô SDE via

$$\underline{A}(t) = A(t) - \frac{1}{2}\sum_{j=1}^{m}(B^j)^2(t)\,. \tag{A.54}$$

The solution of the linear Stratonovich SDE (A.53) in the commutative case, $[A(t), B^j(t')] = [B^{j_1}(t), B^{j_2}(t')] = 0$, reads

$$\boldsymbol{x}(t) = \exp\left[\int_{t_0}^{t} \mathrm{d}t'\, \underline{A}(t') + \sum_{j=1}^{m}\int_{t_0}^{t} \mathrm{d}W^j(t')\, B^j(t')\right]\boldsymbol{x}(t_0)\,, \tag{A.55}$$

which takes the same form as in ordinary calculus.

The Euler–Maruyama scheme and the Milstein scheme presented in the previous sections can in principle also be applied to linear SDEs. For linear SDEs, commutative noise means that the noise matrices all commute, $[B^{j_1}, B^{j_2}] = 0$. However, in many applications, the dimension d of the linear system is large and the problem tends to become stiff as the spectral width of the matrices on the right-hand side grows. Under such conditions, explicit schemes like the Euler or Milstein method are known to perform poorly because numerical stability enforces a very small time step size. This issue due to numerical stiffness also arises for higher-order explicit schemes. Therefore, numerical integration of stiff equations generally requires the use of implicit schemes. However, this can be problematic for SDEs if the stiffness is in the noise term: implicit schemes require the solution of a linear system at each time step, which can become poorly conditioned due to the unboundedness of the Wiener process [183]. Another strategy to handle numerical stiffness in linear SDEs is the use of exponential integrators. This approach often allows one to construct symplectic integrators, which respect certain conservation laws of the underlying system, e.g., unitarity in case of a stochastic Schrödinger equation. In what follows, we discuss stochastic Magnus integration [387, 388] as a powerful and robust method for solving time-dependent linear SDEs.

Stochastic Magnus Integration

The solution of a homogeneous linear system of ODEs

$$\frac{\mathrm{d}}{\mathrm{d}t}\boldsymbol{y}(t) = A(t)\boldsymbol{y}(t) \tag{A.56}$$

with a time-dependent matrix $A(t)$ can formally be expanded in a Dyson series, which leads to the formal representation in terms of the time-ordered exponential

$$\boldsymbol{y}(t) = \mathcal{T}\exp\left[\int_{t_0}^{t} \mathrm{d}t'\, A(t')\right]\boldsymbol{y}_0\,, \tag{A.57}$$

where $\mathcal{T}$ is the time-ordering operator.

A different approach is to express the solution as

$$\boldsymbol{y}(t) = \exp[\Omega(t)]\boldsymbol{y}_0\,, \tag{A.58}$$

in terms of a suitable matrix $\Omega(t)$. This matrix can be written as an infinite series of integrals over nested commutators, known as the Magnus expansion, whose first few terms are given by [388]

$$\begin{aligned}\Omega(t) = &\int_{t_0}^{t} \mathrm{d}\tau\, A_\tau + \frac{1}{2}\int_{t_0}^{t}\mathrm{d}\tau\int_{t_0}^{\tau}\mathrm{d}\sigma\,[A_\tau, A_\sigma] \\ &+ \frac{1}{6}\int_{t_0}^{t}\mathrm{d}\tau\int_{t_0}^{\tau}\mathrm{d}\sigma\int_{t_0}^{\sigma}\mathrm{d}\rho\,\big\{\big[A_\tau,\big[A_\sigma,A_\rho\big]\big] + \big[[A_\tau,A_\sigma],A_\rho\big]\big\} + \ldots\end{aligned} \tag{A.59}$$

This approach can be extended to linear SDEs. For the linear Stratonovich SDE (A.53), we can formally replace $A(t)\,\mathrm{d}t \to \underline{A}(t)\,\mathrm{d}t + \sum_j B^j(t)\circ \mathrm{d}W^j(t)$ in the standard Magnus formula to arrive at the stochastic Magnus expansion [387]

$$\begin{aligned}\Omega(t) = &\int_{t_0}^{t}\big(\underline{A}_\tau\,\mathrm{d}\tau + B^j_\tau\circ\mathrm{d}W^j_\tau\big) + \frac{1}{2}\int_{t_0}^{t}\Big[\underline{A}_\tau\,\mathrm{d}\tau + B^{j_1}_\tau\circ\mathrm{d}W^{j_1}, \int_{t_0}^{\tau}\Big(\underline{A}_\sigma\,\mathrm{d}\sigma + B^{j_2}_\sigma\circ\mathrm{d}W^{j_2}_\sigma\Big)\Big] \\ &+ \frac{1}{4}\int_{t_0}^{t}\Big[\underline{A}_\tau\,\mathrm{d}\tau + B^{j_1}_\tau\circ\mathrm{d}W^{j_1}_\tau, \int_{t_0}^{t}\Big[\underline{A}_\sigma + B^{j_2}_\sigma\circ\mathrm{d}W^{j_2}_\sigma, \int_{t_0}^{\sigma}\Big(\underline{A}_\rho\,\mathrm{d}\rho + B^{j_3}_\rho\circ\mathrm{d}W^{j_3}_\rho\Big)\Big]\Big] \\ &+ \frac{1}{12}\int_{t_0}^{t}\Big[\Big[\underline{A}_\tau\,\mathrm{d}\tau + B^{j_1}_\tau\circ\mathrm{d}W^{j_1}_\tau, \int_{t_0}^{t}\Big(\underline{A}_\sigma + B^{j_2}_\sigma\circ\mathrm{d}W^{j_2}_\sigma\Big)\Big], \int_{t_0}^{\sigma}\Big(\underline{A}_\rho\,\mathrm{d}\rho + B^{j_3}_\rho\circ\mathrm{d}W^{j_3}_\rho\Big)\Big] \\ &+ \ldots\,,\end{aligned} \tag{A.60}$$

where a sum over repeated indices is implied.

As shown in Ref. [387] for constant matrices A and B^j, further evaluation of Eq. (A.60) leads to an expansion in terms of nested commutators involving multiple stochastic integrals, which, in order to arrive at a practicable scheme, must be approximated in a suitable way [183]. Here, we follow the strategy pointed out in Ref. [389] and use integration by parts to avoid the necessity to approximate certain stochastic integrals. To arrive at a practicable scheme, we first make some simplifying assumptions appropriate for our purposes. We assume the time-dependent matrix to have the structure $A(t) = A_0 + f(t)A_1$, where A_0 and A_1 are constant (and in general non-commuting) matrices. (In what follows, we only consider the Stratonovich interpretation and omit the underbar indicating the Stratonovich drift coefficient.) Furthermore, we assume the noise matrices B^j to be time-independent and mutually commuting, $[B^{j_1}, B^{j_2}] = 0$, i.e., we assume commutative noise, as well as $[A_0, B^j] = 0$. These assumptions are fulfilled in the engineered dephasing scenario of Section 2.3.3, where $A_0 = -iH_0/\hbar$ and $A_1 = -iH_{\mathrm{cpl}}/\hbar$ play the role of the unperturbed and coupling Hamiltonian, respectively, and the noise is commutative because each noise process acts locally on each ancilla individually or there is only a

single scalar noise process which globally acts on all ancillas. The commutativity condition on the noise represents a crucial simplification since all commutators in Eq. (A.60) involving only noise matrices vanish. Keeping only terms with simple, but not nested commutators, the stochastic Magnus expansion simplifies to

$$\begin{aligned}\Omega(t) = A_0 \int_{t_0}^{t} \mathrm{d}\tau + A_1 \int_{t_0}^{t} \mathrm{d}\tau\, f(\tau) + \sum_j B^j \int_{t_0}^{t} \circ\, \mathrm{d}W^j(\tau) \\ + [A_0, A_1]\Big\{ \int_{t_0}^{t} \mathrm{d}\tau \int_{t_0}^{\tau} \mathrm{d}\sigma\, f(\sigma) - \int_{t_0}^{t} \mathrm{d}\tau\, f(\tau) \int_{t_0}^{\tau} \mathrm{d}\sigma \Big\} \\ + \frac{1}{2}\sum_{j=1}^{m} [A_1, B^j]\Big\{ \int_{t_0}^{t} \mathrm{d}\tau\, f(\tau) \int_{t_0}^{\tau} \circ\, \mathrm{d}W^j(\sigma) - \int_{t_0}^{t} \circ\, \mathrm{d}W^j(\tau) \int_{t_0}^{\tau} \mathrm{d}\sigma\, f(\sigma) \Big\} + ...\end{aligned} \tag{A.61}$$

Using integration by parts, the stochastic integral in the last term can be rewritten as

$$\int_{t_0}^{t} F(\tau) \circ \mathrm{d}W^j(\tau) = W^j(t)F(t) - \int_{t_0}^{t} W^j(\tau) f(\tau)\, \mathrm{d}\tau\,, \tag{A.62}$$

where $F(t) = \int_{t_0}^{t} f(\tau)\, \mathrm{d}\tau$. We then arrive at

$$\begin{aligned}\Omega(t) = A_0(t - t_0) + A_1 \int_{t_0}^{t} \mathrm{d}\tau\, f(\tau) + \sum_j B^j [W^j(t) - W^j(t_0)] \\ + \frac{1}{2}[A_0, A_1] \int_{t_0}^{t} \mathrm{d}\tau \Big[\int_{t_0}^{\tau} \mathrm{d}\tau\, f(\tau) - f(\tau)(\tau - t_0) \Big] \\ + \sum_{j=1}^{m} [A_1, B^j] \Big\{ \int_{t_0}^{t} \mathrm{d}\tau\, f(\tau) W^j(\tau) - \frac{1}{2}[W^j(t_0) + W^j(t)] F(t) \Big\} + ...\end{aligned} \tag{A.63}$$

Higher-order terms of the stochastic Magnus expansion can be obtained following a similar procedure [389]. Crucially, Eq. (A.63) does not contain any stochastic integrals any more, but merely ordinary Riemann integrals where components of the Wiener process appear in the integrand. These integrals can conveniently be approximated using standard quadrature techniques.

All in all, the stochastic Magnus scheme amounts to the iteration

$$\boldsymbol{y}_{n+1} = \exp(\Omega_n)\boldsymbol{y}_n\,, \tag{A.64}$$

where the matrix Ω_n is given by Eq. (A.63) for $t_0 = t_n$ and $t = t_{n+1}$. At each time step, the current solution is multiplied by the matrix exponential of Ω_n, which can be computed, for instance, using eigen decomposition or by means of the scaling and squaring algorithm [390]. However, this procedure not only costs a lot of computing power, but also requires large amounts of memory since the matrix exponential is typically a dense matrix (even if the exponent is sparse), which makes it unfeasible for large problems. Fortunately, a computation of the full matrix exponential is not required, but

it is sufficient to compute the action of the matrix exponential on a vector. This can efficiently be achieved using Krylov subspace techniques, which require only (sparse) matrix–vector multiplications [80, 171–173]. Moreover, each time step requires the approximation of the integrals in Eq. (A.63). Since this involves only ordinary Riemann integrals, standard numerical integration techniques, e.g., Gaussian quadrature, can be used. The integrals should be approximated using a finer step size than $\Delta t = t_{n+1} - t_n$, the time step size for the Magnus iteration in Eq. (A.64). It should be noted that the computational costs of one Magnus step are usually dominated by the computation of the action of the matrix exponential rather than by the approximation of the integrals.

The Magnus scheme (A.64) for commutative noise is of strong order $\gamma = 1.5$ and weak order $\beta = 2$. The higher computational costs of a single time step compared to explicit Taylor schemes of the same order are outweighed by the increased numerical stability, which allows one to choose larger time steps. In particular, when applied to a stochastic Schrödinger or von Neumann equation describing unitary time evolution, the Magnus scheme preserves the norm of the state up to machine precision. These properties make stochastic Magnus scheme an accurate, efficient, and robust method for solving linear SDEs like those appearing in the engineered dephasing scenario discussed in Section 2.3.3.

B. Classical–Statistical Simulations and Their Range of Validity

In this appendix, we elaborate on the classical–statistical (or truncated Wigner) method employed in Chapter 5 to numerically study the analog reheating scenario in an ultracold Bose gas. After introducing the basic method and describing technical details, we assess the range of validity of classical–statistical simulations for studying reheating dynamics.

The contents of this appendix are taken from Appendix C of Ref. [108]. Most of the text has been quoted verbatim up to minor modifications for a better embedding in the context of this thesis. See List of Publications for a statement of contributions.

B.1. Truncated Wigner Method

In Chapter 5, the dynamics of an ultracold Bose gas, governed by the Heisenberg equations of motion (5.15), has been simulated by means of classical–statistical simulations [324, 325], known in the literature also under the name truncated Wigner simulations [326, 327]. This method takes into account quantum fluctuations in form of stochastic initial conditions, but relies on a deterministic time evolution governed by semi-classical equations of motion. Quantum expectation values are obtained as statistical averages over multiple realizations. The following summary of the truncated Wigner method is mainly based on Refs. [326, 327].

For each realization, the initial field configuration is sampled from the Wigner distribution of the corresponding quantum state, which is commonly taken as the Bogoliubov state in equilibrium. For our purposes, we consider a homogeneous scalar BEC of N atoms at zero temperature in a box of volume V with periodic boundary conditions. The initial wave function is sampled as

$$\Psi_{\mathrm{cl}}(0,\boldsymbol{x}) = \sqrt{n_0}\mathrm{e}^{i\theta_0} + \sum_{\boldsymbol{p}\neq 0}\left[\alpha_{\boldsymbol{p}}u_{\boldsymbol{p}}(\boldsymbol{x}) - \alpha^*_{\boldsymbol{p}}v^*_{\boldsymbol{p}}(\boldsymbol{x})\right]. \tag{B.1}$$

Here, the first term represents the condensate with particle density $n_0 = N/V$ and phase θ_0. Due to the large occupancy of the condensate mode, the finite width of its Wigner function can be neglected, and thus the same value of the density can be used in each realization. To preserve the $U(1)$ symmetry, the phase is randomly sampled from the uniform distribution over the interval $[0, 2\pi)$ for each realization. The mode functions

$$u_{\boldsymbol{p}}(\boldsymbol{x}) = \frac{1}{\sqrt{V}}u_{\boldsymbol{p}}\mathrm{e}^{i\boldsymbol{p}\boldsymbol{x}/\hbar} \quad \text{and} \quad v_{\boldsymbol{p}}(\boldsymbol{x}) = \frac{1}{\sqrt{V}}v_{\boldsymbol{p}}\mathrm{e}^{i\boldsymbol{p}\boldsymbol{x}/\hbar} \tag{B.2}$$

are solutions of the Bogoliubov–de Gennes equations for a uniform system in a periodic box, with real coefficients

$$u_{\boldsymbol{p}} = \sqrt{\frac{\epsilon_{\boldsymbol{p},0} + n_0 g_0}{2\epsilon_{\boldsymbol{p}}} + \frac{1}{2}} \tag{B.3}$$

and $v_{\boldsymbol{p}}$ determined by the normalization $u_{\boldsymbol{p}}^2 - v_{\boldsymbol{p}}^2 = 1$ (cf. Section 5.3.2 for details of the notation) [391]. In order to mimic quantum fluctuations, the quasi-particle amplitudes $\alpha_{\boldsymbol{p}}$ are sampled as complex Gaussian random variables with zero mean, satisfying $\overline{\alpha_{\boldsymbol{p}}^* \alpha_{\boldsymbol{q}}} = \delta_{\boldsymbol{p},\boldsymbol{q}}/2$ at zero temperature. Here, $\overline{(\dots)}$ denotes the ensemble average over all realizations. This vacuum noise corresponds to an average occupancy of half a particle per mode, which is also known as the "quantum half". In the simulations presented in Chapter 5, the vacuum noise is cut off at the highest lattice momentum unless stated otherwise.

For the purposes of Chapter 5, a simplified approach has been used, setting $u_{\boldsymbol{p}} = 1$ and $v_{\boldsymbol{p}} = 0$, such that the mode functions reduce to ordinary plane waves. Effectively, this corresponds to preparing the Bogoliubov ground state of an ideal gas, which is appropriate for the analog reheating scenario since the precise nature of the quasi-particles seeding the parametric resonance is unimportant. As a side effect, we observe a transient growth of population at low momenta at early times (see Fig. 5.2). The resulting p^{-1} behavior of the momentum distribution at low momenta matches the behavior of $u_{\boldsymbol{p}}^2$ and $v_{\boldsymbol{p}}^2$ for $|\boldsymbol{p}| \to 0$. Therefore, the observed growth can be interpreted as an artifact of the effective quench from an ideal Bose gas to a system with finite interaction at time $t = 0$.

In the truncated Wigner method, quantum expectation values are replaced by statistical averages over the Wigner distribution. The latter correspond to expectation values of symmetrically ordered quantum operators. Thus, the momentum distribution obtained from classical–statistical simulations corresponds to the one defined in Eq. (1.8) plus an extra contribution in form of the "quantum half" stemming from the commutation relations,

$$\frac{1}{V}\overline{|\Psi_{\mathrm{cl}}(t,\boldsymbol{p})|^2} = f(t,\boldsymbol{p}) + \frac{1}{2}\,. \tag{B.4}$$

Here, $\Psi_{\mathrm{cl}}(t,\boldsymbol{p}) = \int \mathrm{d}^d x\, \Psi_{\mathrm{cl}}(t,\boldsymbol{x}) \mathrm{e}^{-i\boldsymbol{p}\boldsymbol{x}/\hbar}$ denotes the Fourier transform of the classical field $\Psi_{\mathrm{cl}}(t,\boldsymbol{x})$.

The classical–statistical simulations presented in Chapter 5 have typically been averaged over at least 64 runs. The statistics is even further enhanced through radial averages due to the isotropy of the system. The statistical error bars are thus typically smaller than the line width in the plots.

B.2. Dimensionless Gross–Pitaevskii Equation

Each realization is propagated in time according to the GPE (1.14). To cast this equation into a dimensionless form suitable for numerical simulations, we express time and length in units of the characteristic scales $t_0 = \hbar/n_0 g_0$ and $x_0 = \hbar/\sqrt{m n_0 g_0}$, respectively. In terms of the dimensionless time $\tilde{t} = t/t_0$, position $\tilde{\boldsymbol{x}} = \boldsymbol{x}/x_0$, and field $\tilde{\Psi}_{\mathrm{cl}} = x_0^{d/2}\Psi_{\mathrm{cl}}$, the

GPE takes the form

$$i\partial_{\tilde{t}}\tilde{\Psi}_{\rm cl} = \left(-\frac{1}{2}\tilde{\nabla}^2 + \tilde{g}\big(\tilde{t}\big)\big|\tilde{\Psi}_{\rm cl}\big|^2\right)\tilde{\Psi}_{\rm cl}\,, \tag{B.5}$$

with the dimensionless coupling $\tilde{g} = gt_0/\hbar x_0^d$.

In a quasi-2D system (and in the absence of time-dependent modulations), the dimensionless coupling is, up to logarithmic corrections, given by $\tilde{g} = \sqrt{8\pi}a_s/a_{\rm HO}$, where a_s is the s-wave scattering length and $a_{\rm HO}$ is the oscillator length of the confining harmonic potential in vertical direction [60]. If the wave function is normalized to unity, the coupling changes as $\tilde{g} \to N\tilde{g}$, where N is the particle number. This shows that the parameters N and $\tilde{g}$ enter the classical equations of motion (B.5) only through the product $N\tilde{g}$ as the single relevant model parameter. Moreover, also the dimensionless box length $L/x_0 = \sqrt{N\tilde{g}}$ is fixed by this quantity as a consequence of scale invariance. By contrast, on the quantum level, the relative magnitudes of the parameters N and $\tilde{g}$ do play a role (see Appendix B.3).

The GPE (B.5) has been discretized in space by means of a Fourier pseudospectral discretization and propagated in time using the well-known split-step method [309]. The accuracy of the time evolution has further been enhanced with the help of the optimized fourth-order time splitting scheme given in Table 2 of Ref. [392].

In the 2D simulations of turbulent reheating dynamics in Section 5.4, a spatial $N_g \times N_g$ grid with at least $N_g = 512$ grid points per dimension has been used, while $N_g = 256$ turns out to be sufficient for simulating early-time preheating dynamics (see Section 5.3). For a system of size $L \times L$ with $L/x_0 = 50$, the corresponding grid spacing $\Delta x = L/N_g$ ensures that the healing length $\xi = x_0/\sqrt{2}$, which is the smallest physical length scale in a uniform system, is well-resolved. Numerical stability for late-time dynamics is achieved by choosing the numerical time step $\Delta\tilde{t}$ such that $\Delta\tilde{t}\tilde{k}_{\rm max}^2 \lesssim 2\pi$, where $\tilde{k}_{\rm max} = \pi/\Delta\tilde{x}$ with $\Delta\tilde{x} = \Delta x/x_0$ is the maximum numerical wave number supported by the grid [393].

B.3. Validity of Classical–Statistical Simulations

Quantum dynamics is well described by classical–statistical simulations in the regime of large occupancies and weak couplings [325, 371]. In particular, the truncated Wigner method is known to produce unphysical results if the number of virtual particles added to mimic quantum fluctuations becomes comparable to the number of real particles in the system [326, 327]. At zero temperature, the failure of the classical–statistical approximation is indicated by the instability of the vacuum and a resulting unphysical dependence of observables on the UV cutoff [371]. This decay of the "quantum half", which inevitably occurs at sufficiently late times, naturally restricts the classical–statistical method to the weak coupling regime, where the instability is mitigated via a separation of scales. Moreover, if the coupling is too strong, physical observables risk attaining a dependence on the UV cutoff already at relatively early times through the spurious quantum pressure generated by the decaying vacuum. This is because the coupling controls the relative magnitude of mode occupancies with respect to the vacuum noise, which, in turn, is regulated by the UV cutoff [371].

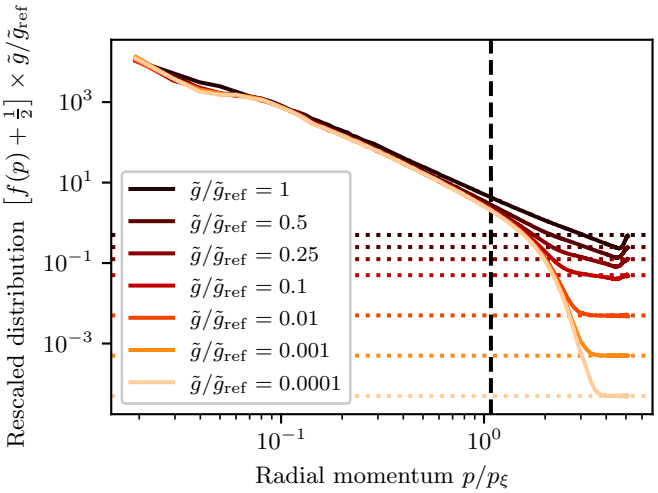

Figure B.1.: Snapshot of the radially averaged, rescaled momentum distribution for the driven turbulent cascade (cf. Fig. 5.4a) at time $t/t_0 = 640$ for different values of the coupling $\tilde{g}$. The particle number is chosen according to $N = N_{\rm ref}(\tilde{g}/\tilde{g}_{\rm ref})^{-1}$, such that the product $N\tilde{g} = N_{\rm ref}\tilde{g}_{\rm ref}$ remains constant. The vertical dashed line marks the characteristic momentum (5.40), calculated for the distribution corresponding to the smallest value of $\tilde{g}$. The horizontal dotted lines mark the location of the "quantum half" after rescaling. Within the range of validity of classical–statistical simulations, the rescaled distributions are expected to collapse to a single curve. Visible undershooting of the quantum half can be observed for $\tilde{g}/\tilde{g}_{\rm ref} \gtrsim 0.1$, indicating a breakdown of the method for larger values of the coupling.

To ensure that the numerical simulations of reheating dynamics in Chapter 5, in particular, in the turbulent scaling regime at late times, lie within the range of validity of the classical–statistical method, we follow a similar procedure as presented in Ref. [371]. Formally, the classical statistical limit is given by $N \to \infty$ and $g \to 0$, where N is the particle number and g is the coupling, such that $Ng = \text{const}$. To approach this limit numerically in 2D, we fix the value $N\tilde{g} = (L/x_0)^2$ by the choice $L/x_0 = 50$ and consider the same simulation repeated for different values of the coupling $\tilde{g}$, using the parametrization $N = N_{\rm ref}(\tilde{g}/\tilde{g}_{\rm ref})^{-1}$ with reference parameters $N_{\rm ref} = 10^6$ and $\tilde{g}_{\rm ref} = 2.5 \times 10^{-3}$. Figure B.1 shows the radially averaged momentum distribution for the driven turbulence scenario in Fig. 5.4a at time $t/t_0 = 640$ for different values of the coupling $\tilde{g}$. All configurations have been averaged over at least 25 single runs. To assess up to which value of the coupling the simulations are valid, the curves have been rescaled by $\tilde{g}/\tilde{g}_{\rm ref}$, in which case they are expected to lie on top of each other in the region $f(t,p)\tilde{g}/\tilde{g}_{\rm ref} \gtrsim 1$. (Note that regions where the occupancy drops below unity are outside of the range of validity *per se*.) The vertical dashed line marks the position of the characteristic momentum (5.40), calculated for the distribution with the lowest value of $\tilde{g}$, around which the UV scaling properties of the distribution are most sensitive. It can be seen that deviations occur for $\tilde{g}/\tilde{g}_{\rm ref} \gtrsim 0.1$. For larger values of the coupling, the shape of the power law changes and the distribution hits the UV cutoff, such that cutoff-independence of the results is no longer guaranteed. Furthermore, the distribution

at large momenta drops below the "quantum half", as indicated by the horizontal dotted lines, which formally corresponds to the unphysical situation of negative occupancies. It has been checked, using a similar approach as in Ref. [371], that the contribution of the vacuum noise to the total energy budget of the system becomes significant for $\tilde{g}/\tilde{g}_{\rm ref} \gtrsim 0.1$, which coincides with the values of the coupling for which deviations in the momentum distribution are observed.

While the early-time preheating dynamics presented in Section 5.3 is only insignificantly affected by these deficiencies for the reference parameters $N_{\rm ref} = 10^6$ and $\tilde{g}_{\rm ref} = 2.5 \times 10^{-3}$, this is no longer true for the late-time turbulent reheating dynamics, as illustrated in Fig. B.1. The results presented in Section 5.4 have therefore been computed for $\tilde{g}/\tilde{g}_{\rm ref} = 0.01$, which safely lies within the range of validity of classical–statistical simulations.

Bibliography

[1] A. Chatrchyan, "Nonperturbative dynamics in the early universe: from axion-like particles to dark matter and condensates," PhD thesis (Heidelberg University, 2020).

[2] J. Reichstetter, "Measurement of currents in optical lattices via the quantum Zeno effect," Bachelor's thesis (Heidelberg University, 2019).

[3] M. A. Nielsen and I. L. Chuang, *Quantum Computation and Quantum Information: 10th Anniversary Edition* (Cambridge University Press, 2010).

[4] RIKEN Center for Computational Science, *Fujitsu Fugaku*, `https://www.r-ccs.riken.jp/en/fugaku/about` (visited on 05/09/2022).

[5] R. P. Feynman, Int. J. Theor. Phys. **21**, 467 (1982).

[6] P. Hauke, F. M. Cucchietti, L. Tagliacozzo, I. Deutsch, and M. Lewenstein, Rep. Prog. Phys. **75**, 082401 (2012).

[7] M. H. Anderson, J. R. Ensher, M. R. Matthews, C. E. Wieman, and E. A. Cornell, Science **269**, 198 (1995).

[8] K. B. Davis, M.-O. Mewes, M. R. Andrews, N. J. van Druten, D. S. Durfee, D. M. Kurn, and W. Ketterle, Phys. Rev. Lett. **75**, 3969 (1995).

[9] S. N. Bose, Zeitschrift für Physik **26**, 178 (1924).

[10] A. Einstein, "Quantentheorie des einatomigen idealen Gases, 2. Abhandlung," in *Sitzungsberichte der Preussischen Akademie der Wissenschaften zu Berlin* (1925).

[11] D. Jaksch, C. Bruder, J. I. Cirac, C. W. Gardiner, and P. Zoller, Phys. Rev. Lett. **81**, 3108 (1998).

[12] M. Greiner, O. Mandel, T. Esslinger, T. W. Hänsch, and I. Bloch, Nature (London) **415**, 39 (2002).

[13] M. Lewenstein, A. Sanpera, and V. Ahufinger, *Ultracold Atoms in Optical Lattices: Simulating quantum many-body systems* (Oxford University Press, Oxford, 2012).

[14] I. Bloch, J. Dalibard, and S. Nascimbène, Nat. Phys. **8**, 267 (2012).

[15] C. Gross and I. Bloch, Science **357**, 995 (2017).

[16] F. Schäfer, T. Fukuhara, S. Sugawa, Y. Takasu, and Y. Takahashi, Nat. Rev. Phys. **2**, 411 (2020).

[17] O. Dutta, M. Gajda, P. Hauke, M. Lewenstein, D.-S. Lühmann, B. A. Malomed, T. Sowiński, and J. Zakrzewski, Rep. Prog. Phys. **78**, 066001 (2015).

[18] W. S. Bakr, J. I. Gillen, A. Peng, S. Fölling, and M. Greiner, Nature (London) **462**, 74 (2009).

[19] J. F. Sherson, C. Weitenberg, M. Endres, M. Cheneau, I. Bloch, and S. Kuhr, Nature (London) **467**, 68 (2010).

[20] V. Galitski and I. B. Spielman, Nature (London) **494**, 49 (2013).

[21] R. Kubo, Rep. Prog. Phys. **29**, 255 (1966).

[22] L. Pan, X. Chen, Y. Chen, and H. Zhai, Nat. Phys. **16**, 767 (2020).

[23] D. Sticlet, B. Dóra, and C. P. Moca, Phys. Rev. Lett. **128**, 016802 (2022).

[24] A. Schuckert and M. Knap, Phys. Rev. Research **2**, 043315 (2020).

[25] A. M. Kaufman, M. E. Tai, A. Lukin, M. Rispoli, R. Schittko, P. M. Preiss, and M. Greiner, Science **353**, 794 (2016).

[26] R. Nandkishore and D. A. Huse, Annu. Rev. Condens. Matter Phys. **6**, 15 (2015).

[27] C. Gogolin and J. Eisert, Reports on Progress in Physics **79**, 056001 (2016).

[28] L. D'Alessio, Y. Kafri, A. Polkovnikov, and M. Rigol, Adv. Phys. **65**, 239 (2016).

[29] J. M. Deutsch, Rep. Progr. Phys. **81**, 082001 (2018).

[30] D. A. Abanin, E. Altman, I. Bloch, and M. Serbyn, Rev. Mod. Phys. **91**, 021001 (2019).

[31] S. Moudgalya, B. A. Bernevig, and N. Regnault, arXiv:`2109.00548 [cond-mat.str-el]` (2021).

[32] D. J. Thouless, Ann. Phys. (N.Y.) **52**, 403 (1969).

[33] A. F. Andreev and I. M. Lifshitz, Zh. Eksp. Teor. Fiz. **56**, [Sov. Phys. JETP **29**, 1107 (1969)], 2057 (1969).

[34] A. J. Leggett, Phys. Rev. Lett. **25**, 1543 (1970).

[35] S. Balibar, Nature (London) **464**, 176 (2010).

[36] M. Boninsegni and N. V. Prokof'ev, Rev. Mod. Phys. **84**, 759 (2012).

[37] J. Léonard, A. Morales, P. Zupancic, T. Esslinger, and T. Donner, Nature (London) **543**, 87 (2017).

[38] J.-R. Li, J. Lee, W. Huang, S. Burchesky, B. Shteynas, F. Ç. Top, A. O. Jamison, and W. Ketterle, Nature (London) **543**, 91 (2017).

[39] A. Putra, F. Salces-Cárcoba, Y. Yue, S. Sugawa, and I. B. Spielman, Phys. Rev. Lett. **124**, 053605 (2020).

[40] L. Tanzi, E. Lucioni, F. Famà, J. Catani, A. Fioretti, C. Gabbanini, R. N. Bisset, L. Santos, and G. Modugno, Phys. Rev. Lett. **122**, 130405 (2019).

[41] F. Böttcher, J.-N. Schmidt, M. Wenzel, J. Hertkorn, M. Guo, T. Langen, and T. Pfau, Phys. Rev. X **9**, 011051 (2019).

[42] L. Chomaz, D. Petter, P. Ilzhöfer, G. Natale, A. Trautmann, C. Politi, G. Durastante, R. M. W. van Bijnen, A. Patscheider, M. Sohmen, M. J. Mark, and F. Ferlaino, Phys. Rev. X **9**, 021012 (2019).

[43] Y. Nambu, Phys. Rev. **117**, 648 (1960).

[44] J. Goldstone, Il Nuovo Cimento (1955-1965) **19**, 154 (1961).

[45] J. Goldstone, A. Salam, and S. Weinberg, Phys. Rev. **127**, 965 (1962).

[46] M. Prüfer, T. V. Zache, P. Kunkel, S. Lannig, A. Bonnin, H. Strobel, J. Berges, and M. K. Oberthaler, Nat. Phys. **16**, 1012 (2020).

[47] T. V. Zache, T. Schweigler, S. Erne, J. Schmiedmayer, and J. Berges, Phys. Rev. X **10**, 011020 (2020).

[48] C. Barceló, S. Liberati, and M. Visser, Living Rev. Relativ. **14**, 3 (2011).

[49] E. W. Kolb and M. S. Turner, *The Early Universe*, 1st ed., Vol. 69, Frontiers in Physics (CRC Press, Boca Raton, 1990).

[50] L. Kofman, A. D. Linde, and A. A. Starobinsky, Phys. Rev. Lett. **73**, 3195 (1994).

[51] R. Micha and I. I. Tkachev, Phys. Rev. D **70**, 043538 (2004).

[52] J. Berges and G. Hoffmeister, Nucl. Phys. **B813**, 383 (2009).

[53] J. Berges, K. Boguslavski, S. Schlichting, and R. Venugopalan, Phys. Rev. Lett. **114**, 061601 (2015).

[54] A. Piñeiro Orioli, K. Boguslavski, and J. Berges, Phys. Rev. D **92**, 025041 (2015).

[55] C.-M. Schmied, A. N. Mikheev, and T. Gasenzer, Int. J. Mod. Phys. A **34**, 1941006 (2019).

[56] A. Mazeliauskas and J. Berges, Phys. Rev. Lett. **122**, 122301 (2019).

[57] L. Pitaevskii and S. Stringari, *Bose–Einstein Condensation and Superfluidity*, International Series of Monographs on Physics (Oxford University Press, Oxford, 2016).

[58] C. Chin, R. Grimm, P. Julienne, and E. Tiesinga, Rev. Mod. Phys. **82**, 1225 (2010).

[59] O. Penrose and L. Onsager, Phys. Rev. **104**, 576 (1956).

[60] Z. Hadzibabic and J. Dalibard, Riv. del Nuovo Cimento **34**, 389 (2011).

[61] N. D. Mermin and H. Wagner, Phys. Rev. Lett. **17**, 1133 (1966).

[62] P. C. Hohenberg, Phys. Rev. **158**, 383 (1967).

[63] D. S. Petrov, M. Holzmann, and G. V. Shlyapnikov, Phys. Rev. Lett. **84**, 2551 (2000).

[64] D. S. Petrov, G. V. Shlyapnikov, and J. T. M. Walraven, Phys. Rev. Lett. **85**, 3745 (2000).

[65] D. S. Petrov, G. V. Shlyapnikov, and J. T. M. Walraven, Phys. Rev. Lett. **87**, 050404 (2001).

[66] W. Bao and Y. Cai, Kinet. Relat. Mod. **6**, 1 (2013).

[67] X. Antoine, A. Levitt, and Q. Tang, J. Comput. Phys. **343**, 92 (2017).

[68] L. Salasnich, A. Parola, and L. Reatto, Phys. Rev. A **65**, 043614 (2002).

[69] C. Mora and Y. Castin, Phys. Rev. A **67**, 053615 (2003).

[70] N. Bogoliubov, Izv. Akad. Nauk Ser. Fiz. **11**, [J. Phys. (USSR) **11**, 23 (1947)], 77 (1947).

[71] N. Goldman, G. Juzeliūnas, P. Öhberg, and I. B. Spielman, Rep. Progr. Phys. **77**, 126401 (2014).

[72] A. M. Rey, Natl. Sci. Rev. **3**, 166 (2015).

[73] C.-C. Chien, S. Peotta, and M. Di Ventra, Nat. Phys. **11**, 998 (2015).

[74] V. Galitski, G. Juzeliūnas, and I. B. Spielman, Phys. Today **72**, 38 (2019).

[75] R. Grimm, M. Weidemüller, and Y. B. Ovchinnikov, Adv. Atom. Mol. Opt. Phy. **42**, 95 (2000).

[76] N. W. Ashcroft and N. D. Mermin, *Solid State Physics* (Saunders College Publishing, New York, 1976).

[77] G. H. Wannier, Phys. Rev. **52**, 191 (1937).

[78] J. I. Cirac and P. Zoller, Nat. Phys. **8**, 264 (2012).

[79] F. Schwabl, *Statistical Mechanics*, 2nd ed., Advanced Texts in Physics (Springer, Berlin, Heidelberg, 2006).

[80] D. Raventós, T. Graß, M. Lewenstein, and B. Juliá-Díaz, J. Phys. B: At., Mol. Opt. Phys. **50**, 113001 (2017).

[81] S. Sachdev, *Quantum Phase Transitions*, 2nd ed. (Cambridge University Press, Cambridge, 2011).

[82] P. Coleman, *Introduction to Many-Body Physics* (Cambridge University Press, Cambridge, 2015).

[83] H. B. Callen and T. A. Welton, Phys. Rev. **83**, 34 (1951).

[84] R. Kubo, J. Phys. Soc. Jpn. **12**, 570 (1957).

[85] A. Einstein, Ann. Phys. **17**, 549 (1905).

[86] J. B. Johnson, Phys. Rev. **32**, 97 (1928).

[87] H. Nyquist, Phys. Rev. **32**, 110 (1928).

[88] U. Marini Bettolo Marconi, A. Puglisi, L. Rondoni, and A. Vulpiani, Phys. Rep. **461**, 111 (2008).

[89] J. von Neumann, *Mathematische Grundlagen der Quantenmechanik* (Springer, Berlin, 1932).

[90] J. von Neumann, *Mathematical Foundations of Quantum Mechanics: New Edition*, edited by N. A. Wheeler, trans. by R. T. Beyer (Princeton University Press, Princeton, 2018).

[91] J. Jensen and A. R. Mackintosh, *Rare Earth Magnetism: Structures and Excitations*, International Series of Monographs on Physics (Clarendon Press, Oxford, 1991).

[92] F. Schwabl, *Quantum Mechanics*, 4th ed., Advanced Texts in Physics (Springer, Berlin, Heidelberg, 2007).

[93] R. de L. Kronig, J. Opt. Soc. Am. **12**, 547 (1926).

[94] H. A. Kramers, Atti del Congresso Internationale dei Fisici, Como **2**, 545 (1927).

[95] J. Berges, "Nonequilibrium Quantum Fields: From Cold Atoms to Cosmology," in *Strongly Interacting Quantum Systems out of Equilibrium: Lecture Notes of the Les Houches Summer School: Volume 99, August 2012*, edited by T. Giamarchi, A. J. Millis, O. Parcollet, H. Saleur, and L. F. Cugliandolo (Oxford University Press, Oxford, 2016) Chap. 2.

[96] P. C. Martin and J. Schwinger, Phys. Rev. **115**, 1342 (1959).

[97] C. Gardiner and P. Zoller, *Quantum Noise: A Handbook of Markovian and Non-Markovian Quantum Stochastic Methods with Applications to Quantum Optics*, 3rd ed., Springer Series in Synergetics (Springer-Verlag Berlin Heidelberg, 2004).

[98] W. Thomas, Naturwissenschaften **13**, 627 (1925).

[99] F. Reiche and W. Thomas, Z. Für Phys. **34**, 510 (1925).

[100] W. Kuhn, Z. Für Phys. **33**, 408 (1925).

[101] R. Jackiw, Phys. Rev. **157**, 1220 (1967).

[102] H. A. Bethe and R. Jackiw, *Intermediate Quantum Mechanics*, 3rd ed. (CRC Press, Boca Raton, 1986).

[103] K. T. Geier and P. Hauke, arXiv:`2104.03983 [cond-mat.quant-gas]` (2021).

[104] A. Salzinger, K. T. Geier, T. Franz, S. Geier, N. Thaicharoen, A. Tebben, C. Hainaut, R. Ott, M. Gärttner, G. Zürn, P. Hauke, and M. Weidemüller, in preparation (2022).

[105] R. J. Glauber, Phys. Rev. **130**, 2529 (1963).

[106] M. O. Scully and M. S. Zubairy, *Quantum Optics* (Cambridge University Press, 1997).

[107] K. Boguslavski and A. Piñeiro Orioli, Phys. Rev. D **101**, 091902(R) (2020).

[108] A. Chatrchyan, K. T. Geier, M. K. Oberthaler, J. Berges, and P. Hauke, Phys. Rev. A **104**, 023302 (2021).

[109] T. V. Zache, N. Mueller, J. T. Schneider, F. Jendrzejewski, J. Berges, and P. Hauke, Phys. Rev. Lett. **122**, 050403 (2019).

[110] B. Sciolla, D. Poletti, and C. Kollath, Phys. Rev. Lett. **114**, 170401 (2015).

[111] J. C. Halimeh and M. F. Maghrebi, Phys. Rev. E **103**, 052142 (2021).

[112] F. Arceri, F. P. Landes, L. Berthier, and G. Biroli, arXiv:2006.09725 [cond-mat.stat-mech] (2020).

[113] J. M. Deutsch, Phys. Rev. A **43**, 2046 (1991).

[114] M. Srednicki, Phys. Rev. E **50**, 888 (1994).

[115] L. Foini, L. F. Cugliandolo, and A. Gambassi, Phys. Rev. B **84**, 212404 (2011).

[116] L. Foini, L. F. Cugliandolo, and A. Gambassi, J. Stat. Mech. Theory Exp. **2012**, P09011 (2012).

[117] E. Khatami, G. Pupillo, M. Srednicki, and M. Rigol, Phys. Rev. Lett. **111**, 050403 (2013).

[118] A. Piñeiro Orioli and J. Berges, Phys. Rev. Lett. **122**, 150401 (2019).

[119] P. Hauke, M. Heyl, L. Tagliacozzo, and P. Zoller, Nat. Phys. **12**, 778 (2016).

[120] M. Brenes, S. Pappalardi, J. Goold, and A. Silva, Phys. Rev. Lett. **124**, 040605 (2020).

[121] R. Costa de Almeida and P. Hauke, Phys. Rev. Research **3**, L032051 (2021).

[122] C. L. Degen, F. Reinhard, and P. Cappellaro, Rev. Mod. Phys. **89**, 035002 (2017).

[123] L. Pezzè, A. Smerzi, M. K. Oberthaler, R. Schmied, and P. Treutlein, Rev. Mod. Phys. **90**, 035005 (2018).

[124] M. Belloni and R. W. Robinett, Am. J. Phys. **76**, 798 (2008).

[125] T. S. Grigera and N. E. Israeloff, Phys. Rev. Lett. **83**, 5038 (1999).

[126] L. Bellon and S. Ciliberto, Phys. D: Nonlinear Phenom. **168-169**, 325 (2002).

[127] R. R. Netz, J. Chem. Phys. **148**, 185101 (2018).

[128] O. Romero-Isart, M. Rizzi, C. A. Muschik, E. S. Polzik, M. Lewenstein, and A. Sanpera, Phys. Rev. Lett. **108**, 065302 (2012).

[129] M. Knap, A. Kantian, T. Giamarchi, I. Bloch, M. D. Lukin, and E. Demler, Phys. Rev. Lett. **111**, 147205 (2013).

[130] J. S. Pedernales, R. Di Candia, I. L. Egusquiza, J. Casanova, and E. Solano, Phys. Rev. Lett. **113**, 020505 (2014).

[131] P. Uhrich, S. Castrignano, H. Uys, and M. Kastner, Phys. Rev. A **96**, 022127 (2017).

[132] M. Kastner and P. Uhrich, Eur. Phys. J. ST **227**, 365 (2018).

[133] P. Uhrich, C. Gross, and M. Kastner, Quantum Sci. Technol. **4**, 024005 (2019).

[134] A. Roggero and J. Carlson, Phys. Rev. C **100**, 034610 (2019).

[135] D. Yang, A. Grankin, L. M. Sieberer, D. V. Vasilyev, and P. Zoller, Nat. Commun. **11**, 775 (2020).

[136] S. Castrignano and J. Evers, Phys. Rev. A **101**, 063842 (2020).

[137] R. El-Ganainy, K. G. Makris, M. Khajavikhan, Z. H. Musslimani, S. Rotter, and D. N. Christodoulides, Nat. Phys. **14**, 11 (2018).

[138] Y. Ashida, Z. Gong, and M. Ueda, Advances in Physics **69**, 249 (2020).

[139] A. Guo, G. J. Salamo, D. Duchesne, R. Morandotti, M. Volatier-Ravat, V. Aimez, G. A. Siviloglou, and D. N. Christodoulides, Phys. Rev. Lett. **103**, 093902 (2009).

[140] C. E. Rüter, K. G. Makris, R. El-Ganainy, D. N. Christodoulides, M. Segev, and D. Kip, Nat. Phys. **6**, 192 (2010).

[141] M. Naghiloo, M. Abbasi, Y. N. Joglekar, and K. W. Murch, Nat. Phys. **15**, 1232 (2019).

[142] W. Cao, X. Lu, X. Meng, J. Sun, H. Shen, and Y. Xiao, Phys. Rev. Lett. **124**, 030401 (2020).

[143] W. Chen, M. Abbasi, Y. N. Joglekar, and K. W. Murch, Phys. Rev. Lett. **127**, 140504 (2021).

[144] F. E. Öztürk, T. Lappe, G. Hellmann, J. Schmitt, J. Klaers, F. Vewinger, J. Kroha, and M. Weitz, Science **372**, 88 (2021).

[145] T. E. Lee, F. Reiter, and N. Moiseyev, Phys. Rev. Lett. **113**, 250401 (2014).

[146] C. A. Parra-Murillo, M. H. Muñoz-Arias, J. Madroñero, and S. Wimberger, Phys. Rev. A **95**, 032125 (2017).

[147] Y. Ashida, S. Furukawa, and M. Ueda, Nat Commun **8**, 15791 (2017).

[148] S. Yao and Z. Wang, Phys. Rev. Lett. **121**, 086803 (2018).

[149] M. Nakagawa, N. Kawakami, and M. Ueda, Phys. Rev. Lett. **121**, 203001 (2018).

[150] R. Hamazaki, K. Kawabata, and M. Ueda, Phys. Rev. Lett. **123**, 090603 (2019).

[151] M. Nakagawa, N. Tsuji, N. Kawakami, and M. Ueda, Phys. Rev. Lett. **124**, 147203 (2020).

[152] J. Wiersig, Photon. Res. **8**, 1457 (2020).

[153] J. Wiersig, Nat. Commun. **11**, 2454 (2020).

[154] G. P. Berman and A. I. Nesterov, Int. J. Quantum Inf. **07**, 1469 (2009).

[155] A. I. Nesterov and G. P. Berman, Phys. Rev. A **86**, 052316 (2012).

[156] B. Misra and E. C. G. Sudarshan, Journal of Mathematical Physics **18**, 756 (1977).

[157] P. Facchi and S. Pascazio, J. Phys. A: Math. Theor. **41**, 493001 (2008).

[158] K. Stannigel, P. Hauke, D. Marcos, M. Hafezi, S. Diehl, M. Dalmonte, and P. Zoller, Phys. Rev. Lett. **112**, 120406 (2014).

[159] H.-P. Breuer and F. Petruccione, *The Theory of Open Quantum Systems* (Oxford University Press, Oxford, 2007).

[160] J. Dalibard, Y. Castin, and K. Mølmer, Phys. Rev. Lett. **68**, 580 (1992).

[161] K. Mølmer, Y. Castin, and J. Dalibard, J. Opt. Soc. Am. B **10**, 524 (1993).

[162] A. J. Daley, Adv. Phys. **63**, 77 (2014).

[163] B. Svensson, Quanta **2**, 18 (2013).

[164] J. R. Garrison and T. Grover, Phys. Rev. X **8**, 021026 (2018).

[165] M. Srednicki, J. Phys. A **32**, 1163 (1999).

[166] P. Sala, T. Rakovszky, R. Verresen, M. Knap, and F. Pollmann, Phys. Rev. X **10**, 011047 (2020).

[167] W.-H. Li, X. Deng, and L. Santos, Phys. Rev. Lett. **127**, 260601 (2021).

[168] M. Serbyn, D. A. Abanin, and Z. Papić, Nat. Phys. **17**, 675 (2021).

[169] G. Aarts and J. Berges, Phys. Rev. D **64**, 105010 (2001).

[170] A. Piñeiro Orioli, "Quantum dynamics and universality far from equilibrium," PhD thesis (Heidelberg University, 2018).

[171] C. Lubich, *From Quantum to Classical Molecular Dynamics: Reduced Models and Numerical Analysis*, Zurich Lectures in Advanced Mathematics (European Mathematical Society, 2008).

[172] M. Hochbruck and A. Ostermann, Acta Numer. **19**, 209 (2010).

[173] T. Jawecki, W. Auzinger, and O. Koch, BIT Numerical Mathematics **60**, 157 (2020).

[174] B. Militello and A. Napoli, Phys. Lett. A **384**, 126355 (2020).

[175] A. Biella and M. Schiró, Quantum **5**, 528 (2021).

[176] G. Kordas, D. Witthaut, P. Buonsante, A. Vezzani, R. Burioni, A. I. Karanikas, and S. Wimberger, Eur. Phys. J. Special Topics **224**, 2127 (2015).

[177] Z. Denis and S. Wimberger, Condens. Matter **3**, `10.3390/condmat3010002` (2018).

[178] D. Jaksch and P. Zoller, New J. Phys. **5**, 56 (2003).

[179] G. Lüders, Ann. Phys. **443**, 322 (1950).

[180] S. Keßler and F. Marquardt, Phys. Rev. A **89**, 061601(R) (2014).

[181] M. Atala, M. Aidelsburger, M. Lohse, J. T. Barreiro, B. Paredes, and I. Bloch, Nat. Phys. **10**, 588 (2014).

[182] C. Maier, T. Brydges, P. Jurcevic, N. Trautmann, C. Hempel, B. P. Lanyon, P. Hauke, R. Blatt, and C. F. Roos, Phys. Rev. Lett. **122**, 050501 (2019).

[183] P. E. Kloeden and E. Platen, *Numerical Solution of Stochastic Differential Equations*, 1st ed., Vol. 23, Stochastic Modelling and Applied Probability (Springer-Verlag Berlin Heidelberg, 1992).

[184] C. Gardiner, *Stochastic Methods: A Handbook for the Natural and Social Sciences*, 4th ed., Vol. 13, Springer Series in Synergetics (Springer-Verlag Berlin Heidelberg, 2009).

[185] H. Hasegawa and H. Ezawa, Progress of Theoretical Physics Supplement **69**, 41 (1980).

[186] A. Barchielli and M. Gregoratti, *Quantum Trajectories and Measurements in Continuous Time: The Diffusive Case*, 1st ed., Vol. 782, Lecture Notes in Physics (Springer-Verlag Berlin Heidelberg, 2009).

[187] K. Jacobs and D. A. Steck, Contemporary Physics **47**, 279 (2006).

[188] H. M. Wiseman and G. J. Milburn, *Quantum Measurement and Control* (Cambridge University Press, Cambridge, 2009).

[189] I. Semina, V. Semin, F. Petruccione, and A. Barchielli, Open Sys. Inf. Dyn. **21**, 1440008 (2014).

[190] N. Gisin and I. C. Percival, J. Phys. A: Math. Gen. **25**, 5677 (1992).

[191] S. D. Huber, E. Altman, H. P. Büchler, and G. Blatter, Phys. Rev. B **75**, 085106 (2007).

[192] M. Morgado and S. Whitlock, AVS Quantum Science **3**, 023501 (2021).

[193] A. Signoles, T. Franz, R. Ferracini Alves, M. Gärttner, S. Whitlock, G. Zürn, and M. Weidemüller, Phys. Rev. X **11**, 011011 (2021).

[194] K. T. Geier, J. Reichstetter, and P. Hauke, arXiv:`2106.12599 [quant-ph]` (2021).

[195] R. Blatt and C. F. Roos, Nat. Phys. **8**, 277 (2012).

[196] C. Schneider, D. Porras, and T. Schaetz, Rep. Progr. Phys. **75**, 024401 (2012).

[197] C. Monroe, W. C. Campbell, L.-M. Duan, Z.-X. Gong, A. V. Gorshkov, P. W. Hess, R. Islam, K. Kim, N. M. Linke, G. Pagano, P. Richerme, C. Senko, and N. Y. Yao, Rev. Mod. Phys. **93**, 025001 (2021).

[198] Y. Imry and R. Landauer, Rev. Mod. Phys. **71**, S306 (1999).

[199] S. Datta, *Quantum Transport: Atom to Transistor* (Cambridge University Press, Cambridge, 2005).

[200] R. E. Prange and S. M. Girvin, *The Quantum Hall Effect*, Second, Maryland Subseries: Based on Lectures at the University of Maryland, College Park (Springer, New York, 1990).

[201] D. Yoshioka, *The Quantum Hall Effect*, 1st ed., Springer Series in Solid-State Sciences (Springer, Berlin, Heidelberg, 2002).

[202] M. O. Goerbig, "Quantum Hall effects," in *Ultracold Gases and Quantum Information: Lecture Notes of the Les Houches Summer School in Singapore: Volume 91, July 2009*, edited by C. Miniatura, L.-C. Kwek, M. Ducloy, B. Grémaud, B.-G. Englert, L. Cugliandolo, A. Ekert, and K. K. Phua (Oxford University Press, Oxford, 2009) Chap. 6.

[203] K. von Klitzing, T. Chakraborty, P. Kim, V. Madhavan, X. Dai, J. McIver, Y. Tokura, L. Savary, D. Smirnova, A. M. Rey, C. Felser, J. Gooth, and X. Qi, Nat. Rev. Phys. **2**, 397 (2020).

[204] C. Cao, E. Elliott, J. Joseph, H. Wu, J. Petricka, T. Schäfer, and J. E. Thomas, Science **331**, 58 (2011).

[205] A. Sommer, M. Ku, G. Roati, and M. W. Zwierlein, Nature (London) **472**, 201 (2011).

[206] L. A. Sidorenkov, M. K. Tey, R. Grimm, Y.-H. Hou, L. Pitaevskii, and S. Stringari, Nature (London) **498**, 78 (2013).

[207] T. Fukuhara, P. Schauß, M. Endres, S. Hild, M. Cheneau, I. Bloch, and C. Gross, Nature (London) **502**, 76 (2013).

[208] P. Jurcevic, B. P. Lanyon, P. Hauke, C. Hempel, P. Zoller, R. Blatt, and C. F. Roos, Nature (London) **511**, 202 (2014).

[209] J. Smith, A. Lee, P. Richerme, B. Neyenhuis, P. W. Hess, P. Hauke, M. Heyl, D. A. Huse, and C. Monroe, Nat. Phys. **12**, 907 (2016).

[210] L. Pitaevskii and S. Stringari, "Second Sound in Ultracold Atomic Gases," in *Universal Themes of Bose-Einstein Condensation*, edited by N. P. Proukakis, D. W. Snoke, and P. B. Littlewood (Cambridge University Press, 2017) Chap. 16, pp. 322–347.

[211] S. Scherg, T. Kohlert, J. Herbrych, J. Stolpp, P. Bordia, U. Schneider, F. Heidrich-Meisner, I. Bloch, and M. Aidelsburger, Phys. Rev. Lett. **121**, 130402 (2018).

[212] P. T. Brown, D. Mitra, E. Guardado-Sanchez, R. Nourafkan, A. Reymbaut, C.-D. Hébert, S. Bergeron, A.-M. S. Tremblay, J. Kokalj, D. A. Huse, P. Schauß, and W. S. Bakr, Science **363**, 379 (2019).

[213] M. A. Nichols, L. W. Cheuk, M. Okan, T. R. Hartke, E. Mendez, T. Senthil, E. Khatami, H. Zhang, and M. W. Zwierlein, Science, `10.1126/science.aat4387` (2019).

[214] A. Farolfi, D. Trypogeorgos, C. Mordini, G. Lamporesi, and G. Ferrari, Phys. Rev. Lett. **125**, 030401 (2020).

[215] P. B. Patel, Z. Yan, B. Mukherjee, R. J. Fletcher, J. Struck, and M. W. Zwierlein, Science **370**, 1222 (2020).

[216] P. N. Jepsen, J. Amato-Grill, I. Dimitrova, W. W. Ho, E. Demler, and W. Ketterle, Nature (London) **588**, 403 (2020).

[217] P. Christodoulou, M. Gałka, N. Dogra, R. Lopes, J. Schmitt, and Z. Hadzibabic, Nature (London) **594**, 191 (2021).

[218] B. Mukherjee, A. Shaffer, P. B. Patel, Z. Yan, C. C. Wilson, V. Crépel, R. J. Fletcher, and M. Zwierlein, arXiv:`2106.11300 [cond-mat.quant-gas]` (2021).

[219] P. Hauke, M. Lewenstein, and A. Eckardt, Phys. Rev. Lett. **113**, 045303 (2014).

[220] N. Fläschner, B. S. Rem, M. Tarnowski, D. Vogel, D.-S. Lühmann, K. Sengstock, and C. Weitenberg, Science **352**, 1091 (2016).

[221] B. Irsigler, J.-H. Zheng, and W. Hofstetter, Phys. Rev. A **100**, 023610 (2019).

[222] M. Gluza and J. Eisert, arXiv:2005.09000 [cond-mat.quant-gas] (2021).

[223] J.-P. Brantut, J. Meineke, D. Stadler, S. Krinner, and T. Esslinger, Science **337**, 1069 (2012).

[224] S. Krinner, D. Stadler, D. Husmann, J.-P. Brantut, and T. Esslinger, Nature (London) **517**, 64 (2015).

[225] C. Laflamme, D. Yang, and P. Zoller, Phys. Rev. A **95**, 043843 (2017).

[226] S. Hacohen-Gourgy, L. S. Martin, E. Flurin, V. V. Ramasesh, K. B. Whaley, and I. Siddiqi, Nature (London) **538**, 491 (2016).

[227] J. T. Monroe, N. Yunger Halpern, T. Lee, and K. W. Murch, Phys. Rev. Lett. **126**, 100403 (2021).

[228] P. G. Harper, Proc. Phys. Soc. London, Sect. A **68**, 879 (1955).

[229] D. R. Hofstadter, Phys. Rev. B **14**, 2239 (1976).

[230] B. A. Bernevig and T. L. Hughes, *Topological Insulators and Topological Superconductors* (Princeton University Press, Princeton, Oxford, 2013).

[231] M. Aidelsburger, M. Atala, M. Lohse, J. T. Barreiro, B. Paredes, and I. Bloch, Phys. Rev. Lett. **111**, 185301 (2013).

[232] H. Miyake, G. A. Siviloglou, C. J. Kennedy, W. C. Burton, and W. Ketterle, Phys. Rev. Lett. **111**, 185302 (2013).

[233] M. Mancini, G. Pagano, G. Cappellini, L. Livi, M. Rider, J. Catani, C. Sias, P. Zoller, M. Inguscio, M. Dalmonte, and L. Fallani, Science **349**, 1510 (2015).

[234] B. K. Stuhl, H.-I. Lu, L. M. Aycock, D. Genkina, and I. B. Spielman, Science **349**, 1514 (2015).

[235] M. E. Tai, A. Lukin, M. Rispoli, R. Schittko, T. Menke, D. Borgnia, P. M. Preiss, F. Grusdt, A. M. Kaufman, and M. Greiner, Nature (London) **546**, 519 (2017).

[236] A. Dhar, M. Maji, T. Mishra, R. V. Pai, S. Mukerjee, and A. Paramekanti, Phys. Rev. A **85**, 041602(R) (2012).

[237] A. Dhar, T. Mishra, M. Maji, R. V. Pai, S. Mukerjee, and A. Paramekanti, Phys. Rev. B **87**, 174501 (2013).

[238] D. Hügel and B. Paredes, Phys. Rev. A **89**, 023619 (2014).

[239] A. Petrescu and K. Le Hur, Phys. Rev. B **91**, 054520 (2015).

[240] S. Greschner, M. Piraud, F. Heidrich-Meisner, I. P. McCulloch, U. Schollwöck, and T. Vekua, Phys. Rev. Lett. **115**, 190402 (2015).

[241] G. Chen, K. R. A. Hazzard, A. M. Rey, and M. Hermele, Phys. Rev. A **93**, 061601(R) (2016).

[242] S. Greschner, M. Piraud, F. Heidrich-Meisner, I. P. McCulloch, U. Schollwöck, and T. Vekua, Phys. Rev. A **94**, 063628 (2016).

[243] C. Romen and A. M. Läuchli, Phys. Rev. B **98**, 054519 (2018).

[244] L. Barbiero, L. Chomaz, S. Nascimbene, and N. Goldman, Phys. Rev. Research **2**, 043340 (2020).

[245] R. Schmied, T. Roscilde, V. Murg, D. Porras, and J. I. Cirac, **10**, 045017 (2008).

[246] P. Hauke, T. Roscilde, V. Murg, J. I. Cirac, and R. Schmied, New J. Phys. **12**, 053036 (2010).

[247] P. Hauke, Phys. Rev. B **87**, 014415 (2013).

[248] J. Struck, M. Weinberg, C. Ölschläger, P. Windpassinger, J. Simonet, K. Sengstock, R. Höppner, P. Hauke, A. Eckardt, M. Lewenstein, and L. Mathey, Nat. Phys. **9**, 738 (2013).

[249] J. Richter, C. Gros, and W. Weber, Phys. Rev. B **44**, 906 (1991).

[250] T. Manovitz, Y. Shapira, N. Akerman, A. Stern, and R. Ozeri, PRX Quantum **1**, 020303 (2020).

[251] P. Soltan-Panahi, J. Struck, P. Hauke, A. Bick, W. Plenkers, G. Meineke, C. Becker, P. Windpassinger, M. Lewenstein, and K. Sengstock, Nat. Phys. **7**, 434 (2011).

[252] T. Matsubara and H. Matsuda, Prog. Theor. Phys. **16**, 569 (1956).

[253] M. Metcalf, C.-Y. Lai, M. Di Ventra, and C.-C. Chien, Phys. Rev. A **98**, 053601 (2018).

[254] N. Roy and A. Sharma, Phys. Rev. B **100**, 195143 (2019).

[255] P. Busch, "'No Information Without Disturbance': Quantum Limitations of Measurement," in *Quantum Reality, Relativistic Causality, and Closing the Epistemic Circle: Essays in Honour of Abner Shimony* (Springer Netherlands, Dordrecht, 2009), pp. 229–256.

[256] H. Kawamura, arXiv:`cond-mat/0202109 [cond-mat.stat-mech]` (2002).

[257] T. Holstein and H. Primakoff, Phys. Rev. **58**, 1098 (1940).

[258] W. J. Caspers and G. I. Tielen, Physica A **135**, 519 (1986).

[259] J. J. García-Ripoll and J. K. Pachos, New J. Phys. **9**, 139 (2007).

[260] L. Isaev and A. M. Rey, Phys. Rev. Lett. **115**, 165302 (2015).

[261] D. Porras and J. I. Cirac, Phys. Rev. Lett. **93**, 263602 (2004).

[262] S. Debnath, N. M. Linke, S.-T. Wang, C. Figgatt, K. A. Landsman, L.-M. Duan, and C. Monroe, Phys. Rev. Lett. **120**, 073001 (2018).

[263] D. Porras and J. I. Cirac, Phys. Rev. Lett. **92**, 207901 (2004).

[264] T. Giamarchi, *Quantum Physics in One Dimension*, Vol. 121, International Series of Monographs on Physics (Clarendon Press, Oxford, 2004).

[265] N. Majlis, *The Quantum Theory of Magnetism*, 2nd (World Scientific, Singapore, 2007).

[266] D. J. Wineland, C. Monroe, W. M. Itano, D. Leibfried, B. E. King, and D. M. Meekhof, J. Res. Natl. Inst. Stand. Technol. **103**, 259 (1998).

[267] J. Eschner, G. Morigi, F. Schmidt-Kaler, and R. Blatt, J. Opt. Soc. Am. B **20**, 1003 (2003).

[268] R. Lechner, C. Maier, C. Hempel, P. Jurcevic, B. P. Lanyon, T. Monz, M. Brownnutt, R. Blatt, and C. F. Roos, Phys. Rev. A **93**, 053401 (2016).

[269] L. Feng, W. L. Tan, A. De, A. Menon, A. Chu, G. Pagano, and C. Monroe, Phys. Rev. Lett. **125**, 053001 (2020).

[270] J.-S. Chen, K. Wright, N. C. Pisenti, D. Murphy, K. M. Beck, K. Landsman, J. M. Amini, and Y. Nam, Phys. Rev. A **102**, 043110 (2020).

[271] P. Schindler, D. Nigg, T. Monz, J. T. Barreiro, E. Martinez, S. X. Wang, S. Quint, M. F. Brandl, V. Nebendahl, C. F. Roos, M. Chwalla, M. Hennrich, and R. Blatt, New J. Phys. **15**, 123012 (2013).

[272] D. Leibfried, D. M. Meekhof, B. E. King, C. Monroe, W. M. Itano, and D. J. Wineland, Phys. Rev. Lett. **77**, 4281 (1996).

[273] C. Roos, "Controlling the quantum state of trapped ions," PhD thesis (University of Innsbruck, Innsbruck, 2000).

[274] F. Gebert, Y. Wan, F. Wolf, J. C. Heip, and P. O. Schmidt, New J. Phys. **18**, 013037 (2016).

[275] M. Um, J. Zhang, D. Lv, Y. Lu, S. An, J.-N. Zhang, H. Nha, M. S. Kim, and K. Kim, Nat. Commun. **7**, 11410 (2016).

[276] S. Ding, G. Maslennikov, R. Hablützel, and D. Matsukevich, Phys. Rev. Lett. **119**, 193602 (2017).

[277] O. Dutta, A. Przysiężna, and J. Zakrzewski, Sci. Rep. **5**, 11060 (2015).

[278] N. Schiller, Y. Oreg, and K. Snizhko, arXiv:2111.05399 [cond-mat.mes-hall] (2021).

[279] D. S. Goldbaum and E. J. Mueller, Phys. Rev. A **77**, 033629 (2008).

[280] O. Romero-Isart, C. Navau, A. Sanchez, P. Zoller, and J. I. Cirac, Phys. Rev. Lett. **111**, 145304 (2013).

[281] A. R. Kolovsky, New J. Phys. **8**, 197 (2006).

[282] L. Amico, D. Aghamalyan, F. Auksztol, H. Crepaz, R. Dumke, and L. C. Kwek, Sci. Rep. **4**, 4298 (2014).

[283] M. Cominotti, M. Rizzi, D. Rossini, D. Aghamalyan, L. Amico, L. C. Kwek, F. Hekking, and A. Minguzzi, Eur. Phys. J. Special Topics **224**, 519 (2015).

[284] L. Kohn, P. Silvi, M. Gerster, M. Keck, R. Fazio, G. E. Santoro, and S. Montangero, Phys. Rev. A **101**, 023617 (2020).

[285] M. D. Caio, G. Möller, N. R. Cooper, and M. J. Bhaseen, Nat. Phys. **15**, 257 (2019).

[286] K. T. Geier, G. I. Martone, P. Hauke, and S. Stringari, Phys. Rev. Lett. **127**, 115301 (2021).

[287] W. Demtröder, *Atoms, Molecules and Photons, An Introduction to Atomic-, Molecular-and Quantum Physics*, 3rd ed., Graduate Texts in Physics (Springer, Berlin, Heidelberg, 2018).

[288] Y. A. Bychkov and E. I. Rashba, J. Phys. C **17**, 6039 (1984).

[289] G. Dresselhaus, Phys. Rev. **100**, 580 (1955).

[290] Y.-J. Lin, K. Jiménez-García, and I. B. Spielman, Nature (London) **471**, 83 (2011).

[291] J. Léonard, A. Morales, P. Zupancic, T. Donner, and T. Esslinger, Science **358**, 1415 (2017).

[292] L. Tanzi, S. M. Roccuzzo, E. Lucioni, F. Famà, A. Fioretti, C. Gabbanini, G. Modugno, A. Recati, and S. Stringari, Nature (London) **574**, 382 (2019).

[293] M. Guo, F. Böttcher, J. Hertkorn, J.-N. Schmidt, M. Wenzel, H. P. Büchler, T. Langen, and T. Pfau, Nature (London) **574**, 386 (2019).

[294] G. Natale, R. M. W. van Bijnen, A. Patscheider, D. Petter, M. J. Mark, L. Chomaz, and F. Ferlaino, Phys. Rev. Lett. **123**, 050402 (2019).

[295] D. Petter, A. Patscheider, G. Natale, M. J. Mark, M. A. Baranov, R. van Bijnen, S. M. Roccuzzo, A. Recati, B. Blakie, D. Baillie, L. Chomaz, and F. Ferlaino, Phys. Rev. A **104**, L011302 (2021).

[296] L. Tarruell, Private communication, 2020.

[297] Y. Li, G. I. Martone, and S. Stringari, "Spin–orbit-coupled Bose–Einstein condensates," in *Annual Review of Cold Atoms and Molecules*, Vol. 3, edited by K. W. Madison, K. Bongs, L. D. Carr, A. M. Rey, and H. Zhai (World Scientific, Singapore, 2015) Chap. 5, pp. 201–250.

[298] W. Zheng, Z.-Q. Yu, X. Cui, and H. Zhai, J. Phys. B **46**, 134007 (2013).

[299] X.-L. Chen, J. Wang, Y. Li, X.-J. Liu, and H. Hu, Phys. Rev. A **98**, 013614 (2018).

[300] T.-L. Ho and S. Zhang, Phys. Rev. Lett. **107**, 150403 (2011).

[301] Y. Li, L. P. Pitaevskii, and S. Stringari, Phys. Rev. Lett. **108**, 225301 (2012).

[302] G. I. Martone, Y. Li, and S. Stringari, Phys. Rev. A **90**, 041604(R) (2014).

[303] G. I. Martone, Eur. Phys. J. Special Topics **224**, 553 (2015).

[304] W. Bao, I.-L. Chern, and F. Y. Lim, J. Comput. Phys. **219**, 836 (2006).

[305] Y. Li, G. I. Martone, and S. Stringari, Europhys. Lett. **99**, 56008 (2012).

[306] J.-Y. Zhang, S.-C. Ji, Z. Chen, L. Zhang, Z.-D. Du, B. Yan, G.-S. Pan, B. Zhao, Y.-J. Deng, H. Zhai, S. Chen, and J.-W. Pan, Phys. Rev. Lett. **109**, 115301 (2012).

[307] G. I. Martone, "Static and dynamic properties of spin–orbit-coupled Bose–Einstein condensates," PhD thesis (University of Trento, 2014).

[308] S. Stringari and G. I. Martone, Private communication, 2020.

[309] X. Antoine, W. Bao, and C. Besse, Comput. Phys. Commun. **184**, 2621 (2013).

[310] G. I. Martone, Y. Li, L. P. Pitaevskii, and S. Stringari, Phys. Rev. A **86**, 063621 (2012).

[311] Y. Li, G. I. Martone, L. P. Pitaevskii, and S. Stringari, Phys. Rev. Lett. **110**, 235302 (2013).

[312] G. I. Martone, T. Bienaimé, and N. Cherroret, Phys. Rev. A **104**, 013510 (2021).

[313] A. Sartori, J. Marino, S. Stringari, and A. Recati, New J. Phys. **17**, 093036 (2015).

[314] L. Chen, H. Pu, Z.-Q. Yu, and Y. Zhang, Phys. Rev. A **95**, 033616 (2017).

[315] G. I. Martone and S. Stringari, SciPost Phys. **11**, 92 (2021).

[316] B. Nowak and T. Gasenzer, New J. Phys. **16**, 093052 (2014).

[317] M. Prüfer, P. Kunkel, H. Strobel, S. Lannig, D. Linnemann, C.-M. Schmied, J. Berges, T. Gasenzer, and M. K. Oberthaler, Nature (London) **563**, 217 (2018).

[318] S. Erne, R. Bücker, T. Gasenzer, J. Berges, and J. Schmiedmayer, Nature (London) **563**, 225 (2018).

[319] A. H. Guth, Phys. Rev. D **23**, 347 (1981).

[320] A. Starobinsky, Phys. Lett. B **91**, 99 (1980).

[321] A. A. Starobinsky, Phys. Lett. B **117**, 175 (1982).

[322] L. Kofman, A. D. Linde, and A. A. Starobinsky, Phys. Rev. D **56**, 3258 (1997).

[323] M. A. Amin, M. P. Hertzberg, D. I. Kaiser, and J. Karouby, Int. J. Mod. Phys. **D24**, 1530003 (2014).

[324] S. Y. Khlebnikov and I. I. Tkachev, Phys. Rev. Lett. **77**, 219 (1996).

[325] J. Berges and T. Gasenzer, Phys. Rev. A **76**, 033604 (2007).

[326] A. Sinatra, C. Lobo, and Y. Castin, J. Phys. B **35**, 3599 (2002).

[327] P. Blakie, A. Bradley, M. Davis, R. Ballagh, and C. Gardiner, Adv. Phys. **57**, 363 (2008).

[328] M. Uhlmann, Y. Xu, and R. Schutzhold, New J. Phys. **7**, 248 (2005).

[329] S. Eckel, A. Kumar, T. Jacobson, I. B. Spielman, and G. K. Campbell, Phys. Rev. X **8**, 021021 (2018).

[330] S.-Y. Chä and U. R. Fischer, Phys. Rev. Lett. **118**, 130404 (2017).

[331] P. Jain, S. Weinfurtner, M. Visser, and C. W. Gardiner, Phys. Rev. A **76**, 033616 (2007).

[332] P. O. Fedichev and U. R. Fischer, Phys. Rev. A **69**, 033602 (2004).

[333] C. Viermann, M. Sparn, N. Liebster, M. Hans, E. Kath, Á. Parra-López, M. Tolosa-Simeón, N. Sánchez-Kuntz, T. Haas, H. Strobel, S. Floerchinger, and M. K. Oberthaler, arXiv:2202.10399 [cond-mat.quant-gas] (2022).

[334] M. Tolosa-Simeón, Á. Parra-López, N. Sánchez-Kuntz, T. Haas, C. Viermann, M. Sparn, N. Liebster, M. Hans, E. Kath, H. Strobel, M. K. Oberthaler, and S. Floerchinger, arXiv:2202.10441 [cond-mat.quant-gas] (2022).

[335] U. R. Fischer and R. Schutzhold, Phys. Rev. A **70**, 063615 (2004).

[336] C. Neuenhahn, A. Polkovnikov, and F. Marquardt, Phys. Rev. Lett. **109**, 085304 (2012).

[337] C. Neuenhahn and F. Marquardt, New J. Phys. **17**, 125007 (2015).

[338] A. Posazhennikova, M. Trujillo-Martinez, and J. Kroha, Phys. Rev. Lett. **116**, 225304 (2016).

[339] T. V. Zache, V. Kasper, and J. Berges, Phys. Rev. A **95**, 063629 (2017).

[340] S. Robertson, F. Michel, and R. Parentani, Phys. Rev. D **98**, 056003 (2018).

[341] S. Butera and I. Carusotto, Phys. Rev. D **104**, 083503 (2021).

[342] K. Staliunas, S. Longhi, and G. J. de Valcárcel, Phys. Rev. Lett. **89**, 210406, 210406 (2002).

[343] P. Engels, C. Atherton, and M. A. Hoefer, Phys. Rev. Lett. **98**, 095301 (2007).

[344] S. E. Pollack, D. Dries, R. G. Hulet, K. M. F. Magalhães, E. A. L. Henn, E. R. F. Ramos, M. A. Caracanhas, and V. S. Bagnato, Phys. Rev. A **81**, 053627, 053627 (2010).

[345] I. Vidanović, A. Balaž, H. Al-Jibbouri, and A. Pelster, Phys. Rev. A **84**, 013618, 013618 (2011).

[346] J.-C. Jaskula, G. B. Partridge, M. Bonneau, R. Lopes, J. Ruaudel, D. Boiron, and C. I. Westbrook, Phys. Rev. Lett. **109**, 220401 (2012).

[347] J. H. V. Nguyen, M. C. Tsatsos, D. Luo, A. U. J. Lode, G. D. Telles, V. S. Bagnato, and R. G. Hulet, Phys. Rev. X **9**, 011052 (2019).

[348] Z. Zhang, K.-X. Yao, L. Feng, J. Hu, and C. Chin, Nat. Phys. **16**, 652 (2020).

[349] J. Berges and J. Serreau, Phys. Rev. Lett. **91**, 111601 (2003).

[350] C.-M. Schmied, M. Prüfer, M. K. Oberthaler, and T. Gasenzer, Phys. Rev. A **99**, 033611 (2019).

[351] J. A. P. Glidden, C. Eigen, L. H. Dogra, T. A. Hilker, R. P. Smith, and Z. Hadzibabic, Nat. Phys. **17**, 457 (2021).

[352] A. Linde, Phys. Lett. B **108**, 389 (1982).

[353] A. Albrecht and P. J. Steinhardt, Phys. Rev. Lett. **48**, 1220 (1982).

[354] P. B. Greene, L. Kofman, and A. A. Starobinsky, Nucl. Phys. **B543**, 423 (1999).

[355] A. Suárez and P.-H. Chavanis, Phys. Rev. D **92**, 023510 (2015).

[356] V. Mukhanov and S. Winitzki, *Introduction to Quantum Effects in Gravity* (Cambridge University Press, Cambridge, 2007).

[357] V. Gritsev, P. Barmettler, and E. Demler, New J. Phys. **12**, 113005 (2010).

[358] M. Olshanii, H. Perrin, and V. Lorent, Phys. Rev. Lett. **105**, 095302, 095302 (2010).

[359] M. Holten, L. Bayha, A. C. Klein, P. A. Murthy, P. M. Preiss, and S. Jochim, Phys. Rev. Lett. **121**, 120401 (2018).

[360] C.-L. Hung, X. Zhang, L.-C. Ha, S.-K. Tung, N. Gemelke, and C. Chin, New J. Phys. **13**, 075019 (2011).

[361] R. Saint-Jalm, P. C. M. Castilho, É. Le Cerf, B. Bakkali-Hassani, J.-L. Ville, S. Nascimbene, J. Beugnon, and J. Dalibard, Phys. Rev. X **9**, 021035, 021035 (2019).

[362] N. W. McLachlan, *Theory and Application of Mathieu Functions* (Clarendon Press, Oxford, 1951).

[363] A. H. Nayfeh, *Perturbation Methods* (Wiley, New York, 1973).

[364] V. E. Zakharov, V. S. L'vov, and G. Falkovich, *Kolmogorov Spectra of Turbulence I: Wave Turbulence*, Springer Series in Nonlinear Dynamics (Springer, Berlin, Heidelberg, 1992).

[365] J. Berges, K. Boguslavski, A. Chatrchyan, and J. Jaeckel, Phys. Rev. D **96**, 076020 (2017).

[366] J. Berges, A. Rothkopf, and J. Schmidt, Phys. Rev. Lett. **101**, 041603 (2008).

[367] C. Scheppach, J. Berges, and T. Gasenzer, Phys. Rev. A **81**, 033611 (2010).

[368] S. Dyachenko, A. Newell, A. Pushkarev, and V. Zakharov, Physica D **57**, 96 (1992).

[369] B. Nowak, J. Schole, D. Sexty, and T. Gasenzer, Phys. Rev. A **85**, 043627 (2012).

[370] N. Navon, A. L. Gaunt, R. P. Smith, and Z. Hadzibabic, Nature (London) **539**, 72 (2016).

[371] J. Berges, K. Boguslavski, S. Schlichting, and R. Venugopalan, J. High Energy Phys. **2014**, 54 (2014).

[372] J. L. Ville, T. Bienaimé, R. Saint-Jalm, L. Corman, M. Aidelsburger, L. Chomaz, K. Kleinlein, D. Perconte, S. Nascimbène, J. Dalibard, and J. Beugnon, Phys. Rev. A **95**, 013632, 013632 (2017).

[373] C. R. Cabrera Córdova, "Quantum liquid droplets in a mixture of Bose–Einstein condensates," PhD thesis (ICFO – Institute of Photonic Sciences, Universidad Politécnica de Cataluña, Barcelona, 2018).

[374] R. L. D. Campbell, R. P. Smith, N. Tammuz, S. Beattie, S. Moulder, and Z. Hadzibabic, Phys. Rev. A **82**, 063611 (2010).

[375] M. Landini, S. Roy, G. Roati, A. Simoni, M. Inguscio, G. Modugno, and M. Fattori, Phys. Rev. A **86**, 033421 (2012).

[376] C. D'Errico, M. Zaccanti, M. Fattori, G. Roati, M. Inguscio, G. Modugno, and A. Simoni, New J. Phys. **9**, 223 (2007).

[377] A. Kurkela and Y. Zhu, Phys. Rev. Lett. **115**, 182301 (2015).

[378] A. L. Gaunt, T. F. Schmidutz, I. Gotlibovych, R. P. Smith, and Z. Hadzibabic, Phys. Rev. Lett. **110**, 200406 (2013).

[379] H. Ritsch, P. Domokos, F. Brennecke, and T. Esslinger, Rev. Mod. Phys. **85**, 553 (2013).

[380] C. Qu and S. Stringari, Phys. Rev. Lett. **120**, 183202 (2018).

[381] J. Radić, T. A. Sedrakyan, I. B. Spielman, and V. Galitski, Phys. Rev. A **84**, 063604 (2011).

[382] P. Langevin, C. R. Acad. Sci. (Paris) **146**, 530 (1908).

[383] D. S. Lemons and A. Gythiel, Am. J. Phys. **65**, 1079 (1997).

[384] K. Itô, Memoirs Amer. Math. Soc. **4**, 1 (1951).

[385] W. H. Press, S. A. Teukolsky, W. T. Vetterling, and B. P. Flannery, *Numerical Recipes: The Art of Scientific Computing*, 3rd ed. (Cambridge University Press, Cambridge, 2007).

[386] J. G. Gaines and T. J. Lyons, SIAM J. Appl. Math. **57**, 1455 (1997).

[387] K. Burrage and P. Burrage, Phys. D: Nonlinear Phenom. **133**, 34 (1999).

[388] S. Blanes, F. Casas, J. Oteo, and J. Ros, Phys. Rep. **470**, 151 (2009).

[389] K. Kamm, S. Pagliarani, and A. Pascucci, J. Sci. Comput. **89**, 56 (2021).

[390] C. Moler and C. Van Loan, SIAM Rev. **45**, 3 (2003).

[391] C. J. Pethick and H. Smith, *Bose–Einstein Condensation in Dilute Gases*, 2nd ed. (Cambridge University Press, Cambridge, 2008).

[392] S. Blanes and P. Moan, J. Comput. Appl. Math. **142**, 313 (2002).

[393] S. A. Chin, Phys. Rev. E **76**, 056708 (2007).